On the recent evolution of Atlantic Water at the entrance to the Arctic Ocean : observations and Mercator Ocean operational model

Marylou Athanase

THESE DE DOCTORAT DE

SORBONNE UNIVERSITE, Sciences

Spécialité: Océanographie

Ecole Doctorale 129

Réalisée au

Laboratoire d'Océanographie et du Climat:

Expérimentations et Approches Numériques

Présentée par

Marylou Athanase

On the recent evolution of Atlantic Water at the entrance to the Arctic Ocean: Observations and Mercator Ocean operational model

Soutenance prevue le 05/11/2020

Devant le jury composé de:

Mme.	Christine Provost	LOCEAN SU, Paris	Directrice
Mme.	Nathalie Sennéchael	LOCEAN SU, Paris	Directrice
Mme.	Pascale Bouruet-Aubertot	LOCEAN SU, Paris	Présidente
Mme.	Ursula Schauer	AWI, Allemagne	Rapporteure
Mme.	Camille Lique	LOPS, Brest	Rapporteure
M.	Jari Haapala	FMI, Finlande	Examinateur
Mme.	Amelie Meyer	UTAS, Australie	Examinatrice
M.	Gilles Garric	Mercator Ocean, Toulouse	Examinateur
Mme.	M-Dolores Pérez Hernández	IOCAG, Grande Canarie	Invitée

Remerciements

Je souhaite tout d'abord remercier les membres du Jury pour avoir accepter de lire et d'évaluer cette thèse.

J'adresse ensuite mes sincères remerciements à mes encadrantes, Christine et Nathalie, pour leur disponibilité, leur energie, leurs conseils et leur soutien pendant ces trois années de thèse. Faire partie de leur équipe a été une opportunité incroyable et enrichissante sur bien des points !

Je remercie également Gilles et Jean-Michel pour nos nombreux échanges sur le modèle Mercator Océan, toujours dans la bonne humeur. Merci également à Lola Pérez-Hernandez, avec qui travailler a été un réel plaisir.

Un grand merci tout particulièrement à Zoé et Camila, qui m'ont beaucoup appris du début à la fin de cette thèse. Je pense bien sûr à Cécilia, Sarah, Camila, Léa, Babette, Aude, et Laureline, qui forment notre super bande des dames ABC: merci pour tous ces rires et ces histoires partagées pendant nos déjeuners ou nos soirées jeux de société !

Je pense également aux anciens du Master OACOS, Lucie, Lilian, Clément et Marie, avec qui j'ai partagé toutes ces UE qui nous ont emmenés vers des parcours si similaires et différents à la fois. Je remercie aussi Sam Cornish, pour sa sublime photographie de glace Arctique en couverture de cette thèse.

Je ne pouvais pas oublier ceux qui m'ont toujours soutenue, dans les bons comme les mauvais moments: Nathalie, Kévin, Vincent, Quentin, Charles, Florian, et Thomas. Merci pour ces fous rires, ces vacances, ces découvertes et tout ce temps partagé ensemble ! Axel, depuis toutes ces années, tu es mon amie et ma famille: merci de m'avoir fait tant rire et de m'avoir amenée à me dépasser sur tant de points.

Enfin, un immense merci à mes parents: à ma mère pour sa présence et son soutien indéféctible, à mon père pour son écoute et ses conseils toujours bienveillants.

SUMMARY

The Arctic is undergoing faster and more severe changes than the rest of the world. September (July) Arctic sea-ice extent has decreased by 45% (26%), relative to 1979 (Onarheim et al., 2018). The numerous ongoing changes observed in all the media (ocean, atmosphere, cryosphere) could have consequences for the global climate and mid-latitude regions in particular (Grassi et al., 2013). In this transitioning Arctic, the area north of Svalbard stands out with a more reduced sea-ice cover in winter than in summer. Indeed, the warm and salty Atlantic Water (AW) inflow entering this region through Fram Strait is larger in winter and maintains ice-free conditions. Combination of observations and model outputs provided insights on the recent oceanic conditions in the Western Eurasian and Nansen basins, entry region for the Atlantic Water.

The IAOOS (Ice Atmosphere Ocean Observing System) 2017 drift gathered a unique 8-months long hydrographic and biogeochemical dataset in the upper Western Eurasian Basin (WEB, 0-350m). Analysis of the IAOOS physical parameters in the WEB indicated a fresher surface layer and shallower AW layer in 2017 than in the 2005–2012 WOA13 (World Ocean Atlas 2013) climatology (Athanase et al., 2020). After favourable comparisons with the IAOOS data, the global 1/12° Mercator Ocean operational system (Lellouche et al., 2018) provided insights on the nature and origin of the mesoscale structures documented by the IAOOS platforms. Two halocline eddies observed in the Amundsen Basin likely resulted from instabilities in the frontal zone between fresher Makarov waters and saltier Eurasian waters. A large AW mesoscale structure in the Nansen Basin (140 km crossed as far as 83.7°N, 34.5°E) corresponded to an AW meander from the boundary current in the model, turning into an anticyclonic eddy after the platforms drifted away. A second AW structure at 82.8°N, 3°W, northwest of the Yermak Plateau, could be identified as an AW recirculating branch detaching from the Yermak Plateau slope back toward Fram Strait.

Datasets such as the IAOOS 2017 drift are rare, and observations remain scarce in the transitioning Western Eurasian and Nansen basins. Amongst the numerous changes documented in the area, IAOOS data showed that the base of the lower halocline corresponded to the particularly dense 27.85 kg/m^3 isopycnal in 2017 (Bertosio et al., 2020). This was in agreement with the very deep winter mixed layers recently observed over the continental slope of the Nansen Basin, indicating intense

winter convection bringing AW towards the ocean surface and altering its hydrographic properties (Polyakov et al., 2017; Pérez-Hernandez et al., 2019). We took advantage of 14 years of fields from the Mercator 1/12° physical system to examine winter conditions in the Western Nansen Basin (WNB) over the 2007-2020 period (Athanase et al., 2020). Prior to the analysis, the performance of the Mercator system was assessed using 12 years (2007-2018) of independent observations in the WNB. This evaluation highlighted the skills of the model in representing a realistic AW layer, as well as reproducing a previously documented deep winter convection event. The model showed that deep winter convection and recurrent outflows from troughs northeast of Svalbard dramatically modified the AW. Over the 2007-2020 period, two winters stood out with extreme deep mixed layers in areas that used to be ice-covered: 2017/18 over the northern Yermak Plateau-Sofia Deep; 2012/13 on the continental slope northeast of Svalbard. The northern Yermak Plateau-Sofia Deep and continental slope areas became “Marginal Convection Zones" in 2011 with, from then on, occasionally ice-free conditions, 50-m-ocean temperatures always above 0°C and highly variable mixed layer depths and ocean-to-atmosphere heat fluxes.

Finally, the Mercator system underlined an overall intensification of current velocities in the WNB over 2008-2020 (Athanase et al., submitted). In particular, the model showed the strengthening of the Yermak Branch (YB) –either flowing along the outer edge of the Yermak Plateau or crossing the Plateau–, which fed the southward Return Yermak Branch (RYB) along the eastern flank of the Plateau. Model fields also highlighted the onset of new AW pathways: a recurrent anticyclonic circulation established in Sofia Deep. An offshore AW circulation developed downstream of the Yermak Plateau (following the 3800-3900 m isobaths), fed by waters from the Yermak Plateau tip to the west. East of 20°E, additional AW from boundary current was injected in this offshore circulation, via enhanced basin-ward mesoscale activity.

RESUME

En Arctique, les effets du changement climatique sont plus intenses et plus rapides que sur le reste du globe. L'étendue de banquise en Septembre (Juillet) a diminué de 45% (26%) par rapport à 1979 (Onarheim et al., 2018). En parallèle, les nombreux changements observés dans tous les milieux (océan, atmosphère, cryosphère) pourraient avoir des conséquences sur le climat global et en particulier sur les latitudes moyennes (Grassi et al., 2013). Dans cet Arctique en transition, le nord du Svalbard se démarque par une surface de glace plus réduite en hiver qu'en été. En effet, dans cette région, les eaux Atlantiques entrant en Arctique par le détroit de Fram sont plus chaudes et salées en hiver et maintiennent l'océan libre de glace. L'analyse combinée d'observations in-situ et de sorties de modèle océanique haute-résolution a apporté un nouvel éclairage sur les récentes conditions océaniques du Bassin Eurasien Arctique occidental, région d'entrée des eaux Atlantiques.

En 2017, deux bouées IAOOS (*Ice Atmosphere Ocean Observing System*) ont collecté 8 mois de données hydrographiques et biogéochimiques dans le Bassin Eurasien occidental (0-350 m). L'analyse des paramètres physiques de ce jeu de données a indiqué que la couche de surface observée en 2017 était moins salée qu'en 2007-2012, et la couche chaude des eaux Atlantiques était plus proche de la surface comparé à la climatologie World Ocean Atlas 2013 (Athanase et al., 2019). Après une comparaison favorable aux données IAOOS, le modèle opérationnel global 1/12° Mercator Océan a apporté des informations complémentaires sur l'origine et la nature de quatre structures de méso-échelle documentées par les plateformes IAOOS. Dans le Bassin Amundsen, deux tourbillons de halocline résultaient probablement d'instabilités dans la zone frontale entre les eaux salées du Bassin Eurasien et les eaux plus douces du Bassin Makarov. Dans le Bassin Nansen, la large structure à 83.7°N, 34.5°E fut identifiée comme un méandre d'eaux Atlantiques se détachant du courant de bord et évoluant en un tourbillon anticyclonique après le passage des bouées IAOOS. La seconde structure à 82.8°N, 3°W concordait avec un méandre d'eaux Atlantiques se détachant du Plateau de Yermak pour recirculer vers le Détroit de Fram au sud.

Les jeux de données tels que la dérive IAOOS 2017 sont rares en Arctique, et les observations restent sporadiques dans les Bassins Eurasien et Nansen occidentaux. Parmi les nombreux changements documentés, les données IAOOS ont montré que la

base de halocline corrrespondait à l'isopycne 27.85 kg/m^3 en 2017, un niveau particulièrement dense (Bertosio et al., 2020). Ceci est en accord avec les couches de mélange profondes observées en hiver sur le talus continental du Bassin Nansen, indicatives d'une convection hivernale intense entraînant les eaux Atlantiques vers la surface, modifiant leur propriétés (Polyakov et al., 2017; Pérez-Hernandez et al., 2019). Les 14 années de sorties du modèle Mercator ont été utilisées pour examiner les conditions hivernales dans le Bassin Nansen occidental en 2007-2020 (Athanase et al., 2020). Au préalable, 12 ans (2007-2018) de données non-assimilées par le modèle sont utilisés pour évaluer sa performance dans la région. Cette évaluation a démontré la capacité du modèle à représenter les eaux Atlantiques de façon réaliste, ainsi qu'à reproduire un évènement de convection hivernale. Les sorties du modèle ont montré que les propriétés des eaux Atlantiques ont été considérablement modifiées par la convection hivernale profonde et par l'écoulement récurrent d'eaux relativement moins chaudes et salées venant du plateau continental. De 2007 à 2020, deux hivers exceptionnels se démarquent avec des couches de mélange particulièrement profondes dans des zones précédemment couvertes de glace: 2017/18 sur le Plateau de Yermak et Sofia Deep; 2012/13 sur le talus continental à l'est du Svalbard. Ces régions sont devenues des « Zones Marginales de Convection » avec, à partir de 2011, l'absence occasionnelle de banquise en hiver ainsi que des couches de mélanges et flux océan-atmosphère fortement variables.

Enfin, le modèle Mercator a indiqué l'amplification des courants dans les Bassin Nansen occidental (Athanase et al., submitted). En particulier, le modèle a montré l'intensification de la Yermak Branch et sa circulation le long de flanc ouest du Plateau de Yermak ou traversant directement le Plateau, allant alimenter la Return Yermak Branch sur le flanc est du Plateau. Les sorties du modèle ont également souligné la mise en place de nouveaux chemins empruntés par les eaux Atlantiques: dans le Sofia Deep, une circulation anticyclonique récurrente s'est développée. En aval du Plateau de Yermak, un courant s'est mis en place le long des isobathes 3400-3900 m, alimenté pour sa partie Ouest (orientée vers le sud-est) par les eaux venant de l'extrémité nord-est du Plateau, et par le courant de bord à l'est de 20°E pour sa partie est (orientée vers le nord-est) via l'injection régulière de structures de méso-échelles.

Table of contents

CHAPTER 1

Introduction

1.1. Geography and bathymetry of the Arctic

Covering 9.4 million km², the Arctic ocean is in fact the smallest of the world's five major oceans (Jones, 2001). It lies entirely in the Arctic Circle, and it is remarkable in its relative isolation from the other oceans. Indeed, the Arctic is surrounded by land and linked to the Pacific and Atlantic oceans through two major straits: the narrow Bering Strait for the Pacific Ocean (55 m of maximum depth, 85 km width), and the

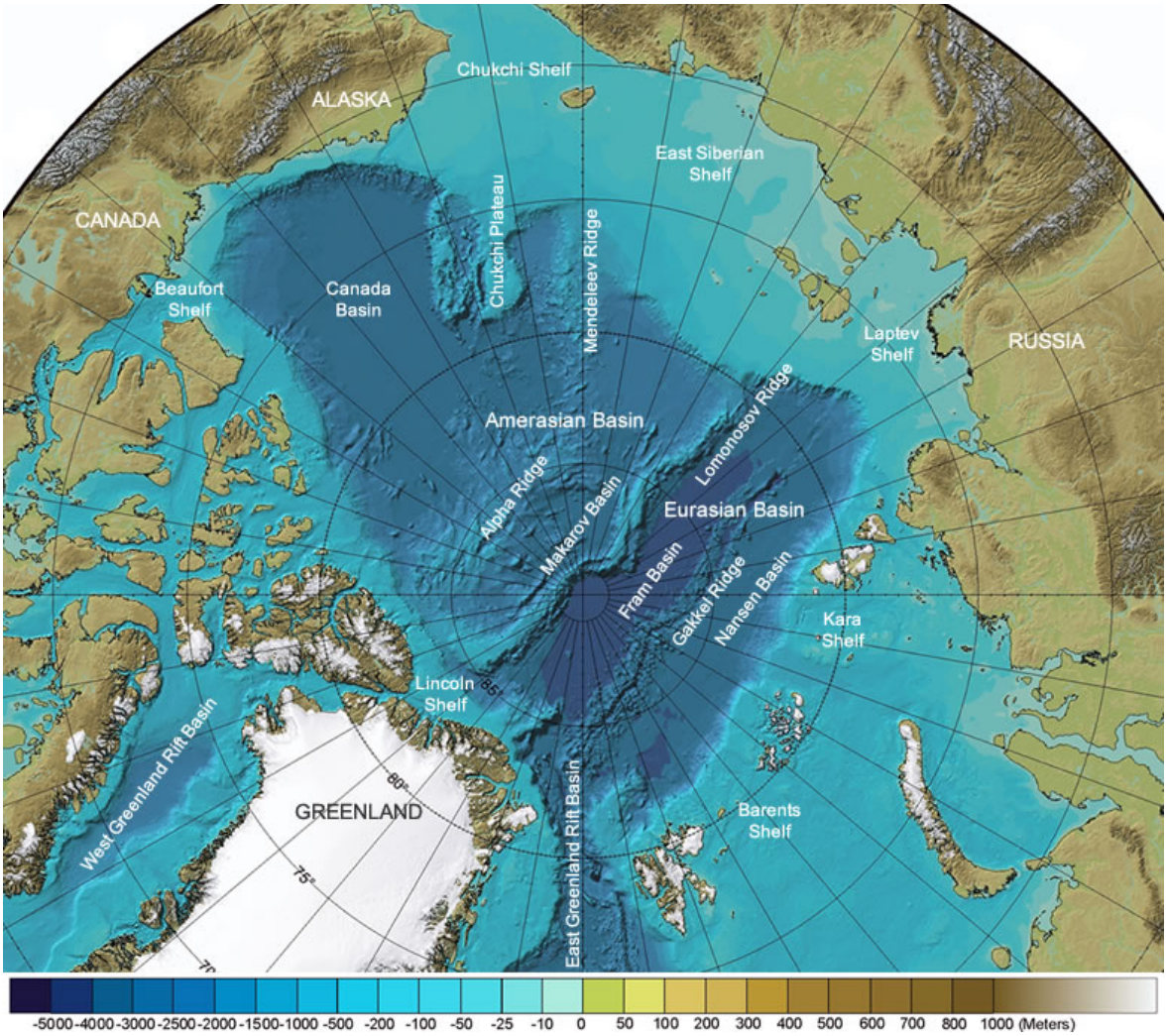

Figure 1.1: International Bathymetric Chart of the Arctic Ocean, annotated with topographic (capital letters) and bathymetric (lower case) features (IBCAO, Jakobsson et al., 2014).

larger and deeper Fram Strait (450 km of width and 2600 m depth) and the Barents Sea for the Atlantic (Figure 1.1, Woodgate, 2013). The Atlantic inflow is thus the main water input to the Arctic ocean, with about 7 Sv of inflow through the Fram Strait, whereas only 0.8 Sv of Pacific water flow through the Bering Strait.

The central Arctic ocean, the deep part of the Arctic ocean, contains several bottom ridges that divide it in several sub-basins. Here we focus on the main ridge of the Arctic Basin, the Lomonosov Ridge, which extends from the Siberian continental shelf to the vicinity of Greenland at a depth of 1500-2000 m. It partitions the Arctic in two main basins: the Canadian Basin on the Pacific side and the Eurasian Basin on the Atlantic side. In the Eurasian Basin, the Gakkel Ridge separates the southern Nansen Basin from the northern Amundsen Basin. In the Canada Basin, the Makarov Basin is isolated from the southern Canada Basin by the Alpha Ridge.

1.2. Circulation in the Arctic Ocean

1.2.1. Surface currents

The Arctic Ocean is also remarkable for its perennial sea-ice cover. The latter tends to substantially reduce the action of the wind on the surface current. Hence, the surface current speed is relatively low, on the order of a few cm/s, even if it tends to move faster than a few decades ago due to the decrease of the sea-ice extent and thickness (Spreen et al., 2011). Two main surface currents coexist in the Arctic Ocean (blue arrows on Figure 1.2):

- The combination of the effect of strong westerly winds and important Siberian rivers, discharging into the Arctic Ocean, generates a dominant current in the Eurasian Basin: the Transpolar Drift, or Transarctic Current (Aagaard, 1989). This main current traverses the ocean from north of the Bering Strait and exits the Arctic along the eastern coast of Greenland as the East Greenland current. The Transpolar Drift and East Greenland current carry large amount of sea-ice and Eurasian river runoff across the Arctic Ocean and through Fram Strait.

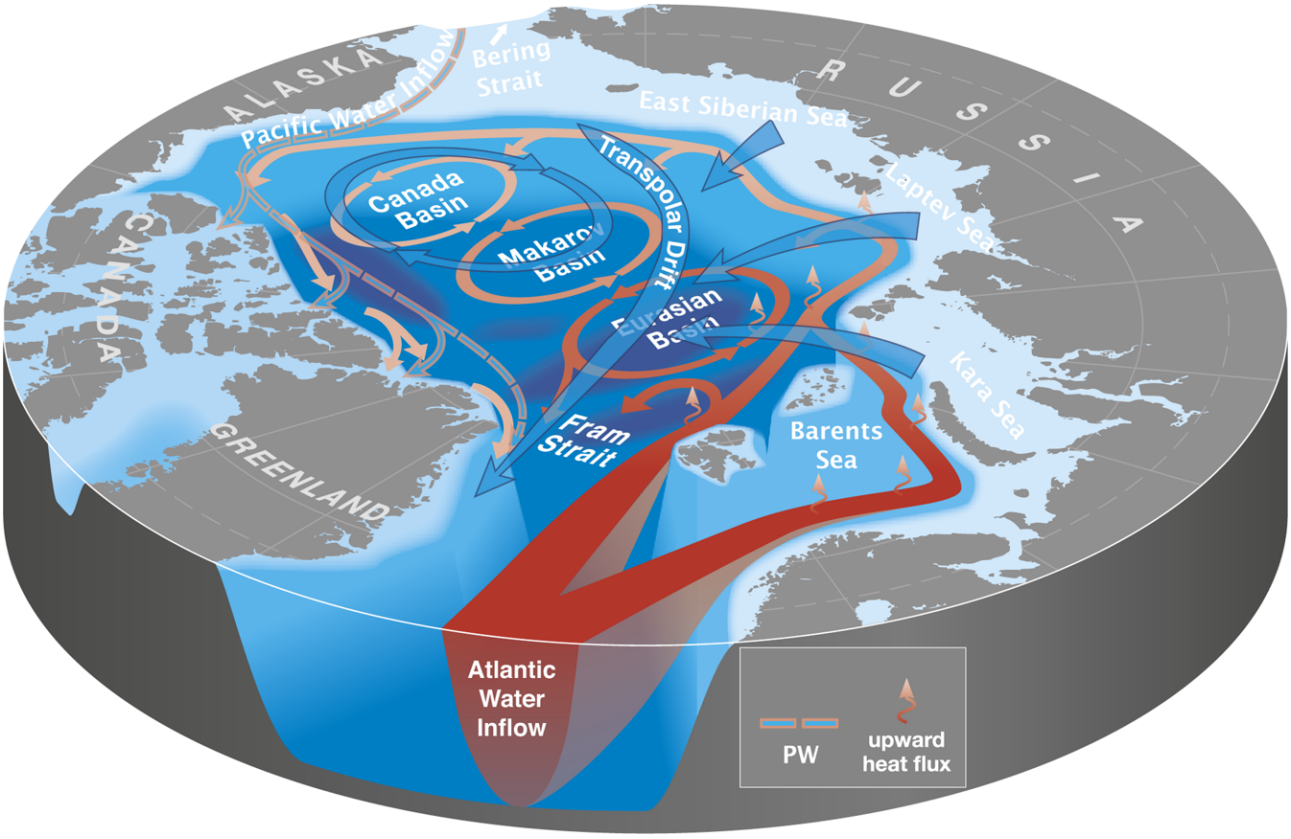

Figure 1.2: Circulation in the Arctic Ocean, with surface currents in blue arrows and subsurface currents of Atlantic Water in red arrows. PW: Pacific Water. From Carmack et al., 2015.

- The Arctic is characterized by a zone of high sea-level pressure (SLP) centered on the northern part of the Beaufort Sea, at the south of the Canada Basin. This induces an anti-cyclonic gyre in the upper layer of the ocean, called the Beaufort Gyre (Aagaard, 1984; Plueddemann et al., 1998). Zhang et al. (2016) recently showed that the Beaufort Gyre has been intensifying during the 1992-2015 period, concurrent with a range of changes in sea ice in the Canadian Basin.

1.2.2. Subsurface current: Atlantic Water Boundary Current

In the major part of the Arctic Ocean at depths greater than a few tens of meters, the circulation is, to the first order, decoupled from the surface (Aagaard, 1989).

Due to the the conservation of the potential vorticity, a mainly barotropic boundary current circulates cyclonically following the topographic slopes (Rudels et al., 1999b; Woodgate et al., 2001; Shimada et al., 2004).

Entering through the wide Fram Strait and the Barents Sea, the denser Atlantic Water is the dominant source for this sub-surface boundary current (red arrows on Figure 1.2). It flows along the basin margin, between 500 and 3000 m, along the southern edge of the Eurasian Basin up to the junction of the Lomonosov ridge. There, it splits into two branches: the first flows northwards in the direction of Greenland along the edge of the Eurasian side of the Lomonosov ridge, whereas the second branch continues towards the Canadian Basin (Figure 1.2).

The cyclonic trajectory of the boundary current is less documented to the east of the Lomonosov ridge. It is possible that a part of this current is diverted towards the interior of the ocean along the Mendeleyev ridge. Then, the current seems to loop southwards around the Chukchi abyssal plain, the turns northwards around the Chukchi plateau. Beyond the northern part of the Chukchi plateau, it is possible that there is mass transfer from the boundary current towards the interior of the basin. The time required to cross the border region of the Chukchi Sea is at least several years, based on an advection rate of 1-2 cm/s (600 km/yr) (Woodgate et al., 2001).

1.2.3. Mesoscale activity

In the ocean, eddies are generated by baroclinic instabilies, frontal instabilities or intense surface buoyancy fluxes (Figure 1.3). They influence the horizontal transport of heat, momentum, nutrients and anomalous water properties. Halocline eddies can reduce the stability of the stratification of the halocline, which isolates warm deep water from the upper ocean in contact with sea ice (Zhao et al., 2014).

Subsurface eddies can be detected across all Arctic basins. Usually, anticyclonic eddies are dominant, and we can find both warm core and cold core eddies. Past studies showed that in the Canadian Basin, eddies are concentrated in the halocline. These eddies have core depths between 30 and 300 m depth and lifetimes from months to years (Manley and Hunkins, 1985). Previous studies (Hunkins, 1974; Zhao et al., 2014; Manley and Hunkins, 1985) have shown that eddies found in the Arctic basin have radii of the order of the Rossby deformation radius in the Arctic, i.e. 8 km (for the Eurasian side) to 13 km (for the Canadian side).

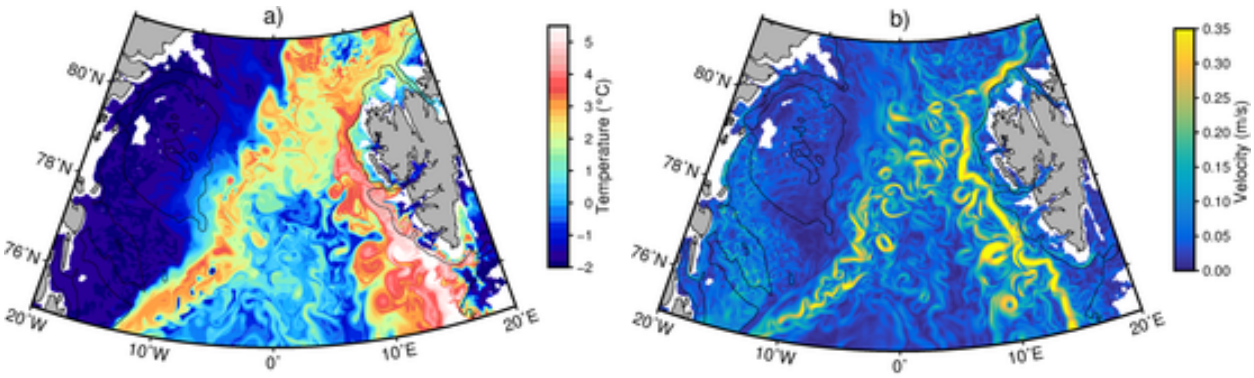

Figure 1.3: Snapshots showing the mesoscale activity West of Svalbard in (a) temperature and (b) velocity at 75 m depth on 31 March 2004 in the FESOM_1km model. The black contour shows the 250 m isobath. From Wekerle et al., (2017).

1.3. General hydrography

In this manuscript, we use the International Thermodynamic Equations of Seawater (TEOS-10) framework (McDougall et al., 2012) with conservative temperature CT (°C) and absolute salinity SA (g/kg). In the Arctic Ocean, absolute salinity values exceed practical salinity values by about 0.16, and conservative temperature values are very close to the in-situ temperatures in the upper 1000 m. We follow water mass definitions from previous studies, often using practical salinity. Hence, temperatures are adapted here in CT (°C) and salinity is given absolute salinity units and recalled in in practical salinity units (for sake of reference) in this section.

1.3.1. Pacific Water

Pacific Water (PW) is found on the Canada Basin side, and episodically also up to the Makarov Basin and Lomonosov ridge (Jones et al., 1998). It has a major influence on the Arctic, providing an important source of heat, nutrients and low salinity-water (Walsh et al., 1989; Aagaard and Carmack, 1989; Woodgate et al., 2010). The temperature and salinity (TS) characteristics of the PW vary greatly according to the season. The PW takes several months to transit the Chukchi Sea before entering the deep Arctic Basin. During this transit, the PW is subject to some modifications, which have a strong seasonal and inter-annual variability that depends on the atmospheric conditions, which control the development of ice (Timmermans et al., 2014).

At the beginning of the winter season, there are large areas of free water, the air-sea

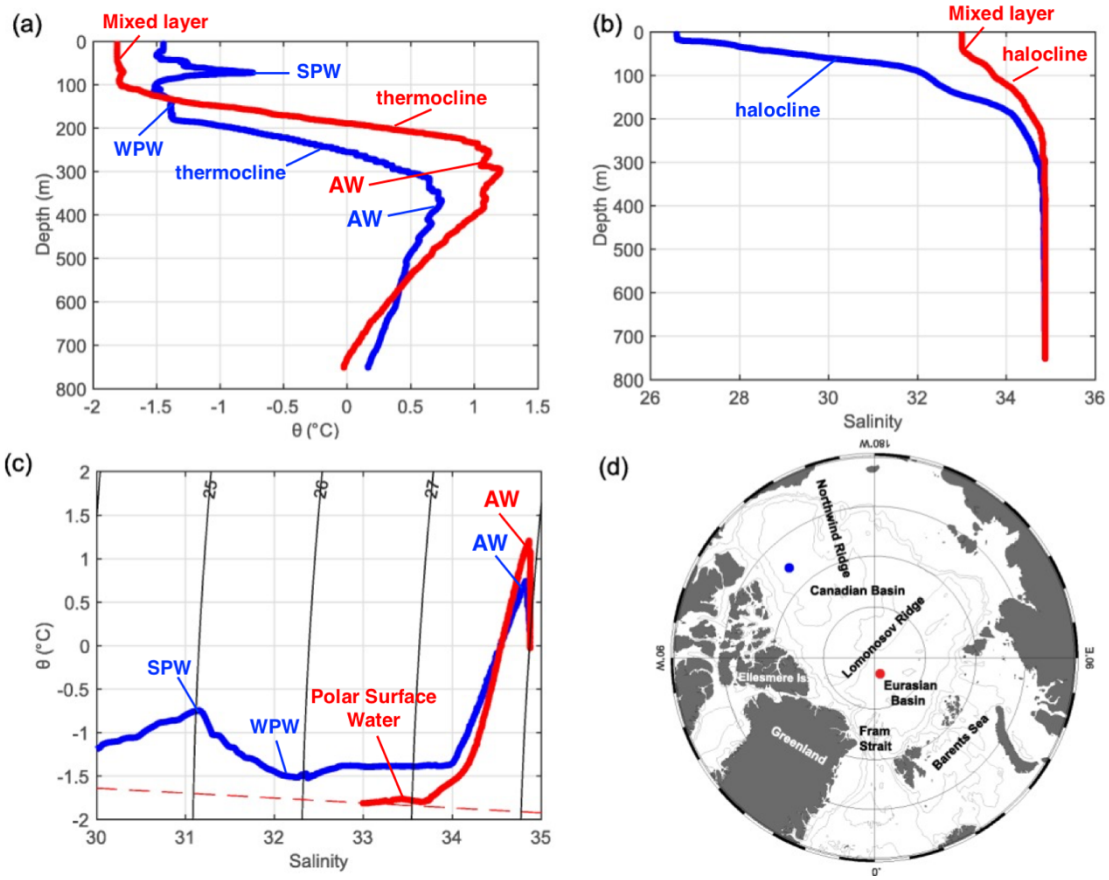

Figure 1.4: (a) Vertical profiles of potential temperature (°C) and (b) salinity (psu) typically found in the Eurasian Basin (red) and Canada Basin (blue). (c) Corresponding θS diagrams, the dashed line indicating the freezing temperature. (d) Geographical features of the Arctic Ocean, with the location of the profiles shown in (a)-(c). AW: Atlantic Water; WPW: Winter Pacific Water; SPW: Summer Pacific Water. Figure annotated from Shibley et al. (2017).

interaction is stronger and thus the winter cooling of the surface layer will favor more rapidly the formation of sea ice. This production of sea-ice induces the salinization of the water column: Winter Pacific Water (WPW) is then relatively colder and saltier. Inversely, when the ice cover is large, as at the beginning of the summer season, little ice will be formed, hence the salinization in the water column is small. The warmer and fresher Summer Pacific Water (SPW) crosses the Chukchi Sea without being greatly modified. As a consequence, the WPW, denser and characterized by a temperature minimum around freezing at a higher salinity (32.15 to 34.65 g/kg, i.e. 32 to 34.5 psu), stabilizes at 100-120 m depth, whereas the SPW, characterized by a shallow temperature maximum at low salinity (30.15 to 33.15 g/kg, i.e. 30.5 to 33 psu), stabilizes into the Arctic Ocean water column at about 50-80 m depth (Figure 1.4; Timmermans et al., 2014).

1.3.2. Atlantic Water

The **Atlantic Water (AW)** can be traced by its TS signature. This subsurface layer of Atlantic Water (0-500 m) is warm (>0°C) and salty (35.05 to 35.65 g/kg, i.e. 34.9 to 35.5psu; Figure 1.4; Rudels et al., 2000).

The AW penetrating into the Arctic Ocean via the Fram Strait constitutes the warm Fram Strait Branch Water (FSBW). Part of the AW inflow does not enter through Fram Strait but flows through the Barents Sea before reaching the Arctic Ocean. This branch of AW is cooled down in the shallow, summer ice-free Barents Sea, forming the cooler and denser Barents Sea Branch Water (BSBW). A lot of uncertainties still remain concerning the transport of FSBW and BSBW.

The FSBW, a relatively narrow stream (a few tens of km), circulates eastward in the boundary current along the continental margin of the Nansen Basin up to the St. Anna Trough, where it meets the Barents Sea Branch (Figure 1.5; Schauer et al., 1997; Rudels et al., 2013; 2015; Dmitrenko et al., 2015). By mixing with the BSBW, the FSBW is cooled down. The merging of the two branches during the eastward transport by the boundary current leads to strong isopycnal mixing and to the creation of intrusive layers (Kuzmina et al., 2011; Rudels et al., 2013).

However, Rudels et al., (2015) highlighted a strong contrast between the low Atlantic Water salinity in the Amundsen Basin and the higher salinity Atlantic Water core in the Nansen Basin, combined with a salinity minimum below the Atlantic layer. This suggests that the Fram Strait Branch mainly remains in the Nansen Basin, while the Barents Sea Branch continues along the continental slope, enters the Amundsen Basin and provides most of the AW in the Makarov and Canada basins. This transport of AW throughout the deep Arctic Ocean produces a temperature maximum between 100 m depth to the west of Svalbard and down to 500 m in the Canadian Basin.

Along its path through the Arctic Ocean, Atlantic Water is cooled and freshened. After circulating in the Arctic Basin, a part of these Modified Atlantic Water (MAW) is returning toward the Fram Strait (Rudels, 1989). MAW is characterized by relatively lower values of conservative temperature (<2°C) or absolute salinity (34.65 to 35.65 g/kg, i.e. 34.5 to 35.5 psu) than the AW.

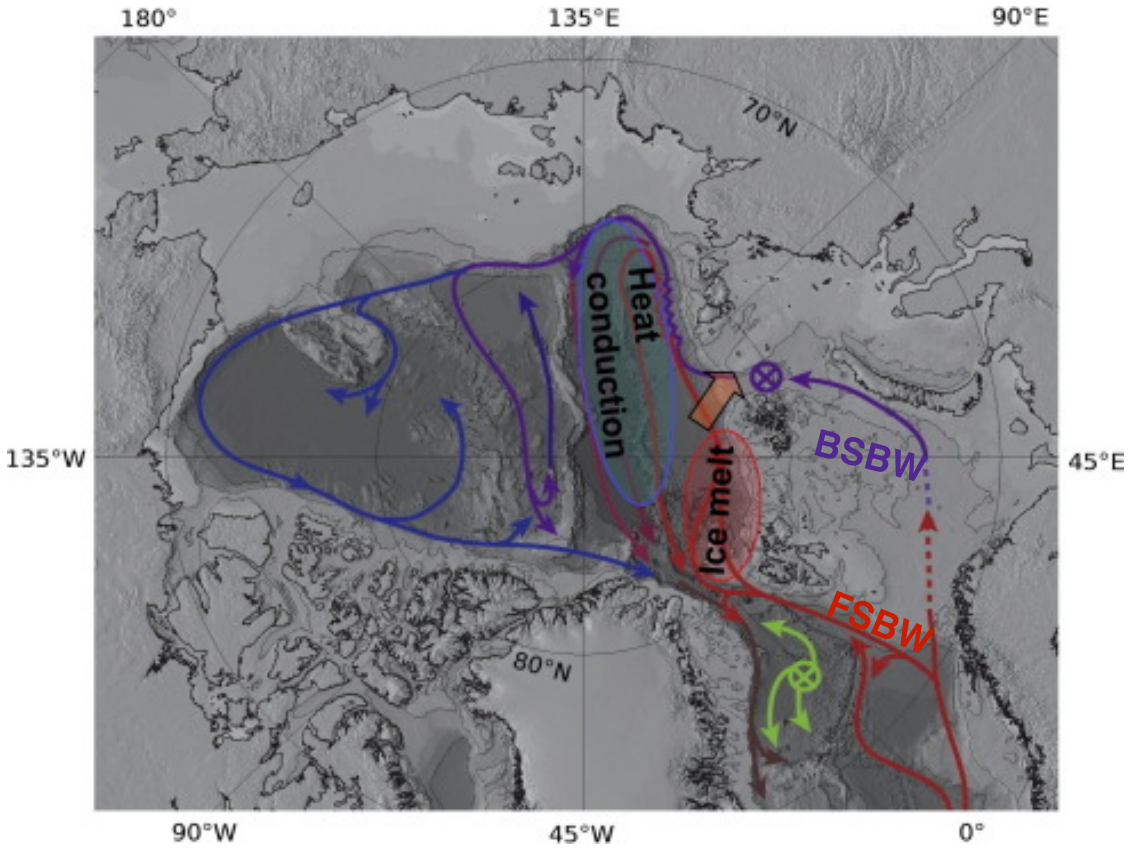

Figure 1.5: Schematic of circulation of the two branches of Atlantic Water in the Arctic Ocean, annotated from Rudels etal (2015). The red area shows where the Atlantic water is transformed into halocline water by melting sea ice and losing heat to the atmosphere. The orange wide arrow indicates the possible transfer of warm Atlantic water from the Fram Strait branch (red streams) to the Barents Sea branch (purple streams) as they meet near Santa Anna Trough (purple cross). The blue area is where we suggest that the heat transport takes place by double-diffusive convection from the Atlantic layer to the mixed layer. The green streams indicate Arctic Intermediate Water created by convection in the Greenland Sea and partly advected into the Arctic Ocean through Fram Strait. BSBW: Barents Sea Branch Water; FSBW: Fram Strait Branch Water. The different colors of the arrows show the relative contributions from the two branches in different parts of the Arctic Ocean.

1.3.3. Polar Surface Water

The **Polar Surface Water (PoSW)** is a low salinity (<34.65 g/kg i.e. 34.5 psu), upper water that follows the boundary current eastward (Rudels et al., 2000). The PoSW is formed by the mixing of two parent water masses: the AW inflow, and fresh water from river run-off and precipitations. There are two hypotheses regarding the formation of these PoSW:

- Atlantic Water could be entrained into the upper layer by wind driven mixing

generated at the sea surface.

- All mixing between the Atlantic Water and the fresh water supply is assumed to take place on the shelves. Rudels (1989) showed that this shelf approach reproduces more accurately the stratification of the present Arctic Ocean. As the AW inflow melts the sea-ice, a sub-category of PoSW is formed, the warm PoSW. In the following, we will distinguish the latter wPoSW (CT>0°C) from the PoSW (CT<0°C).

1.4. Stratification in the Arctic Ocean

1.4.1. Halocline

The halocline is a subsurface layer of large vertical salinity gradient, insulating the cold and fresh surface mixed layer from the warm and salty Atlantic Waters in the Arctic Ocean (Figure 1.4). At low temperatures, typical of polar regions, density changes are mainly driven by salinity changes. Hence, the Arctic halocline also corresponds to a layer of large density stratification, the pycnocline, and acts as a barrier preventing upwelling of the warm AW towards the surface.
The Arctic halocline is usually located between 20 and 200 m depth, but undergoes large seasonal variations (Bourgain and Gascard, 2011). In winter, sea-ice growth induces brine rejection: the mixed layer becomes cooler, saltier and deepens by convection. The halocline is thus deeper and saltier. In summer, sea-ice melts and releases fresh and cold water. As a consequence, surface stratification increases and the halocline shoals.

In the Arctic, identifying the origins of the halocline is complex, as it consists of diverse water masses and source regions (Rudels et al., 1996; Steele and Boyd, 1998; Rudels et al., 2004; Alkire et al., 2017). The halocline can be divided into lower, cold and upper halocline layers. The lower halocline waters (LHW) are formed by the mixing of AW with sea-ice melt water as they enter the Arctic North of Svalbard or though the Barents Sea (Rudels et al.,1996). The LHW have temperature and salinity (34<S<34.5) increasing with depth until the upper limit of the AW layer. The cold halocline waters (CHW), characterized by near freezing temperatures and large vertical salinity gradient (33<S<34), result of additional influences from the Siberian seas (Steele and

Boyd, 1998; Rudels et al., 2004; Alkire et al., 2017). The upper halocline waters (UHW) are made of fresher, lighter Pacific-derived contributions and are mainly found in the Amerasian Basin (e.g. Anderson et al., 2013; Alkire et al., 2019).

1.4.2. Thermocline and double diffusion

The thermocline of the Arctic Ocean is a layer of large vertical temperature gradient marking the transition from the cold temperature-mixed layer to the warmer Atlantic Water layer. The Arctic thermocline is most generally located below the halocline base (Figure 1.4). Under certain circumstances, the thermocline can be affected by double diffusion processes (Turner and Stommel, 1964). In particular, in the deep basin, the weak turbulence associated to a strong stratification of the water column enables the appearance of other processes rather than mechanical ones and vertical mixing by molecular diffusion becomes possible.

Double diffusion is caused by the difference of diffusivities between temperature and salinity (Turner, 1965; Rudels et al., 2009): the thermal conduction coefficient is 1.5×10^{-3} cm^2/s whereas the diffusion coefficient of salt is only 1 to 2×10^{-5} cm^2/s. The temperature is thus diffusing 1000 times quicker than salinity. Double diffusion can develop in an environment where both vertical gradients are in the same direction. Two types of double-diffusive convection can emerge in a stably stratified ocean (Turner and Chen, 1974):

- The diffusive convection (DC) mode of double diffusion occurs when both temperature and salinity increase with depth.

- The case when both temperature and salinity decrease with depth is referred to as the salt-finger (SF) regime.

When the isotherms (and isohalines) are forced to get closer by a perturbation, molecular diffusion of heat increases and water above the most intense gradient will warm up while water below will cool down. This triggers convection inside both layers, with the water warmed up convecting upward and the colder one convecting downwards. These two convective layers contribute to create homogeneous potential temperature and salinity mixed layers (from a few to tens of meters thick), and increase

the potential temperature and salinity gradients at the interfaces, leading to the staircase-like microstructures (Figure 1.6).

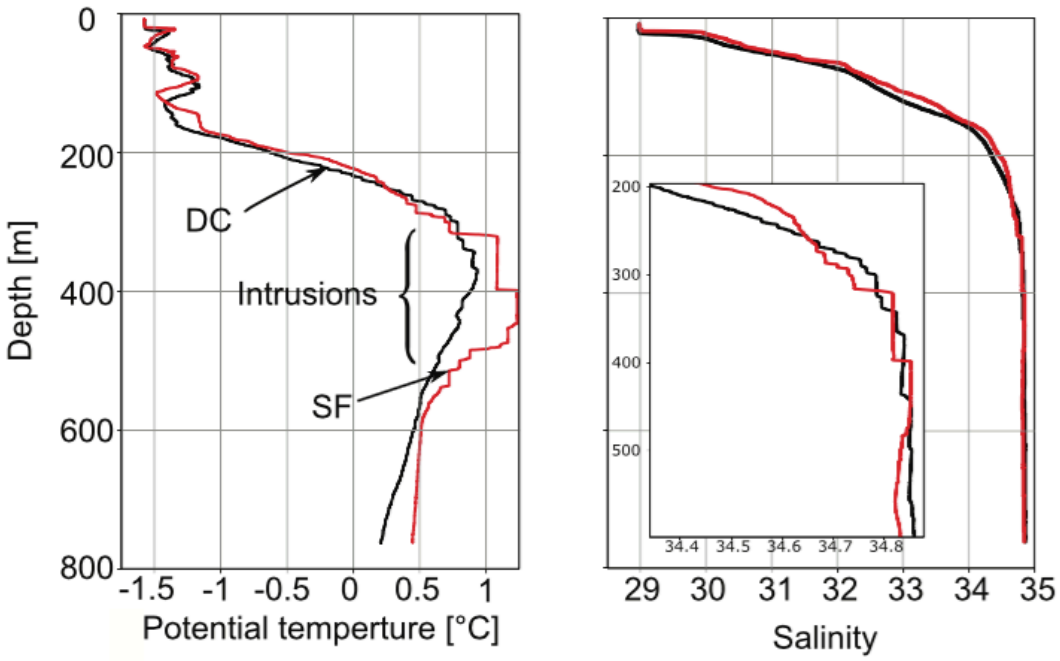

Figure 1.6: Example of staircase structures in the potential temperature (left) and salinity (right) profiles, formed by diffusive convection (DC) and salt-fingering (SF) measured by an ice-tethered profiler (ITP) in the Canada Basin. From Bebieva and Timmermans (2016).

Staircase-like structures deriving from the two types of double diffusion were documented troughout much of the deep Arctic basin (e.g. Padman and Dillon, 1987, 1988; Rudels et al., 1999a; Timmermans et al., 2008; Polyakov et al., 2018).

The development of staircase structures in the Arctic Ocean can be characterized by the magnitude of the vertical density ratio R_ρ (Turner, 1965), defined as:

$$R_\rho = \left(\beta \frac{\partial S}{\partial z}\right) / \left(\alpha \frac{\partial \theta}{\partial z}\right),$$

where $\frac{\partial S}{\partial z}$ is the vertical gradient of salinity, $\frac{\partial \theta}{\partial z}$ the vertical gradient of potential temperature, β is the haline contraction coefficient and α the thermal expansion coefficient. For a stable stratification of the water column, R_ρ is greater than 1, and when R_ρ is closer to 1, the DC is more likely to occur, as the unstable vertical temperature gradient enhances convection, typically when $1 < \overline{R_\rho} < 1.1$.

1.5. Specificities of the Western Nansen Basin

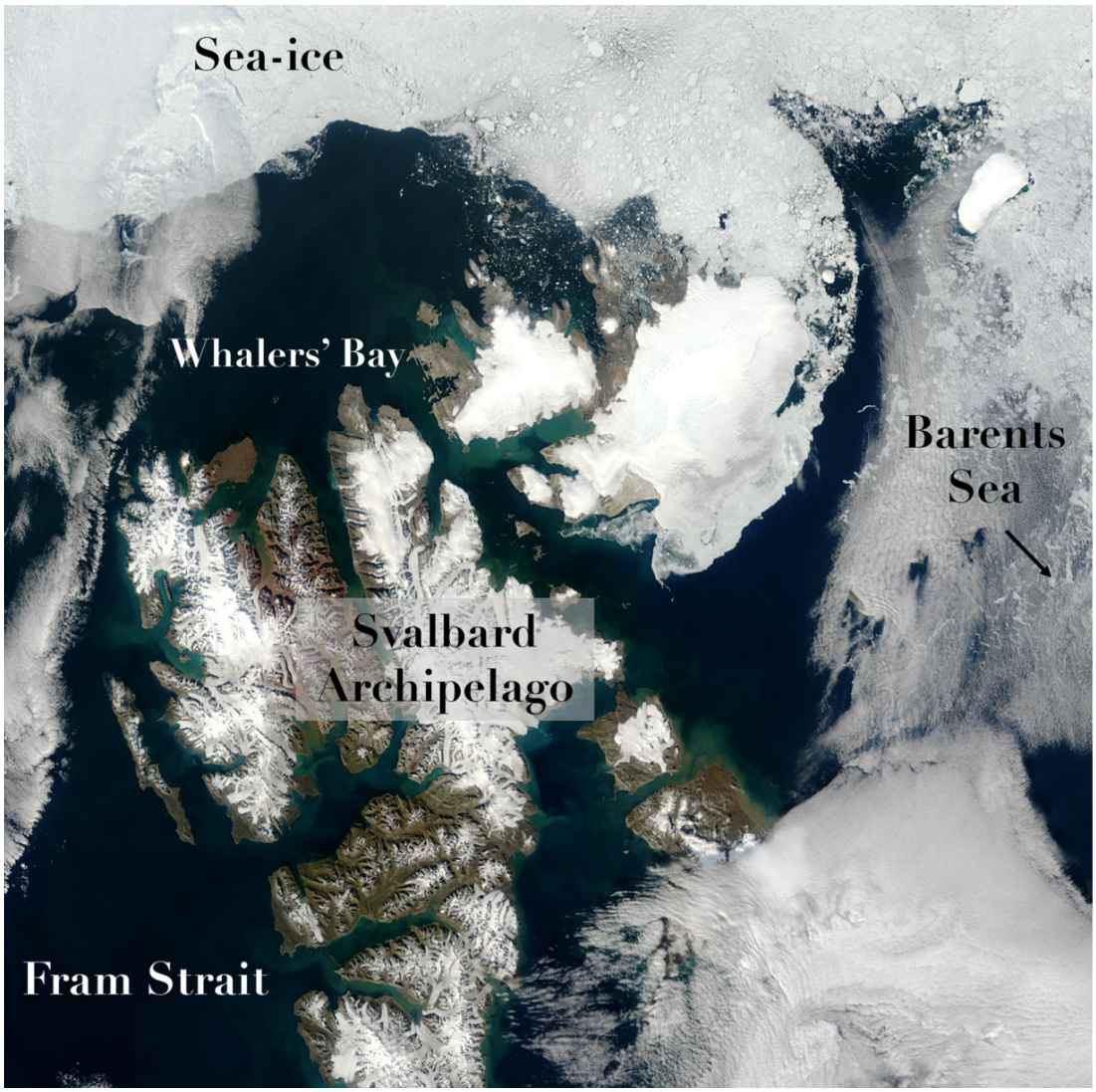

Figure 1.7: Annotated true-color image from Moderate Resolution Imaging Spectroradiometer (MODIS) of the Svalbard Archipelago, captured on the 27 August 2003 by the Terra Satellite. © Jacques Descloitres, MODIS Rapid Response Team, NASA/GSFC

The specificity of the Western Nansen Basin (WNB) lies in the existence of the "Whalers Bay" North of Svalbard, a year-round open water area more extended in winter than in summer (Figure 1.7). Several studies (Aagard et al., 1987; Saloranta and Haugan, 2004; Cokelet et al., 2008) stated that the warm and shallow winter AW inflow circulating along the Svalbard shelf provides sufficient oceanic heat to keep the area ice-free.

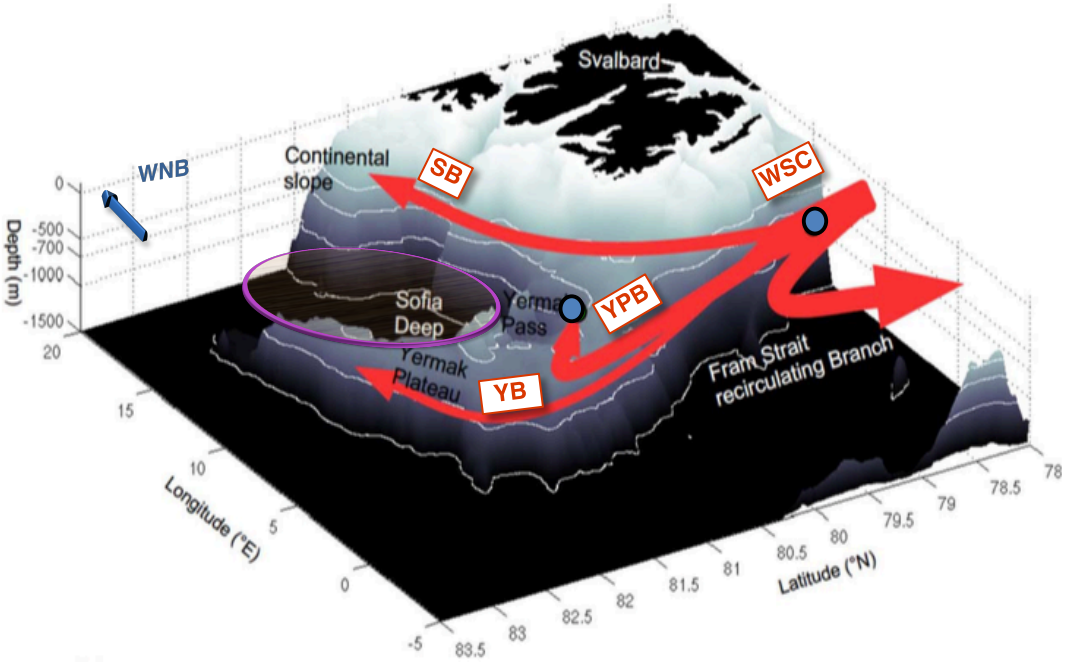

Figure 1.8: 3-D schematic of the AW water inflow north of Svalbard. The red arrows represent the pathways of the Atlantic Water across and around the Yermak Plateau. WSC: West Spitsbergen Current; SB: Svalbard Branch; YB: Yermak Branch; YPB: Yermak Pass Branch. The white lines are the 500, 700, 1,000, and 1,500 m isobaths, bathymetry from IBCAO. Blue dots indicate the location of two mooring lines (Koenig et al., 2017b). The purple circle delineates the area where uncertainties remain. The Western Nansen Basin (WNB) direction is indicated by the blue arrow. Adapted from Koenig et al. (2017b).

1.5.1. Atlantic Water pathways to the WNB

The Atlantic Water inflow through Fram Strait is the major oceanic source of heat and salt to the Arctic Ocean (Aagaard et al., 1987).

In Fram Strait, the West Spitsbergen Current (WSC) carries the AW northward along the west coast of Svalbard. The seasonal variability of Atlantic Water inflow is important, with a stronger flow and larger AW volume transport in winter than in summer in the WSC (Beszczynska-Moller et al., 2012). A fraction of the flow does not reach the Western Nansen Basin and circulates back towards the Fram Strait (Schauer et al., 2004; Beszczynska-Möller et al., 2012; Rudels et al., 2015): such recirculation branches have been shown to be largely dominated by eddies (Von Appen et al., 2016; Hattermann et al., 2016; Werkele et al., 2017).

North of 79°N, the WSC splits into several branches (Figure 1.8): the upper-slope, shallow Svalbard Branch is deflected eastward along the 400–500 m isobaths of the

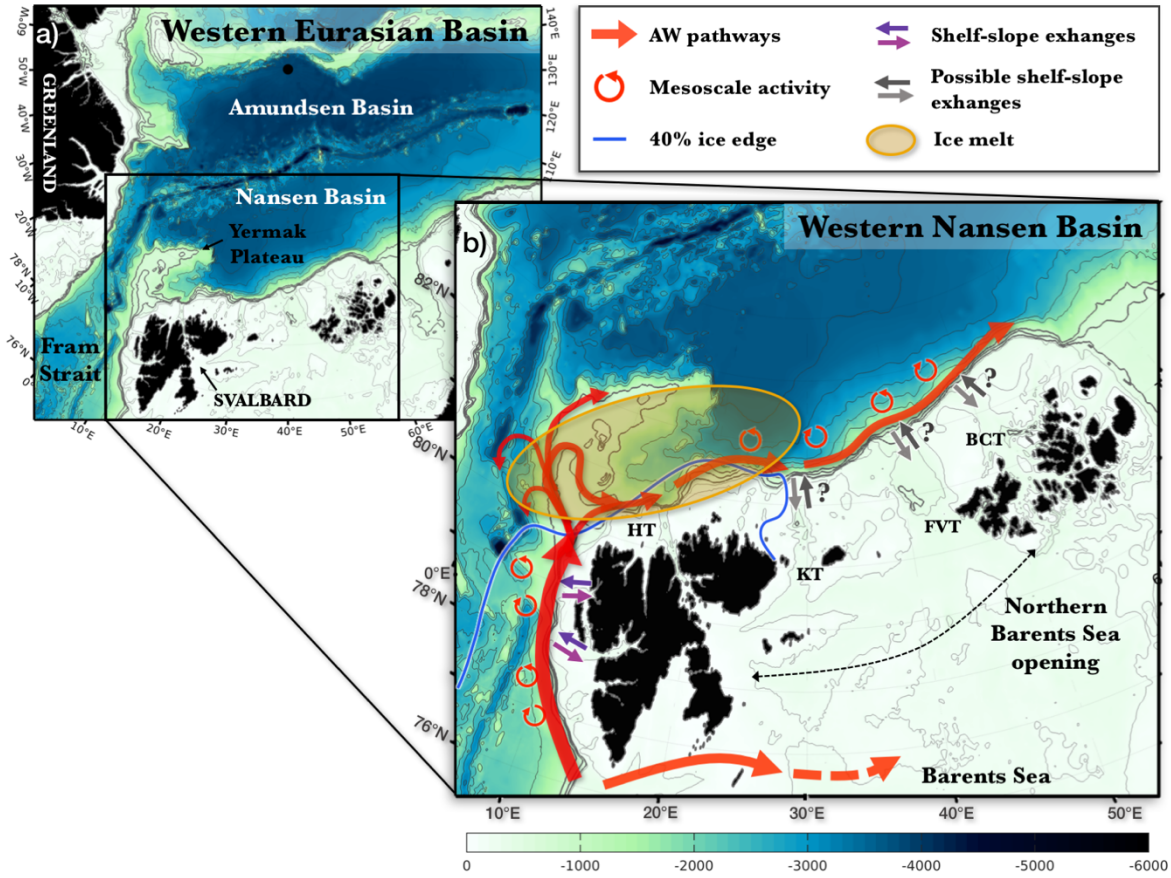

Figure 1.9: (a) Bathymetry of the Western Eurasian Basin (background color, m). The black box delineates the Western Nansen Basin (WNB), detailed in (b). (b) Schematic representation of processes modifying Atlantic Water (AW) properties in the WNB. Red to orange arrows are the schematic AW pathways. The blue contour is the typical 40% ice edge in January in the Whaler's Bay over the 2010s' decade. Purple arrows are shelf-slope exchanges, grey arrows possible occurrences of shelf-slope exchanges. Curled red arrows indicate mesoscale activity along the AW boundary current. HT: Hinlopen Trough; KT: Kvitøya Trough; FVT: Franz-Victoria Trough; BCT: British Channel Trough.

continental slope inshore of Yermak Plateau (Cokelet et al., 2008; Muench et al., 1992; Sirevaag et al., 2011).

The Yermak Pass Branch crosses the Yermak Plateau further north, around 81°N, following the 700 m isobath (Gascard et al., 1995; Koenig et al., 2017b; Menze et al., 2019). The deeper Yermak Branch follows the 1500 m isobath along the western slope of Yermak Plateau (Manley, 1995; Manley et al., 1992). It is thought the branches merge again to rejoin the Atlantic Water Boundary Current along the Svalbard slope, however pathways east of the northern tip of Yermak Plateau remain unclear (Hatterman et al., 2016; Meyer et al., 2017; Koenig et al., 2017a; Crews et al., 2019).

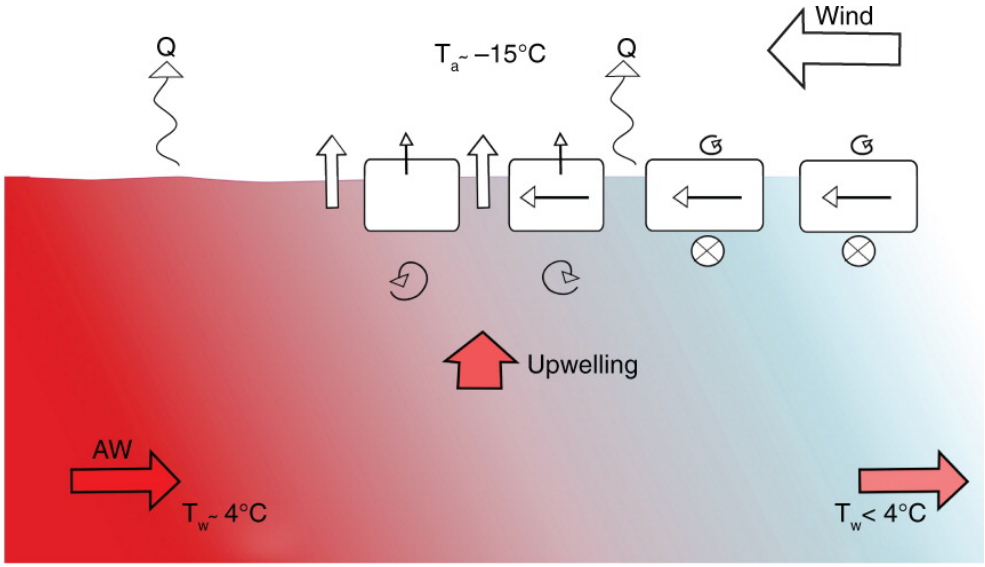

Figure 1.10: Schematic of air-ice-sea interactions north of Svalbard. Northerly winds transport sea ice from the Arctic Ocean (slightly deflected to the right) and bring cold air masses, favoring larger ice cover. Upwelling of warm Atlantic Water (AW, reddish) melts the approaching sea ice, and a fresh, cold layer forms below the ice (bluish). Depending on the vertical mixing below the ice, the freshwater layer reduces further ice melt. The large ocean-to-atmosphere heat flux, Q, is strongly reduced by the presence of sea ice. Ta: air temperature, and Tw: water temperature. From Onarheim et al. (2014).

1.5.2. Atlantic Water modification

The western Nansen Basin (delineated in Figure 1.9a) is a key region for the modification of warm and salty Atlantic Water. Along the different paths, the AW is cooled and freshened through a large variety of processes.

North of Svalbard, the warm Atlantic Water melts the sea-ice, inducing the injection of fresher water at the ocean surface (Figures 1.9b, 1.10; Ivanov et al., 2012; Onarheim et al., 2014; Rudels et al., 2015). Convective mixing, bringing heat from the deeper AW core towards the surface, also favors ocean-air or ocean-ice heat loss, which could be sufficient to maintain the Whaler's Bay area ice free or slow down sea-ice formation (Onarheim et al., 2014; Koenig et al., 2017a; Ivanov et al., 2018).

Other processes contribute to the modification of the AW in subsurface. West of Svalbard, troughs linking fjords to the continental slope favor shelf-slope exchanges, which cool and freshen the AW carried northward in the WSC (Boyd and d'Asaro, 1994; Nilsen et al., 2016; Goszczko et al., 2018). The Western Nansen Basin is also connected to the Barents Sea through the northern Barents Sea Opening (BSO), constituted of a

series of troughs between Svalbard and Franz-Joseph Land (Hinlopen, Kvitøya, Franz-Victoria and British Channel troughs; Figure 1.9). While some studies focused on AW entering Barents Sea from the north (Lind and Igvaldsen, 2012), Schauer et al. (1997) and Matishov et al. (2009) suggested that water from the Barents Sea may drain from the troughs into the AW boundary current, possibly further contributing to modify the core properties of the AW (Schauer et al., 1997; Lind and Ingvaldsen, 2012).

Both West and North of Svalbard, barotropic and baroclinic instabilities in the AW boundary current has been documented (von Appen et al., 2016; Pérez-Hernández et al. 2017), shedding numerous eddies in consequence (Cokelet et al., 2008; Dmitrenko et al., 2008; Våge et al., 2016; Hattermann et al., 2016; Crews et al., 2017; Wekerle et al., 2017; Pérez-Hernández et al. 2017; Athanase et al., 2019). These AW eddies contribute to enhance lateral exchanges, injecting AW from the slope into the WNB interior (Zhao et al., 2014; Våge et al., 2016).

1.6. Motivations and scientific goals

1.6.1. The Arctic: a system undergoing rapid changes

In a context of global warming, the Arctic is undergoing faster changes than in the rest of the world. The Intergovernmental Panel on Climate Change (IPCC) reported an increase in average sea surface temperature (SST) of 0.09°C/decade, which is 50% higher than the whole Northern Hemisphere (Smithson, 2002). IPCC simulations (Solomon et al., 2007) also predict that "climate changes in polar regions is expected to be among the largest and most rapid of any region on the Earth", indicating a warming twice or three times greater than the one predicted for lower latitudes (Figure 1.11). This phenomenon is known as Arctic Amplification and includes a large number of processes and feedbacks (e.g. between sea-ice extent, surface albedo, clouds, ocean and atmosphere heat transport) all affecting the energy budget.

Arctic sea-ice loss remains one of the most evident of these rapid changes. Since the end of the 1970s, the sea-ice extent has been decreasing by about 4% per decade (Figure 1.11), and the multiyear ice area by 14% per decade (Stroeve et al., 2012;

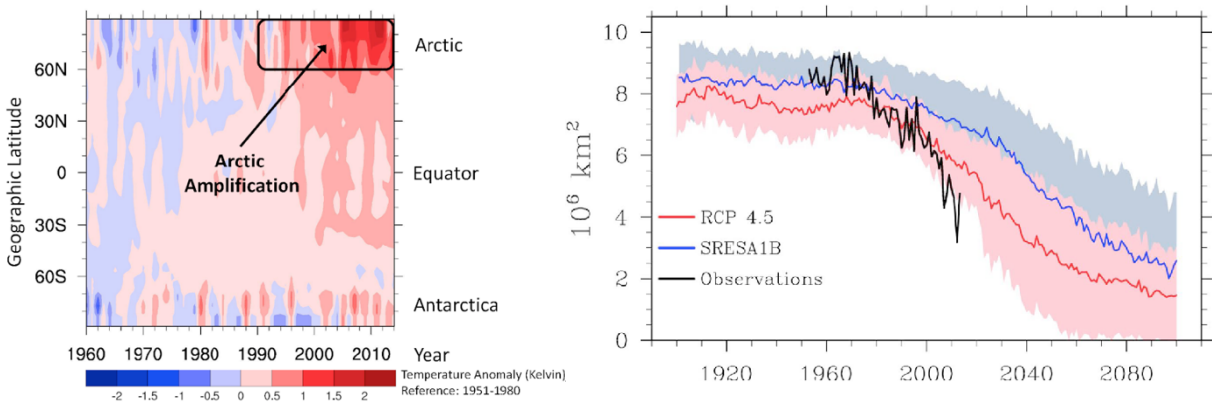

Figure 1.11: (Left) Anomaly of zonal mean temperatures for the years 1960 to 2014 in reference to the 1951-1980 mean. The black box shows the amplified warming in the Arctic. From Wendisch et al. (2017). (Right) Observed September Arctic sea ice extent (black) compared to the climate model inter-comparison CMIP3 (blue) and CMIP5 (red). Shaded areas show ±1 standard deviation of the multi-model mean. From Stroeve et al., (2012).

Stocker et al., 2013), this rate accelerating over the past decades (Comiso et al., 2008). Updated through 2016, the sea-ice extent in September (July) has decreased by 45% (26%), relative to 1979 (Onarheim et al., 2018). The historical minimum sea-ice extent was reached in September 2012 with only 3.39 millions of km² (nsidc.org), and recent projections (June 2020 report from the Sea Ice Prediction Network, arcus.org) would place September 2020 at 4.33 millions of km², i.e. the second lowest extent ever recorded.

While most of the Arctic Ocean experience a maximum sea-ice decrease in summer, in the Whaler's Bay area the largest ice loss has occurred during winter (Onarheim et al., 2014). Studies showed that the extra oceanic heat from the Atlantic Water brought into the region is likely to have caused this sea ice reduction (Ivanov et al., 2012; Onarheim et al., 2014).

Indeed, in a recent study, Polyakov et al. (2017) showed an "Atlantification" of the Eurasian Basin of the Arctic Ocean: the recent shoaling of the Atlantic Water layer, combined with the sea-ice retreat and weakened upper-ocean stratification, progressively allow deeper convective mixing and thus, enhanced heat fluxes from the AW layer towards the surface (Figure 1.12). Further complicating the picture, Ivanov et al. (2016) suggested a positive feedback between sea-ice reduction and oceanic heat North of Svalbard: under ice-depleted conditions in summer, more atmospheric heat is

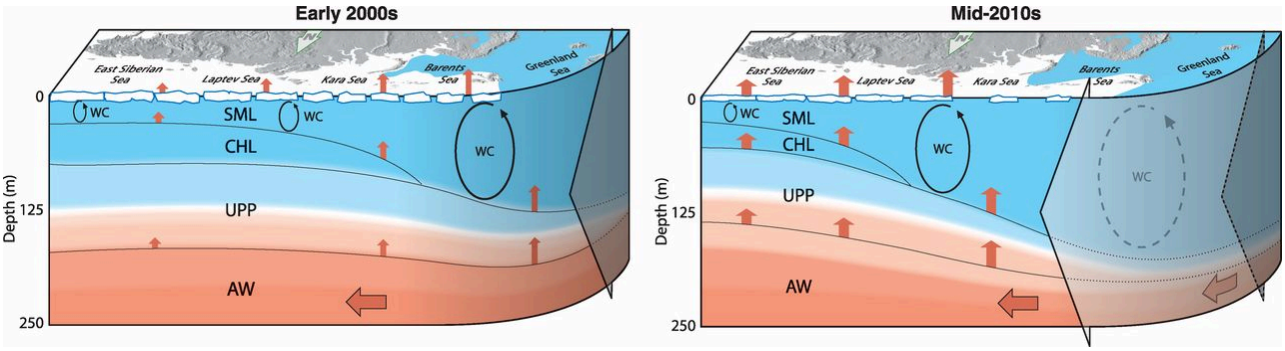

Figure 1.12: Conceptual model of "Atlantification" of the Eurasian Basin continental margin in recent years. The broad arrow extending from the right hand side shows the encroachment of a suite of processes associated with Atlantification: (1) increased penetration of surface signature of AW (increased flow, heat content or both) into the Eurasian Basin, (2) reduction in ice cover resulting in (3) greater surface heat and moisture flux and (4) increased depth of winter penetrative convection, bringing additional heat and nutrients from AW into the Arctic Surface water and transformation of the permanent cold halocline layer (CHL) to a seasonal halocline. SML and UPP indicate the surface mixed layer and upper permanent pycnocline. WC shows winter convection; red arrows indicate upward heat fluxes. Horizontal red arrows show inflows. From Polyakov et al. (2017).

stored in the upper layer of the ocean and sea-ice growth in the following winter is likely further reduced. This would contribute to maintain a thin, fragile and mobile ice cover North of Svalbard, more likely to allow lead opening during the passage of winter storms (Graham et al., 2019).

Atmospheric changes have also been documented in the Arctic. Woods and Caballero, (2016) reported an increased frequency of intrusions of warm, moist air into the Arctic region, causing a retreat of the ice margin which persists for several days after the intrusion has passed, and thus further contributing to maintain a reduced sea-ice cover.

In summary, the Arctic system is rapidly transitioning into a new regime, with lower sea ice extent and an increased role of the Atlantic Water on the surface conditions. By impacting weather patterns and ocean budgets, these changes in the Arctic also have consequences for mid-latitude regions. For example, several studies (Honda et al., 2009; Liu et al., 2012; Grassi et al., 2013) established a connection between Arctic sea ice reduction and increased precipitation events (snow, rain) over the Eurasian continent and even the entire Mediterranean Basin. Basin. Hence, this confirms that the rapid changes observed in the Arctic will likely affect in turn the climate system far beyond the Arctic region itself.

1.6.2. PhD. scientific objectives

Despite the amplitude of these changes and their implications for the climate system on a broader scale, the Arctic remains rather little documented. Indeed, the sea-ice cover and harsh winter conditions during polar night make this region difficult to access for scientific missions. Collecting Arctic observations requires considerable efforts and resources, thus significant uncertainties persist on the Arctic Ocean recent hydrographic properties and governing processes of water mass transformation.

The Western Eurasian Basin plays a key role in the Atlantic Water inflow and transformation. This region constitutes the antechamber of the AW into the high Arctic Ocean, and experiences some the first and most substantial changes in the Arctic transition to a new regime. Hence, it is important to document the properties of the Western Eurasian Basin in the latest years, as well as the physical and dynamical processes governing the distribution of heat and salt in the basin.

We attempted answer or at least provide elements of response to the following questions. **In this context of reduced sea-ice cover and transitioning Arctic:**

Q1. What are the recent hydrographic properties of Western Eurasian Basin?

Q2. What are the major processes contributing to the modification of Atlantic Water, as it enters the Arctic North of Svalbard?

Q3. What are the changes in Atlantic Water circulation and volume transport in the area North of Svalbard?

These questions are addressed using a dual approach, combining the analyses of observations and model outputs.

A particular attention is given to the *in-situ* measurements gathered by the **IAOOS platforms** (Ice Atmosphere Ocean Observing System, www.iaoos.ipev.fr). The IAOOS platforms were developed conjointly by the French polar institute Paul-Emile Victor (IPEV) and French laboratory LOCEAN (Laboratoire d'Oceanography et du Climat:

Expérimentations et Approches Numériques). The IAOOS autonomous platforms are equipped with instruments documenting the four media (ocean, ice, snow, and atmosphere) while drifting with the ice (Provost et al., 2015) and provide valuable observations in the high Arctic Ocean.

As recent observations in the Western Eurasian Basin remain fragmentary, we further extended our investigations using fields from the **1/12° Mercator Ocean global operational system**. The model was developed for the Copernicus Marine Environment Monitoring Service (http://marine.copernicus.eu/) and was parametrized and ran at Mercator Océan (Ramonville-Saint-Agne, France). In order to understand and assess the model capibilities, skills and limitations in the Western Eurasian Basin (WEB), a **thorough evaluation of the system in the WEB** was carried out in close collaboration with Mercator Océan. To do so, we gathered **independent oceanic profiles** (not used in the model assimilation) from various sources: hydrographic cruises, autonomous ice-tethered platforms, mooring data. As satellite data is lacking at such high latitudes (north of 70°N), we additionally used a **prototype multi-mission product of sea-level anomaly** (SLA) developed at CLS (Ramonville-Saint-Agne, France) to complement the validation and examine the performance of the modelled SLA. Once the evaluation had been carried out, model fields were used to extend our analysis on a larger regional scale and over the 2007-2020 period of available model outputs.

In summary, we aimed to:

- Answer scientific questions **Q1**, **Q2** and **Q3** using:
    - IAOOS oceanic profiles (**tool 1**);
    - Mercator Ocean operational system fields (**tool 2**).
- Carry out the model regional evaluation using:
    - Independent oceanic data (**tool 3**);
    - A prototype Arctic altimetry product (**tool 4**).

This manuscript is organized as follows.

Chapter 2 presents the recent hydrographic measurements gathered by the IAOOS 2017 drift in the upper Western Eurasian Basin. We focus on the changes documented in physical properties across different sub-regions.

In Chapter 3, mechanisms of Atlantic Water modification in the Western Nansen Basin (WNB) is investigated. Prior to the analysis, the performance of the Mercator 1/12° system is assessed using independent hydrographic profiles in the WNB. We then used 12 years (2007-2018) of fields from the Mercator 1/12° system to examine two processes likely to substantially contribute to modify AW properties North of Svalbard: winter convection and outflows from troughs.

Chapter 4 aims to investigate the circulation of Atlantic Water in the WNB using the Mercator Ocean system. The changes in Atlantic Water pathways and volume transports over 2008-2020 are presented. Model fields are used to provide insights on potentially previously undocumented circulation patterns, in a context of increased progression of Atlantic Water towards the basin interior.

Finally, Chapter 5 draws the main conclusions of this thesis and presents some perspectives.

CHAPTER 2

Recent Hydrography of the upper Arctic Western Eurasian Basin with 2017 IAOOS measurements

Contents

2.1. Introduction

Recent observations are rare and valuable in the Eurasian Arctic Basin. Some areas received a particular attention and have been relatively well documented: in the eastern Fram Strait with repeated hydrographic sections and the maintained mooring array (Beszczynska-Möller et al., 2012; Von Appen et al., 2016); along the continental slope (Rudels et al., 2013, 2015; Vage et al., 2016; Pérez-Hernandez et al., 2017; Renner et al., 2018) and near Yermak Plateau with the N-ICE 2015 cruise campaign (Koenig et al., 2017a, 2017b; Meyer et al., 2017). However, to our knowledge very little studies presented recent hydrographic observations (late 2010s') in the Amundsen and Nansen Basin interior.

Autonomous platforms are a good tool to gather rather exhaustive hydrographic data in the remote high Arctic, as they profile through several hundreds of meters of the upper ocean while crossing different sub-regions along their drifts. The Barneo ice camp, a temporary drifting station located always north of 88°N, constitutes a good deployment point for these autonomous platforms. Entrained by the Transpolar Drift, the platforms often follow a direct southwestward trajectory, crossing the

Figure 2.1: (Left) The LOCEAN team (from left to right: Mathieu Labaste, Victoire Rérolle and Zoé Koenig) during the deployment of the IAOOS platforms near the Barneo ice camp 2017. (Right) IAOOS 24, once deployed in 2017. © Reidar Arnesen, arcticlapse.com

westernmost edges of the Amundsen and Nansen Basin before exiting through Fram Strait.

In April 2017, two IAOOS buoys were deployed from the Barneo ice camp by a team from LOCEAN (Figure 2.1). They acquired data in the Western Eurasian Basin during 8 months. The two platforms followed an unusually meandering trajectory, circulating eastward in the Nansen Basin interior before looping back towards Fram Strait. At the time of redaction of this thesis, the IAOOS 2017 dataset is the longest, most eastly IAOOS dataset in the Eurasian Basin. Here, we present the 8 months of physical and biogeochemical data provided by the IAOOS 2017 in the Western Eurasian Basin.

2.2. New Hydrographic measurements of the upper Arctic Western Eurasian Basin in 2017 reveal fresher mixed layer and shallower warm layer than in the 2005-2012 Climatology

JGR Oceans

RESEARCH ARTICLE
10.1029/2018JC014701

New Hydrographic Measurements of the Upper Arctic Western Eurasian Basin in 2017 Reveal Fresher Mixed Layer and Shallower Warm Layer Than 2005–2012 Climatology

Marylou Athanase[1], Nathalie Sennéchael[1], Gilles Garric[2], Zoé Koenig[1], Elisabeth Boles[1], and Christine Provost[1]

[1]Laboratoire LOCEAN-IPSL, Sorbonne Université (UPMC, Université Paris 6), CNRS, IRD, MNHN, Paris, France, [2]Mercator Ocean, Parc Technologique du Canal, Ramonville-Saint-Agne, France

Abstract In 2017, Ice Atmosphere Ocean Observing System autonomous drifting platforms provided extensive physical and biogeochemical data in the upper 350 m of the western Eurasian Basin through their 8-month drift across the Amundsen Basin, the Gakkel Ridge, the Nansen Basin and western Fram Strait. Comparison with WOA13 climatology indicates a fresher surface layer and shallower warm layer in 2017 than in 2005–2012. The Ice Atmosphere Ocean Observing System 2017 data feature two halocline eddies in the Amundsen Basin and two Atlantic Water (AW) mesoscale structures in the Nansen Basin. Analysis of the global (1/12)° Mercator Ocean operational system suggests that the halocline eddies resulted from instabilities in the frontal zone between fresher Makarov waters and saltier Eurasian waters. This frontal region appears to have shifted further southeast in 2017 (near 88°N, 10°E) compared to 2005–2012. The operational system depicts the large AW structure in the Nansen Basin (140 km crossed as far as 83.7°N, 34.5°E) as an AW meander from the Arctic Circumpolar Boundary Current, which turned into an anticyclonic eddy about a month after the platforms drifted away. The AW structure at 82.8°N, 3°W, northwest of the Yermak Plateau, corresponds to an AW recirculating branch detaching from the Yermak Plateau slope back toward Fram Strait.

Plain Language Summary In 2017, IAOOS (Ice Atmosphere Ocean Observing System) autonomous drifting platforms provided extensive physical and biogeochemical data in the upper 350 m of the Western Eurasian Basin through their 8-month drift. The surface layer is fresher and the warm layer shallower in 2017 than in 2005-2012. The IAOOS 2017 measurements document several medium scale ocean structures. Simulations from a high resolution ((1/12)°) model (Mercator Ocean operational model) provide insights on the nature and origin of these observed structures.

Key Points:
- Autonomous profilers provide an extensive physical and biogeochemical characterization of the western Eurasian Basin upper 350 m in 2017
- The western Eurasian Basin exhibits a fresher surface layer and shallower warm Atlantic Water layer in 2017 than in 2005-2012
- Mercator Ocean operational model outputs bring insights on the observed mesoscale structures in the halocline and warm layer

Correspondence to:
M. Athanase,
mathanase@locean-ipsl.upmc.fr

Citation:
Athanase, M., Sennéchael, N., Garric, G., Koenig, Z., Boles, E., & Provost, C. (2019). New hydrographic measurements of the upper Arctic western Eurasian Basin in 2017 reveal fresher mixed layer and shallower warm layer than 2005–2012 climatology. *Journal of Geophysical Research: Oceans*, *124*, 1091–1114. https://doi.org/10.1029/2018JC014701

Received 19 OCT 2018
Accepted 19 JAN 2019
Accepted article online 25 JAN 2019
Published online 20 FEB 2019

1. Introduction

Over the recent decades, the Arctic has experienced numerous changes; drastic sea ice loss during summers and reduced sea ice thickness and volume are evident signs of global climate change (Carmack et al., 2015; Jeffries et al., 2013; Stroeve et al., 2012). The causes of this sea ice reduction involve a complex combination of changes in the atmospheric and oceanic heat, freshwater, and momentum fluxes (Comiso et al., 2008; Polyakov et al., 2010; Serreze & Barry, 2011). A large part of the Arctic sea ice loss results from summer solar heating of the ocean surface mixed layer through leads in the ice and open water (Perovich et al., 2011). Further decrease of the seasonal ice extent and increase of the open water surface enhance atmospheric forcing onto the ocean and accelerate feedback processes (Carmack et al., 2015; Stroeve et al., 2012).

In most of the Arctic Ocean, the strongly stratified halocline prevents the heat of the warm Atlantic Water (AW) from reaching the surface. One notable exception is the western Nansen Basin, where the weaker halocline allows vertical ventilation of the AW up to the surface (Carmack et al., 2015; Koenig et al., 2017; Onarheim et al., 2014). However, the Arctic Ocean has undergone a substantial weakening of the stratification at the base of the mixed layer (Polyakov et al., 2017; Toole et al., 2010). Hence, conditions previously unique to the western Nansen Basin (weaker halocline, shallower AW layer) are now observed in the eastern Eurasian Basin as well (Polyakov et al., 2017). This northeastward progression of the western Eurasian Basin conditions (enhanced upward AW heat fluxes, diminished sea ice cover and volume) has been called

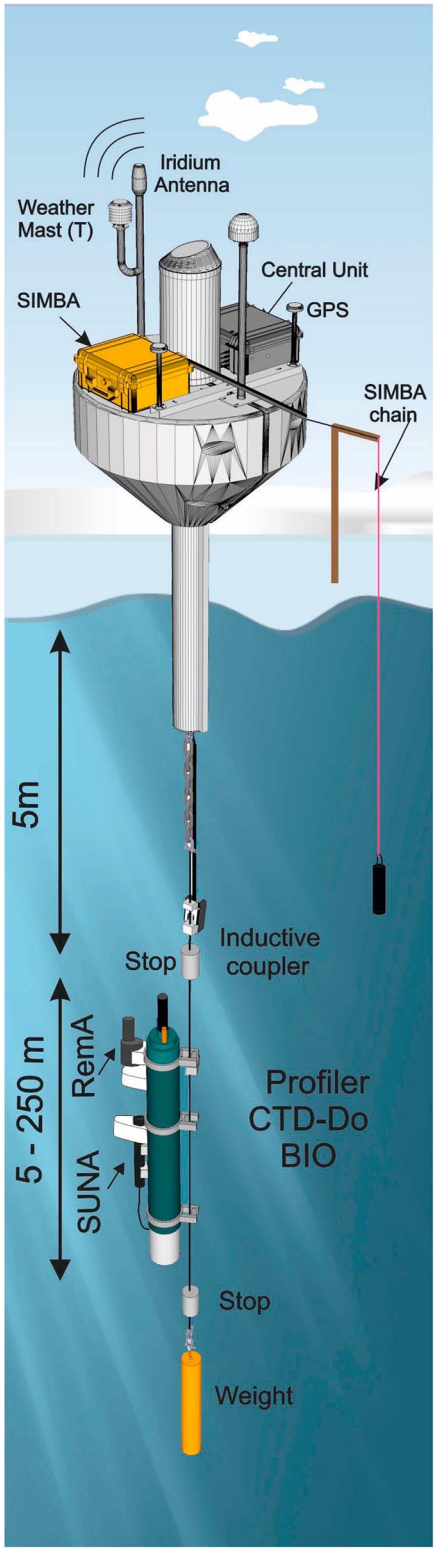

Figure 1. Schematic of IAOOS platform 24. The ocean profiler was equipped with bio-optics sensor suite (pack Rem-A) and a nitrate sensor (SUNA) in addition to the traditional CTD-DO sensors. SIMBA = Scottish Association for Marine Sciences ice mass balance for the Arctic; CTD = conductivity, temperature, and depth; SUNA = submersible ultraviolet nitrate analyzer.

"Atlantification" of the Arctic Ocean (Polyakov et al., 2017). The recent weakening of the halocline, combined with the shoaling of AW, is the main driver for these changes (Polyakov et al., 2017; Rabe et al., 2014). In this context of Atlantification, the role of AW in sea ice reduction in the Eurasian Basin is likely becoming increasingly important (Carmack et al., 2015; Polyakov et al., 2017).

Since 2004, autonomous drifting systems such as ice-tethered profilers (Krishfield et al., 2008) have helped to document water physical properties (temperature and salinity) across a vast portion of the Arctic Ocean's top 800 m. Recently, sensors have been added to profilers to document dissolved oxygen (DO) concentration (Timmermans et al., 2010) or upper ocean bio-optical properties (e.g., Laney et al., 2014). In parallel with observational efforts, performances of operational models in the Arctic have significantly improved in the past decade. For example, Mercator Ocean operational model outputs have been shown to compare fairly well with profiler data from autonomous drifting IAOOS (Ice Atmosphere Ocean Observing System) platforms north of Svalbard (Koenig et al., 2017) and helped put the observations in perspective.

Two IAOOS platforms (Figure 1) provided an 8-month-long data set in the Eurasian Basin in 2017. One of the ocean profilers was equipped with biogeochemical capabilities and in particular measured nitrate concentration and colored dissolved organic matter (CDOM). The ocean data acquired during the meandering IAOOS platform trajectories (Figure 2) uniquely document the physical and biogeochemical characteristics of the upper water column in the western Eurasian Basin (>790 profiles) in 2017.

The paper is organized as follows. Section 2 presents the IAOOS data, Mercator Ocean operational system, and WOA13 climatology. Section 3 describes the different hydrographic regions sampled by the profilers. Notable mesoscale structures in the halocline and in the warm AW layer are studied in section 4. The IAOOS 2017 data are compared to the 2005–2012 WOA13 climatology in section 5.1. In section 5.2, the Mercator Ocean model performance is evaluated against the 2017 IAOOS observations. The contribution of the model outputs to the analysis of the observed mesoscale structures is discussed in section 5.3. Results are summarized and discussed in section 6.

2. Data

2.1. IAOOS Ocean and Ice Data

The IAOOS autonomous platforms document the four media —ocean, ice, snow, and atmosphere— while drifting with the ice (Provost et al., 2015). The standard IAOOS platform carries a weather mast and a micro-lidar for the atmosphere (Mariage et al., 2017), an ice mass balance instrument (K. Jackson et al., 2013), and an ocean profiler (Koenig et al., 2016). Two platforms (IAOOS 23 and IAOOS 24) were deployed at the North Pole from the Russia-operated Barneo ice camp on 12 April 2017. The platforms have slightly different configurations, with one of them carrying additional biogeochemical sensors (Figure 1 and Table 1). Although we focus here on the physical parameters, we also examine selected biogeochemical parameters considered as water mass tracers to the first order, namely, DO concentration, nitrate concentration, and CDOM.

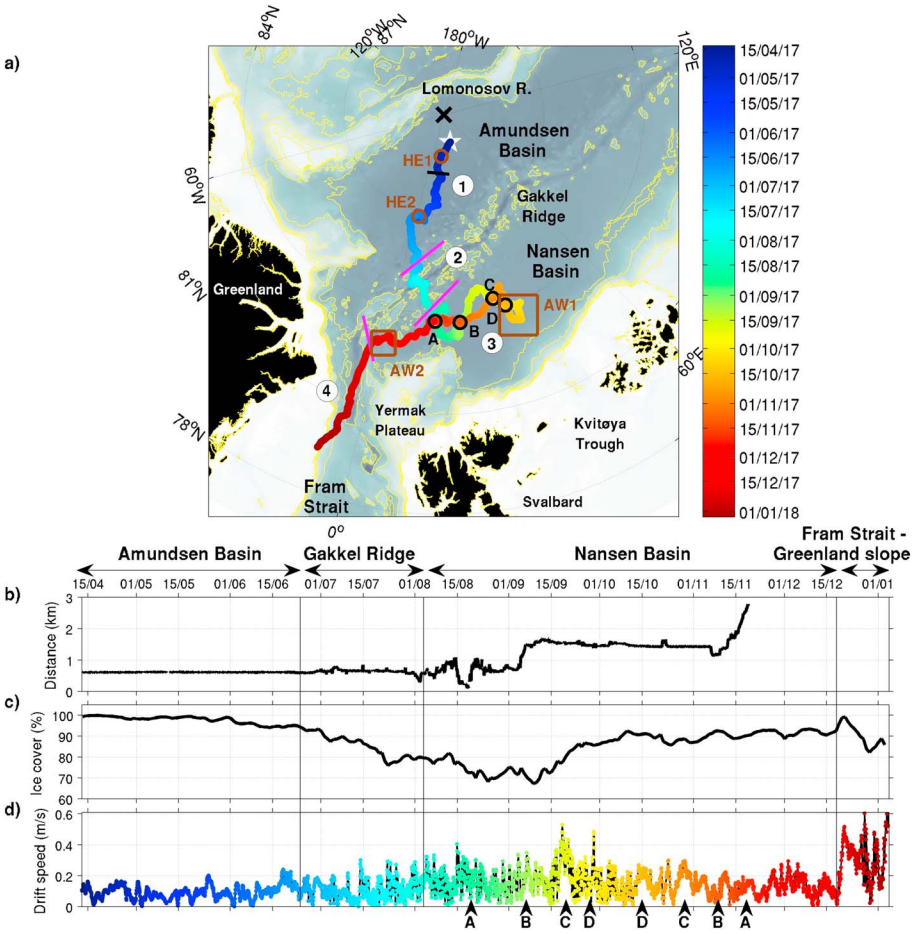

Figure 2. (a) Drift trajectory of the IAOOS platforms from 12 April 2017 to 4 January 2018. Color code is time, bathymetry (IBCAO) is in gray scale with yellow isolines at 0, 500, 700, 1,000, 2,000, and 3,200 m. Magenta lines delineate the four regions: (1) the Amundsen Basin, (2) the Gakkel Ridge, (3) the Nansen Basin, and (4) the western Fram Strait and Greenland continental slope. Black line at 88.2°N indicates a frontal zone. Black circles indicate the four crossover points (A, B, C, and D). Brown circles indicate the location of two halocline eddies (HE1 and HE2), and brown boxes the location of two Atlantic Water (AW) mesoscale structures (AW1 and AW2). The black cross marks the North Pole. (b) Time series of the distance between the two platforms. (c) Sea ice concentration (%) from Mercator Ocean operational model collocated with the drift. (d) Drift speed (m/s) of the platforms. Arrows on the top and vertical lines through panels (b) to (d) indicate the limits of the regions. Dates of the crossover points are indicated below panel (d).

The ocean profiler on IAOOS 24 was a PROVOR SPI (from French manufacturer NKE) equipped with a Seabird SBE41 conductivity, temperature, and depth and a DO Aandera 4330 optode. The profiler on IAOOS 23 carried additional biogeochemical sensors including a bio-optics sensor suite and a nitrate sensor (Figure 1). The bio-optics sensor suite (called Pack Rem-A) combines a three-optical-sensor instrument (ECO Triplet, WET Labs Inc.) and a multispectral radiometer (OCR-504, Satlantic Inc.). We use the CDOM fluorescence (excitation/emission 370/460 nm) from the WETLabs ECO sensor. The nitrate sensor was a submersible ultraviolet nitrate analyzer (SUNA, Satlantic-Seabird Inc.), a chemical-free ultraviolet nitrate sensor. The profilers were set to perform two upward profiles per day from 250 m (IAOOS 23) and 350 m (IAOOS 24) starting at approximately 6 a.m. and 6 p.m. UT. They provided a unique 8-month-long data set, by gathering a total of 793 profiles of the temperature, salinity, and oxygen (upper 350 m) and 427 profiles of CDOM and nitrate concentrations (upper 250 m; Table 1). No bottle observations were collected.

The conductivity, temperature, and depth data have a vertical resolution of 1 db. We use the International Thermodynamic Equations of Seawater (TEOS-10) framework (McDougall et al., 2012) with conservative temperature CT (°C) and absolute salinity (g/kg). In our study region, absolute salinity values exceed practical salinity values by about 0.16. After data quality control processing, 97% of IAOOS 23 and 95% of IAOOS

Table 1
Summary of IAOOS 23 and 24 Ocean Data: Sensors, Sampling Rates and Number of Profiles

Platform	Dates of acquisition			Wire length (m)	Acquisition duration (days)		Profiles performed			Profiles validated	
IAOOS 23	12 April 2017 – 4 January 2018			250	268		439 (82% of expected)			427 (97% of performed)	
IAOOS 24	12 April 2017 – 16 November 2017			350	219		387 (88% of expected)			366 (95% of performed)	
Equipment/sensor	SUNA	ECO triplet	ECO triplet	ECO triplet	OCR	OCR	CTD	CTD	CTD	CTD	DO optode
Parameters	$[NO_3^-]$ (μM)	Chl a (μg/L)	CDOM (ppb)	BP (m^{-1})	PAR	Ed	T (°C)	S (g/kg)	Depth (dbar)	DO (μM)	
Accuracy	±2 μM	±0.025 μg/L	±0.28 ppb	±0.003 m^{-1}	±0.01	±0.0025	±0.005°C	±0.02 g/kg	±2 dbar	±3 μM	
Vertical resolution	10 dbar	1 dbar	1 dbar	1 dbar	1 dbar	1 dbar	1 dbar	1 dbar	1 dbar	2 dbar	
IAOOS 23	Yes	Yes	Yes	Yes	Yes	Yes	Yes	Yes	Yes	Yes	
IAOOS 24	No	No	No	No	No	No	Yes	Yes	Yes	Yes	
Used (U)/Not Used (NU)	U	NU	U	NU	NU	NU	U	U	U	U	

Note. IAOOS = Ice Atmosphere Ocean Observing System; SUNA = submersible ultraviolet nitrate analyzer; CTD = conductivity, temperature and depth; DO = dissolved oxygen; CDOM = colored organic matter.

24 data were retained. The data from the two profilers were corrected independently from one another. We removed salinity spikes associated with sharp gradients within double-diffusive thermohaline staircases as in Dmitrenko et al. (2008). The two profilers' data sets showed great coherence and an offset of 0.01 g/kg in salinity, corrected by applying an offset +0.005 and −0.005 g/kg to data from profilers 23 and 24, respectively. The accuracy was estimated to be 0.005 °C in temperature and 0.02 g/kg in salinity.

The DO data have a 2-db vertical resolution. DO concentrations were retrieved following Thierry et al. (2016). Apparent oxygen utilization (AOU) was computed from the profilers' DO concentrations and compared to AOU derived from DO bottle measurements from the North Pole Environmental Observatory, years 2013 and 2014 (ftp://northpoleftp.apl.washington.edu/../NPEO_Data_Archive/NPEO_Chemistry/CTD-Oxygens/). The comparisons (not shown) suggested a systematic negative offset (about −26 μmol/kg for the IAOOS 24 optode at 250 m and −30 μmol/kg for the IAOOS 23 optode at 360 m), which was corrected. AOU values from the two profilers were consistent throughout the drift with a nearly constant difference of 2.5 μmol/kg at 250-m depth, while the values ranged from 20 to 60 μmol/kg. The nitrate concentration was computed from the observed spectrum (submersible ultraviolet nitrate analyzer) using the Temperature Compensated Salinity Subtracted algorithm developed by Sakamoto et al. (2009) following ARGO DAC protocol (Johnson et al., 2018). Nitrate concentrations were calibrated using 2014 NPEO bottle data and adjusting the optical wavelength offset to 212.5 nm (Johnson et al., 2018). The estimated accuracy of the nitrate observations is 2 μmol/kg (comparison with NPEO values and theoretical sensor accuracy), with a vertical resolution of 10 db. The CDOM fluorescence data are presented as reported by the ECO triplet converted from raw counts to the physical unit (ppb) but uncorrected for any offset beyond that determined during factory calibration. CDOM data have a 1-db vertical resolution, and a manufacturer accuracy of ±0.28 ppb.

The two platforms were initially located 600 m from each other. They drifted together following meandering trajectories, reaching as far as 30°E in the Nansen Basin in mid-October 2017, when they changed direction and drifted back toward Fram Strait (Figure 2a). The profiler IAOOS 24 stopped transmitting on 16 November 2017, the two platforms being separated by about 3 km at that time (Figure 2b). Profiler IAOOS 23 acquired data until 4 January 2018. The meandering drift paths led to four crossover points visited at different times (points A, B, C, and D in Figure 2). Differences between two measurements made some time apart at the same location can be due to either natural in situ variations or instrumental drift. The platforms visited location 83.79°N, 12.55°E (point A in Figure 3) within a 94-day interval (18 August and 20 November 2017). Temperature, salinity, DO, and CDOM were very consistent in the 150- to 250-m depth range indicating that there was no sizable instrumental drift throughout the 8-month-long data set. Interesting differences were observed in the upper 150 m: These are the consequence of seasonal variations and are examined in section 3.3. Nitrate concentrations show a constant difference of about 1.5 μmol/kg over the 150- to 250-m range between the two visits to point A. This offset is small compared to the range of the nitrate concentrations of IAOOS 23 (0 to 12.5 μmol/kg), which is the range of the relatively scarce observations in that part of the Arctic Ocean (e.g., Codispoti et al., 2013; Randelhoff & Guthrie, 2016).

Several profiles did not reach the near surface: a strong stratification in the halocline could have impeded the ascent of the profiler, particularly in July–August 2017 when sea ice melted (Figure 2c) to inject fresh water underneath the sea ice, resulting in a strong density gradient at about 30-m depth (Figure 4). Large drift velocities (>30 cm/s) encountered in the Nansen Basin (Figure 2d) also contributed to prevent the ascent of the profiler. Several profiles are missing late August and late September due to data logger issues (now resolved for future IAOOS deployments).

The two platforms were also equipped with a Scottish Association for Marine Sciences ice mass balance for the Arctic (SIMBA) system: a 5-m chain measuring temperature and a proxy of the

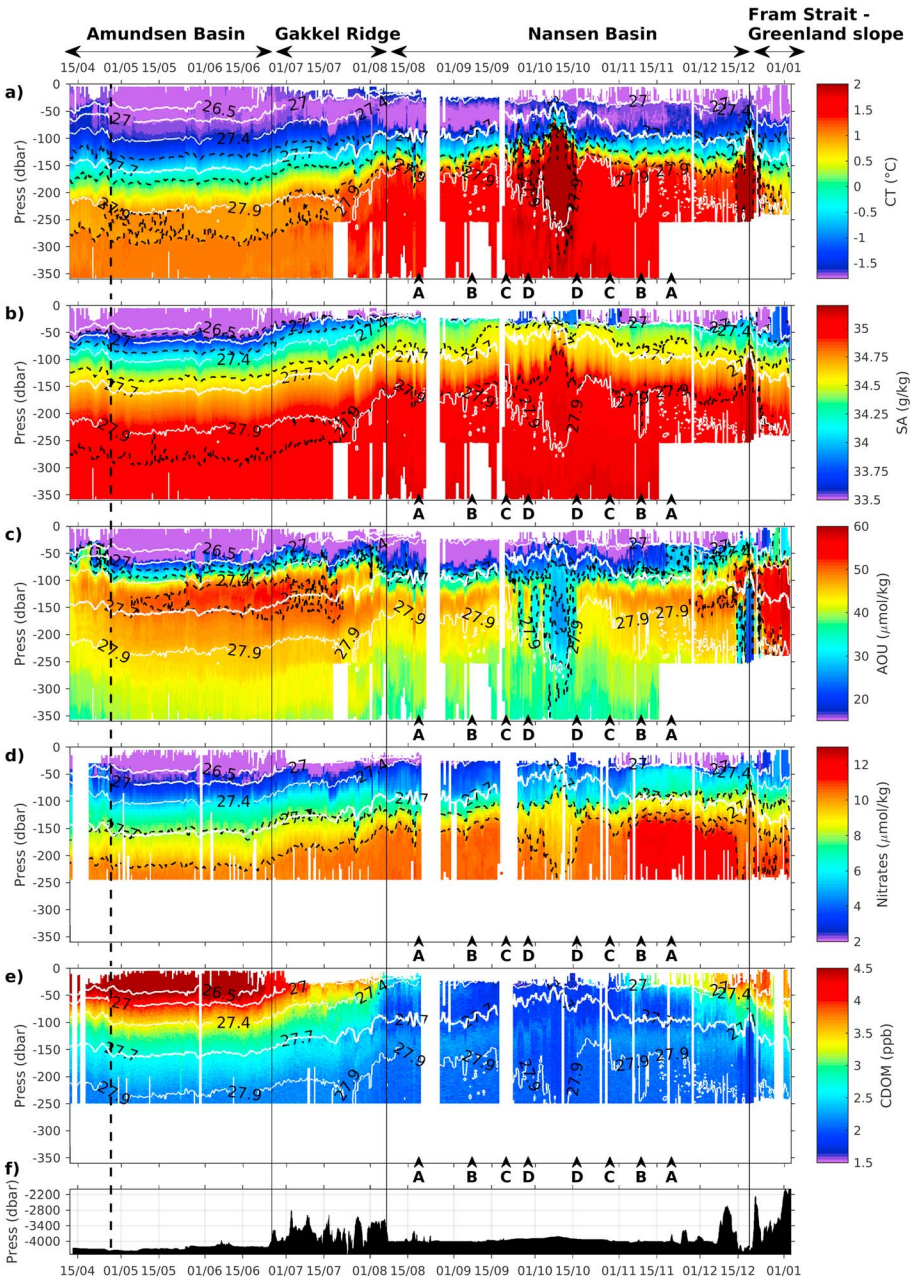

Figure 3. Composite sections from the two profilers: (a) conservative temperature (°C; the thick dashed black line marks the 0 °C isotherm), (b) absolute salinity (g/kg), and (c) apparent oxygen utilization (µmol/kg). Composites were obtained by averaging the data from the two profilers when available and keeping the available data otherwise. (d) Nitrate (µmol/kg) and (e) colored dissolved organic matter (ppb) from biogeochemical profiler IAOOS 23. (f) Bathymetry along the drift trajectory. Black dashed lines are, respectively, temperature, salinity, apparent oxygen utilization and nitrate isolines. White lines are isopycnals, and the thick one marks 27.7 kg/m^3. The four regions are labeled on top of panel (a) and their limits indicated with vertical lines through all panels. The dashed vertical line marks the 88.2°N latitude. Crossover points A, B, C, and D from Figure 2 are reported below the sections.

thermal resistivity of the media with a 2-cm vertical resolution (K. Jackson et al., 2013). The sampling frequency was set to 2 hr, and the sensor accuracy is 0.1 °C (Table 1). The SIMBA record on IAOOS 23 was short (not shown). The SIMBA on IAOOS 24 acquired data from 13 April to 12 November 2017. The tripod to which the chain was attached fell down on 30 July 2017, and the data in the upper part of the chain (air, snow and upper part of the sea ice) are not reliable after that date. The ocean-ice interface was

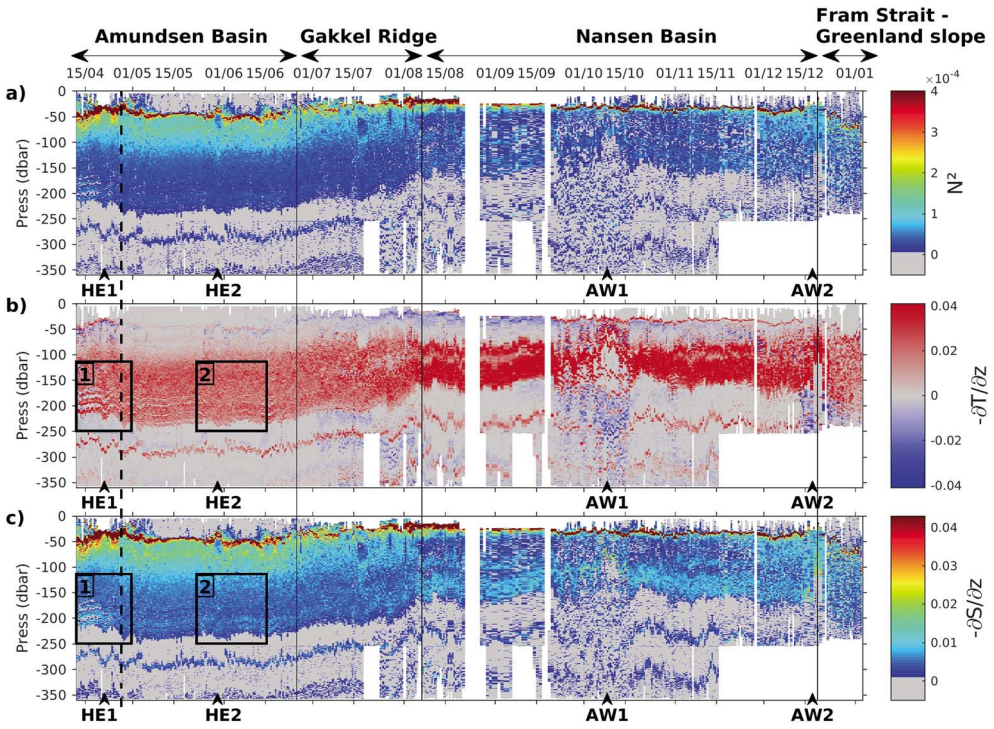

Figure 4. Sections of (a) Brunt-Väisälä frequency (N^2), (b) vertical gradient of conservative temperature $\partial T/\partial z$ (°C/m), and (c) vertical gradient of absolute salinity $\partial S/\partial z$ (g/kg/m) derived from the composite sections. The four regions are labeled on top of panel (a) and their limits indicated with vertical lines through all panels. The dashed vertical line marks the 88.2°N latitude. In (b) and (c), box 1 indicates the position of three steps in temperature and salinity at the base of the thermocline. South of 88.2°N, the steps are substantially eroded and hardly distinguishable in box 2.

estimated following the method described in Provost et al. (2017), based on the detection of changes in the vertical temperature gradient.

The information regarding the data acquired during platform drifts (resolution, sampling accuracy) is summarized in Table 1.

2.2. World Ocean Atlas Climatology

World Ocean Atlas 2013 version 2 (WOA13 V2; Locarnini et al., 2013; Zweng et al., 2013; https://www.nodc.noaa.gov/OC5/woa13/) is a long-term set of objectively analyzed climatologies of temperature, salinity, oxygen, phosphate, silicate, and nitrate available at annual, seasonal, and monthly resolution for the World Ocean. Here we use the WOA13 version 2 monthly averages over the most recent 2005–2012 period. The temperature and salinity fields have a (1/4)° horizontal resolution, with 102 vertical levels of resolution 1 m at the surface to 200 m at 5,500 m.

2.3. Mercator Ocean Operational System

The (1/12)° global Mercator Ocean operational system was developed for the Copernicus Marine Environment Monitoring Service (http://marine.copernicus.eu/), with a (1/12)° horizontal resolution and 50 vertical z levels. The modeling component is based on the NEMO (Nucleus for European Modeling of the Ocean; Madec, 2008) platform and the assimilation system is a multidata and multivariate reduced order Kalman filter based on the singular extended evolutive Kalman filter formulation introduced by Pham et al. (1998). The model uses the LIM2 thermodynamic sea ice model and is driven at the surface by atmospheric analysis and forecasts from the Integrated Forecasting System operational system at European Centre for Medium-Range Weather Forecasts. The assimilated observations are along-track satellite altimetry, sea surface temperature (OSTIA SST), and in situ vertical profiles of temperature and salinity. The system PSY4V3 assimilates OSI SAF (http://cmems-resources.cls.fr/documents/QUID/CMEMS-OSI-QUID-011-001to007-009to012.pdf) sea ice concentration in both hemispheres with a monodata and monovariate scheme. A particular treatment is applied for areas potentially covered in sea ice: The observation error in the multivariate

singular extended evolutive Kalman filter increases linearly (less weight in the analysis) with the decrease of the SST from −1 to −1.7 °C, and the observation is rejected if SST is less than −1.7 °C (i.e., an approximation of the freezing point). In other words, apart from the sea ice concentration no quantities are assimilated in ice covered oceans. A monthly runoff climatology based on coastal runoffs and 100 major rivers from the Dai et al. (2009) database is used. A full description of the system components is available in Lellouche et al. (2018). The system starts in October 2006 from a "cold" start (initial currents are null) and from EN4.2.1 hydrographic temperature and salinity data (Good et al., 2013).

3. Hydrography of the Western Eurasian Basin in April 2017 to January 2018

We define water mass boundaries following Rudels et al. (2000); see Figure 5g. In the Eurasian Basin, the upper layer mainly comprises Polar Surface Water (PoSW, density σ_θ<27.7 kg/m^3). The mixed layer depth is estimated to be at the point of maximum buoyancy frequency N^2, that is, depth of maximum stratification. The stratification at the bottom of the mixed layer evolves geographically and seasonally. The thermocline is predominantly found below the halocline (Figures 5a and 5b), with differences in depth of up to 75 m. The warm layer typically extends between about 150 and 500 m and comprises two main water types: Atlantic Water (AW, $T > 2$ °C) and Modified Atlantic Water (MAW, $T < 2$ °C). Both warm water types occupy the same potential density range of 27.7–28.0 kg/m^3 (Rudels et al., 2000; Schauer et al., 2002; AW and MAW in Figure 5g). In the present data set, the lowest apparent oxygen utilization (AOU ~ −10 to +20 μmol/kg) is located near the surface (Figure 3c). A thin layer of maximum oxygen utilization (AOU ~ 50 μmol/kg) is observed near 120-m depth. Nitrate concentrations monotonically increase with depth, from $[NO_3^-]$ ~ 1–4 μmol/kg near the surface up to a maximum of $[NO_3^-]_{max}$ ~ 12 μmol/kg at 250 m (Figure 3d).

During their drift, the IAOOS platforms crossed several hydrographic regions with distinct characteristics (delineated by the magenta lines in Figure 2a): the Amundsen Basin from 12 April to 25 June (region 1 in Figure 2a), the Gakkel Ridge from 26 June to 5 August (region 2), the Nansen Basin from 6 August until 19 December (region 3), and the western Fram Strait-Greenland slope from 20 December until the end of the acquisition on 4 January 2018 (region 4).

Each region is described in the following subsections and the main characteristics are summarized in Table 2.

3.1. Amundsen Basin: 12 April to 25 June 2017 (152 Profiles)

Two hydrographic regions subdivide the Amundsen Basin. North of 88.2°N (vertical dashed line in Figures 3, 4, and 6), surface salinities lower than 32.5 g/kg were observed in the 30-m-deep mixed layer, with temperatures close to the associated warmer freezing point (S ~ 32.18 g/kg, T ~ −1.7 °C, Figures 6a and 6c). Below the mixed layer, waters are warmer, saltier, and denser and have larger AOU and nitrate concentrations than in the rest of the Amundsen Basin (Figures 3 and 6). South of 88.2°N, the mixed layer exhibits slightly larger salinities and temperatures close to the cooler freezing point (S ~ 32.86 g/kg, T ~ −1.77 °C). This frontal region results from the confluence of fresher water from the Makarov Basin (Timmermans et al., 2011) and Eurasian water, north and south, respectively, of 88.2°N (Figures 3 and 6).

During the platforms' drift through the entire Amundsen Basin, the ice thickness increased (growth ~ 10 cm, Figure 6a). A notable CDOM maximum in the upper 100 m ([CDOM] > 3 ppb) was associated with a minimum in nitrate ($[NO_3^-]$ ~ 0–4 μmol/kg; green curves in Figures 5; Figures 6d and 6e) and overlays a thick zone of maximum oxygen utilization (AOU ~ 45 μmol/kg between 100- and 200-m depths; Figures 5d and 6d). This is the vestige of past biological activity in the water mass. This water is likely a mixture of shelf water and fresh Siberian river runoff that is carried by the Transpolar Drift (TPD) across the central Arctic Basin to reach the Amundsen Basin (Figure 6c; Damm et al., 2018; Kipp et al., 2018).

The thermocline extended between 80 and 220 m ($|\partial_z T|$ ~ 0.02 °C/m; Figures 4b and 5a), while the halocline is between 30 and 220 m deep with a relatively moderate salinity gradient ($|\partial_z S|$ ~ 7×10^{-3} g/kg/m; Figures 4c and 5b). In the Makarov-origin water north of 88.2°N, three homogeneous layers of temperature and salinity and very weak stratification (hereafter called "steps") are visible at the base of the thermocline (characterized by N^2~0, $|\partial_z T|$ ~ 0 °C/m and $|\partial_z S|$ ~ 0 g/kg/m, box 1 in Figures 4b and 4c). The steps are located at roughly 165-, 180-, and 200-m depths and have a vertical extent of ~10 m. South of 88.2°N, the steps are substantially eroded in temperature and are no longer visible in salinity (box 2 in Figures 4c and 4d).

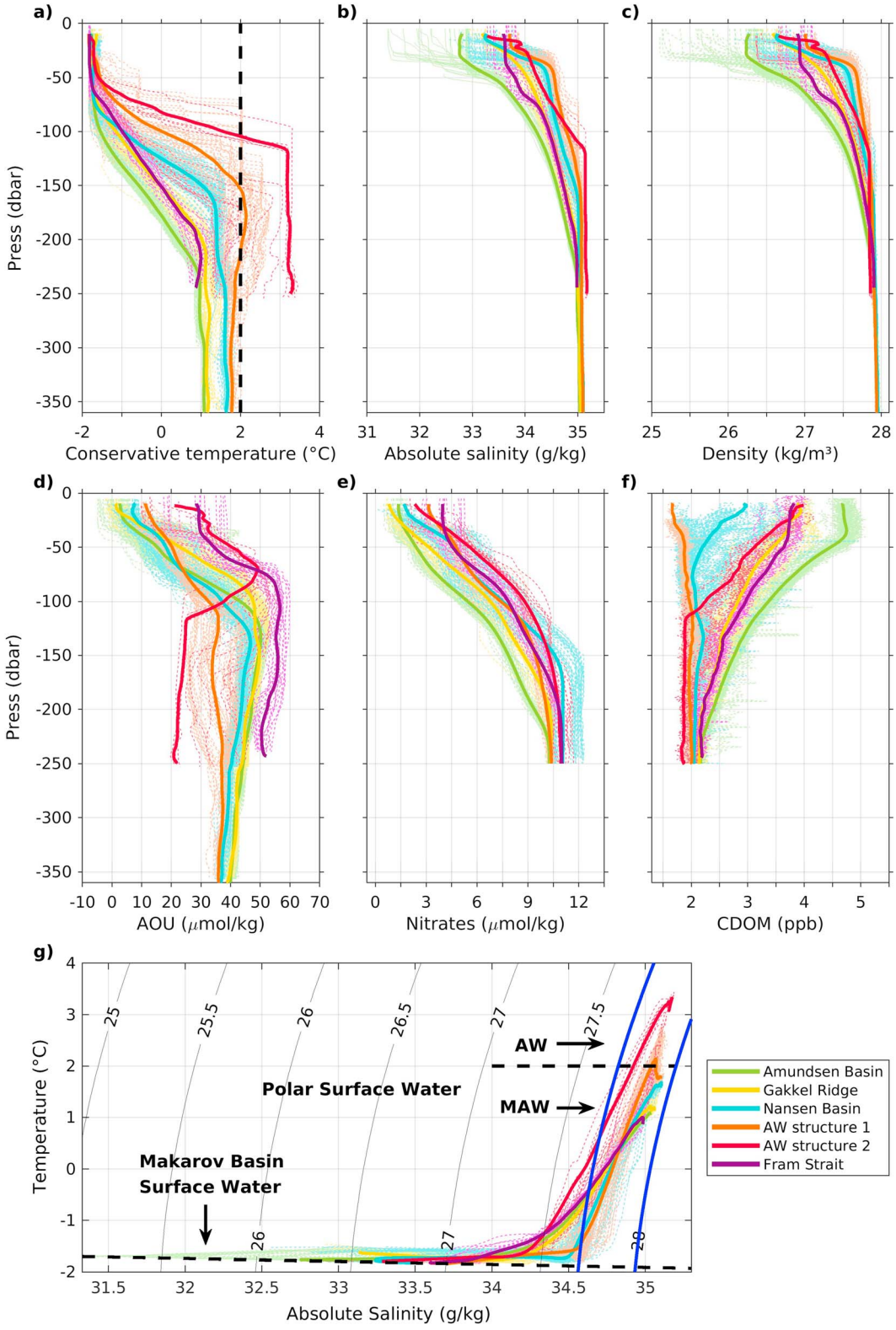

Figure 5. Vertical profiles of (a) conservative temperature (°C), (b) absolute salinity (g/kg), (c) density anomaly (kg/m^3), and (d) apparent oxygen utilization (μmol/kg) from the two profilers. (e) Nitrate (μmol/kg) and (f) CDOM (ppb) from IAOOS 23. (g) TS diagram. Colors correspond to the different regions: the Amundsen Basin in green, the Gakkel Ridge in yellow, the Nansen Basin in blue, AW structure 1 in orange, AW structure 2 in red, and the Fram Strait in purple. Dashed lines are daily profiles; thick lines average profiles in each region. In (a) and (g), the thick black dashed line indicates the 2 °C temperature limit distinguishing MAW (<2 °C) and AW (>2 °C). CDOM = colored dissolved organic matter; AW = Atlantic Water.

Table 2
Hydrographic Characteristics of the Four Regions

		Amundsen Basin				
		North of 88.2°N	South of 88.2°N	Gakkel Ridge	Nansen Basin	Fram Strait - Greenland slope
Dates		12 April 26 April	26 April 25 June	25 June 5 August	5 August 19 December	19 December 4 January
STM or NSTM		No	No	Yes	Yes	No
Mixed layer[a]	Depth (m)[a]	22 ± 10	36 ± 9	Tilted isolines	30 ± 6	40 ± 6
	$\overline{CT}$ (°C)[a]	−1.70 ± 0.02	−1.77 ± 0.01		−1.76 ± 0.01	−1.80 ± 0.01
	$\overline{SA}$ (g/kg)[a]	32.18 ± 0.20	32.86 ± 0.04		33.74 ± 0.12	33.62 ± 0.02
	$\overline{[CDOM]}$ (ppb)[a]	4.70 ± 0.28	4.71 ± 0.28		2.83 ± 0.28	3.73 ± 0.28
50 m	$\overline{CT}$ (°C)	−1.65 ± 0.02	−1.77 ± 0.01	Tilted isolines	−1.69 ± 0.03	−1.75 ± 0.03
	$\overline{SA}$ (g/kg)	33.42 ± 0.08	33.40 ± 0.05		34.43 ± 0.02	33.85 ± 0.09
	$\overline{AOU}$ (μmol/kg)	28.66 ± 10.91	12.35 ± 3.70		20.23 ± 6.96	33.77 ± 4.46
	$\overline{NO_3^-}$ (μmol/kg)	3.63 ± 2.00	2.34 ± 2.00		4.82 ± 2.00	4.59 ± 2.00
	$\overline{[CDOM]}$ (ppb)	4.33 ± 0.28	4.50 ± 0.28		2.19 ± 0.28	3.54 ± 0.28
MAW layer	Depth (m)	144 ± 4	158 ± 4	Tilted isolines	86 ± 23	128 ± 16
	$\overline{CT}$ (°C) top core	0.92 ± 0.01		1.12 ± 0.01	1.40 ± 0.04	0.98 ± 0.03
	$\overline{CT}$ (°C) lower core	1.08 ± 0.01		1.15 ± 0.02	1.61 ± 0.02	NA
	$\overline{SA}$ (g/kg) top core	34.99 ± 0.02		35.00 ± 0.02	35.03 ± 0.02	34.98 ± 0.02
	$\overline{SA}$ (g/kg) lower core	35.03 ± 0.02		35.04 ± 0.02	35.07 ± 0.02	NA
	$\overline{AOU}$ (μmol/kg)	45.23 ± 0.06		45.12 ± 0.49	42.72 ± 0.60	53.00 ± 0.63
	$\overline{NO_3^-}$ (μmol/kg)	9.32 ± 2.00		10.03 ± 2.00	10.27 ± 2.00	10.34 ± 2.00
	$\overline{[CDOM]}$ (ppb)	2.34 ± 0.28		2.34 ± 0.28	2.11 ± 0.28	2.28 ± 0.28

Note. For each parameter, region-averaged value is accompanied with its corresponding standard deviation. The mixed layer depth is estimated with a 0.03 kg/m^3 density difference with the surface values. Several profiles are missing above 20m whereas the 50 m level is well documented. Hence, $\overline{CT}$, $\overline{SA}$, $\overline{AOU}$, $\overline{NO_3^-}$ and $\overline{[CDOM]}$ at 50 m provide a robust characterization of the near-surface regional variations. The MAW layer depth corresponds to the depth of the 27.7 kg/m^3 isopycnal. NSTM = near surface temperature maximum; CDOM = colored dissolved organic matter; AOU = apparent oxygen utilization; MAW = Modified Atlantic Water; NA = not available.
[a]Subject to caution as several profiles do not reach the surface (< 20 m deep).

In the Amundsen Basin, the warm layer is shallower north of the frontal zone (~140 m) than south (~160 m) and is composed of MAW. Figure 4 shows two distinct, thick MAW layers of homogeneous temperature and salinity (N^2~0). The top layer is slightly thinner than the lower layer (respectively, ~50 and 70 m). They are separated by a thin, sharp interface of positive of N^2 corresponding to steep vertical temperature and salinity gradients of 0.035 °C/m and 0.005 g/kg/m (Figures 4b and 4c). This interface is located at 270 m north of 88.2°N and 290 m south (in temperature, salinity, and N^2). For the top and lower layers, temperatures are around 0.92 and 1.08 °C, and salinities are about 34.99 and 35.03 g/kg (Figures 3 and 5).

Two cold core anticyclonic halocline eddies were detected (core depth ~50 m) near 87°N, 5°E and 89°N, 8°E, at a time when the drift trajectory was straight (indicated as HE1 and HE2 in Figures 2, 4, and 6) using the method described in Zhao et al. (2014) based on isopycnal displacements. The two eddies have characteristics typical of surface water: salinity similar to the environment (S ~ 33.75 g/kg), colder temperature (ΔT ~ 0.15 °C), oxygen-enriched (ΔAOU ~ −25 μmol/kg), and nitrate depleted (ΔNO_3^- ~ −1.5 μmol/kg). Due to the limitations of the eddy detection method, which requires at least four profiles in a relatively straight line (Zhao et al., 2014), several eddy-like isopycnal displacements during a sinuous trajectory were disregarded.

3.2. Gakkel Ridge: 26 June to 5 August 2017 (78 Profiles)

The Gakkel Ridge hydrographic region marks the transition between the Amundsen and Nansen basins, with tilted isolines corresponding to a shoaling of the warm MAW layer (Figure 3, yellow curves in Figure 5). CDOM sharply decreases and salinity increases (respectively, from 4.7 to 2.8 ppb and from

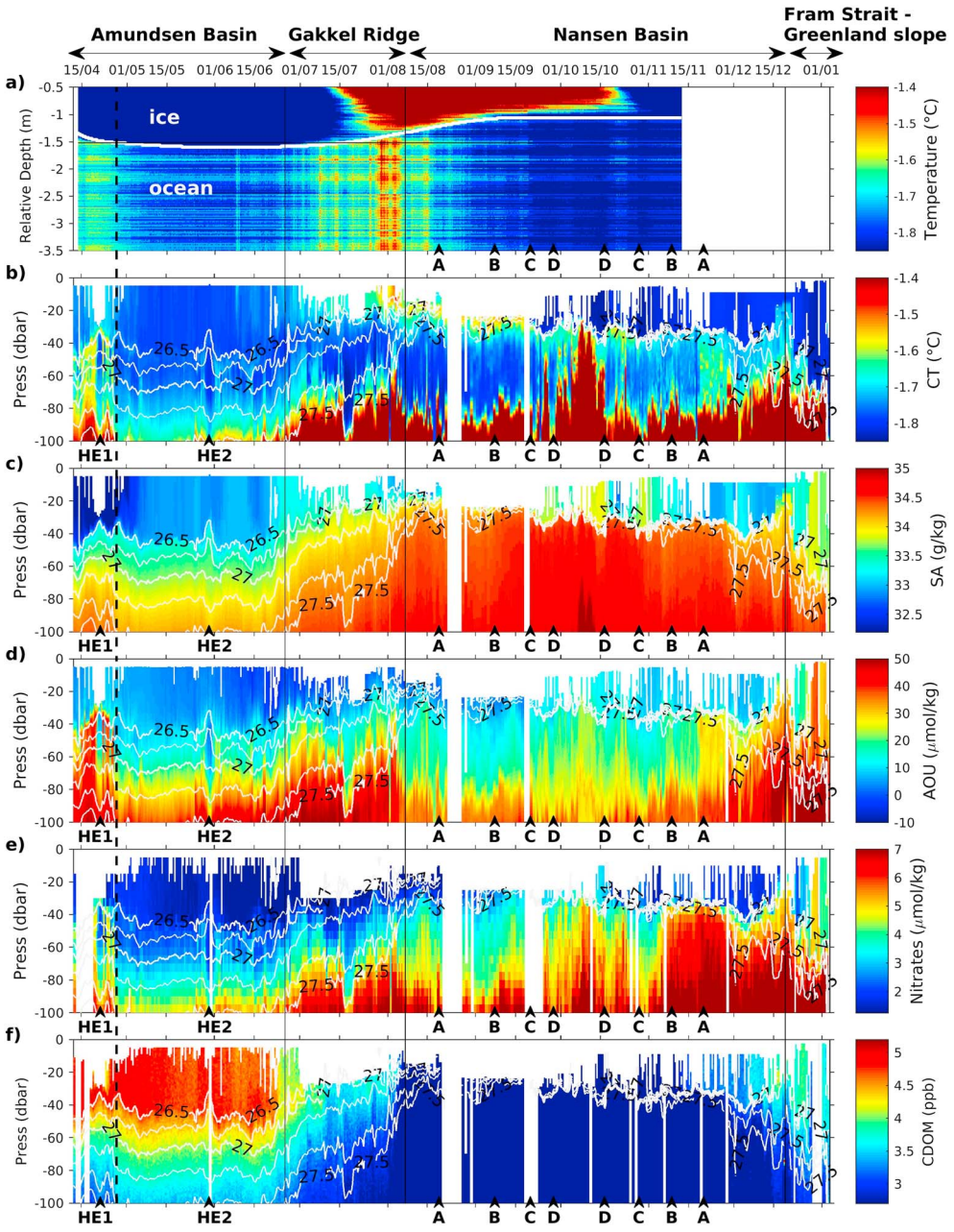

Figure 6. (a) Temperature in the ice and upper 2 m of the ocean from SIMBA chain. The white line delineates the ice-ocean interface. Composite sections in the upper 100 m of (b) conservative temperature (°C), (c) absolute salinity (g/kg), and (d) apparent oxygen utilization (AOU; μmol/kg). (e) Nitrate (μmol/kg) and (f) CDOM (ppb) from profiler 23 in the upper 100 m. Thin white lines are isopycnals. The four regions are indicated as in Figure 3. Halocline eddies (HE1 and HE2) and crossover points A, B, C and D are reported below the sections. The dashed vertical line marks the 88.2°N latitude, the southern limit of surface water fresher than 32.5. SIMBA = Scottish Association for Marine Sciences ice mass balance for the Arctic; CDOM = colored dissolved organic matter.

32.85 to 33.35 g/kg on average at 30-m depth; Figures 3 and 5). From late June to early August 2017, sea ice cover and thickness decrease by 15% and 25 cm, respectively (Figure 2c and 6a), the upper ocean warms by solar radiation and a surface temperature maximum is formed (Figures 6a and 6b; $\partial T/\partial z < 0$ at the surface in Figure 4b). The maximum surface temperature is reached in early August 2017 ($T \sim -1.45$ °C). Above the Gakkel Ridge, the homogeneous MAW layers sharply shoal from below 220 m in the Amundsen Basin to 150 m depth in the Nansen Basin (Figure 4).

Significant eddy-like isopycnal displacements are observed in the halocline, often associated with anomalies in temperature, AOU and nitrate (such as the anomaly observed around 17 July 2017 in Figure 6). However, the complex trajectory during this period prevents an interpretation in terms of halocline eddies. Isopycnals depths show a notable variability at the profile sampling rate (12 hr), probably indicative of topographically induced motions intensified above the Gakkel Ridge (Figure 4). The internal wave field in the Arctic, whether due to surface generated near-inertial waves or topographically induced internal tides (evanescent north of the critical latitude 74.5°N), has frequencies falling within the near-inertial frequency band (Dosser et al., 2014). The IAOOS platforms, set to perform profiles on a 12-hr frequency, only provide an estimate of the minimum internal wave amplitude of ~2 m above the Gakkel Ridge, in the Nansen Basin, and in the Fram Strait (Appendix A).

3.3. Nansen Basin: 6 August to 19 December (188 Profiles)

In the Nansen Basin, the platforms' meandering trajectory extensively documents the 83–85°N, 5–30°E area, except in the upper 20 m (Figure 3).

Near-surface salinities are in the range 32.8–33.8 g/kg (Figures 3 and 6, blue curves in Figure 5). Sea ice thickness decreases until mid-September and stabilizes around 1 m (Figure 6a). Sea ice melt, combined with the shoaling of the warm layer at ~80 m, induces a strong vertical salinity (and density) gradient between 20- and 40-m depths: the summer halocline ($|\partial_z S| \sim 6 \times 10^{-2}$ g/kg/m, Figures 4c and 5b; J. M. Jackson et al., 2010). The previously formed surface temperature maximum is progressively capped by cold and lighter water, leading to a near-surface temperature maximum (NSTM, Figure 6b). The NSTM located at 30-m depth by late September progressively mixes with the surrounding water (first passage at points C and D, Figure 6b). A thin layer of remnant NSTM persists as the platforms exit the Eurasian Basin in December 2017 (Figure 6b). The "lower halocline" is located between 40- and 160-m depth, with a significantly smaller vertical salinity gradient ($|\partial_z S| \sim 5 \times 10^{-3}$ g/kg/m, Figures 4c and 5b).

The thermocline is shallower and sharper than in the Amundsen Basin, between 70 and 150 m ($|\partial_z T| \sim 0.04$ °C/m, Figures 4b and 5a). The warm layer, mostly MAW, is located below 90-m depth, ~50 m closer to the surface than in the Amundsen Basin, and is nitrate enriched ($[NO_3^-] \sim 9$–12 μmol/kg). Along with the top of the warm layer, the two layers of MAW shoal below 150 m and thicken. They are separated by an interface at ~230 m (Figures 4 and 5). The MAW layers exhibit warmer temperatures (respectively, ~1.4 and 1.6 °C) and larger salinities (respectively, 35.03 and 35.07 g/kg) than observed in the Amundsen Basin (Figures 3 and 5).

CDOM concentrations in the Nansen Basin are particularly low ([CDOM] ~ 2.1 ppb) and mostly homogeneous in the upper 250 m (Figures 3 and 5). However, at the level of the lower halocline (~130-m depth) a local CDOM maximum is observed ([CDOM] ~ 2.4 ppb) and matches the thin layer of maximum oxygen utilization (AOU ~ 50 μmol/kg, Figures 3c, 3e, 5d, and 5f), possibly indicating an active remineralization.

Two remarkable AW mesoscale structures are encountered in the Nansen Basin (Figures 2a and 3). The first structure, called hereafter AW1, was encountered near 83.5°N, 35°E between 24 September and 18 October 2017. The second structure, called hereafter AW2, was crossed north of the Yermak Plateau, near 82.8°N, 3°W between 14 and 20 December 2017. Both structures exhibited cores with temperatures larger than 2 °C, densities in the range 27.7–28 kg/m^3 and salinities larger than the surrounding MAW of the Nansen Basin ($\Delta S \sim +0.15$ g/kg): These core properties correspond to AW (Figure 5g). The two structures, examined in section 4.2, show significantly lower oxygen utilization than their environment as well as slightly lower nitrate concentrations (ΔAOU ~ 15–25 μmol/kg, $\Delta NO_3^- \sim -1$ μmol/kg).

3.4. Fram Strait-Greenland Slope: 20 December to 4 January (19 Profiles)

Platform 23 reached 83°N, 1°W on 19 December and exited the Eurasian Basin through the western Fram Strait. The profiler was lost on the Greenland continental shelf.

The near surface shows salinity around 33.3–33.8 kg/m^3 (purple curves in Figure 5; Figure 6) and a local CDOM maximum ([CDOM] ~ 3.5 ppb) associated with a surface nitrate maximum ($[NO_3^-] \sim 4.5$ μmol/kg; Figures 5 and 6). Oxygen use is the highest recorded across the four regions (AOU ~ 50–60 μmol/kg). The variety of profiles corresponds to a frontal zone between the southward fresh and cold East Greenland Current and the salty and warmer AW recirculation branches (Sutherland & Pickart, 2008). In the

western Fram Strait, the warm layer, located below 130-m depth, is composed of cooler (~0.98 °C) and fresher (~34.98 g/kg) MAW exiting the Arctic Ocean (Sutherland & Pickart, 2008; Figures 3 and 5).

The next section focuses on the mesoscale structures crossed during the drift in the halocline near the North Pole and in the warm layer in the southwestern Nansen Basin.

4. Mesoscale Structures in the Western Eurasian Basin

4.1. Halocline Eddies

Two mesoscale structures located in the halocline were crossed at 89°N, 8°E and 87°N, 5°E in the Amundsen Basin (HE1 and HE2 in Figures 2, 4, and 6). They were identified as anticyclonic halocline eddies following Zhao et al. (2014). For halocline eddies 1 and 2, respectively (HE1 and HE2), six and nine consecutive profiles from each profiler showed anomalous convex isopycnal displacements while the drift trajectory was fairly straight (Figure 7). Assuming that both halocline eddies were crossed in their center, they have radii R_{HE} ~ 12 km, which is of the order of the Rossby deformation radius R_d in the region (in the Eurasian Basin R_d ~ 8 km, in the Canada Basin R_d ~ 13 km; Zhao et al., 2014; Figures 7a and 7b). Baroclinic velocities derived from density provide horizontal velocity difference between the eddy boundary and the center of about 5 and 3.5 cm/s for HE1 and HE2, respectively (Figures 7c and 7d). The eddy core depths are considered to be at the depth of the minimum temperature within the eddy (red markers in Figures 7e and 7f). The thickness of the eddy is defined by the distance between local maxima of the Brunt-Väisälä frequency N^2 above and below the eddy core (blue markers in Figures 7e and 7f). As HE1 does not have a maximum in N^2 below its core, its lower edge is roughly estimated from the temperature anomaly (cyan markers in Figure 7e). Both halocline eddies have core depths and thicknesses on the same order, with HE1 being slightly shallower and thicker (core depth ~ 45 and 55 m thick) than HE2 (core depth ~ 55 and 40 m thick). Maximum azimuthal baroclinic velocities are roughly at the same depth as the property cores (Figures 7c and 7d). Associated isopycnal displacements are visible as deep as 280 m for HE1 and possibly below (Figure 3) and extend down to 220 m for HE2 (Figure 4).

HE1 and HE2 are located, respectively, north and south of the frontal zone of Makarov-origin water at 88.2°N: Hence, the characteristics of their surrounding waters are rather different (as described in section 3.1). However, the two cores carry similar PoSW properties, with temperatures significantly colder than their environment (ΔT_{HE1} ~ −0.2 °C, ΔT_{HE2} ~ −0.08 °C), oxygen-enriched (ΔAOU_{HE1} ~ −30 μmol/kg, ΔAOU_{HE2} ~ −15 μmol/kg), and nitrate-depleted (ΔNO_3^-HE1 ~ −2 μmol/kg, ΔNO_3^-HE2 ~ −1 μmol/kg). The CDOM concentration in the cores is also somewhat lower ($\Delta CDOM_{HE1}$ ~ −0.4 ppb, $\Delta CDOM_{HE2}$ ~ −0.5 ppb) at the upper edge of the property cores. This suggests that the two halocline eddies were formed from the same surface water mass, despite their present location in different water masses. Possible sources of generation of these eddies are discussed in section 5.3.

4.2. AW Mesoscale Structures

Two AW mesoscale structures were crossed in the Nansen Basin (Figure 2a). The first AW structure (AW1) was encountered north of Kvitøya Trough (83.5°N, 35°E) as the platforms followed a hairpin turn (Figure 8a). AW1 is documented with 40 profiles over 22 days (40 from each profiler) from 25 September to 17 October 2017. The AW structure north of the Yermak Plateau (82.8°N, 3°W; AW2) was crossed in a straight line from 14 to 20 December 2017 (14 profiles in 7 days over 55 km and down to 250 m).

The AW mesoscale structures exhibit larger temperature and salinity than the surrounding MAW at about 1.5 °C and 35.05 g/kg in the Nansen Basin (Table 2). Their T-S characteristics are consistent with AW (orange curves for AW1 and red curves for AW2 in Figure 5). They are oxygen enriched compared to their environment (AOU_{env} ~ 45 μmol/kg). The core of AW2 is warmer (3 to 3.5 °C), saltier (35.2 g/kg), and more oxygen enriched (AOU_{AW2} ~ 20 μmol/kg) than the AW1 core (2.5 °C, 35.1 g/kg, AOU_{AW1} ~ 30 μmol/kg), which is likely explained by its greater proximity to the original inflow of AW through the Fram Strait (Figures 2a and 3). Both AW structures are nitrate-enriched compared to the surrounding PoSW at their upper boundary (ΔNO_3^- ~ +1.5 μmol/kg) although they are nitrate-depleted compared to the MAW layer (ΔNO_3^- ~ −1 μmol/kg).

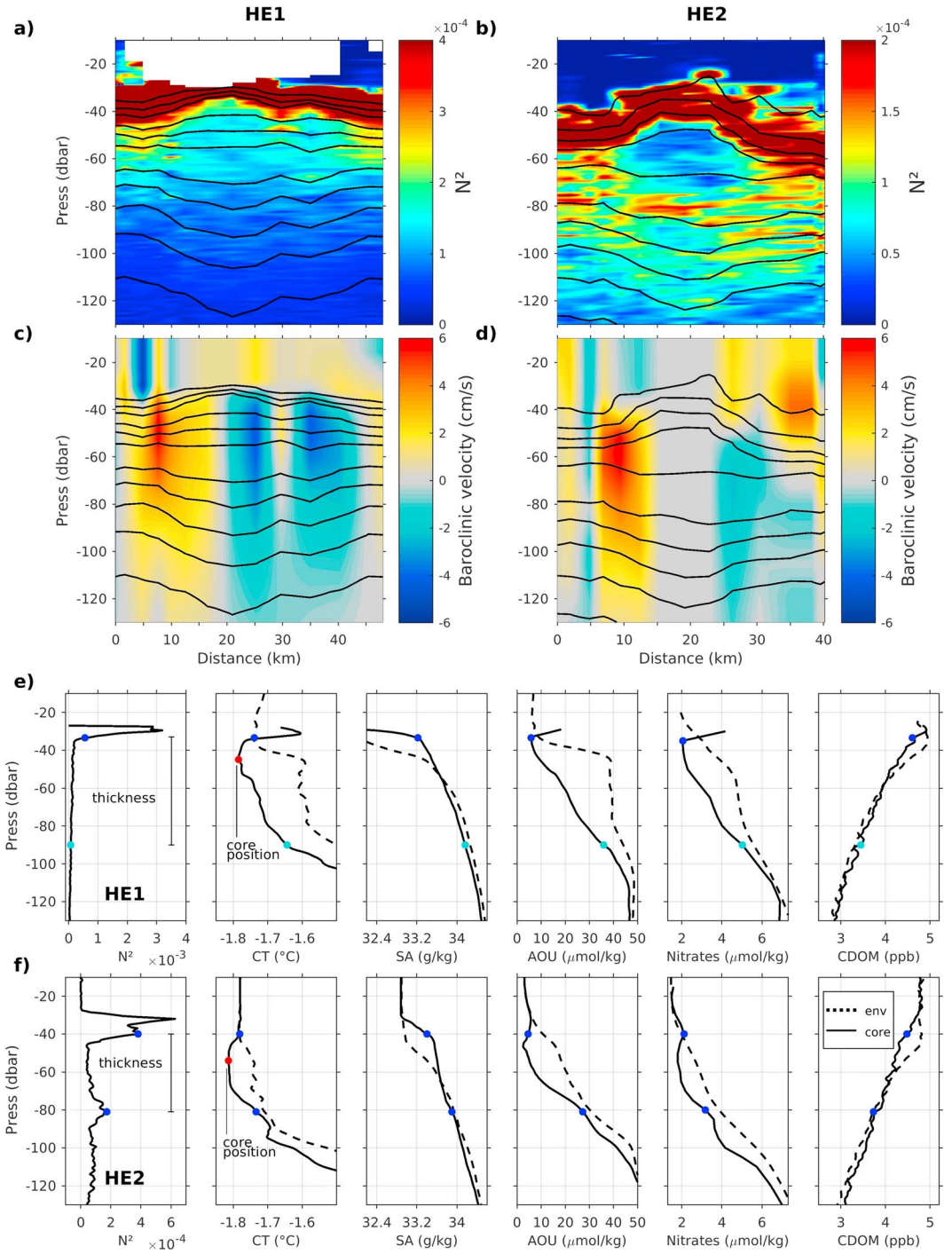

Figure 7. (a, b) Brunt-Väisälä frequency (N^2) in halocline eddies HE1 (crossed at 87°N, 5°E late April) and HE2 (crossed at 89°N, 8°E late May), respectively. (c, d) Baroclinic velocities (cm/s) in HE1 and HE2, respectively. Black lines are isopycnals. (e, f) Vertical profiles of N^2, conservative temperature (°C), absolute salinity (g/kg), AOU (μmol/kg), nitrate (μmol/kg) and CDOM (ppb) in the eddies core HE1 and HE2, respectively (solid black profiles). Dashed black profiles are from the eddy environment. AOU = apparent oxygen utilization; CDOM = colored dissolved organic matter; SA = salinity.

Both AW cores (depth of maximum temperature) are located around 180 m (Figures 3 and 5). AW1's thickness is about 190 m, with top and bottom edges at respectively 80 and 270 m (limits of the 2 °C criterion). AW2's top edge is located at 100 m; its thickness cannot be estimated (not documented below 250 m). A

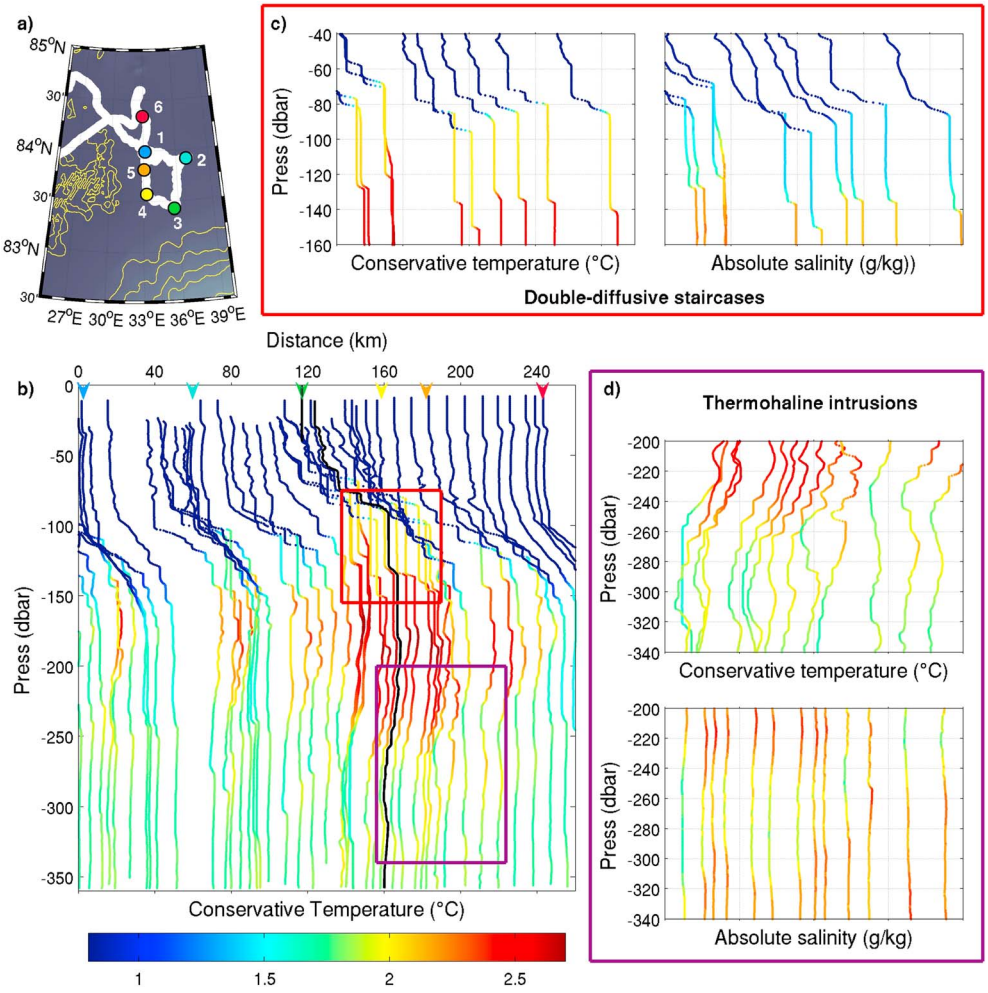

Figure 8. (a) Close-up on the platform trajectory when crossing mesoscale feature AW1 (white line). Yellow lines are bathymetry contours (−3,200, −2,000, −1,000, −500, and 0 m). Locations 1 to 6, in chronological order, are reported in (b). (b) Sequence of conservative temperature (°C) profiles from profiler IAOOS 24 from 24 September to 18 October within AW1. Each profile is offset from the previous one proportionally to the profile distance. Color code indicates conservative temperature. The black profile indicates the profile after which the platform backtracked. Double diffusive staircases are observed on the upper part of AW1 (red box), and intrusions are observed at the bottom edge of AW1 (purple box). The thick black profile indicates the southernmost location (labeled 3 in panel a). (c) Close-up on the red box: staircase-like features (double diffusive interfaces) in temperature and salinity. (d) Close-up on the purple box: inversions in temperature and salinity, consistent across several profiles, indicate thermohaline intrusions.

close examination of the temperature and salinity vertical profiles reveals intrusions and staircase structures, likely generated by double-diffusive processes (Figure 8). Several studies (e. g. Bebieva & Timmermans, 2016; Dmitrenko et al., 2008; Polyakov et al., 2018) used parameters such as the vertical density ratio to provide a quantitative characterization of the double-diffusive modes and to differentiate double-diffusive steps and intrusions. However, as the vertical resolution of the data set is around 1 dbar, we only provide a qualitative assessment of the vertical structure and double-diffusive features observed.

The “staircase structure” in AW1 indicates the presence of double-diffusive steps about 10 to 20 m thick at the upper limit of the structure in the thermocline (orange curves in Figure 5; Figures 8b and 8c). Thermohaline intrusions are observed above, on the sides of, and below AW1 (Figure 8d). In the upper part of AW1 (80 to 180 m), particularly thick (50 m) double-diffusive staircases are observed, separated by sharp, thin interfaces of strong vertical gradient in temperature (about 0.1 °C/m) and salinity (about 0.005 g/kg/m; Figures 4b and 8b). In the lower part of AW1 (180 to 270 m), vertically alternating intrusions and double-

diffusive staircases are observed (Figure 8), corresponding to successive positive and negative values of $\partial T/\partial z$ (Figure 4b).

AW2 exhibits somewhat different features with thicker steps in the core (up to 70 m thick, red curves in Figure 5), pronounced thermohaline intrusions on the sides (not shown) and no double-diffusive staircases in the thermocline.

To gain further perspective on the data set, we examine monthly climatological data from the decade 2002–2013 (WOA13) and Mercator Ocean operational outputs.

5. Perspective From WOA13 Climatology and Mercator Ocean Operational Model

5.1. Comparison With the 2005–2012 WOA13 Climatology

We temporally (month by month) and spatially collocated WOA13 monthly climatologies with the IAOOS drift then interpolated the climatological profiles to the vertical resolution of the IAOOS data. Data shallower than 20 m are not considered. Differences are computed as $\text{data}_{\text{IAOOS}} - \text{data}_{\text{WOA13}}$ and are presented in scatter plots for three regions in Figure 9. We distinguish three layers: a near-surface layer, a thermocline and halocline layer, and a warm MAW layer (see Figure 9 caption for details).

Major differences in conservative temperatures are observed in the thermocline and upper MAW layer, with a general warming reaching values up to +0.75 °C in the Nansen Basin, +0.5 °C above the Gakkel Ridge and +0.3 °C in the Amundsen Basin (Figures 9a–9c). This warming is associated to a salinification on the order of +0.25 g/kg (Figures 9d–9f). On the other hand, the warmest and deeper part of the sampled MAW layer (~350 m) does not show this warming trend. These changes are the signature of the shoaling of the AW layer upper boundary. Polyakov et al. (2017) described a 40-m shoaling of the AW in the eastern Eurasian Basin between 2003 and 2015. Similarly, in the western Eurasian Basin, we document an average shoaling of the AW layer upper boundary (27.7-kg/m^3 isopycnal) of 22 m between 2005–2012 and 2017 (not shown). Figure 9h shows that at 145 m, temperatures on the order of ~1 °C are located further North in the 2017 data set than in the 2005–2012 climatology.

Furthermore, while surface temperatures show little variation, IAOOS 2017 surface salinities exhibit a significant fresh evolution when compared to the 2005–2012 WOA13 climatology (Figures 9d–9f). In the 2017 observations, the frontal region between Makarov and Eurasian waters is at 88.2°N, 10°E in April. The same frontal region in WOA13 in April appears further west than in the observations by about 40° (Figure 9g). This difference appears to be mainly responsible for the large surface salinity difference in the Amundsen Basin (Figure 9d). In WOA13, the frontal region varies in intensity and location from month to month (not shown): The freshest conditions near the North Pole are reached in September after summer sea ice melt, corresponding to a position of the frontal region comparable to the April 2017 observations (Figure 9g).

Korhonen et al. (2013) analyzed the evolution of pan-Arctic hydrographic properties over the 1991–2011 period. They observed a clear warming of the AW layer in the Eurasian Basin, mostly confined to the Nansen Basin (~+0.3 °C per decade). Our results indicate a reduced warming rate within the AW layer of +0.05 °C in the Eurasian Basin between 2005–2012 and 2017. The shoaling of the AW we observed between 2005 and 2012 and 2017 is consistent with the thickening of the AW layer (about 18 to 22 m per decade) described in Korhonen et al. (2013).

Rabe et al. (2014) pointed out to an Arctic-wide freshening of the upper layer between 1992 and 2012 with an overall salinity decrease of −0.6 g/kg. Peralta-Ferriz and Woodgate (2015) showed that the Eurasian Basin mixed layer freshened by ~−0.7 g/kg per decade from 1979 to 2012. Our results are consistent with a continuation of the freshening at the same rate between the 2005–2012 decade and 2017 (Figures 9d and 9f).

5.2. Mercator Ocean Operational System: Comparison to IAOOS 2017 Observations

The daily Mercator Ocean analyses are collocated in space and time with the IAOOS profiler data and interpolated to the data vertical resolution (Figures 10a and 10b). Temperature and salinity show a global agreement with the daily averaged observations, with a remarkably well located 27.7-kg/m^3 isopycnal (characterizing the top of the MAW and AW layer) and well-positioned AW mesoscale structures (Figures 10a and 10b).

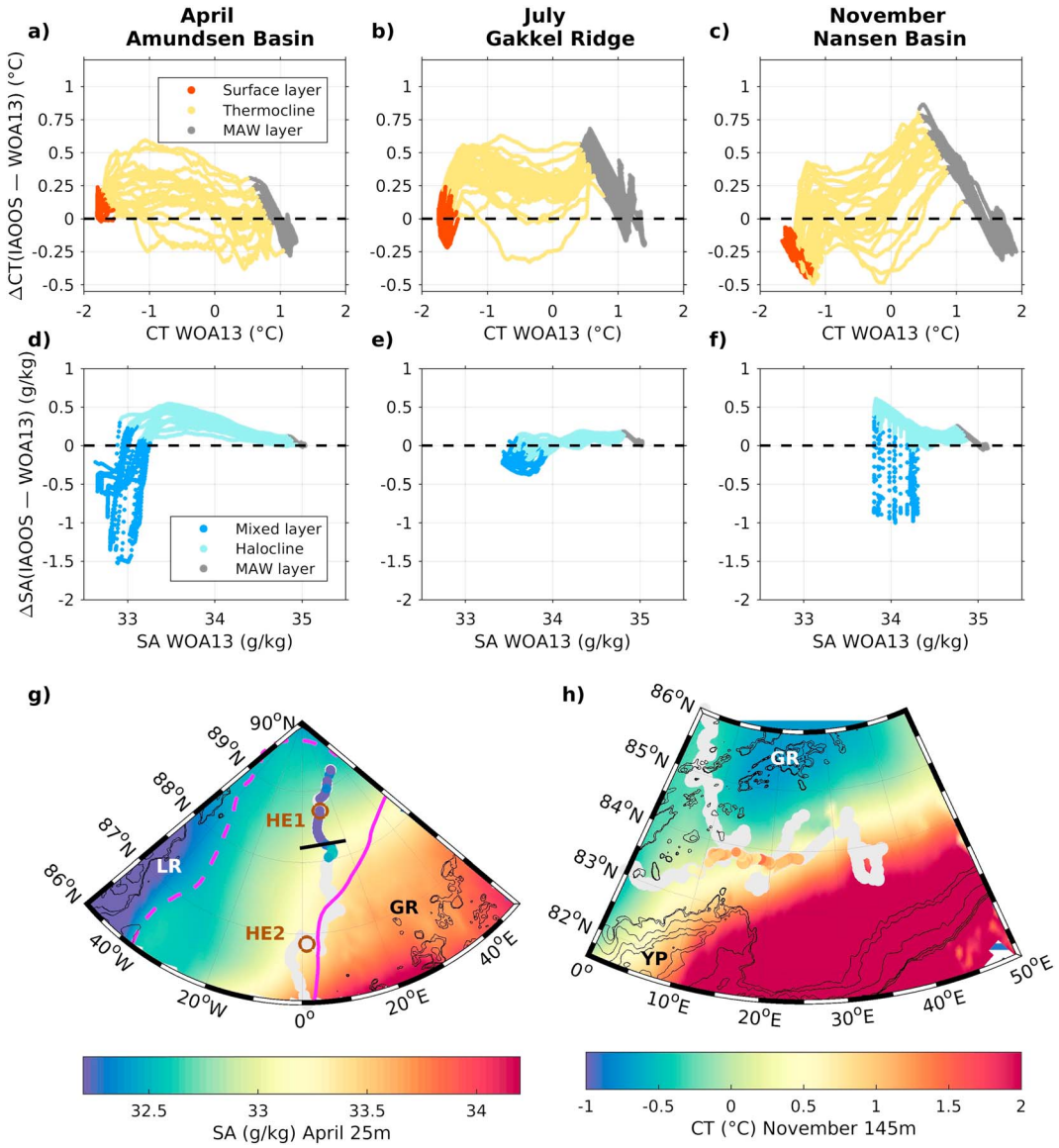

Figure 9. (a–f) Scatter plots of differences between Ice Atmosphere Ocean Observing System (IAOOS) observations and collocated WOA13 climatological data, in the Amundsen Basin (April, left panels), above the Gakkel Ridge (July, middle panels), and in the Nansen Basin (November, right panels). (a–c) Conservative temperature (°C). Red markers correspond to the isothermal near-surface layer ($CT \leq CT_{surf} + 0.2$ °C). Yellow markers represent the thermocline. Gray markers indicate the homogeneous Modified Atlantic Water layer (such as $|\partial_z T| \sim 0$ and $|\partial_z S| \sim 0$). (d–f) Absolute salinity (g/kg). Dark blue markers correspond to the mixed layer (down to the depth of N^2_{max}). Cyan markers correspond to the halocline. (g) Absolute salinity (g/kg) at 25 m in April and (h) conservative temperature (°C) at 145 m in November. Background is WOA13 2005–2012 climatology, and markers are IAOOS 2017 observations. Magenta lines in (g) are the 32.5 g/kg isohaline, representative of the frontal zone, in April (solid line) and September (dashed line) in the WOA13 2005–2012 climatology. Bathymetry isolines are in the thin black lines. GR, LR, and YP stand for Gakkel Ridge, Lomonosov Ridge, and Yermak Plateau, respectively.

However, the sections of model-observation differences (Figures 10c and 10d) reveal biases. The cold and slightly fresh bias at 150 m, larger in the Nansen Basin close to Fram Strait (−1.5 °C and −0.2 g/kg in November), results from an overly deep representation of the thermocline and MAW layer. A major bias in salinity (>1 g/kg) is observed in the surface layer near the North Pole (beginning of the time series; Figures 10b and 10c). The salinity bias (>0.5 g/kg^3) in the surface layer starting in November accompanies excessive sea ice formation in the model compared to the observations. The formation and deepening of the

NSTM in the model are consistent with observations, however the model NSTM is cooler (~−0.15 °C) and fresher (~−1 g/kg) than observed. In the western Fram Strait-Greenland slope region, a large patch of AW is visible in the model outputs (Figures 9 and 10). A plausible explanation is that the platforms drifted close to the AW recirculation branch in Fram Strait and the edge of this branch is likely rendered somewhat further west in the model outputs.

The first AW mesoscale structure (AW1) in the Nansen Basin is well located. In the model, AW1 is too warm (+0.5 °C; Figures 10c and 10e) and its bottom edge is located about 100 m deeper than in the observations (360-m depth in the model whereas 250-m depth in the observations; Figures 10a and 10e). The second mesoscale structure (AW2), close to Fram Strait, is not exactly at the same location as in the observations, leading to a large dipole-like difference in temperature and salinity (Figures 10c and 10d).

In summary, in spite of biases, the model is generally in good agreement with the observations and represents well the AW. We therefore use the model to investigate the origin and evolution of the AW mesoscale structures.

5.3. Observed Mesoscale Structures: Insights From Mercator Ocean System

5.3.1. Halocline Eddies

Mercator Ocean outputs have a significant salinity bias in the upper layer of the Amundsen Basin during the buoy sampling time (April–May), and the frontal region between the fresher Canadian waters and saltier Eurasian waters is represented much further west than the observations do at that time, by about 20° (Figure 11a). However, as in WOA13 the position of the frontal region in September in the model is further east and thus more comparable to the April observations (thin vs. dashed lines in Figure 11a). In Mercator Ocean outputs, the frontal region sheds numerous near-surface eddies in September. An example of an eddy occurring near the trajectory of the buoy during this chosen month is shown in Figures 11b–11d. While the modeled anticyclonic eddy occurs later in the year than the observed eddies HE1 and HE2 (September rather than April), their temperature, salinity and N^2 are quite similar (Figures 11b–11d). This suggests that halocline eddies HE1 and HE2 probably resulted from instabilities of the surface front. The modeled eddies have slightly larger radii (~20 km) than those observed (12 km) and are rather short-lived (4–18 weeks), as the model grid ((1/12)°) cannot resolve the mixed layer deformation radius (about 4 km; Brannigan et al., 2017).

5.3.2. AW Mesoscale Structures

The AW mesoscale structures in the model show great coherence with the observations. The first AW structure (AW1) crossed by the platforms (at 83.5°N, 35°E) is particularly well represented in the Mercator Ocean outputs. Model snapshots (Figure 12) reveal that it is likely an AW meander being shed from the Arctic Circumpolar Boundary Current, which later turned into an AW eddy. Model outputs indicate that the meander formed in late September. It detached from the boundary current by mid-November 2017 (at 83.7°N, 34.5°E) to form an anticyclonic AW eddy. The model suggests a radius ~30 km, significantly larger than the Rossby deformation radius R_d in this area (R_d on the order of 10 km). In the model outputs, the eddy is characterized by salinity in the range 35.06–35.11 g/kg and temperature between 2 and 2.7 °C in its core, consistent with observations (Figure 10), and a maximum azimuthal speed of 2.5 cm/s at its edge (Figure 12). Model outputs show a slightly northwestward propagation for 2.5 months until late January 2018 (at 83.85°N, 34°E) when the rotation decays (Figure 12). In March 2018, the rotating motion disappears and the T-S characteristics are eroded due to mixing with the surrounding water (Figure 12i).

To examine the performance of the Mercator Ocean operational model regarding AW eddies in the region, we compare model outputs to an AW anticyclonic eddy extensively described by Våge et al. (2016). The eddy was encountered in September 2012 above the shelf slope of Kvitøya Through (81.75°N, 30°E) and has a radius R ~ 10–15 km, comparable with R_d. Its core was warmer (2–3.3 °C) and saltier (35.08–35.2 g/kg) than AW1. The maximum azimuthal speed at the edge of the eddy is ~7 cm/*S*. Mercator Ocean outputs reproduce the AW eddy described by Våge et al. (2016) remarkably well (not shown) in particular its location, temperature, salinity, and core depth (~250 m) at the precise date (21 September 2012). The model exhibits an azimuthal speed of ~5 cm/s somewhat smaller than the observations by $\Delta|u| \sim -2$ cm/s, falling within the acoustic Doppler current profiler instrument error (±2 cm/s; Våge et al., 2016). The simulated eddy radius and bottom edge depth are on the order of the observations, even if slightly overestimated (respectively $\Delta R \sim +15$ km and $|\Delta z| > +200$ m). Indeed, as mentioned above, the model grid resolution (about 6 km in

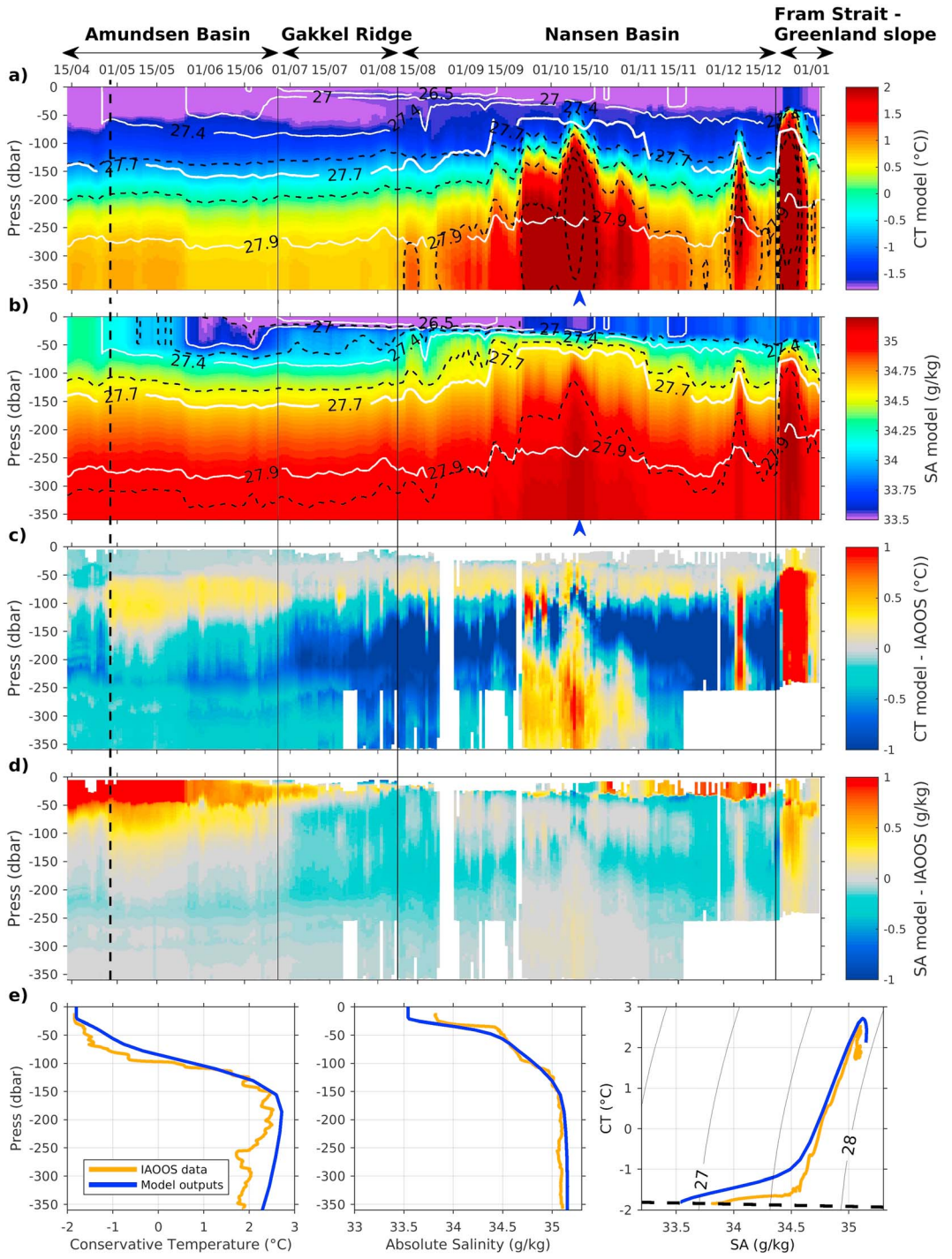

Figure 10. (a) Conservative temperature (°C) and (b) absolute salinity (g/kg) from daily Mercator Ocean model outputs collocated with the platform drift and interpolated to the data vertical resolution. Black dashed lines are temperature and salinity isolines in the model. Thin white lines are isopycnals. The thick white line is the 27.7-kg/m^3 isopycnal. The four regions are indicated as in Figure 3. Differences between model outputs and Ice Atmosphere Ocean Observing System observations in (c) conservative temperature (°C) and (d) absolute salinity. (e) CT, SA profiles, and associated TS diagram in observations (yellow) and model outputs (blue) at the time of AW1 (blue arrow on 7 October under panels a and b).

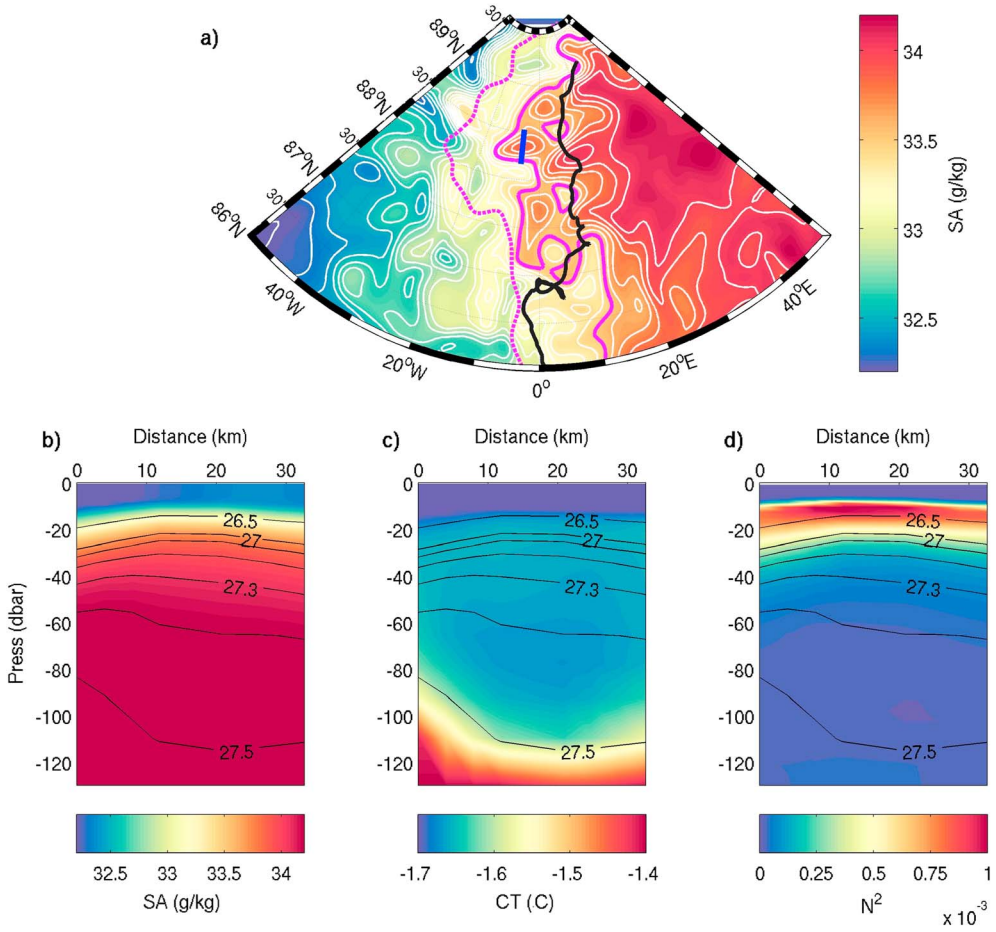

Figure 11. (a) Mercator Ocean salinity (SA) field at 25-m depth on 4 September 2017, with white isolines every 0.1 g/kg. The buoy trajectory is shown in black, and the location of the eddy section in blue. As the model exhibits a large salinity bias near the North Pole (>1 g/kg^3), the 33.5-g/kg isoline (magenta lines) is considered representative of the frontal zone instead of 32.5 g/kg in Figure 9. Its position on 4 September (solid) is reported, as well as in April (dashed) when the buoy was in this region. (b–d) Sections through the anticyclonic eddy and along the blue line in (a) from south to north, depicting (b) absolute salinity (g/kg), (c) conservative temperature (°C), and (d) Brunt-Väisälä frequency (N^2), with isopycnal contours overlayed in black.

the area) is too large to resolve explicitly the Rossby deformation radius. Hence, the simulated eddies have necessarily radii $R \geq R_d$.

AW2 is encountered at 82.8°N, 3°W between 12 and 22 December 2017 (Figures 2 and 3). In the model, the AW recirculation branch represented between 20 and 30 December 2017 at 81°N, 4°W to 82.7°N, 4°W (Figure 10) shows very similar T-S properties to AW2 observed close by, suggesting that AW2 is an AW recirculation branch.

6. Summary and Discussion

The 8-month-long physical and biogeochemical data set documented the upper 350 m of four regions with distinct hydrographic characteristics in the Western Eurasian Arctic Basin (summarized in Table 2).

The IAOOS 2017 campaign provided new insights on the recent state of the Arctic western Eurasian Basin. High CDOM and low nitrate in the upper Amundsen Basin allowed the backtracking of the water mass as shelf-origin water, enriched in Siberian river runoff and carried by the TPD across the central Arctic Basin (Damm et al., 2018; Kipp et al., 2018).

Comparison with WOA13 climatology indicates a shallower AW layer in 2017 than over the 2005–2012 period in the western Eurasian Basin, consistent with the thickening of the AW layer described in Korhonen

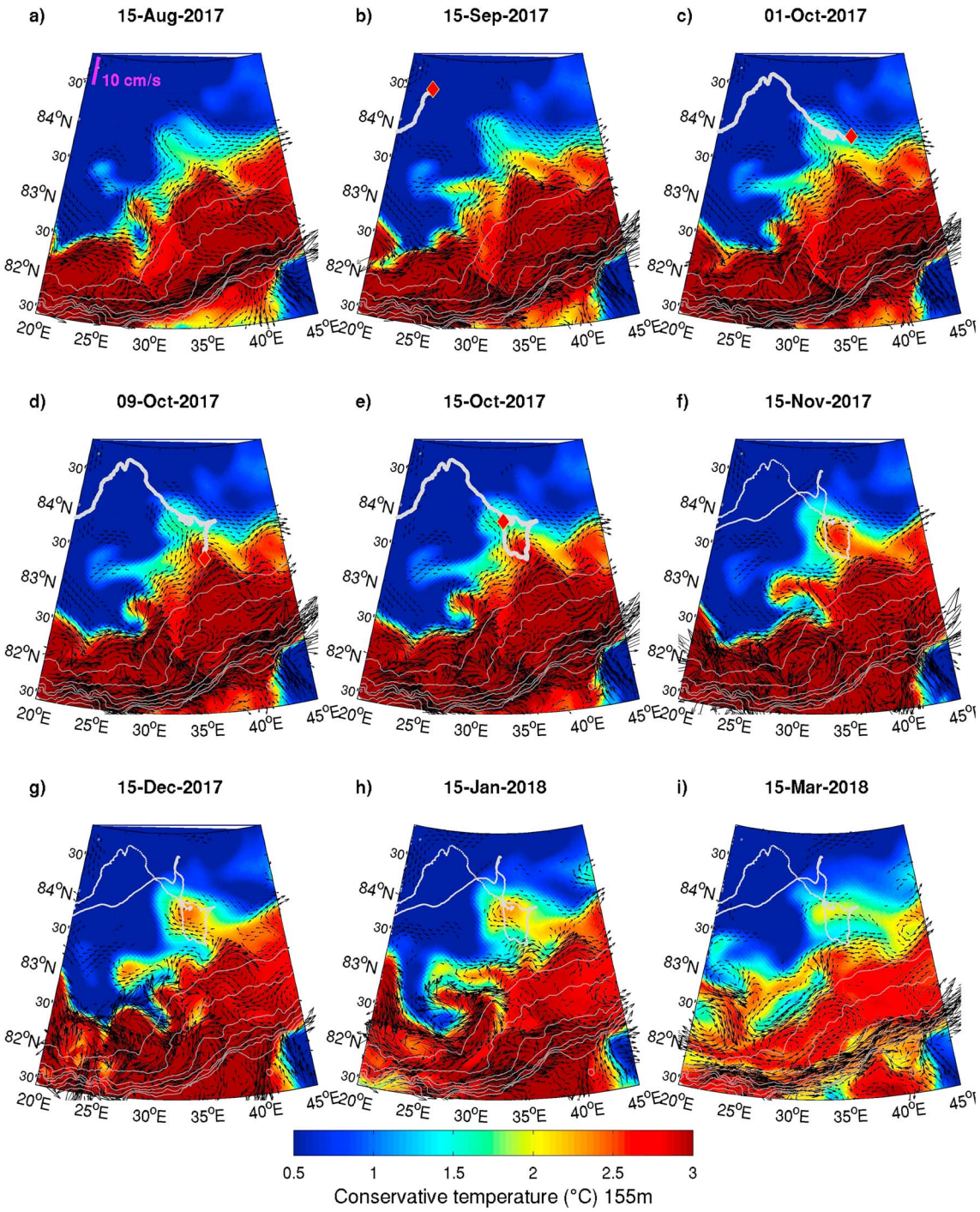

Figure 12. Selected snapshots of the Atlantic Water mesoscale structure in Mercator Ocean model outputs shown at 155 m. The white line corresponds to the Ice Atmosphere Ocean Observing System platforms trajectory. The red diamond marks the position of the platforms at each selected date. Gray isolines are bathymetry contours. Black arrows are the current at 155 m in the model; the scale is indicated in (a). Velocities lower than 1 cm/s are not shown.

et al. (2013). Polyakov et al. (2017) showed that this shoaling of the AW layer, together with the sea ice decline and weakened halocline, are the symptoms of the progressive Atlantification of the Eurasian Basin. In 2017, the mixed layer is fresher than in 2005–2012, indicating the continuation of the freshening described in Rabe et al. (2014) and Peralta-Ferriz and Woodgate (2015). Coincidently, the frontal zone at the confluence of fresher surface water from the Makarov Basin and saltier Eurasian surface water appears to have shifted further southeast (near 88.2°N, 10°E) compared to 2005–2012 (near 88.5°N, 45°E).

Alkire et al. (2015) point out the large interannual variability in surface salinity in the central Arctic, partly attributed to shifts in the alignment of the TPD. Several studies document the contribution of the Arctic Oscillation index in the shifts of the TPD and Arctic general surface circulation (Alkire et al., 2015; Armitage et al., 2018; Morison et al., 2012). However, the relationship between Arctic Oscillation and river runoff pathways in the present data set remains unclear.

The IAOOS platforms documented mesoscale structures within the halocline as well as in the warm layer during their drift through the Arctic Eurasian Basin. Two anticyclonic halocline eddies are identified in the Amundsen Basin, near 87°N, 5°E and 89°N, 8°E, respectively, with radii R_{HE} ~ 12 km (~R_d in the region). They carry surface water properties (colder temperature ΔT ~ 0.15 °C, oxygen-enriched ΔAOU ~ −25 μmol/kg and nitrate-depleted ΔNO_3^- ~ −1.5 μmol/kg) despite salinities similar to their environment (S ~ 33.75 g/kg). Mercator Ocean model outputs suggest that these halocline eddies probably resulted from instabilities in the surface front between the fresher Makarov waters and saltier Eurasian waters. However, while Timmermans et al. (2008) and Zhao et al. (2014) observed such halocline eddies with lifetimes from months to years, the modeled eddies have slightly larger radii (~20 km) and are rather short-lived (4–18 weeks), as the model grid cannot resolve the mixed layer deformation radius (about 4 km). However, as far as we know it is the first time that such halocline eddies in the central Arctic Basin have been reproduced in a model.

Two AW mesoscale structures were encountered in the Nansen Basin. They exhibit cores of AW with temperatures larger than 2 °C and salinities larger than their environment (ΔS ~ + 0.1–0.2 g/kg). They are oxygen enriched compared to their environment and slightly nitrate depleted. One AW structure was encountered north of the Yermak Plateau in December 2017 (near 83°N, 1°W). Even though this structure is not reproduced at the same time and location in the model, the Mercator Ocean outputs have provided evidence that is it likely an AW recirculating branch, circulating back toward the Fram Strait. The large AW structure, crossed in October 2017 unusually northeast in the Nansen Basin (at 83.5°N, 35°E), is particularly well represented in the model and identified as a meander of AW detaching from the Arctic Circumpolar Boundary Current. The model outputs suggest that the AW meander turned into an anticyclonic AW eddy about a month after the platforms drifted away, propagating slightly northwestward for 2.5 months until reaching 83.7°N, 34.5°E in February 2018.

Comparisons with an eddy documented by Våge et al. (2016) underlined the good performance of the (1/12)° Mercator Ocean model in representing AW eddies. However, the (1/12)° horizontal resolution grid is only eddy permitting in the Eurasian Basin, with a spatial resolution of ~4 km in the area. These limitations are likely to prevent the detection of smaller sized eddies and eddy tracking in the Basin interior. Crews et al. (2017) provided a first fine resolution (800 m × 800 m) model-based quantitative survey of eddy-mediated transport of AW from the boundary current to the Eurasian Basin. 177 eddies in 2 years were detected on the Svalbard continental shelf, but the large majority (98%) stayed south of 83°N, as in the Mercator Ocean model. To our knowledge, it is the first time that an AW meander is documented as far as 83.5°N, 35°E in the Nansen Basin interior.

Several studies suggest that eddies have a significant influence on the lateral current-to-basin interior exchanges of heat, salt, tracers, and nutrients (Mathis et al., 2007; Nishino et al., 2011; Zhao et al., 2014). Mathis et al. (2007) and Nishino et al. (2011) indicate that in the Canada Basin, eddies are likely major nutrients providers to the upper layer. Here, measurements within the AW meanders and eddies crossed in autumn-winter 2017 suggest a possible similar input of nutrients in the Eurasian Basin upper layer.

This study highlights the recent physical changes in the western Eurasian Basin. In this increasingly ice-free ocean, the fresher surface water and shallower warm AW layer are likely to have significant impacts on the biogeochemistry of the Arctic Ocean (Arrigo & van Dijken, 2015; Bluhm et al., 2015; Timmermans et al., 2010). These will be discussed in a forthcoming paper presenting the biogeochemical observations and near-surface pCO_2 evolution from IAOOS 2017 data.

Appendix A: Estimation of the Minimum Internal Wave Amplitude

Despite the nonadapted sampling frequency of the IAOOS platforms (every 12 hr), we suggest that the IAOOS data can provide an estimate of the minimum internal wave amplitude in the still sparsely documented Eurasian Basin, following the method described in Dosser et al. (2014).

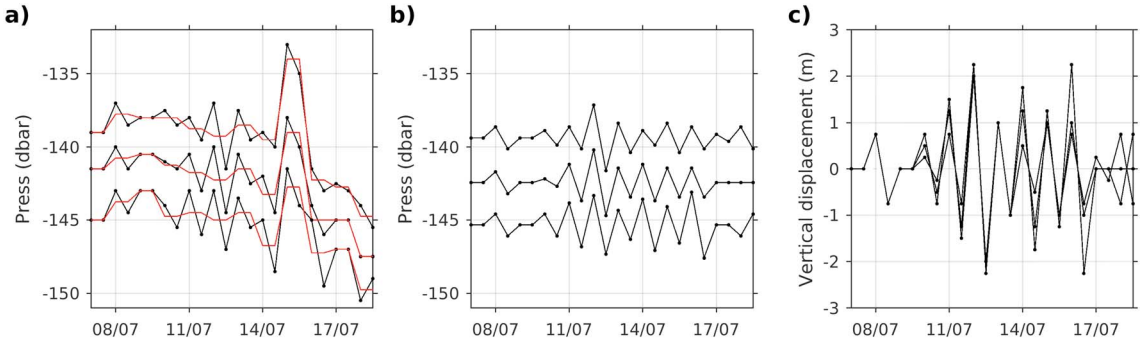

Figure A1. (a) Example of three sample isopycnals over a 12-day period (7 to 18 July 2017, over the Gakkel Ridge). The black lines show the depth of the isopycnals, and the red line shows the daily mean depth of the three isopycnals. (b) The same isopycnals with the mean removed, leaving only displacements near the inertial frequency. (c) Vertical displacements of the three isopycnals combined to maximize the number of points available.

Vertical displacements of isopycnals are estimated by tracking density surfaces, originally regularly distributed (each 3 m) in the first profile, along the drift (Figure A1a). Near-inertial waves typically have horizontal wavelengths on the order of kilometers and vertical wavelengths on the order of 10–100 m. For each isopycnal, the daily mean is removed. Vertical displacements are combined with those of the isopycnals immediately above and below, tripling the number of available data points per estimate and reducing the impact of random noise (Figure A1b). The estimation of isopycnals depths is limited by instrument noise and vertical resolution (~1 m); thus, vertical displacements smaller than 1 m were not considered. This implies that the present estimation does not apply to the quiescent Amundsen Basin, where displacements do not exceed the 1-m limit. In the end, we estimated the minimum near-inertial internal wave amplitude to be ~2 m above and south of the Gakkel Ridge in the upper 350 m of the Eurasian Basin (Figure A1c).

Acknowledgments
We are deeply grateful to the many people who participated to the development and tests of the biogeochemical profiler at Ifremer facilities in Brest (France) and during the N-ICE 2015 ice camp from RV Lance north of Svalbard: Magali Garracio, Antoine Guillot, Christine Drezen and Michel Calzas, Nicolas Villacieros Robineau, Jean-Philippe Savy, and Victoire Rérolle. We thank Matthieu Labaste, Victoire Rérolle, and Sergey Pisarev for their contribution to the preparation and deployment of the IAOOS platforms form the North Pole in April 2017. Magali Garracio was essential to the data recovery and decoding processes. Discussions with Catherine Schmechtig on the data processing are gratefully acknowledged. Véronique Garçon and Carole Barus contributed to the addition of the Rem-A package to the profiler. The development and field work were funded through the ANR EQUIPEX IAOOS project through ANR-10-EQX-32-01 grant and the ICE-ARC programme from the European Union 7th Framework Programme, grant 603887. Marylou Athanase, Zoe Koenig, and Elisabeth Boles were supported through the Pan Arctic Options Belmont Forum project (ANR-14-AORS-003-01). Profiler data are available at SEANOE (https://doi.org/10.17882/57288). The model outputs are available at Copernicus Marine Environment Monitoring Service (CMEMS; http://marine.copernicus.eu/). We are deeply grateful to Editor Laurence Padman and two anonymous reviewers for their thorough comments, which helped us improve the manuscript.

References

Alkire, M. B., Morison, J., & Andersen, R. (2015). Variability in the meteoric water, sea-ice melt, and Pacific water contributions to the central Arctic Ocean, 2000–2014. *Journal of Geophysical Research: Oceans*, *120*, 1573–1598. https://doi.org/10.1002/2014JC010023

Armitage, T. W. K., Bacon, S., & Kwok, R. (2018). Arctic sea level and surface circulation response to the Arctic Oscillation. *Geophysical Research Letters*, *45*, 6576–6584. https://doi.org/10.1029/2018GL078386

Arrigo, K. R., & van Dijken, G. L. (2015). Continued increases in Arctic Ocean primary production. *Progress in Oceanography*, *136*, 60–70. https://doi.org/10.1016/j.pocean.2015.05.002

Bebieva, Y., & Timmermans, M. L. (2016). An examination of double-diffusive processes in a mesoscale eddy in the Arctic Ocean. *Journal of Geophysical Research: Oceans*, *121*, 457–475. https://doi.org/10.1002/2015JC011105

Bluhm, B. A., Kosobokova, K. N., & Carmack, E. C. (2015). A tale of two basins: An integrated physical and biological perspective of the deep Arctic Ocean. *Progress in Oceanography*, *139*, 89–121. https://doi.org/10.1016/j.pocean.2015.07.011

Brannigan, L., Johnson, H., Lique, C., Nycander, J., & Nilsson, J. (2017). Generation of subsurface anticyclones at Arctic surface fronts due to a surface stress. *Journal of Physical Oceanography*, *47*(11), 2653–2671. https://doi.org/10.1175/JPO-D-17-0022.1

Carmack, E., Polyakov, I., Padman, L., Fer, I., Hunke, E., Hutchings, J., Jackson, J., et al. (2015). Toward quantifying the increasing role of oceanic heat in sea ice loss in the new Arctic. *Bulletin of the American Meteorological Society*, *96*(12), 2079–2105. https://doi.org/10.1175/BAMS-D-13-00177.1

Codispoti, L. A., Kelly, V., Thessen, A., Matrai, P., Suttles, S., Hill, V., et al. (2013). Synthesis of primary production in the Arctic Ocean: III. Nitrate and phosphate-based estimates of net community production. *Progress in Oceanography*, *110*, 126–150. https://doi.org/10.1016/j.pocean.2012.11.006

Comiso, J. C., Parkinson, C. L., Gersten, R., & Stock, L. (2008). Accelerated decline in the Arctic sea ice cover. *Geophysical Research Letters*, *35*, L01703. https://doi.org/10.1029/2007GL031972

Crews, L., Sundfjord, A., Albretsen, J., & Hattermann, T. (2017). Mesoscale eddy activity and transport in the Atlantic Water inflow region north of Svalbard. *Journal of Geophysical Research: Oceans*, *123*, 201–215. https://doi.org/10.1002/2017JC013198

Dai, A., Qian, T., Trenberth, K. E., & Milliman, J. D. (2009). Changes in continental freshwater discharge from 1948 to 2004. *Journal of Climate*, *22*(10), 2773–2792. https://doi.org/10.1175/2008JCLI2592.1

Damm, E., Bauch, D., Krumpen, T., Rabe, B., Korhonen, M., Vinogradova, E., & Uhlig, C. (2018). The Transpolar Drift conveys methane from the Siberian Shelf to the central Arctic Ocean. *Scientific Reports*, *8*(1), 4515. https://doi.org/10.1038/s41598-018-22801-z

Dmitrenko, I. A., Kirillov, S. A., Ivanov, V. V., & Woodgate, R. A. (2008). Mesoscale Atlantic water eddy off the Laptev Sea continental slope carries the signature of upstream interaction. *Journal of Geophysical Research*, *113*, C07005. https://doi.org/10.1029/2007JC004491

Dosser, H. V., Rainville, L., & Toole, J. M. (2014). Near-inertial internal wave field in the Canada Basin from ice-tethered profilers. *Journal of Physical Oceanography*, *44*(2), 413–426. https://doi.org/10.1175/JPO-D-13-0117.1

Good, S. A., Martin, M. J., & Rayner, N. A. (2013). EN4: Quality controlled ocean temperature and salinity profiles and monthly objective analyses with uncertainty estimates. *Journal of Geophysical Research: Oceans*, *118*, 6704–6716. https://doi.org/10.1002/2013JC009067

Jackson, J. M., Carmack, E. C., McLaughlin, F. A., Allen, S. E., & Ingram, R. G. (2010). Identification, characterization, and change of the near-surface temperature maximum in the Canada Basin, 1993–2008. *Journal of Geophysical Research*, *115*, C05021. https://doi.org/10.1029/2009JC005265

Jackson, K., Wilkinson, J., Maksym, T., Meldrum, D., Beckers, J., Haas, C., & Mackenzie, D. (2013). A novel and low-cost sea ice mass balance buoy. *Journal of Atmospheric and Oceanic Technology*, *30*(11), 2676–2688. https://doi.org/10.1175/JTECH-D-13-00058

Jeffries, M. O., Overland, J. E., & Perovich, D. K. (2013). The Arctic. *Physics Today*, *66*(10), 35–40. https://doi.org/10.1063/PT.3.2147

Johnson, K., Pasqueron De Fommervault, O., Serr, R., D'Ortenzio, F., Schmechtig, C., Claustre, H., & Poteau, A. (2018). Processing Bio-Argo nitrate concentration at the DAC Level. Version 1.1, March 3rd 2018. IFREMER for Argo Data Management (22 pp.). https://doi.org/10.13155/46121

Kipp, L. E., Charette, M. A., Moore, W. S., Henderson, P. B., & Rigor, I. G. (2018). Increased fluxes of shelf-derived materials to the central Arctic Ocean. *Science Advances*, *4*(1), eaao1302. https://doi.org/10.1126/sciadv.aao1302

Koenig, Z., Provost, C., Villacieros- Robineau, N., Sennechael, N., & Meyer, A. (2016). Winter ocean-ice interactions under thin sea ice observed by IAOOS platforms during N-ICE2015: Salty surface mixed layer and active basal melt. *Journal of Geophysical Research: Oceans*, *121*, 7898–7916. https://doi.org/10.1002/2016JC012195

Koenig, Z., Provost, C., Villacieros- Robineau, N., Sennechael, N., Meyer, A., Lellouche, J.-M., & Garric, G. (2017). Atlantic waters inflow north of Svalbard: Insights from IAOOS observations and Mercator Ocean global operational system during N-ICE2015. *Journal of Geophysical Research: Oceans*, *122*, 1254–1273. https://doi.org/10.1002/2016JC012424

Korhonen, M., Rudels, B., Marnela, M., Wisotzki, A., & Zhao, J. (2013). Time and space variability of freshwater content, heat content and seasonal ice melt in the Arctic Ocean from 1991 to 2011. *Ocean Science*, *9*(6), 1015–1055. https://doi.org/10.5194/os-9-1015-2013

Krishfield, R., Toole, J., Proshutinsky, A., & Timmermans, M. L. (2008). Automated ice-tethered profilers for seawater observations under pack ice in all seasons. *Journal of Atmospheric and Oceanic Technology*, *25*(11), 2091–2105. https://doi.org/10.1175/2008JTECHO587.1

Laney, S. R., Krishfield, R. A., Toole, J. M., Hammar, T. R., Ashjian, C. J., & Timmermans, M. L. (2014). Assessing algal biomass and bio-optical distributions in perennially ice-covered polar ocean ecosystems. *Polar Science*, *8*(2), 73–85. https://doi.org/10.1016/j.polar.2013.12.003

Lellouche, J. M., Greiner, E., le Galloudec, O., Garric, G., Regnier, C., Drevillon, M., et al. (2018). Recent updates to the Copernicus Marine Service global ocean monitoring and forecasting real-time 1/ 12° high-resolution system. *Ocean Science*, *14*(5), 1093–1126. https://doi.org/10.5194/os-14-1093-2018

Locarnini, R. A., Mishonov, A. V., Antonov, J. I., Boyer, T. P., Garcia, H. E., Baranova, O. K., et al. (2013). World ocean atlas 2013, volume 1: Temperature. In S. A. M. Levitus & A. Mishonov (Eds.), *NOAA Atlas NESDIS 73* (40 pp.). https://doi.org/10.7289/V55X26VD

Madec, G. (2008). NEMO, the ocean engine, Note du Pole de modelisation, Institut Pierre-Simon Laplace (IPSL), France, no 27 ISSN no 1288–1619.

Mariage, V., Pelon, J., Blouzon, F., Victori, S., Geyskens, N., Amarouche, N., et al. (2017). Iaoos microlidar-on-buoy development and first atmospheric observations obtained during 2014 and 2015 Arctic drifts. *Optics Express*, *25*(4), A73–A84. https://doi.org/10.1364/OE.25.000A73

Mathis, J. T., Pickart, R. S., Hansell, D. A., Kadko, D., & Bates, N. R. (2007). Eddy transport of organic carbon and nutrients from the Chukchi shelf: Impact on the upper halocline of the western Arctic Ocean. *Journal of Geophysical Research*, *112*, C05011. https://doi.org/10.1029/2006JC003899

McDougall, T. J., Jackett, D. R., Millero, F. J., Pawlowicz, R., & Barker, P. M. (2012). A global algorithm for estimating absolute salinity. *Ocean Science*, *8*(6), 1123–1134. https://doi.org/10.5194/os-8-1123-2012

Morison, J., Kwok, R., Peralta-Ferriz, C., Alkire, M., Rigor, I., Andersen, R., & Steele, M. (2012). Changing Arctic ocean freshwater pathways. *Nature*, *481*(7379), 66–70. https://doi.org/10.1038/nature10705

Nishino, S., Itoh, M., Kawaguchi, Y., Kikuchi, T., & Aoyama, M. (2011). Impact of an unusually large warm-core eddy on distributions of nutrients and phytoplankton in the southwestern Canada Basin during late summer/early fall 2010. *Geophysical Research Letters*, *38*, L16602. https://doi.org/10.1029/2011GL047885

Onarheim, I. H., Smedsrud, L. H., Ingvaldsen, R. B., & Nilsen, F. (2014). Loss of sea ice during winter north of Svalbard. *Tellus A: Dynamic Meteorology and Oceanography*, *66*(1), 23933. https://doi.org/10.3402/tellusa.v66.23933

Peralta-Ferriz, C., & Woodgate, R. A. (2015). Seasonal and interannual variability of pan-Arctic surface mixed layer properties from 1979 to 2012 from hydrographic data, and the dominance of stratification for multiyear mixed layer depth shoaling. *Progress in Oceanography*, *134*, 19–53. https://doi.org/10.1016/j.pocean.2014.12.005

Perovich, D. K., Richter-Menge, J. A., Jones, K. F., Light, B., Elder, B. C., Polashenski, C., et al. (2011). Arctic sea-ice melt in 2008 and the role of solar heating. *Annals of Glaciology*, *52*(57), 355–359. https://doi.org/10.3189/172756411795931714

Pham, D. T., Verron, J., & Roubaud, M. C. (1998). A singular evolutive extended Kalman filter for data assimilation in oceanography. *Journal of Marine Systems*, *16*(3–4), 323–340. https://doi.org/10.1016/S0924-7963(97)00109-7

Polyakov, I. V., Padman, L., Lenn, Y. D., Pnyushkov, A., Rember, R., & Ivanov, V. V. (2018). Eastern Arctic Ocean diapycnal heat fluxes through large double-diffusive steps. *Journal of Physical Oceanography*, *2018*.

Polyakov, I. V., Pnyushkov, A. V., Alkire, M. B., Ashik, I. M., Baumann, T. M., Carmack, E. C., et al. (2017). Greater role for Atlantic inflows on sea-ice loss in the Eurasian Basin of the Arctic Ocean. *Science*, *356*(6335), 285–291. https://doi.org/10.1126/science.aai8204

Polyakov, I. V., Timokhov, L. A., Alexeev, V. A., Bacon, S., Dmitrenko, I. A., Fortier, L., et al. (2010). Arctic Ocean warming contributes to reduced polar ice cap. *Journal of Physical Oceanography*, *40*(12), 2743–2756. https://doi.org/10.1175/2010JPO4339.1

Provost, C., Pelon, J., Sennéchael, N., Calzas, M., Blouzon, F., Desautez, A., et al. (2015). IAOOS (ice-atmosphere-arctic ocean observing system, 2011-2019). *Mercator Ocean Quarterly Newsletter*, *51*, 13–15.

Provost, C., Sennéchael, N., Miguet, J., Itkin, P., Rösel, A., Koenig, Z., et al. (2017). Observations of flooding and snow-ice formation in a thinner arctic sea ice regime during the N-ICE2015 campaign: Influence of basal ice melt and storms. *Journal of Geophysical Research: Oceans*, *122*, 7115–7134. https://doi.org/10.1002/2016JC012011

Rabe, B., Karcher, M., Kauker, F., Schauer, U., Toole, J. M., Krishfield, R. A., et al. (2014). Arctic Ocean basin liquid freshwater storage trend 1992–2012. *Geophysical Research Letters*, *41*, 961–968. https://doi.org/10.1002/2013GL058121

Randelhoff, A., & Guthrie, J. D. (2016). Regional patterns in current and future export production in the central Arctic Ocean quantified from nitrate fluxes. *Geophysical Research Letters*, *43*, 8600–8608. https://doi.org/10.1002/2016GL070252

Rudels, B., Meyer, R., Fahrbach, E., Ivanov, V. V., Østerhus, S., Quadfasel, D., et al. (2000). Water mass distribution in Fram Strait and over the Yermak Plateau in summer 1997. *Annales Geophysicae*, *18*(6), 687–705. https://doi.org/10.1007/s00585-000-0687-5

Sakamoto, C. M., Johnson, K. S., & Coletti, L. J. (2009). Improved algorithm for the computation of nitrate concentrations in seawater using an in situ ultraviolet spectrophotometer. *Limnology and Oceanography: Methods*, *8*(6), 1123–1134. https://doi.org/10.5194/os-8-1123-2012

Schauer, U., Rudels, B., Jones, E. P., Anderson, L. G., Muench, R. D., Björk, G., et al. (2002). Confluence and redistribution of Atlantic water in the Nansen, Amundsen and Makarov basins. *Annales Geophysicae*, *20*(2), 257–273. https://doi.org/10.5194/angeo-20-257-2002

Serreze, M. C., & Barry, R. G. (2011). Processes and impacts of Arctic amplification: A research synthesis. *Global and Planetary Change*, *77*(1–2), 85–96. https://doi.org/10.1016/j.gloplacha.2011.03.004

Stroeve, J. C., Serreze, M. C., Holland, M. M., Kay, J. E., Malanik, J., & Barrett, A. P. (2012). The Arctic's rapidly shrinking sea ice cover: A research synthesis. *Climatic Change*, *110*(3–4), 1005–1027. https://doi.org/10.1007/s10584-011-0101-1

Sutherland, D. A., & Pickart, R. S. (2008). The East Greenland coastal current: Structure, variability, and forcing. *Progress in Oceanography*, *78*(1), 58–77. https://doi.org/10.1016/j.pocean.2007.09.006

Thierry V., Bittig, H., Gilbert, D., Kobayashi, T., Sato, K., & Schmid, C. (2016). Processing Argo OXYGEN data at the DAC level, v2.2. https://doi.org/10.13155/39795

Timmermans, M. L., Krishfield, R., Laney, S., & Toole, J. (2010). Ice-tethered profiler measurements of dissolved oxygen under permanent ice cover in the Arctic Ocean. *Journal of Atmospheric and Oceanic Technology*, *27*(11), 1936–1949. https://doi.org/10.1175/2010JTECHO772.1

Timmermans, M. L., Proshutinsky, A., Krishfield, R. A., Perovich, D. K., Richter-Menge, J. A., Stanton, T. P., & Toole, J. M. (2011). Surface freshening in the Arctic Ocean's Eurasian Basin: An apparent consequence of recent change in the wind-driven circulation. *Journal of Geophysical Research*, *116*, C00D03. https://doi.org/10.1029/2011JC006975

Timmermans, M. L., Toole, J., Proshutinsky, A., Krishfield, R., & Plueddemann, A. (2008). Eddies in the Canada Basin, Arctic Ocean, observed from ice-tethered profilers. *Journal of Physical Oceanography*, *38*(1), 133–145. https://doi.org/10.1175/2007JPO3782.1

Toole, J. M., Timmermans, M. L., Perovich, D. K., Krishfield, R. A., Proshutinsky, A., & Richter-Menge, J. A. (2010). Influences of the ocean surface mixed layer and thermohaline stratification on Arctic Sea ice in the central Canada Basin. *Journal of Geophysical Research*, *115*, C10018. https://doi.org/10.1029/2009JC005660

Våge, K., Pickart, R. S., Pavlov, V., Lin, P., Torres, D. J., Ingvaldsen, R., Sundfjord, A., et al. (2016). The Atlantic Water boundary current in the Nansen Basin: Transport and mechanisms of lateral exchange. *Journal of Geophysical Research: Oceans*, *121*, 6946–6960. https://doi.org/10.1002/2016JC011715

Zhao, M., Timmermans, M. L., Cole, S., Krishfield, R., Proshutinsky, A., & Toole, J. (2014). Characterizing the eddy field in the Arctic Ocean halocline. *Journal of Geophysical Research: Oceans*, *119*, 8800–8817. https://doi.org/10.1002/2014JC010488

Zweng, M. M., Reagan, J. R., Antonov, J. I., Locarnini, R. A., Mishonov, A. V., Boyer, T. P., et al. (2013). World ocean atlas 2013, volume 2: Salinity. In S. A. M. Levitus & A. Mishonov (Eds.), *NOAA Atlas NESDIS 74* (39 pp.).

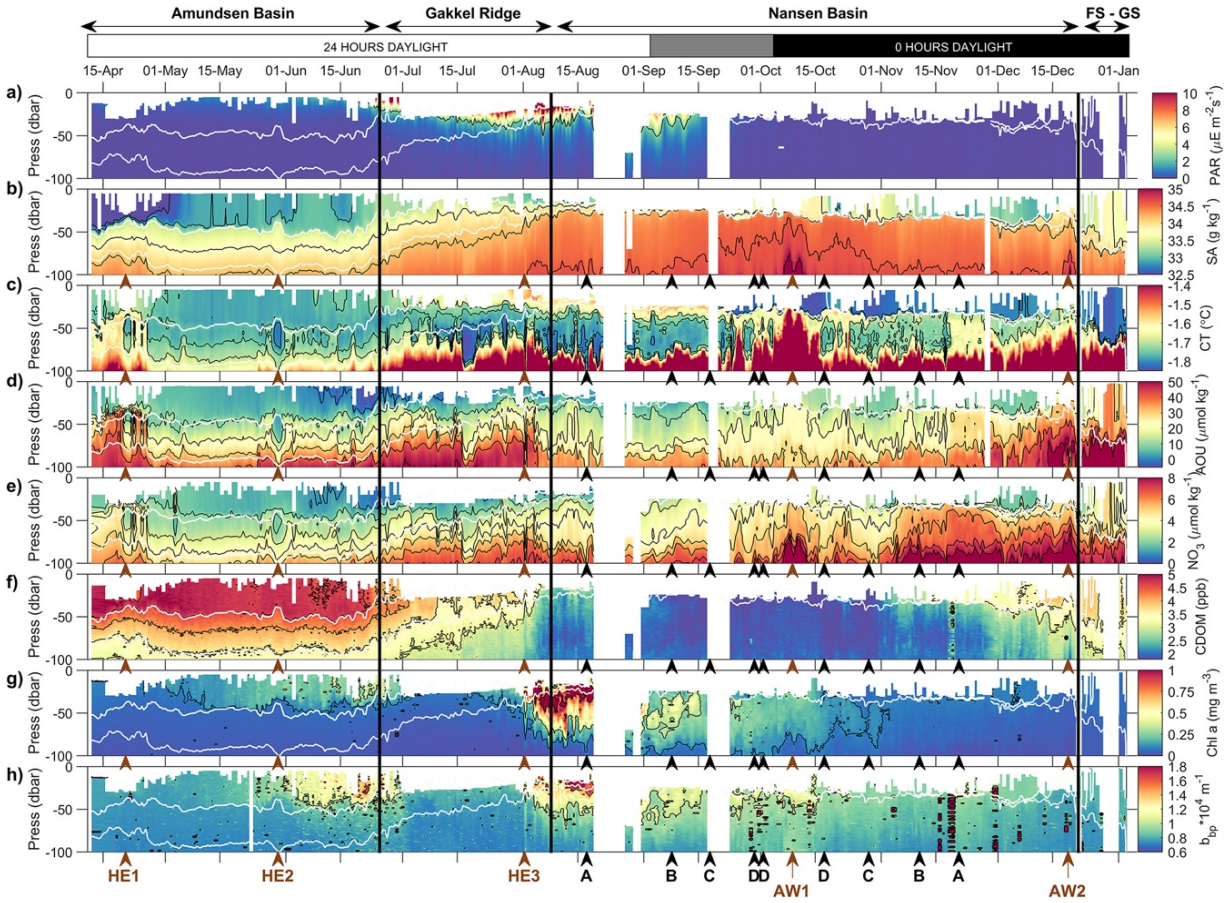

Figure 2.2: Sections of hydrographic variables along the IAOOS 2017 drift trajectory at 0-100m: (a) photosynthetically active radiation (PAR, µE m−2 s−1), (b) absolute salinity (SA, g kg−1), (c) conservative temperature (CT, °C), (d) apparent oxygen utilization (AOU, µmol kg−1), (e) nitrate (NO3, µmol kg−1), (f) colored dissolved organic matter fluorescence (CDOM, ppb), (g) chlorophyll a (Chl a, mg m−3), and (h) backscatter (bbp, m−1). White lines are the 26.7 and 27.3 kg/m³ isopycnals; black lines are isolines of respective variables. The limits of the four regions (as in Athanase et al., 2019) are marked with vertical black lines. Hours of daylight are also shown at the top of the figure. Positions of HE1, HE2, AW1, AW2, and the four crossing points are marked at the bottom. From Boles et al., 2020.

2.3. The IAOOS 2017 drift

The interpretation of the IAOOS 2017 physical data set up the stage for analyses of the biogeochemistry data. Indeed, the quality of the data gathered with the suite of biogeochemical sensors onboard IAOOS 23 profiler permitted to examine **under-ice phytoplankton blooms** (Boles et al., 2020) and the **halocline structure using the quasi-conservative NO parameter** (Bertosio et al., 2020).

Data focusing on the upper 100 m are presented in Figure 2.2 (from Boles et al., 2020). Two distinct periods of primary production were encountered. The first bloom developed in the mixed layer in Amundsen Basin in May, reaching maximum

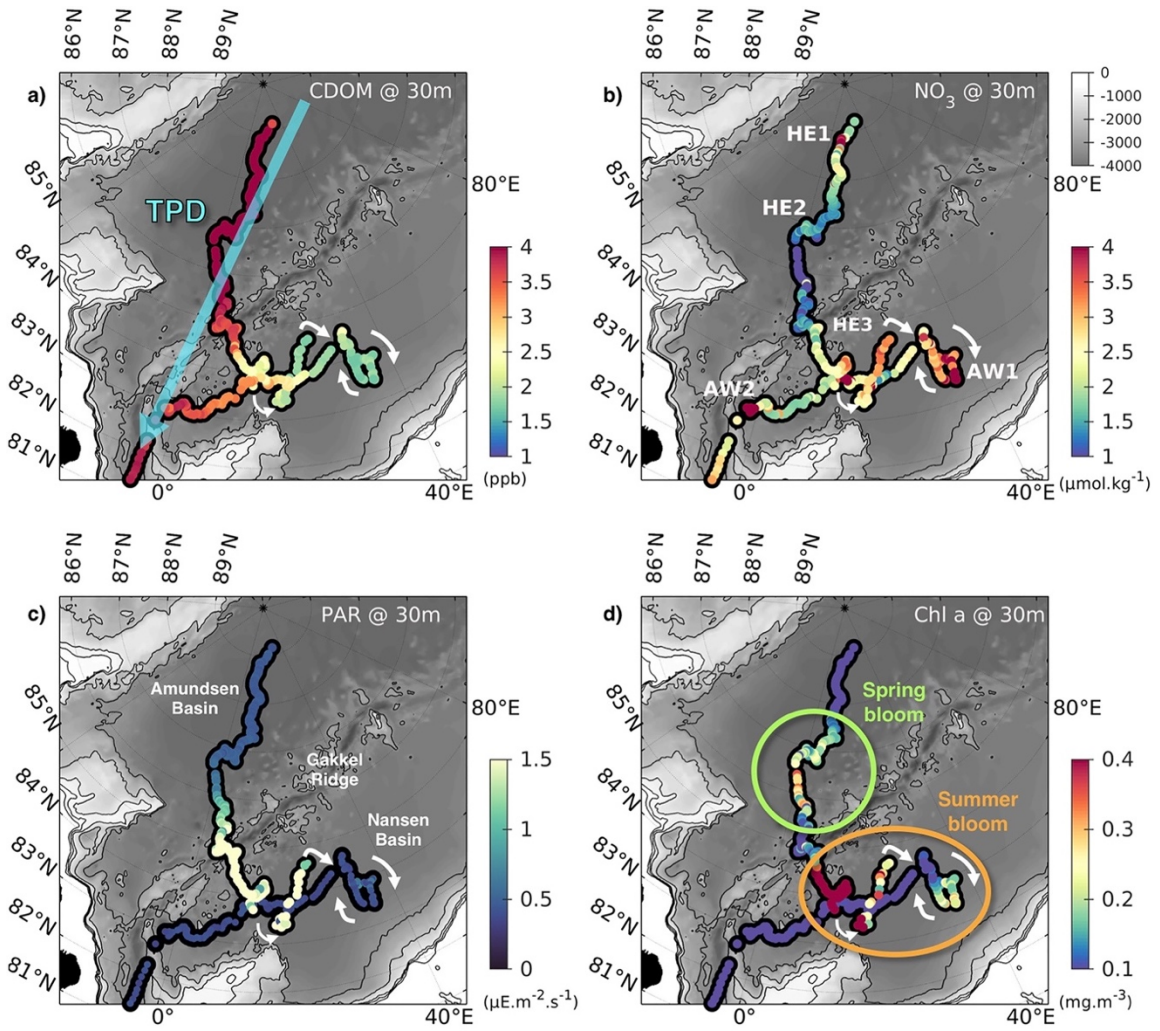

Figure 2.3: Maps of select variables along the drift at 30 m: (a) CDOM, with the blue arrow overlay representing the transpolar drift, (b) NO3, (c) PAR, and (d) Chl a. White arrows mark the direction of the platforms' drift. From Boles et al. 2020.

chlorophyll *a* concentrations on the order of ~ 0.5 mg m^{-3} by the end of June. This bloom occurred earlier in the year than any other recorded bloom in Amundsen Basin, despite very limited under-ice light due to a thick layer of snow. The second bloom, encountered in Nansen Basin in August, was significantly larger (mean profile maximum chlorophyll *a* was 1.45 mg m^{-3}). Examinations of the optical community index and colored dissolved organic matter concentrations suggest that the spring bloom consisted of small phytoplankton which may have been mixotrophic, while the summer bloom contained a greater diversity of planktonic size classes. The data set demonstrates the heterogeneity of Arctic under-ice primary production (Figure 2.3)

Dissolved oxygen and nitrate data, measured for the first time by an autonomous ice-tethered profiler in the Arctic Ocean, were combined to compute the NO parameter, a

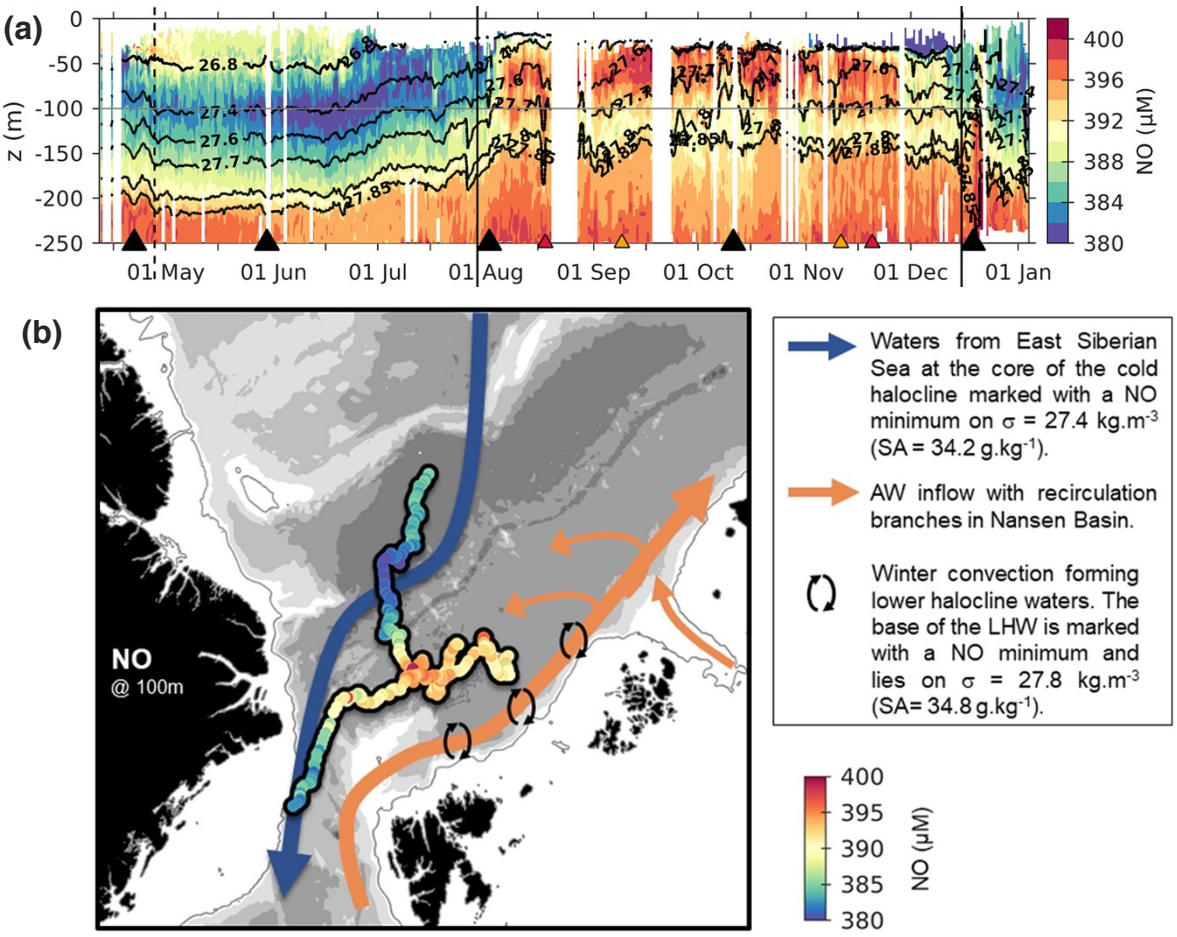

Figure 2.4: (a) Vertical profiles of NO parameter (μM) along the IAOOS 2017 drift. Vertical black lines delimit boundaries between basins. The dashed vertical lines indicate the position of a frontal zone at 88.2°N. Black triangles are the mesoscale structures crossed, colored triangles correspond to the crossing points. (b) NO concentration at 100m along the drift and schematics of processes associated with NO distribution. The 100-m depth is close to the core of the cold halocline in Amundsen Basin and to the base of the lower halocline in the Nansen Basin. The NO minimum (380 μM) in the TPD results from advection of low NO waters (depleted in DO) from the East Siberian Seas contributing to the cold halocline on σ–horizon 27.4 (SA = 34.2 g/kg). The relatively low NO values (390 μM) in Nansen Basin mark the base of the lower halocline. From Bertosio et al. (2020).

tracer useful for differentiating oceanic water masses (Bertosio et al., 2020). Together with ocean and sea-ice model simulations, the spatial distribution of this NO parameter provided valuable insights into the structure and sources of the water in the central Arctic. The halocline, a layer near the surface where salinity increases rapidly with depth, isolates sea ice from the heat stored in the salty Atlantic water below. Waters in the halocline could be traced back to twor different sources: the East Siberian Sea continental slope and the slope north of Svalbard where deep winter convection is important (Figure 2.4). Additionally, our analyses show that previous definitions of the bounds of the halocline layer no longer apply, likely because of increasing influence of saltier Atlantic water near the surface.

CHAPTER 3

Atlantic Water modification in the Western Nansen Basin

Contents

3.1. Introduction

Numerous changes have been documented in the Eurasian Basin of the Arctic Ocean in the recent years, (section 1.6.1; Onarheim et al., 2014; Woods and Caballero, 2016; Polyakov et al., 2017; Graham et al., 2019; Athanase et al., 2019). In parallel with the Arctic-wide summer ice reduction (Stroeve et al., 2012; Stocker et al., 2013), the Whaler's Bay area (section 1.5.) experienced a large sea-ice loss during winter (Onarheim et al., 2014). As the winter sea-ice cover retreats, deep convection events are likely to emerge (Lique et al., 2018). Particularly deep winter mixed layers have been recently observed over the continental slope of the Nansen Basin, indicating intense winter convection bringing Atlantic Water towards the ocean surface (Polyakov et al., 2017; Pérez-Hernandez et al., 2019). In this context, several studies showed the increasingly important role of the warm Atlantic Water in the Eurasian Basin, with enhanced ocean-to-ice and ocean-to-air heat fluxes (Ivanov et al., 2012; Onarheim et al., 2014; Polyakov et al., 2017; Renner et al., 2018). Investigating processes driving the modification of Atlantic Water entering the Arctic via the Western Nansen Basin (WNB) is thus a key issue.

Yet, datasets such as the IAOOS 2017 drift are particularly rare, and *in-situ* measurements remain scarce in this changing WNB. Indeed, gathering observations requires substantial efforts and resources in the ice-covered Arctic Ocean. Hence, operational models such as the global 1/12° Mercator Ocean physical system

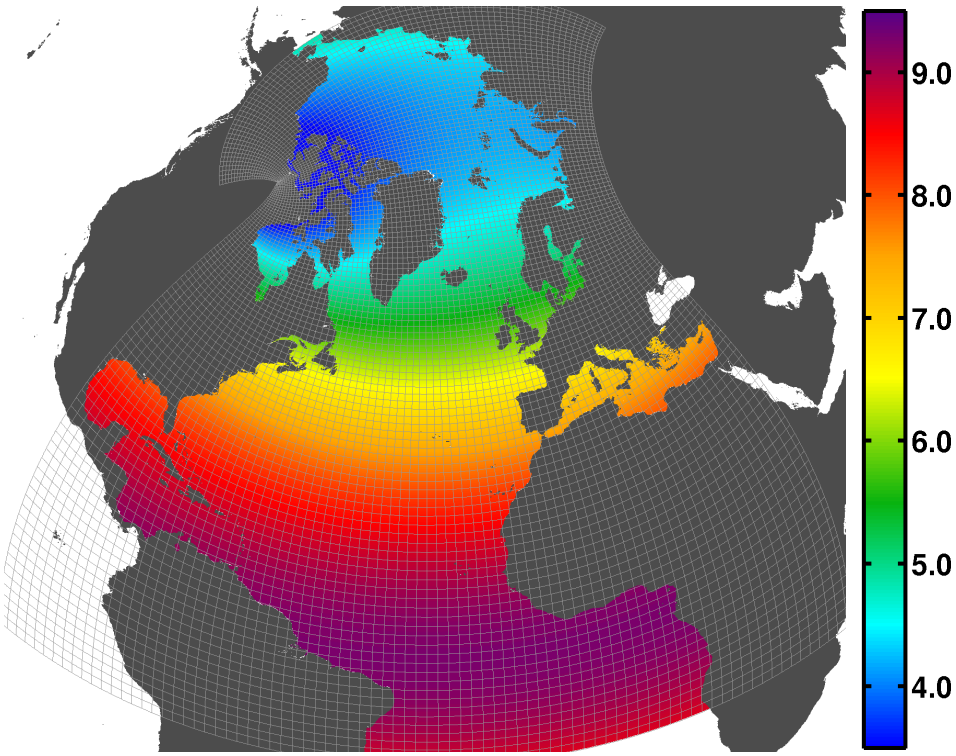

Figure 3.1: Sub-domain of the global ORCA12 horizontal mesh grid of the 1/12° Mercator Ocean physical system, every 20 grids. The ORCA12 grid is a tripolar global ocean grid (one at the South Pole and two located over the continents in the Arctic). The color shows the resolution in kilometers. In vertical, 50 levels with layer thickness smoothly increased from 1.05m at the surface to 453.13m at the last level. Enhanced resolution is applied to the surface layer (<2m resolution for top 10m). Partial steps is also utilized to better resolve the sea floor. From http://knossos.eas.ualberta.ca

(Lellouche et al., 2018) are useful to put observations in a broader spatio-temporal context and examine interannual variations.

Several comparisons between the Mercator Ocean system (called PSY4 hereafter) and *in-situ* data were previously carried out in the Eurasian Basin. The PSY4 system has shown some skills in reproducing the ice conditions, hydrography and seasonal signals in the WNB (Koenig et al., 2017a, 2017b; Athanase et al., 2019). PSY4 also accurately reproduced several mesoscale structures documented in the WNB (Athanase et al., 2019), although the model grid is only eddy-permitting in the area (~4-5 km, Figure 3.1.).

Here, 14 years of PSY4 fields are used to investigate Atlantic Water modification in the Western Nansen Basin. A particular attention is given to AW ventilation via winter convection. We further evaluate the model performance in representing realistic AW inflow, properties, and winter ventilation processes in the WNB, using an extended

dataset (nearly 1500 independant temperature-salinity profiles and five years of current measurements).

3.2. Atlantic Water modification North of Svalbard in the Mercator Physical system from 2007 to 2020

JGR Oceans

RESEARCH ARTICLE
10.1029/2020JC016463

Atlantic Water Modification North of Svalbard in the Mercator Physical System From 2007 to 2020

Marylou Athanase[1], Christine Provost[1], M. Dolores Pérez-Hernández[2], Nathalie Sennéchael[1], Cécilia Bertosio[1], Camila Artana[3], Gilles Garric[3], and Jean-Michel Lellouche[3]

[1]Laboratoire LOCEAN-IPSL, Sorbonne Université (UPMC, University Paris 6), CNRS, IRD, MNHN, Paris, France, [2]Unidad de Océano y Clima, Instituto de Oceanografía y Cambio Global, IOCAG, Universidad de Las Palmas de Gran Canaria, UPGC, Unidad Asociada ULPGC-CSIC, Spain, [3]MERCATOR-OCEAN, Parc Technologique du Canal, 8-10 rue Hermès, Ramonville Saint Agne, France

Key Points:
- Performance of the Mercator 1/12° system is assessed using 12 years (2007–2018) of independent observations in the Western Nansen Basin
- Winters 2012/13 and 2017/18 stood out with the deepest mixed layers and exceptional sea-ice retreat on the slope and Yermak Plateau
- Winter deep convection and recurrent troughs outflows northeast of Svalbard dramatically modified Atlantic Water

Supporting Information:
- Supporting Information S1
- Movie S1
- Movie S2

Correspondence to:
M. Athanase,
mathanase@locean-ipsl.upmc.fr

Citation:
Athanase, M., Provost, C., Pérez-Hernández, M. D., Sennéchael, N., Bertosio, C., Artana, C., et al. (2020). Atlantic water modification north of Svalbard in the Mercator physical system from 2007 to 2020. *Journal of Geophysical Research: Oceans*, *125*, e2020JC016463. https://doi.org/10.1029/2020JC016463

Received 30 MAY 2020
Accepted 12 SEP 2020
Accepted article online 17 SEP 2020

Abstract The Atlantic Water (AW) inflow through Fram Strait, largest oceanic heat source to the Arctic Ocean, undergoes substantial modifications in the Western Nansen Basin (WNB). Evaluation of the Mercator system in the WNB, using 1,500 independent temperature-salinity profiles and five years of mooring data, highlighted its performance in representing realistic AW inflow and hydrographic properties. In particular, favorable comparisons with mooring time-series documenting deep winter mixed layers and changes in AW properties led us to examine winter conditions in the WNB over the 2007–2020 period. The model helped describe the interannual variations of winter mixed layers and documented several processes at stake in modifying AW beyond winter convection: trough outflows and lateral exchange through vigorous eddies. Recently modified AW, either via local convection or trough outflows, were identified as homogeneous layers of low buoyancy frequency. Over the 2007–2020 period, two winters stood out with extreme deep mixed layers in areas that used to be ice-covered: 2017/18 over the northern Yermak Plateau-Sofia Deep; 2012/13 on the continental slope northeast of Svalbard with the coldest and freshest modified AW of the 12-year time series. The northern Yermak Plateau-Sofia Deep and continental slope areas became "Marginal Convection Zones" in 2011 with, from then on, occasionally ice-free conditions, 50-m-ocean temperatures always above 0 °C and highly variable mixed layer depths and ocean-to-atmosphere heat fluxes. In the WNB where observations require considerable efforts and resources, the Mercator system proved to be a good tool to assess Atlantic Water modifications in winter.

Plain Language Summary The Atlantic Water inflow through Fram Strait, largest oceanic heat source to the Arctic Ocean, undergoes severe modifications in the Western Nansen Basin in winter. We used 14 years of high-resolution ocean model simulations to identify winters with intense Atlantic Water modifications (cooling and freshening) in this region. Over the 2007–2020 period, two winters stood out with extreme deep convection events in areas that used to be ice-covered: 2017/18 over the northern Yermak Plateau; and 2012/13 on the continental slope northeast of Svalbard, with the coldest, freshest modified Atlantic Water over 2007–2020. The northern Yermak Plateau and continental slope became "Marginal Convection Zones" in 2011 as they started to occasionally exhibit open-ocean conditions in winter. In this region where observations require considerable efforts and resources, the model simulations proved to be a good tool to assess Atlantic Water modifications in winter. As the transition towards a seasonally ice-free Arctic Ocean continues, more years of extreme Atlantic Water modification can be expected.

1. Introduction

The Atlantic Water (AW) inflow through Fram Strait is the largest oceanic heat source to the Arctic Ocean (Aagaard et al., 1987). The West Spitsbergen Current carries the AW northward in Fram Strait and splits into several branches north of 79°N (Figure 1). A fraction of the water carried by the current does not enter the Arctic Ocean and recirculates back into Fram Strait through several recirculation pathways (e.g. Schauer et al., 2004; von Appen et al., 2016, Wekerle et al., 2017). The entrance of AW into the Nansen Basin divides into branches around and above the topographic obstacle of the Yermak Plateau: the Svalbard Branch crosses the Plateau following the 500 m isobath; the Yermak Pass Branch crosses further north around

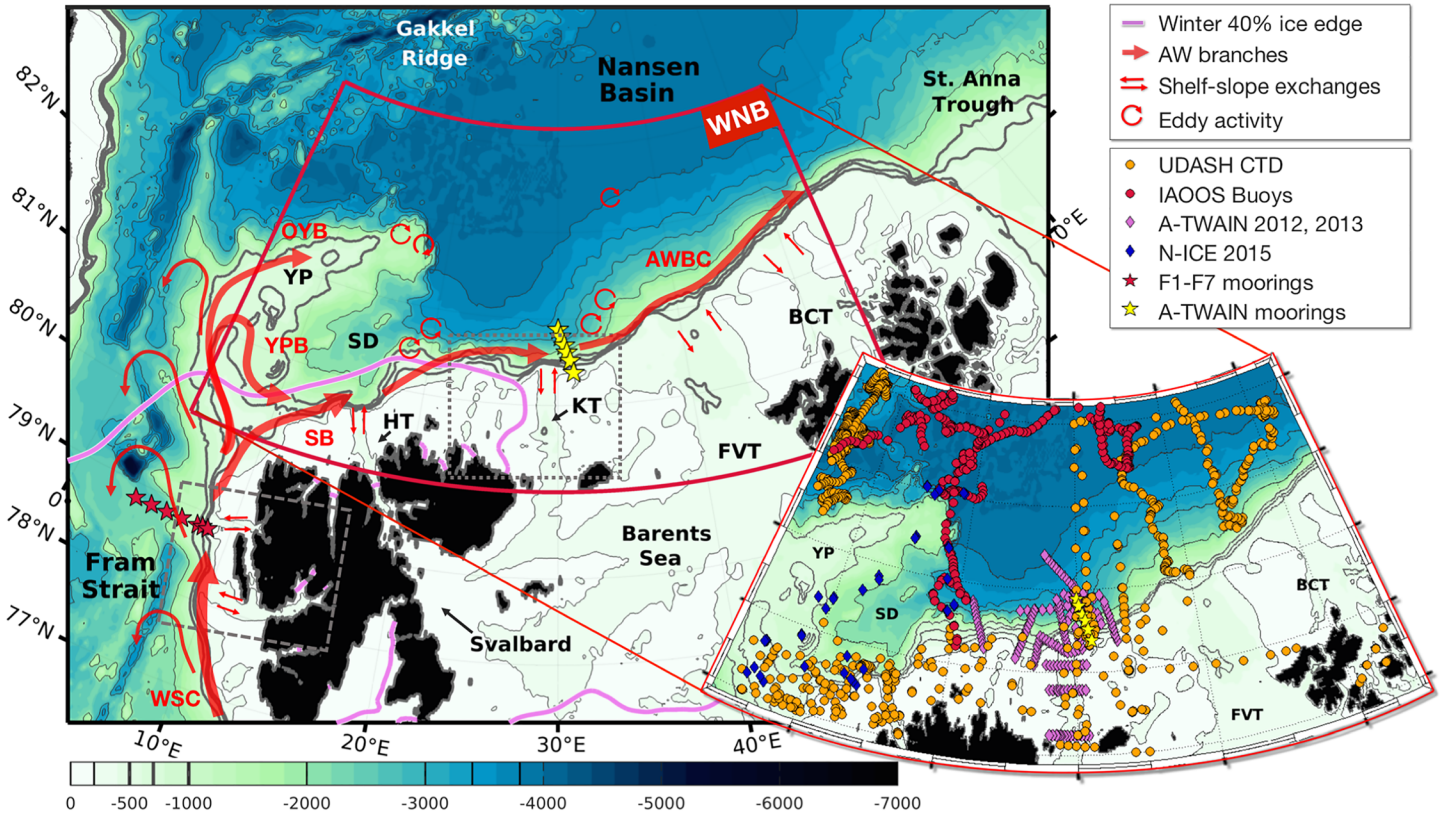

Figure 1. Major AW routes (red arrows) in the Western Nansen Basin (WNB; red box). WSC: West Spitsbergen current; SB: Svalbard branch; YPB: Yermak pass branch; OYB: Outer Yermak branch; AWBC: Atlantic water boundary current. Thin red lines in the Fram Strait represent recirculation branches. Winter ice edge (violet contour) corresponds to the 40% isoline of the mean ice cover during winter months from October to march, over the 2007–2018 period. This winter ice-free area is the whalers' bay. The boxes in dashed and dotted gray lines delineate areas presented in Figure 5 (a-b) and (c-d) respectively. Markers indicate datasets used to evaluate the performance of the PSY4 system in the WNB. None of these *in-situ* data was assimilated. Red markers correspond to data used for detailed PSY4 model-observations comparisons in previous studies (IAOOS buoys in Koenig, Provost, Villacieros-Robineau, et al., 2017 and Athanase et al., 2019; Fram Strait moorings in Koenig, Provost, Sennéchael, et al., 2017). IBCAO bathymetry is in background color, with YP: Yermak plateau; SD: Sofia deep; HT: Hinlopen trough; KT: Kvitøya through; FVT: Franz-Victoria trough; BCT: British Channel trough.

81°N following the 700 m isobath, and the Outer Yermak Branch follows the western side of the Yermak Plateau above the 1,000 m isobath. The hydrographic properties and strength of the branches vary over a broad range of time scales (with strong seasonal and interannual components). The branches merge again east of the Yermak Plateau in a complex yet unclear way to contribute to the Arctic Circumpolar Boundary Current which follows the continental slope around the deep Arctic Ocean basin (e.g. Crews et al., 2019; Hattermann et al., 2016; Koenig, Provost, Villacieros-Robineau, et al., 2017). To complicate further the picture, eddies have been observed in all branches (e.g. Athanase et al., 2019; Koenig, Provost, Sennéchael, et al., 2017; Våge et al., 2016).

Along the different paths, the AW is cooled and freshened as it melts the sea-ice, loses heat to the atmosphere and mixes with shelf waters (Rudels et al., 2015). West and north of Svalbard, the AW heat maintains ice-free conditions in winter in an area called the Whalers' Bay (e.g. Onarheim et al., 2014). Over the 1979–2014 period, the largest ice-free areas occurred during winter 2012/13 with the ice edge located as far as 81°N, 32°E in January 2013 (Ivanov et al., 2016). In this period, particularly deep mixed layers (reaching 500 m) were observed over the continental slope at 30°E (Pérez-Hernández et al., 2019; Renner et al., 2018). Within these deep mixed layers, AW became colder and fresher due to convective mixing. The resulting modified AW retained its properties as it was advected downstream. These were the first (and only so far) *in-situ* measurements documenting the formation and evolution of ventilated AW in the Western Nansen Basin (WNB). Waters modified through deep convection are the major contributors to the lower halocline waters (LHW) of the Arctic (Alkire et al., 2017; Rudels et al., 2004).

Other processes contribute to the modification of the AW in the boundary current for example exchange with shelf waters and lateral eddy fluxes. The presence of troughs linking fjords to the continental slope west of Svalbard enhances shelf-slope exchange that cool and freshen the AW carried northward in the West Spitsbergen Current (Boyd & D'Asaro, 1994; Goszczko et al., 2018; Koenig et al., 2018; Nilsen et al., 2016). Troughs north of Svalbard (Hinlopen, Kvitøya, Franz-Victoria and British Channel troughs; Figure 1) connect the Barents Sea to the deep western Nansen Basin. Schauer et al. (1997) showed that the shelf water draining from the Barents Sea via the troughs could significantly modify the core properties of the AW and influence the internal dynamics of the eastward current. Lind and Ingvaldsen (2012) focused on the variability and impacts of the AW entering the Barents Sea from the north between Svalbard and Franz Josef Land.

The AW boundary current has been shown to be unstable both west (e.g. von Appen et al., 2016) and north of Svalbard (e.g. Pérez-Hernández et al., 2017; Schauer et al., 1997) and spawn eddies as a result of barotropic and baroclinic instabilities. AW eddies are numerous in Fram Strait (e.g. von Appen et al., 2016), not uncommon in the WNB (e.g. Athanase et al., 2019; Cokelet et al., 2008; Våge et al., 2016) and are quite well represented in high-resolution models (e.g. Athanase et al., 2019; Appen et al., 2016; Crews et al., 2018; Hattermann et al., 2016; Wekerle et al., 2017). These warm core eddies enhance lateral exchange injecting AW from the slope into the deep basin (e.g. Våge et al., 2016).

In spite of recent efforts, observations in the area remain scarce and models are useful to provide a broader spatial and temporal context. The 1/12° Mercator Ocean operational physical system has shown some skills in reproducing the hydrography, mesoscale structures and seasonal signals in the WNB (Athanase et al., 2019; Koenig, Provost, Sennéchael, et al., 2017; Koenig, Provost, Villacieros-Robineau, et al., 2017). The objective of this paper is to take advantage of 14 years of fields from the Mercator Ocean system to revisit AW modification along the continental slope north and northeast of Svalbard from synoptic to interannual scales, with a particular focus on AW ventilation through winter convection. Indeed, winter ventilation of the AW layer appears to be a rather localized phenomena in time and space as it requires near-surface AW inflow and appropriate atmospheric forcing (pushing the ice away and large negative heat fluxes) (Ivanov et al., 2018; Koenig, Provost, Sennéchael, et al., 2017; Renner et al., 2018). Hence, a model can be a useful tool to carry such a study. An important issue is to determine whether the deep mixed layers and intense AW ventilation episode documented in winter 2012/13 (Pérez-Hernández et al., 2019) was exceptional in the last decade, as Meyer et al. (2017) observed much shallower mixed layers in winter 2015.

We further evaluate the Mercator Ocean system performance by examining AW inflow at Fram Strait during five years and by comparing model outputs to various non-assimilated datasets in the WNB (Figure 1). The paper is structured as follows. Section 2 presents the Mercator Ocean operational system and independent observational data used to evaluate the model. The performance of the model in representing realistic AW inflow, properties, and winter ventilation processes in the WNB is examined in section 3. In section 4, locations and years of extreme deep mixed layers are investigated and corresponding deep convection is described. Other processes contributing to AW modification such as lateral exchange either with the Barents Sea via the troughs or with the offshore open ocean via the mesoscale eddies are examined in section 5. Results are summarized and discussed in section 6.

2. Data

2.1. Mercator Ocean Operational System

The 1/12° global Mercator Ocean operational system (hereafter PSY4) was developed for the Copernicus Marine Environment Monitoring Service (CMEMS; http://marine.copernicus.eu/). A full description of the system components is available in Lellouche et al. (2018), and only some elements are presented here. The model component is based on the NEMO ocean model, with a 1/12° ORCA grid type (i.e. horizontal resolution of 4 km in the WNB; Hu et al., 2019). The water column is composed of 50 vertical levels, with typically 1 m resolution at the surface decreasing to 450 m at the bottom and 22 levels within the upper 100 m. The bathymetry used in the system is a combination of interpolated ETOPO1 (Amante & Eakins, 2009) and GEBCO8 (Becker et al., 2009) databases. ETOPO1 datasets are used in regions deeper than 300 m and GEBCO8 is used in regions shallower than 200 m with a linear interpolation in the 200–300 m layer. The forcing atmospheric fields are obtained from the European Centre for Medium-Range Weather

Table 1
Data used for model evaluation (number of profiles in the WNB area)

Dataset	Parameters	Dates	Reference	Web site
Fram Strait moorings F1 to F7	T, S U, V *	January 2007 to October 2012	Beszczynska-Möller et al. (2012)	https://doi.org/10.1594/PANGAEA.900883
A-TWAIN mooring array	T, S U, V **	September 2012 to September 2013	Pérez-Hernández et al. (2019) Renner et al. (2018)	WHOI moorings: https://doi.org/10.18739/A2S569 NPI moorings: https://doi.org/10.21334/npolar.2017.73d0ea3a
UDASH database CTD & ITP	T, S 888 profiles	January 2007 to December 2015	Behrendt et al. (2018)	https://doi.pangaea.de/10.1594/PANGAEA.872931
IAOOS ITP 7,8	T, S 111 profiles	January to March 2015	Koenig, Provost, Villacieros-Robineau, et al. (2017)	SEANOE: https://doi.org/10.17882/59516
23, 24	264 profiles	April 2017 to January 2018	Athanase et al. (2019)	SEANOE: https://doi.org/10.17882/57288
A-TWAIN CTD	T, S 49 profiles 167 profiles	September 2012 September 2013	Våge et al. (2016) Pérez-Hernández et al. (2017)	http://atwain.whoi.edu/
N-ICE 2015 CTD	T, S 51 profiles	January to June 2015	Meyer et al. (2017)	https://doi.org/10.21334/npolar.2017.92262a9c

*Number of profiles: See Figures 2 and 3 **TS profiles from MMPs: 1437 daily profiles; UV profiles from upper ADCPs: 2173 daily profiles

Forecasts-Integrated Forecast System (ECMWF-IFS) at 3-hr resolution, in order to reproduce the diurnal cycle. Observations assimilated in PSY4 are along-track satellite altimetry, sea surface temperature (OSTIA SST), *in-situ* vertical profiles of temperature and salinity, and OSI SAF sea-ice concentration. OSI SAF products are based on manual interpretation of a large set of high-resolution satellite data, including AMSR2 products (Advanced Microwave Scanning Radiometer 2, https://nsidc.org/data/). During the assimilation procedure, a particular treatment is applied to areas potentially covered with sea-ice: all observations errors in the multivariate SEEK filter increase linearly (less weight in the analysis) with the decrease of the SST from −1 °C to −1.7 °C and the observations are rejected if SST is less than −1.7 °C (i.e. an approximation of the freezing point). In other words, apart from the sea ice concentration no other quantities are assimilated in ice-covered oceans. The PSY4 system starts in October 2006 from a "cold" start (initial currents are null) using initial climatological conditions from EN4.2.1 hydrographic temperature and salinity data (Good et al., 2013). Daily outputs from January 2007 to May 2020 are used in this paper.

2.2. Non-assimilated Data Used for Model Evaluation

Data used for the evaluation include temperature and salinity profiles from the UDASH database (Behrendt et al., 2018) plus recent observations (N-ICE 2015, A-TWAIN 2012/13 and IAOOS platforms), and mooring data (Figure 1, Table 1). From 1997 onwards, a mooring array has been maintained over the eastern slope of Fram Strait at 78.85°N by the Alfred Wegener Institute. Here we use the easternmost moorings F1 to F7 temperature, salinity, and current data (between 3.5°E and 9°E i.e. in the WSC core and offshore branch following Beszczynska-Möller et al., 2012) from 2007 (first full year available in PSY4) to 2012. The A-TWAIN mooring array, located between 81.4°N-31.2°E and 81.9°N-30°E (yellow stars on Figure 1), was maintained from 24 September 2012 to 15 September 2013 as part of the international project "Long-term variability and trends in the AW inflow region" (Table 1). The six A-TWAIN moorings provided current and hydrographic measurements in the boundary current north of Svalbard.

3. Performance of the Mercator Ocean PSY4 System in the WNB

Daily PSY4 fields were collocated in time and space (closest grid cell) with conservative temperature (CT) and absolute salinity (SA) profiles from drifting buoys and CTD stations. Model and *in-situ* profiles were interpolated to the same 2-m vertical resolution. Mooring measurements and the associated colocated model fields were 10-day low-pass filtered.

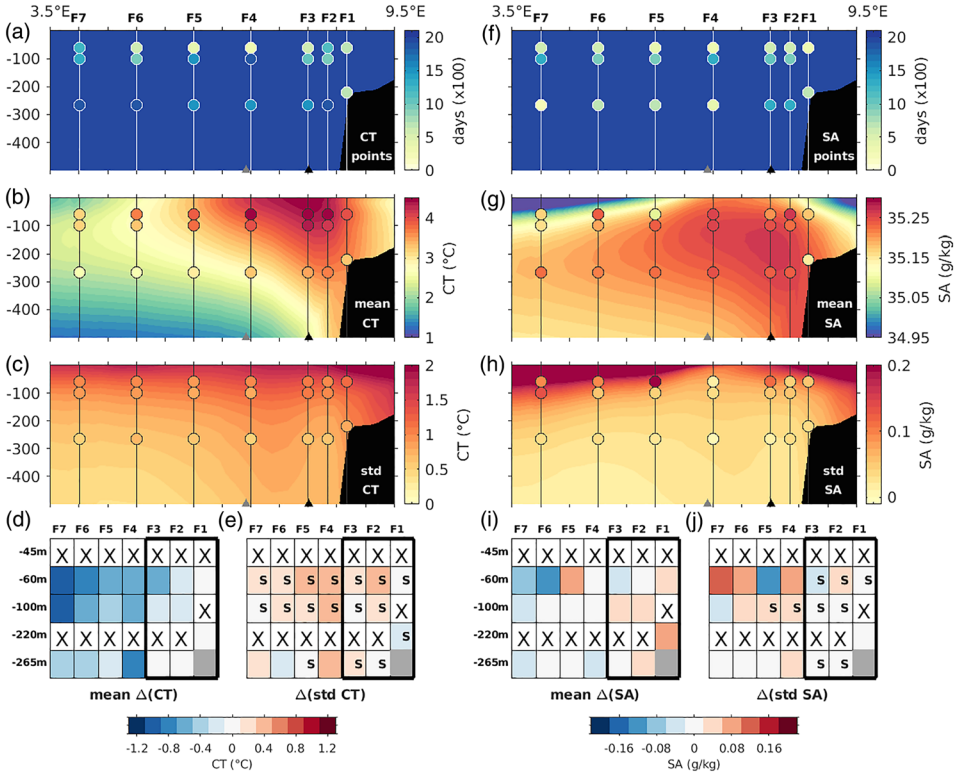

Figure 2. (a) Number of data points available over the 2007–2012 period in the model (background) and mooring observations (colored dots). Model fields cover 2,190 days, while moorings data coverage varies between 250 and 1990 days because of data gaps. (b) Mean conservative temperature (CT, °C) over the 2007–2012 period and (c) associated STD, along the F1-F7 mooring array. Isobaths 1,000 and 1,500 m are marked by the black and gray triangles respectively. In (d) and (e), model fields have been collocated in time with observations. (d) Average model-observations differences of CT (°C) and (e) differences of STD in CT (°C) for moorings F1 to F7 at different levels, over the 2007–2012 period. Gray cells indicate the continental shelf, crossed cells have no available data. 'S'-marked cells have model-observations correlation above the 90% confidence level. The thick black frame delineates cells in the West Spitsbergen current core as in Beszczynska-Möller et al. (2012). (f) To (j): Same for absolute salinity (SA, g/kg).

3.1. AW Inflow at the Fram Strait Mooring Array

For more precise comparisons, model fields were collocated in time and depth to match the number of available data points. The major difference in the mean was a cold and fresh bias in the upper 100 m offshore of the WSC core (ΔCT ~ 0.6–1 °C, ΔSA ~ 0.08 g/kg; Figures 2d, 2i). Modeled T-S fields showed standard deviations (STD) matching observations, in spite of larger values in the upper 100 m (Figures 2c, 2e, 2h, 2j). Overall, the mooring array provided more velocity data days than temperature and salinity data days (Figures 3a, 3f; 2a, 2f). Modeled current speed fields were rather realistic for both zonal and meridional components, as detailed below (Figures 3b, 3c, 3g, 3h).

Within the WSC core (F1 to F3), the modeled temperature and salinity matched moorings data, with small differences (cold bias ~ 0.4–0 °C, ΔSA ± 0.08 g/kg; Figures 2d, 2i) and statistically significant correlation coefficients r (CT) and r (SA) (to the 90% confidence level) in the ranges 0.7–0.95 and 0.4–0.75 (respectively). Both meridional and zonal current velocities were well reproduced at F2 mooring location (Figures 3d, 3i). The modeled WSC core (defined as V > 15 cm/s, e.g. Beszczynska-Möller et al., 2012) was located slightly further offshore than in the observations and modeled meridional current velocities were 0.15 m/s smaller (0.05 m/s larger) than observed ones at F1 (at F3) (Figure 3d). In the WSC, modeled velocities exhibited temporal variations of the right amplitude and were well correlated with observations, with statistically significant correlation coefficients in the range 0.4–0.7 for both components (S-marked cells in Figures 3e, 3j).

The offshore WSC branch, with larger vertical temperature gradient and meridional velocities between 0 and 15 cm/s (e.g. Beszczynska-Möller et al., 2012), extends from 6.5 to 7.5°E (F4-F5) in the model, as in the

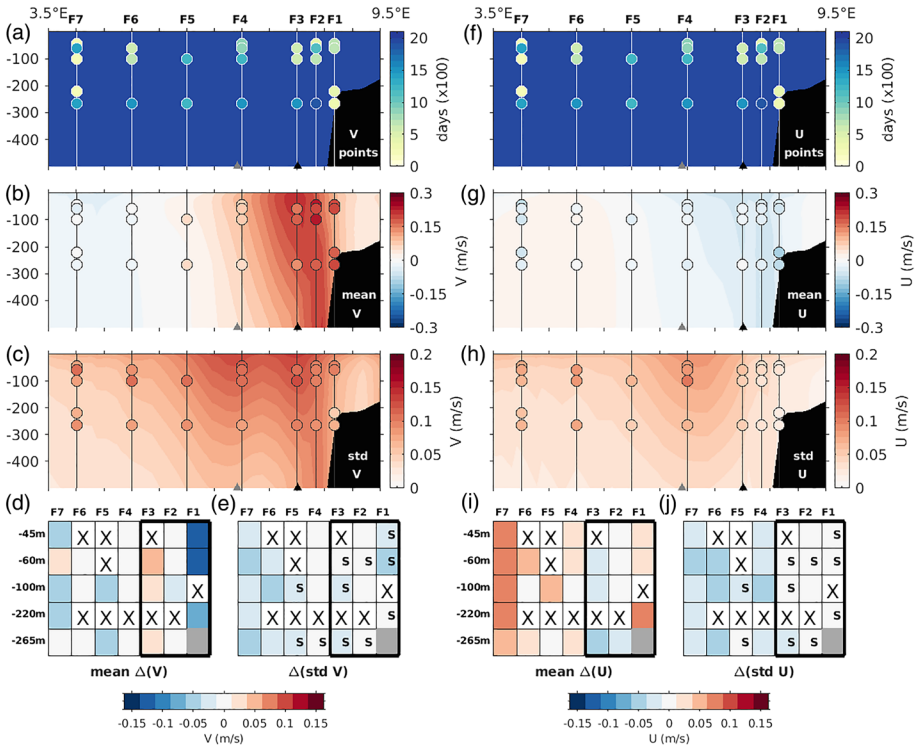

Figure 3. (a) Number of data points available over the 2007–2012 period in the model (background) and mooring observations (colored dots). Model fields cover 2,190 days, while moorings data coverage varies between 190 and 1960 days because of data gaps. (b) Mean meridional speed (V, m/s) over the 2007–2012 period and (c) associated STD, along the F1-F7 mooring array. Background colors correspond to model fields, colored dots to mooring data. In (d) and (e), model fields have been collocated in time with observations to take data gaps into account. Isobaths 1,000 and 1,500 m are marked by the black and gray triangles respectively. (d) Average model-observations differences of meridional speed V (m/s) and (e) differences of STD in V for mooring F1 to F7 at different levels, over the 2007–2012 period. Gray cells indicate the continental shelf, crossed cells have no available data. 'S'-marked cells have model-observations correlation above the 90% confidence level. The thick black frame delineates cells localized in the WSC core as in Beszczynska-Möller et al. (2012). (f) To (j): Same for zonal speed (U, m/s).

observations (Figures 2b, 3b, Figure 2 in Beszczynska-Möller et al., 2012). The increased STDs between F3 and F4 locations in all parameters (Figures 2c, 2h, 3c, 3h) likely marked the transition between the WSC core and this offshore branch. West of 6°E, where the variable recirculation branches of the Fram Strait interior can be found (F6-F7), modeled velocities showed less variations than observations and correlations were less significant (S-marked cells in Figures 3e, 3j). The weak correlations in salinity at 65 m between F7 and F4 are found in a complex region, with variable ice cover and water properties (front migration).

In summary, PSY4 represented well the AW inflow properties, spatial structure and temporal variability. There was no seasonality in model-observation differences in the WSC core. To our knowledge, it was the first time that such a five year-long model validation was conducted at Fram Strait.

3.2. Temperature-Salinity Profiles in the WNB

Nearly 1,500 T-S profiles were gathered in the upper 750 m of the WNB over the 2017–2018 period (section 2, Figures 4a, 4f). The AW layer (such as CT > 1 °C, SA > 35.05 g/kg) was on average located between 150 and 600 m, with its core near 250 m (i.e. where temperature is maximum) both in model and observations (respectively red and black in Figure 4b). The model exhibited a cold and fresh bias in the 100–250 m layer (less than 0.5 °C and 0.04 g/kg; Figures 4c, 4e), as the modeled mean thermocline and halocline were too smooth and extended about 50 m too deep (Figures 4b, 4d). AW properties in the 250–550 m layer were well reproduced (biases less than 0.2 °C and 0.01 g/kg), with STDs similar in average profiles and T-S differences (shaded envelopes on Figures 4b, 4c). Below 600 m, the model shows a moderately warm and salty bias

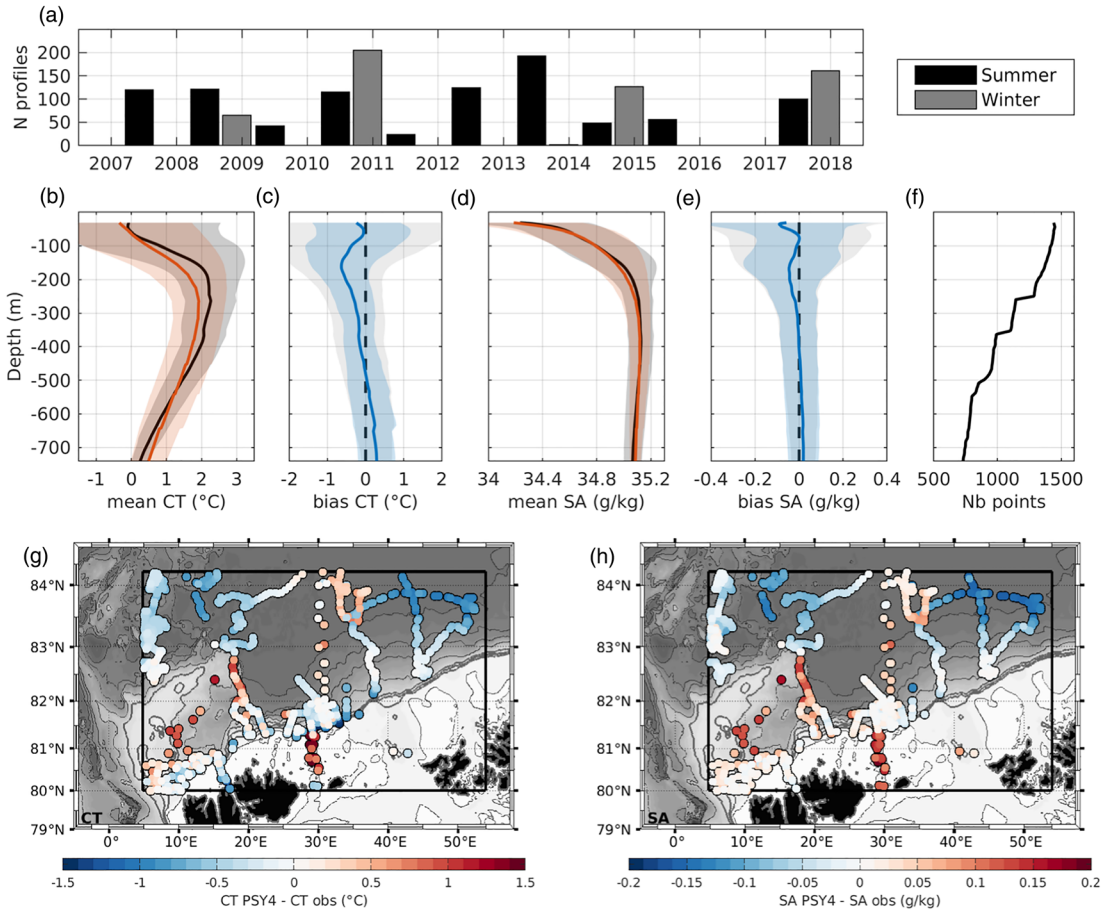

Figure 4. (a) Number of *in-situ* temperature and salinity profiles available in the Western Nansen Basin between 2007 and 2018 from CTD stations and ITPs (see Table 1). (b) Mean conservative temperature (CT, °C) profile in observations (black) and the collocated model outputs (red) over the 2007–2018 period (thick lines). Shaded envelopes are STD around the mean (observations in gray, light red for model). (c) Model-observations difference of mean CT (°C). Shaded envelopes are the bias STD (blue) and the sum of model and observations STDs (gray) at each level. (d-e) Same for absolute salinity (SA, g/kg). (f) Number of data points available at each level, for observations and colocated model profiles. (g) Model-observations differences at 265 m in CT (°C) and (h) SA (g/kg).

(e.g. +0.25 °C and +0.02 g/kg at 700 m, Figures 4c, 4e). This is likely explained by the model vertical resolution which decreases with depth (1-m thick layers near the surface, 19-m thick at the layer centered at 109 m, and 130-m thick at the 763 m layer). Nonetheless, at 265 m (near the AW core), model-observation differences were small along the slope in the AW boundary current ($\Delta CT \sim 0$ to -0.2 °C, $\Delta SA \sim \pm 0.03$ g/kg; Figures 4g and 4h). STD envelopes around mean profiles are of the same order of magnitude in PSY4 and in observations (Figures 4b and 4d). The bias envelope (root mean squared difference, light blue in Figures 4c and 4e) is smaller than the square-root of the sum of model and observations variances (light gray in Figures 4c and 4e), illustrating the model skills.

Overall, PSY4 well represented the temperature and salinity in the AW layer in spite of a cold bias ($\Delta CT \sim 0.2$ °C). We now examine the model performance in reproducing two sources of AW modification in the WNB: shelf-basin exchange and winter convective mixing.

3.3. Shelf-Basin Exchange in the Model

Both west and north of Svalbard, PSY4 reproduced circulation patterns described by Nilsen et al. (2016) and Pérez-Hernández et al. (2017): modeled warm and salty AW entered the troughs along their southern (or western, respectively) edge and cooled down and freshened as it flowed cyclonically along the edges of the troughs (Figure 5).

We illustrated shelf-basin exchange west of Svalbard with model temperature, salinity and velocity fields in late July 2017, a time of northerly or weak winds, allowing waters accumulated on the shelf during strong

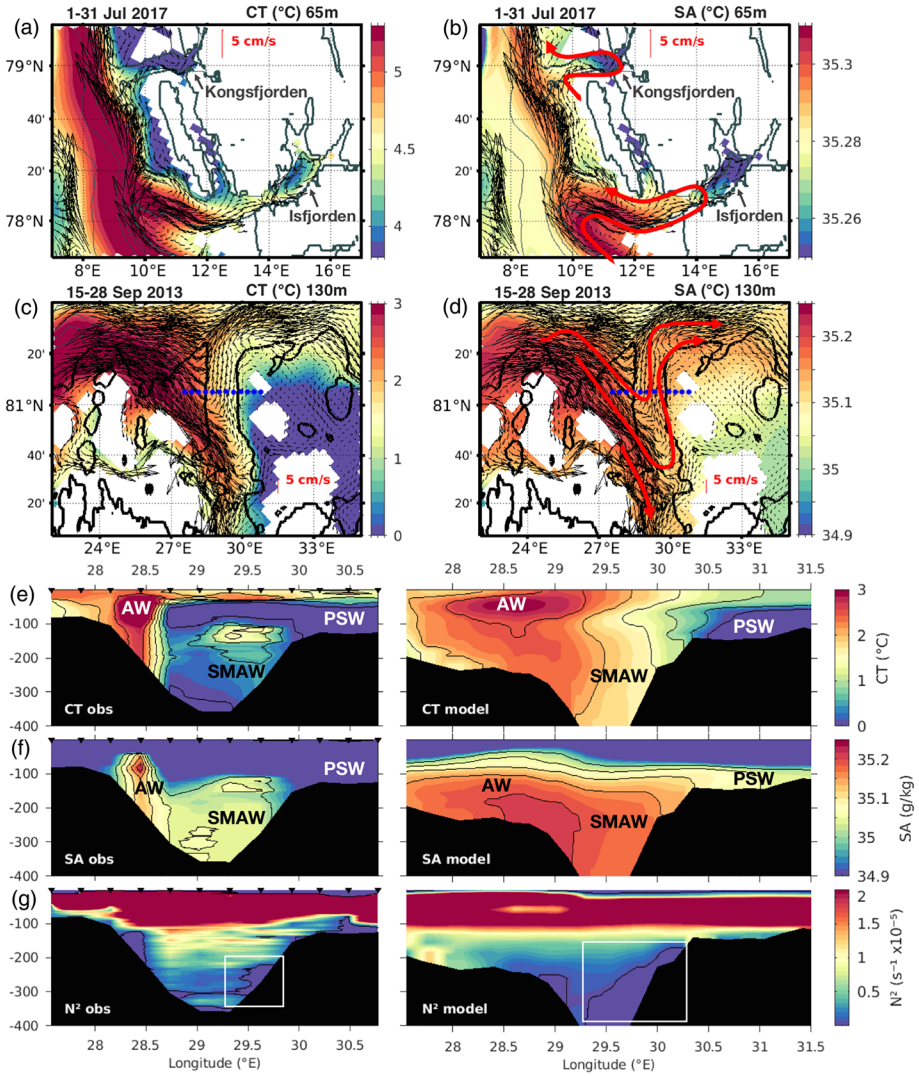

Figure 5. (a) Conservative temperature (°C) and (b) absolute salinity (g/kg) fields from PSY4 at 65 m west of Svalbard in late July 2017 (at the time of the observations from Koenig et al., 2018). When velocities (arrows) were larger than 12 cm/s, arrows were removed for sake of clarity. Red arrows schematize the circulation in Kongsfjorden and Isfjorden (from Nilsen et al., 2016). (c) Conservative temperature (°C) and (d) absolute salinity (g/kg) fields from PSY4 at 130 m over the Kvitøya trough region located north-east of Svalbard in late September 2013 (at the time of the observations from Pérez-Hernández et al., 2017; blue dots). Velocities as in (a), (b). The 200 m isobath (thick black line) from IBCAO shows a narrow entrance and a north–south orientation. In the model, the Kvitøya trough mouth is too large and its main axis is tilted to the west (see Figure A1). (e), (f), (g) cross sections of conservative temperature (°C), absolute salinity (g/kg) and brunt-Väisälä frequency N^2 (s^{-1}). Left panels are from observations (blue dots), right panels are from PSY4. The white box in (g) highlights the low-N^2 water getting out of the trough. AW: Atlantic water; SMAW: Shelf-modified Atlantic water; PSW: Polar surface water.

southerly winds in early July to flow back down the slope (Koenig et al., 2018; Figure 5a, 5b). AW from the WSC that circulated in the troughs was mixed with fresher and much colder waters from the shelf as discussed in the literature (e.g., Nilsen et al., 2016). The cross-shelf exchange signal seen in Koenig et al. (2018) as small cold and fresh lenses (less than 10 km wide) with high particle concentrations, lay at the limit of the PSY4 resolution (4 km in the area). However, the model produced cold and fresh water patches coming out of the fjords in accordance with the wind forcing (not shown).

North of Svalbard, the model bathymetry (see appendix) does not accurately follow the Arctic region-dedicated IBCAO bathymetry (Jakobsson et al., 2012) in Kvitøya Trough: the trough entrance is too wide (western bank too deep) and the trough axis is tilted to the West (Figures 5c, 5d, and A1). This locally imprecise

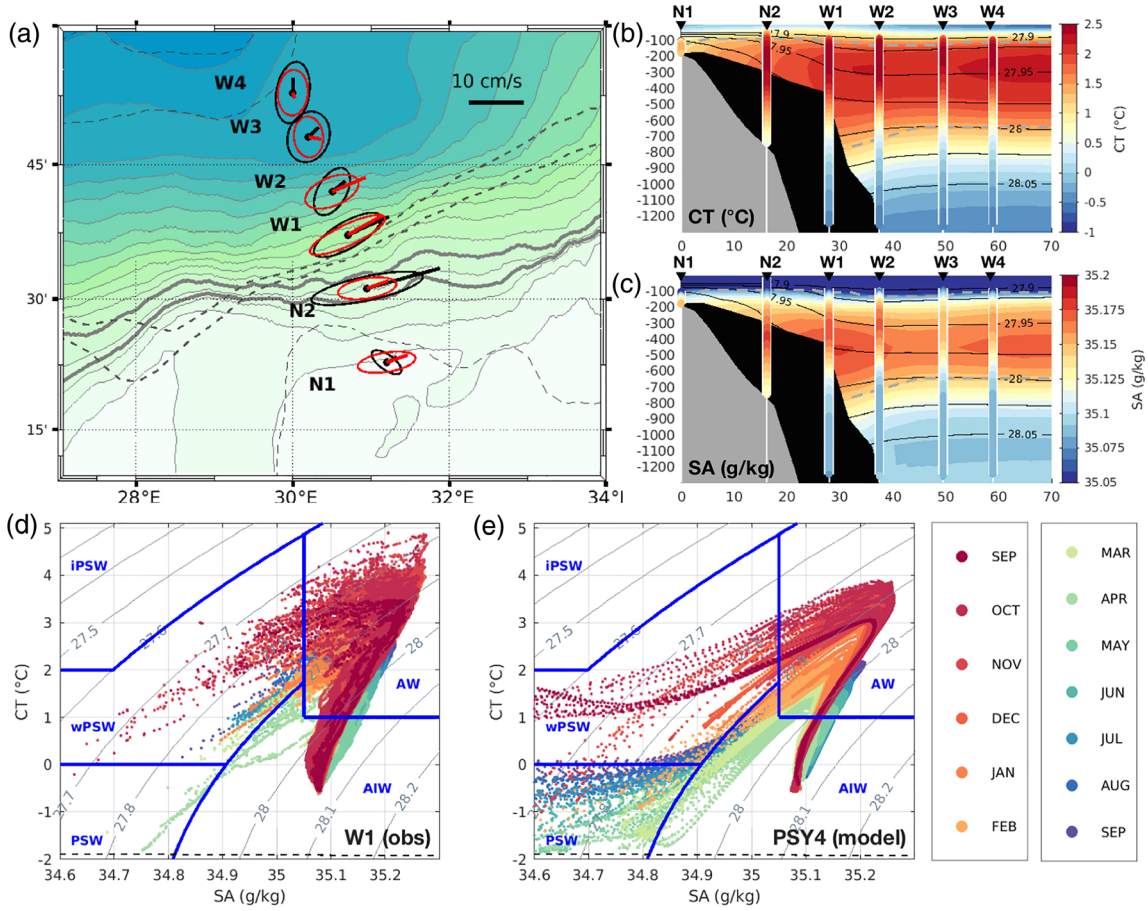

Figure 6. (a) Year-long current velocity averaged over the upper 70 m, together with their variance ellipses, at the A-TWAIN mooring sites. Observations from acoustic Doppler current profilers are in black, collocated model outputs in red. IBCAO bathymetry is in background color with isobaths 700 and 1,000 m in thick gray lines. Dashed lines are model isobaths (200 m on the western flank of Kvitøya trough, 700 and 1,000 m in thick lines, 3,200 and 3,200 m offshore matching IBCAO isobaths, see Figure A1). (b) Year-long averages of conservative temperature (CT, °C) and (c) absolute salinity (SA, g/kg) at the a-TWAIN mooring sites (indicated as N for NPI and W for WHOI moorings), from the model (background color) and mooring data (vertical profiles bordered in white). IBCAO bathymetry is in gray, model bathymetry in black. Isopycnals (black contours) are plotted from 27.9 to 28.05 kg/m^3 every 0.025 kg/m^3. Dashed gray lines are the AW layer limits. (d) CT-SA diagram using WHOI-1 data from September 2012 to September 2013 (no data above 100 m depth). Months are in colors. (e) Same using collocated PSY4 CT and SA. Water mass boundaries are adapted from Pérez-Hernández et al. (2019), with AW such as CT > 1 °C and SA > 35.05 g/kg (i.e. 34.9 psu). AW: Atlantic water; AIW: Arctic intermediate water; PSW: Polar surface water; wPSW: Warm polar surface water; iPSW: Inshore polar surface water.

bathymetry is likely responsible for the salty and warm biases observed in Kvitøya Trough at 265 m (Figures 4g, 4h). Nevertheless, the model showed some skill. The comparison to the K2 section from Pérez-Hernández et al. (2017) showed AW entering the western flank of the trough, being cooled down and freshened through mixing with the cold, fresh Polar Surface Water (PSW, Figures 5e, 5f) from the shelves. The shelf-modified AW (hereafter SMAW, Figures 5e, 5f) circulated back towards the AW boundary current (difference in SMAW salinity between observations and model of 0.1 g/kg). These SMAW, injecting anomalously cold, fresh water into the AW boundary current, are vertically homogeneous and marked by a particularly low value of Brunt-Väisälä frequency ($N^2 < 10^{-6}$, Figure 5g). In the model part of the AW entering Kvitøya trough continued southward, towards the Barents Sea, in agreement with the observations (Figure 5c, 5d).

3.4. Comparisons to the 30°E A-TWAIN Moorings

The A-TWAIN mooring array provided a unique dataset documenting deep mixed layers and intense AW ventilation during winter 2012/13 (Pérez-Hernández et al., 2019). Modeled mean current velocities were of the same order of magnitude as the observations with similar directions (Figure 6a). The modeled AW jet was located further offshore than in the observations in Figure 6a, as the slope in the model

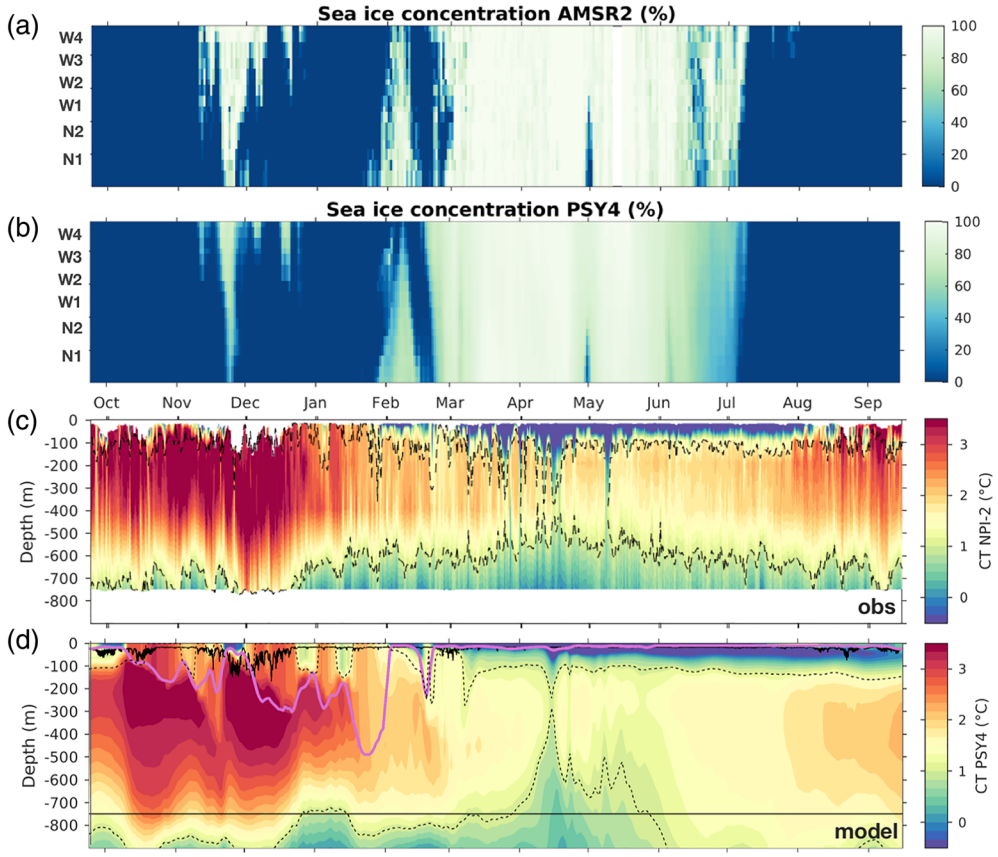

Figure 7. (a) AMSR2 sea-ice concentration (%, in colors) along the A-TWAIN array (y-axis) from September 2012 to September 2013. (b) Same for PSY4. (c) Time-depth conservative temperature (CT, °C) from mooring NPI-2 data. (d) Collocated modeled conservative temperature (CT, °C).Dashed lines in (c) and (d) mark the top and bottom boundaries of the AW layer (defined as in Figure 6). In (d), the purple line indicates the MLD estimate provided by the Mercator Ocean system, defined as the depth where density exceeds the surface density by 0.01 kg/m^3, while the black lines show the vertical extent of the mooring data (variable near surface due to blow-downs).

bathymetry was about 15 km too far north (isobath 700 m in Figures 6a-c, A1). As a result, maximal velocities were found at the WHOI-1 and WHOI-2 locations and not at NPI-2 and WHOI-1 as in the observations. Offshore of the modeled AW jet, at WHOI-3 and WHOI-4 currents exhibited smaller variations than *in-situ* data (major axis of 3 cm/s instead of 4.5 cm/s). Note that current mean and variance were well reproduced at WHOI-1. Modeled AW salinity and temperature (Figures 6b–6e) were similar to the observations presented in Renner et al. (2018) and Pérez-Hernández et al. (2019). In the 100–500 m layer, biases in CT and SA did not exceed 0.5 °C and 0.05 g/kg respectively (not shown), and reproduced the observed seasonal variations (Figures 6d, 6e).

Modeled sea-ice matched AMSR2 3.125-km resolution satellite ice product (https://nsidc.org/data/) very well, both in cross-slope distribution and temporal evolution (Figures 7a, 7b; recall that PSY4 assimilates sea-ice concentration data). The evolution of temperature and salinity was well reproduced (example CT at NPI-2, Figures 7c, 7d), although the modeled AW layer (CT > 1 °C) extended ~150 m deeper than in the A-TWAIN mooring observations, likely due to the model vertical resolution (as mentioned in section 3.2). Pérez-Hernández et al. (2019) have documented deep mixed layers along the continental slope during winter 2012/13, likely formed by local winter convection and ventilating the AW layer. The model accurately reproduced the deepening of the mixed layer in November–December, resulting in particularly deep mixed layers (~450 to 500 m) in January 2013, with MLDs matching observations (Figure 7d; Figure 10 in Pérez-Hernández et al., 2019). A-TWAIN mooring observations showed for the first time that even after local convection ceased, the AW remained anomalously cold and fresh until the end of the moorings record, likely due to the advection of ventilated AW from upstream. Such behavior was also reproduced

in PSY4, confirming the capability of the model in representing local winter convection and AW ventilation in the WNB (Figures 7c-d).

4. Aw Ventilation in the WNB: Insights From 14 Years of PSY4 Fields

The good performance of PSY4 in representing the AW ventilation in the WNB being assessed, we examined deep mixed layers formation and AW modification in a broader spatio-temporal context, using 14 years of PSY4 over the WNB.

4.1. Identifying Extreme Mixed Layer Depths in the WNB Over 2007–2020

The mixed layer depth (MLD) was defined as the shallowest depth at which potential density exceeded the surface value by 0.01 kg/m^3 (Boyer Montégut et al., 2004; Peralta-Ferriz & Woodgate, 2015). We called maximum MLD the deepest MLD reached at each grid point every year, from June 1 of one year to May 31 of the following year. This time frame is chosen in order to avoid splitting the winter period into two time-series. Therefore, we obtain 13 year-long time spans from 2007/08 to 2019/20.

At each location, we obtained time-series of yearly maximum MLD and noted the associated sea-ice cover at the time of each detected maximum MLD. The largest 13-year average maximum MLDs (>300 m) were found over the continental slope following the lateral extent of the AW boundary current, with an associated sea-ice cover lower than 40% (Figures 8a and 8c). In this area, stds of maximum MLDs over the 13 years exceeded 200 m and corresponded to the largest ice cover stds in the area (above 40%) (Figures 8b and 8d).

Examination of years in which maximum MLDs were reached over the 2007–2020 period revealed two major signals (Figure 8e). Year 2012/13 (red area on Figure 8e) exhibited the deepest MLDs over the 13 years nearly everywhere east of 24°E and north-northeast of Yermak Plateau. Year 2017/18 (blue area on Figure 8e) was also highlighted with the deepest modeled MLDs over Yermak Plateau and Sofia Deep (west of 24°E). In contrast, winters 2014/15 and 2010/11 were the mildest in terms of winter mixed layer depths (purple and yellow areas in Figure 8f). Time series of MLDs averaged over boxes A and B (defined in Figure 8) confirmed that these extreme winters (deepest and shallowest MLDs) stood out in the 13 years (Figures 9e, 9j).

A striking change in sea-ice cover, net atmospheric heat fluxes, upper ocean temperatures (10 and 50 m), and MLDs occurred in 2011 in both boxes (Figures 9). Prior to 2011, there were no open ocean conditions (Figures 9a, 9f); ocean temperatures at 10 and 50 m were mostly below 0 °C (Figures 9d, 9i) and winter air temperatures below −15 °C (Figures 9c, 9h); annual cycles in heat fluxes and MLDs were rather regular, with heat fluxes mostly above −150 W/m^2 and MLDs not exceeding ~100 m (Figures 9c, e, h, j).

From 2012 onward, interannual variability increased with occurrences of open ocean conditions (Figures 9a, f). At 10 m, ocean temperatures exceeded 0 °C in the absence of ice cover and returned to freezing temperatures under sea-ice, thus exhibiting a striking increase in variability after 2011 (Figures 9d, 9i). A clear trend in ocean temperatures at 50 m was observed (~+0.21 °C/year in box A i.e. northern Yermak Plateau; ~+0.09 °C/year in box B i.e. continental slope). The smaller trends in temperature at 10 and 265 m (between 0.03 and 0.08 °C/year) were only marginally significant (to the 90% confidence level. After 2011, 50-m ocean temperatures remained above 0 °C over the continental slope and even around 2 °C over Yermak Plateau, while winter air temperatures exceeded −15 °C (Figures 9d, 9i). However, over Yermak Plateau MLDs seldomly exceeded 100 m except for winter 2012/13 (reaching 180 m) and the exceptional winter 2017/18 with MLD exceeding 300 m (examined in section 4.2; Figure 9e). In contrast, on the continental slope the change in 2011 was clear-cut in MLD amplitude and net atmospheric heat fluxes range (Figures 9i, 9j).

Through the 13 winters, large variations in air temperature were observed (Figures 9c, 9h). They were associated with storms passing by and favored upper ocean mixing.

During winter 2010/11, MLDs shallower than 70 m coincided with an ice cover greater than 80%, and weak negative heat fluxes (> -50 W/m^2) in the two areas (Figure 9). Ocean temperatures at 50 m were around 0 °C (Figures 9d, 9i). In contrast, large winter MLDs (>200 m) were observed after 2011 (winters 2012/13 and 2017/18, red and blue shades in Figure 9) and corresponded to open ocean conditions with winds pushing the ice away (examples in Figures 10a, 10c) and large negative heat fluxes (<-200 W/m^2). Temperatures at 50 m exceeded 1 °C at the beginning of winter (Figures 9d, 9i). In the highly variable post-2011 period, the

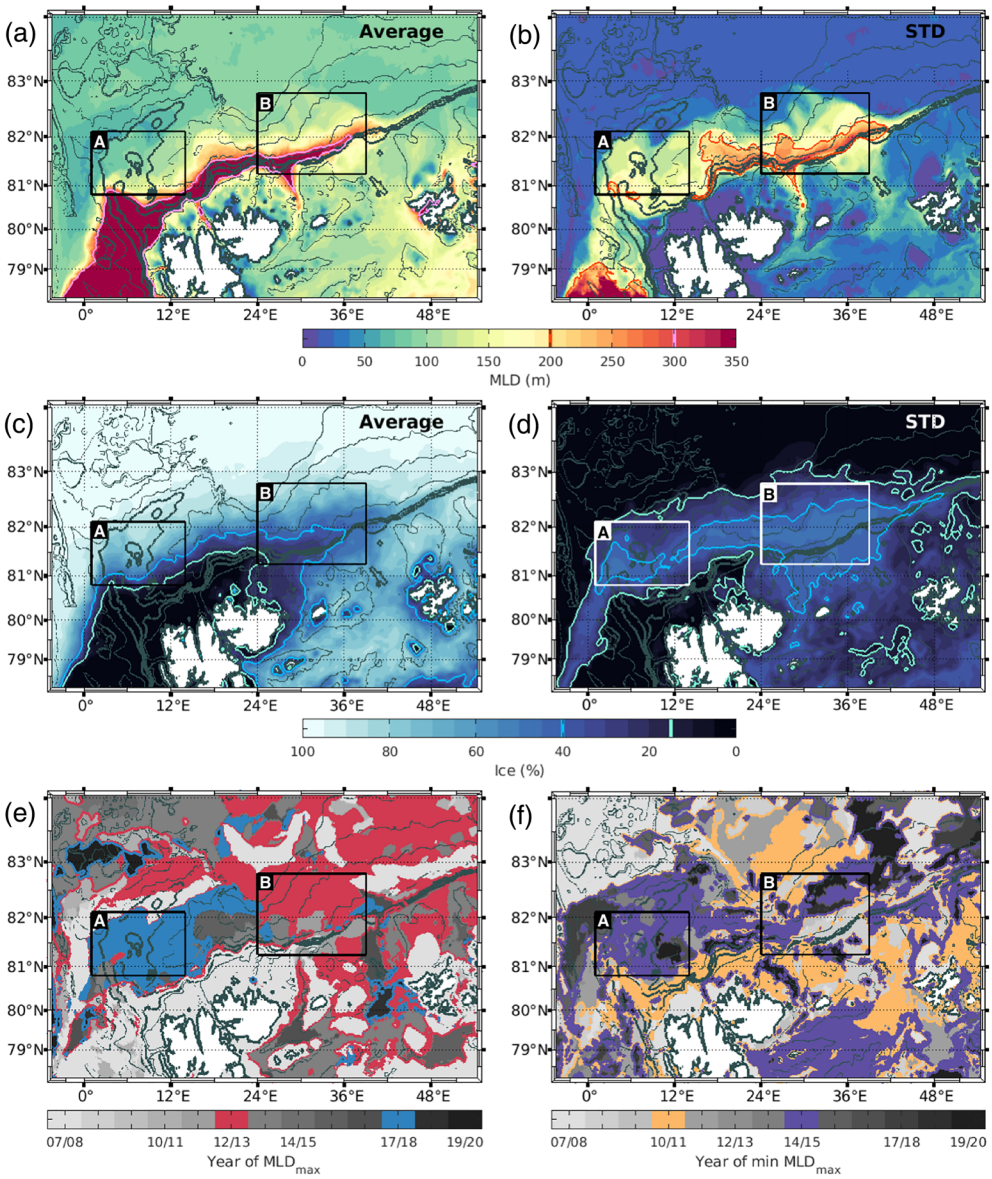

Figure 8. (a) Mean over 13 years of the annual mixed layer depth (MLD) maxima (in m) at each point and (b) its interannual STD. (c) Mean over 13 years of the ice cover (%) on the date of the annual MLD maximum at each point and (d) interannual STD. (e) Year of the maximum MLD at each point over the 2007–2020 period. (f) Year when the annual maximum of MLD was the smallest at each point. Light pink contours delineate areas where $MLD_{max} > 300$ m (a); red contour areas where std (MLD_{max}) > 200 m (b); green and cyan contours are respectively the 15 and 40% ice cover limit (c, d). Year-long time spans were taken from June to may (included) of the following year. Time-series of several parameters averaged over boxes a and B are shown in Figure 9.

2014/15 winter stood out as a rather moderate MLD year in both boxes (Figure 9, purple shade) with a high percentage in ice cover and remarkably weak heat fluxes (Figures 9b-d, 9g-i). Over Yermak Plateau (box A), mixed layers also remained shallow in winters 2016/17, 2018/19 and 2019/20, as atmospheric conditions (wind direction and few storms) maintained a significant ice cover (Figures 9a-b, 9e). Model fields suggested that the particularly deep MLDs in winters 2012/13 and 2017/18 shoaled drastically when winds imported sea-ice and meltwater in the respective areas (Figures 9, 10b, 10d).

In summary, deep MLDs (>100 m) did not occur between 2007 and 2011. They are occasionally observed from 2012 onwards, with two exceptional winters in terms of deep convection: 2012/13 and 2017/18.

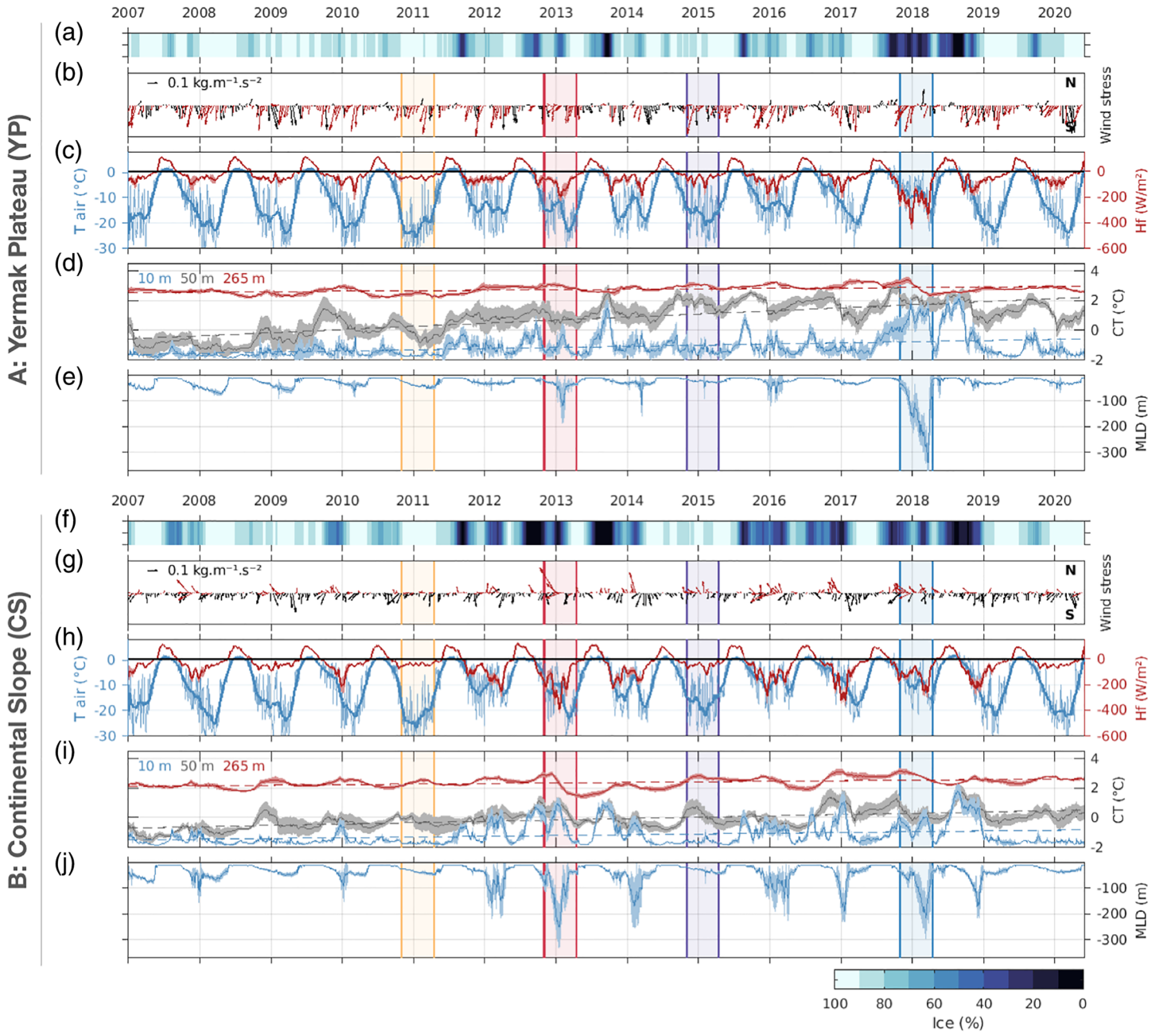

Figure 9. Spatially averaged time series over boxes a (Yermak plateau) and B (continental slope) from Figure 8. (a, f) ice cover (%). (b, g) wind stress (kg.M^{-1}.S^{-2}), favorable to ice-free conditions in red (easterlies for a and southeasterlies for B). (c, h) net total heat flux (W/m^2) and air temperature at 2 m (°C, blue), 3-month low-pass filtered (thick blue line). (d, i) conservative temperature in the ocean (°C) at 10 m (blue), 50 m (gray) and 265 m (red) (linear trends in dashed lines). (e, j) mixed layer depth (MLD, m). Shaded envelopes are spatial stds over the boxes. Vertical lines highlight winters selected in Figures 8e and 8f. Wind velocities and net total heat fluxes are low-pass filtered with a 1-month cut-off. For sake of clarity, wind arrows are plotted every 10 days.

4.2. Winter 2017/18 Over Yermak Plateau

The oceanic heat carried by warm near-surface AW is responsible for the quasi-perennial ice-free conditions as far north as 81°N in an area called Whalers' Bay, located northwest of Svalbard (e.g. Onarheim et al., 2014). Winter 2017/18 exhibited open ocean conditions up to 82.5°N over the Yermak Plateau, associated with deep mixed layers exceeding 300 m (Figures 11a-b). The development of these exceptional deep mixed layers coincided with the presence of warm near-surface AW (above 3 °C in early-winter) reaching as far as

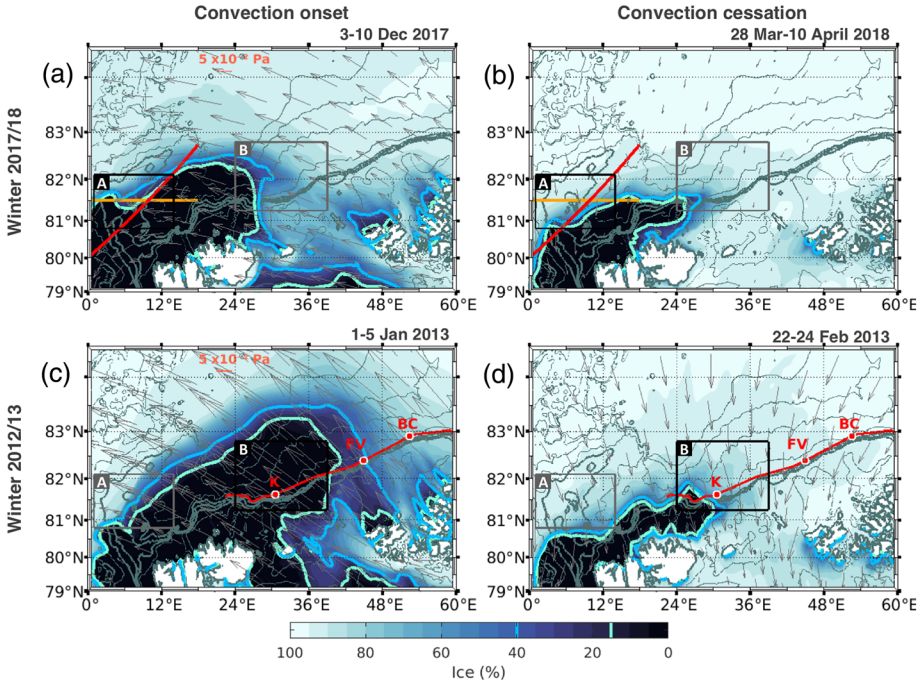

Figure 10. (a) Wind stress (gray arrows, pa; plotted every 15 grid cell) and sea-ice concentration (background color, %) averaged during the onset and (b) cessation of deep convection in winter 2017/18. Green and cyan contours are respectively the 15 and 40% ice cover limit. The red and orange sections over the northern Yermak plateau (box a) are presented in Figure 11. (c) Same for the onset and (d) cessation of deep convection in winter 2012/13. The red section along the continental slope (box B) is presented in Figure 13. Boxes a and B are the same as in Figures 8 and 9.

83°N, the occurrence of storms inducing strong mixing, large negative heat fluxes (mean of −230 W/m^2 during 4 months), and wind conditions favorable to pushing the ice out of the area (Figures 9a-e, 10a, Supporting Information S1).

Deep mixed layers in excess of 300 m lasted for over 4 months. In mid-December they developed under widely ice-free conditions on the western part of Yermak Plateau and with AW temperatures above 3 °C extending from the surface down to 450 m at 81.5°N (Figure 11c). On December 22, MLDs were about 100 m in the Fram Strait part of the section (0–2°E), reached 300 m in the core of the AW northward flow (2–6°E), 170 m in the southward Yermak Pass Branch (6–9°E), 200 m within a mesoscale structure detached from the slope over the Sofia Deep (12–14°E) and 80 m in the westward flow above the offshore part of the Svalbard Continental Slope (SCS, 16–18°E; Figure 11c). The corresponding T-S diagram showed that convection over Yermak Plateau (YP) and Sofia Deep (SD) could reach the 27.85 σ-horizon at that time (low-N^2 points circled in black in Figure 12a).

Three months later, the northern part of YP was ice-covered with the ice edge at 10°E (Figure 11d upper panel). Local deep convection ceased over the northern YP while it continued over SD and the continental slope which were still ice-free (Figure 11d). Convected waters over YP were found down to 500 m (reaching the YP sea-floor; Figure 11d) and had densities between 27.9 and 27.95 kg/m^3 over a reduced temperature and salinity range (CT: 2.0–2.8 °C, SA: 35.1–35.2 g/kg, red dots in Figure 12b). Mixed layers in the SD were denser (> 27.95 kg/m^3, also down to 500 m), with even more reduced temperature and salinity range (centered around 2 °C, 35.15 g/kg; blue dots, Figure 12b). Convecting waters over the Svalbard branch (down to 600 m; SCS in Figure 11d) had characteristics slightly warmer and saltier than in the SD straddling isopycnal 27.95 kg/m^3 (centered around 2.4 °C, 35.17 g/kg; green dots circled in black, Figure 12b).

At the same date (29 March 2018), a southwest-northeast section showed that convection was still active over the still ice-free southern part of YP (south of 81°N), and had ceased over the northern SD as northerly winds imported sea-ice and meltwater (ice edge at 10°E; Figure 10b, Supporting Information S1). Ventilated waters extended as far northward as 82.2°N-16°E (Figure 11e). At the north-east edge of the section, mixed layer

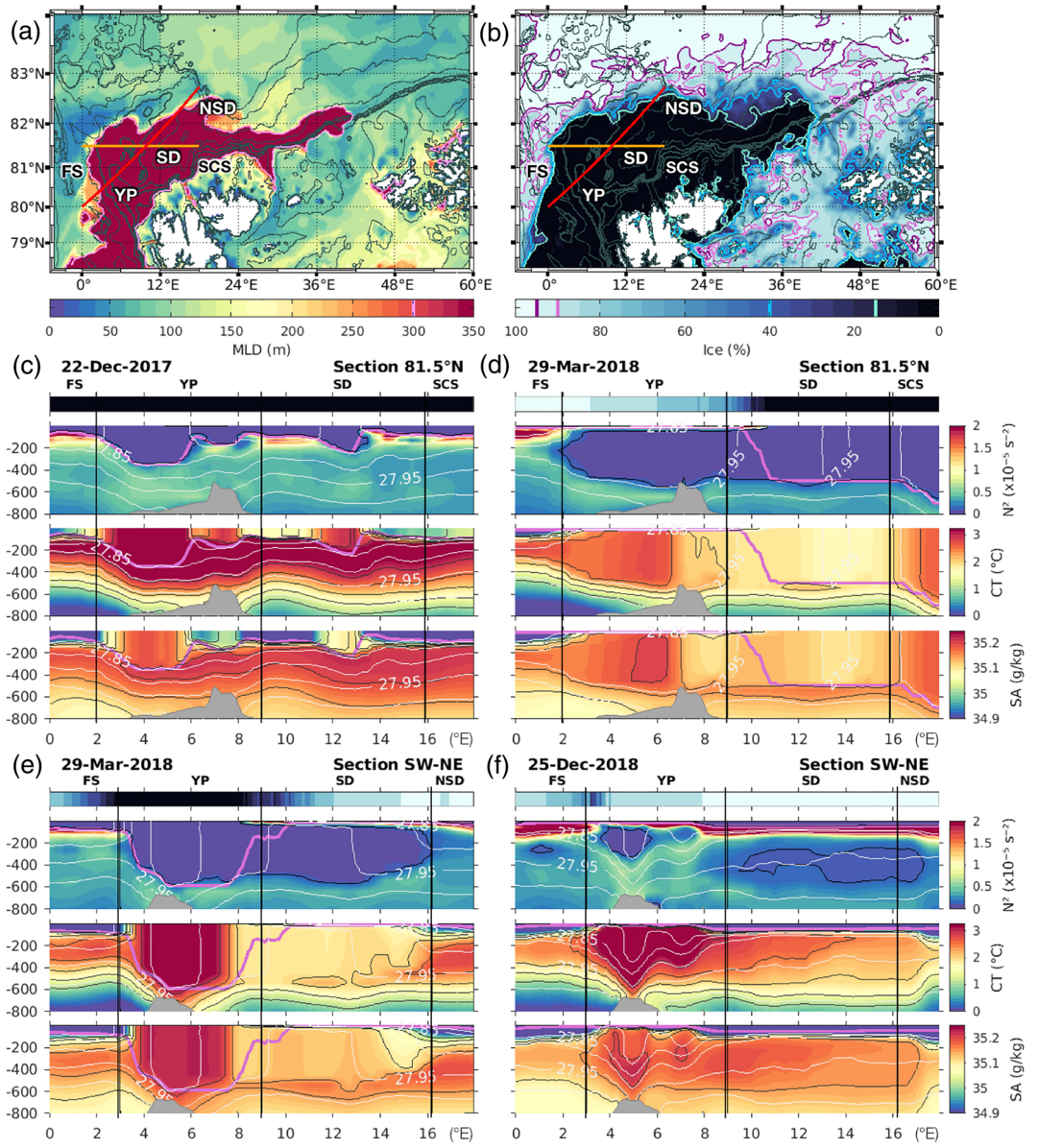

Figure 11. (a) Maximum MLD (in m) reached at each point in winter 2017–2018. (b) Associated Sea-ice coverage (%). Contours are 15 (green), 40 (blue), 90 (pink) and 95% (purple). (c)-(d) (top panel) snapshots of sea-ice coverage (%), colorbar same as (b). (second panel) Brunt-Väisälä frequency (N^2, s^{-1}), (third panel) conservative temperature (CT, °C), and (lower panel) absolute salinity (SA, g/kg) on the 81.5°N zonal section (orange segment in a and b). (e)-(f) same on the SW–NE section (red line in a and b). X-axis is longitude (degrees), y-axis depth in m. the thick pink line is the MLD. Black isolines are the $1x10^{-6}$ s^{-1} threshold in N^2, isotherms every 0.5 °C from 1 to 3 °C, and isohalines every 0.05 g/kg from 35 to 35.2 g/kg. White isolines are isopycnals from 27.8 to 28 kg/m^3 every 0.05 kg/m^3. Vertical black lines delineate the regions FS: Fram Strait; YP: Yermak plateau, SD: Sofia deep; NSD: Northern Sofia deep and SCS: Svalbard continental slope. IBCAO bathymetry along the sections is in gray filled areas.

depths never exceeded 100 m: the AW below was not ventilated that winter and remained warmer and saltier than AW in SD (2.7 °C, 35.18 g/kg, Figure 11e east of 16°E, purple dots in Figure 12c). Comparisons between Figures 11d and 11e west of 7°E highlighted the intense cooling and freshening of the AW inflow along its northward progression on the westward part of YP (−1.5 °C and −0.2 g/kg over 80 km). Indeed, low-N^2 AW undergoing strong modifications over the southern YP (red dots circled in black centered at 27.91 kg/m^3, 35.22 g/kg and 3.2 °C, Figure 12c) were much warmer, saltier and lighter

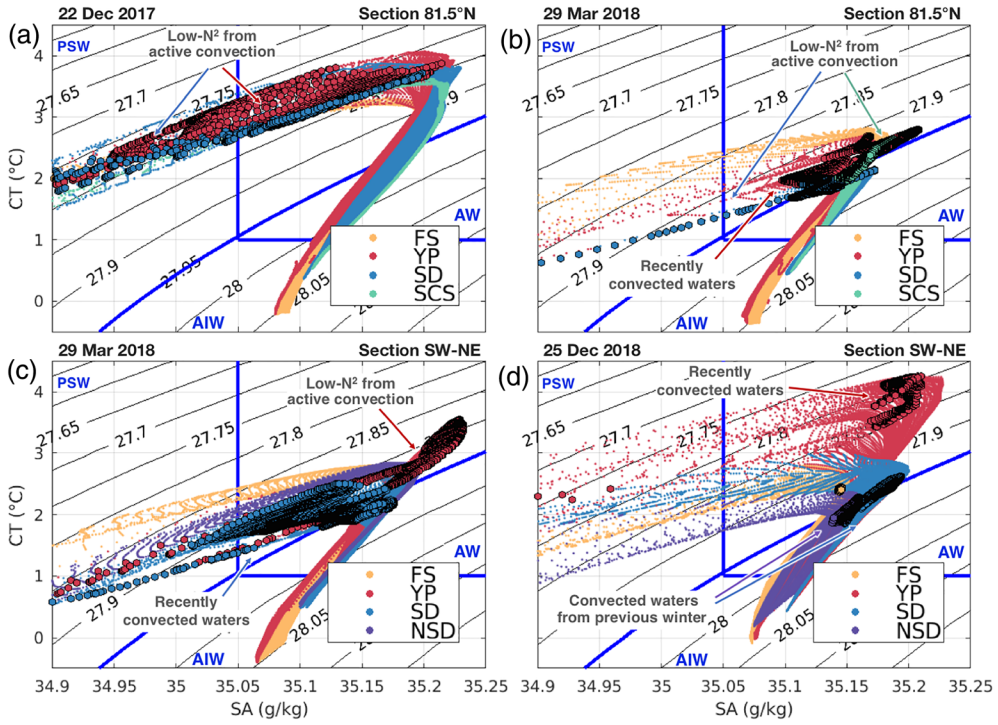

Figure 12. CT-SA diagrams of the sections (c) to (e) shown in Figure 11, upper 800 m of the water column, focused on the AW properties. (a) 22 December 2017 (corresponding to Figure 11c), (b) 29 march 2018 (corresponding to Figure 11d) at the zonal section (orange, Figure 11a). Profiles in the Fram Strait (FS) are in yellow, over Yermak plateau (YP) in red, Sofia deep (SD) in blue, and over the Svalbard continental slope (SCS) in green. (c) 29 march 2018 (corresponding to Figure 11e), (d) 25 December 2018 (corresponding to Figure 11f) at the SW–NE section (red, Figure 11a). Profiles in the Fram Strait (FS) are in yellow, over Yermak plateau (YP) in red, Sofia deep (SD) in blue, and northern Sofia deep (NSD) in purple. Water parcels with low-N^2 ($<10^{-6}$) are circled in black. Isopycnal 27.95 kg m^{-3} is highlighted in blue. AW: Atlantic water; AIW: Arctic intermediate water; PSW: Polar surface water.

than low-N^2 AW encountered further north (red dots circled in black above the 27.95 kg/m^3 isopycnal in Figure 12b).

Deep convection stopped soon afterward and, by mid-April the 81.5°N section was fully ice-covered and the upper water column stratified all over (not shown). Convection over the AW inflow above YP impacted a wide range of water T-S characteristics down to isopycnal 27.95 kg/m^3 (CT ~ 2.1–3.4 °C, SA ~ 35.09–35.22 g/kg; isopycnal range 27.90–27.95 kg/m^3) and reached an even deeper horizon of 27.97 kg/m^3 over the continental slope off Svalbard (CT ~ 1.8–2.3 °C; SA ~ 35.13–35.17 g/kg; narrow isopycnal range 27.95–27.97 kg/m^3) and the SD (CT ~ 1.7–2.3 °C, SA ~ 35.1–35.17 g/kg; large isopycnal range 27.91–27.97 kg/m^3) (Figures 12b, 12c). Over the Fram Strait part of the sections, conditions remained mostly ice-covered and no deep convection developed.

We attempted to follow the low-N^2 waters (Supporting Information S1). Part of those that formed over YP were advected into SD where they joined the dense SD-ventilated waters. At the beginning of the following winter (on December 25, Figure 11f), low-N^2 waters formed during the previous winter ventilation were still present in SD on the 27.95 σ-horizon (CT ~ 1.8–2.7 °C, blue and purple dots circled in black in Figure 12d), while convection had started again on the western side of YP (recently convected waters with CT ~ 3.5–4.3 °C, red dots circled in black in Figure 12d).

4.3. Low-N^2 Waters Along the Continental Slope in Winter 2012/13

The extreme winter 2012/13 along the slope was documented with the A-TWAIN mooring array. Pérez-Hernández et al. (2019) examined deep mixed layer formation and subsequent AW characteristics evolution, while Renner et al. (2018) quantified AW heat loss over the slope. PSY4 was shown to accurately reproduce the A-TWAIN observations (section 3.4).

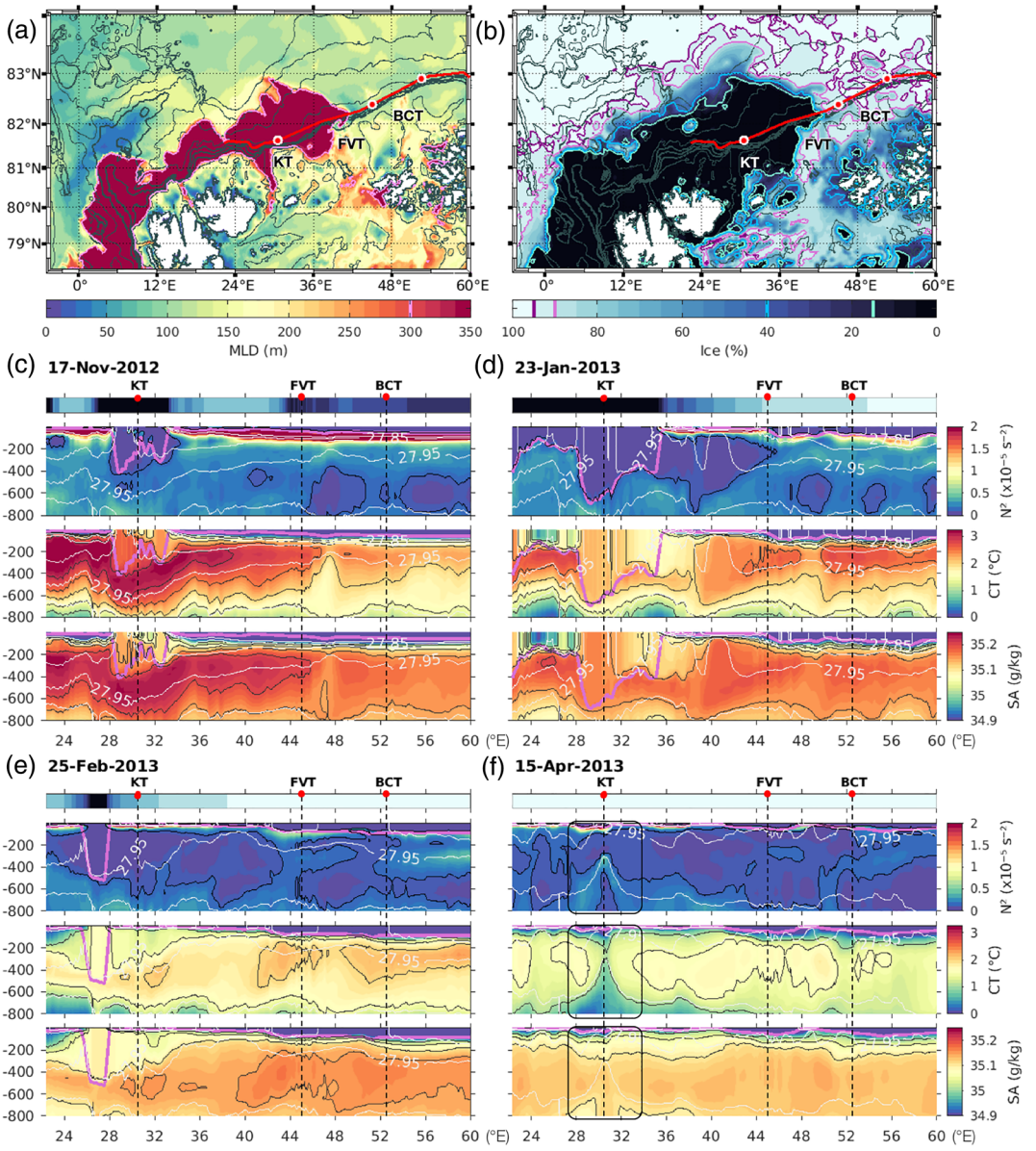

Figure 13. (a) Maximum MLD (in m) reached at each point in 2012–2013 winter. (b) Associated Sea-ice cover (%). Highlighted contours are 15, 40, 90, and 95% in green, blue, pink, and purple respectively. (c)-(f) (top panel) snapshots of sea-ice coverage (%), colorbar same as (b). (second panel) Brunt-Väisälä frequency (N^2, s^{-1}), (third panel) conservative temperature (CT, °C), and (lower panel) absolute salinity (SA, g/kg) at the along-slope section shown on (b) (red line along the 1,000 m isobath). The thick pink line is the MLD at each date. Vertical dashed lines indicate the eastern flank location of the three troughs north-east of Svalbard; KT: Kvitøya trough, FVT: Franz-Victoria trough, BCT: British Channel trough. The A-TWAIN array (mooring WHOI-1) was located at 31°E just east of Kvitøya trough. Black isolines are the $1x10^{-6}$ s^{-1} threshold in N^2, isothermals from 1 to 3 °C every 0.5 °C, and isohalines from 35 to 35.2 g/kg every 0.05 g/kg. White isolines are isopycnals, from 27.8 to 28 kg/m^3 every 0.05 kg/m^3. Black boxes on (f) indicate the dense outflow described in section 5.2.

In 2012/13, modeled MLDs exceeding 200 m were not confined to the continental slope (isobaths 200–2000 m), they extended as far as 82.7°N above isobaths 3,400–3,800 m (offshore) (Figure 13a). These deep MLDs formed over open water areas as strong northwestward winds exported the ice away (Figures 10c, 13b, Supporting Information S2). The loose sea-ice cover (40 to 95% coverage) in the rest of the basin led to maximum MLDs above 100 m. In contrast, the minimum MLDs, less than 50 m seen on the north of Yermak Plateau (in blue in Figure 13a), corresponded to a steep sea-ice concentration gradient associated with active ice melt creating a fresh layer at the surface (Figure 13b).

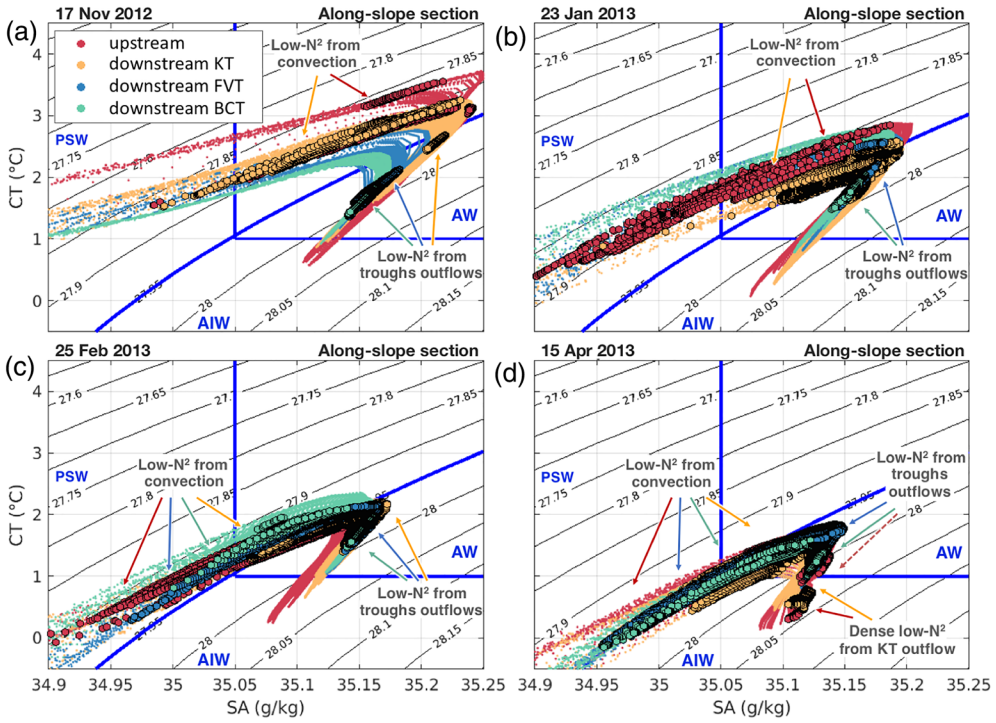

Figure 14. CT-SA diagrams of the sections (c) to (e) shown in Figure 13, upper 800 m of the water column, focused on the AW properties. Every other profile is plotted for sake of clarity. (a) 17 November 2013 (corresponding to Figure 13c), (b) 23 January 2013 (corresponding to Figure 13d), (c) 25 February 2013 (corresponding to Figure 13e) and (d) 15 April 2013 (corresponding to Figure 13f) at the along-slope section (red, Figure 13a). Profiles upstream of Kvitøya trough are in red. Profiles between Kvitøya and Franz-Victoria troughs are in yellow (downstream KT), between Franz-Victoria and British Channel troughs in blue (downstream FVT), and downstream of British Channel trough in green (downstream BCT). Water parcels with low-N^2 ($<10^{-6}$ s^{-1}) are circled in black. Isopycnal 27.95 is highlighted in blue. AW: Atlantic water; AIW: Arctic intermediate water; PSW: Polar surface water.

We closely monitored the evolution of ice, N^2, temperature and salinity on a section along the 1,000 m isobath (red line on Figure 13b). Four snapshots illustrated the beginning of winter convection (17 November 2012), a time of particularly deep convection (23 January 2013), continuous freshening and cooling throughout the upper 800 m (25 February) and restratification in early spring (15 April). Regions with isopycnals outcropping to the surface corresponded to ice-free regions with active convection taking place: isopycnal 27.90 kg/m^3 outcropped between 28 and 32°E on November 17 (Figure 13c); isopycnal 27.95 kg/m^3 on January 23 (Figure 13d). On November 17, the AW core layer was warm and salty (>3 °C, >35.2 g/kg) and the 27.95 kg/m^3 isopycnal was depressed down to 600 m while active convective mixing took place down to 400 m. On January 23, when the A-TWAIN mooring WHOI-1 (point KT on Figure 13d) first registered deep MLD (>400 m deep), the model showed convection down to 600 m supporting the extreme MLDs observed *in-situ* (Pérez-Hernández et al., 2019). AW was considerably cooled and freshened through convective mixing in the ice-free areas (Figures 13c, 13d). Later, northerly winds imported sea-ice in the area (Figure 10d; Supporting Information S2), restratification took place and, below a thin cold and fresh layer, the water column remained with a small N^2, low temperature and salinity (below 2 °C and 35.15 g/kg) (Figure 13e). CT-SA diagrams corresponding to the sections in Figure 13 illustrated further the spectacular contraction in AW properties (cooling, freshening, densifying) through winter and the respective contributions from surface convection and from the troughs to low-N^2 waters (Figure 14).

Plumes of low-N^2 waters below the 27.95 isopycnal were often observed at depths throughout the year, for example in Figures 13c-f. As seen in section 3.3 and Figure 5, outflows of shelf-modified AW (SMAW) from troughs showed low-N^2 values. The source of the low-N^2 plumes were outflows from the following troughs: Kvitøya (KT), Franz-Victoria (FVT), and British-Channel troughs (BCT) (Figures 1, 13c-f). At the beginning of winter, the lighter low-N^2 waters from surface convection were clearly separated from the denser low-N^2 waters transported from trough outflows (Figure 14a), whereas later in winter there was a continuum in low-

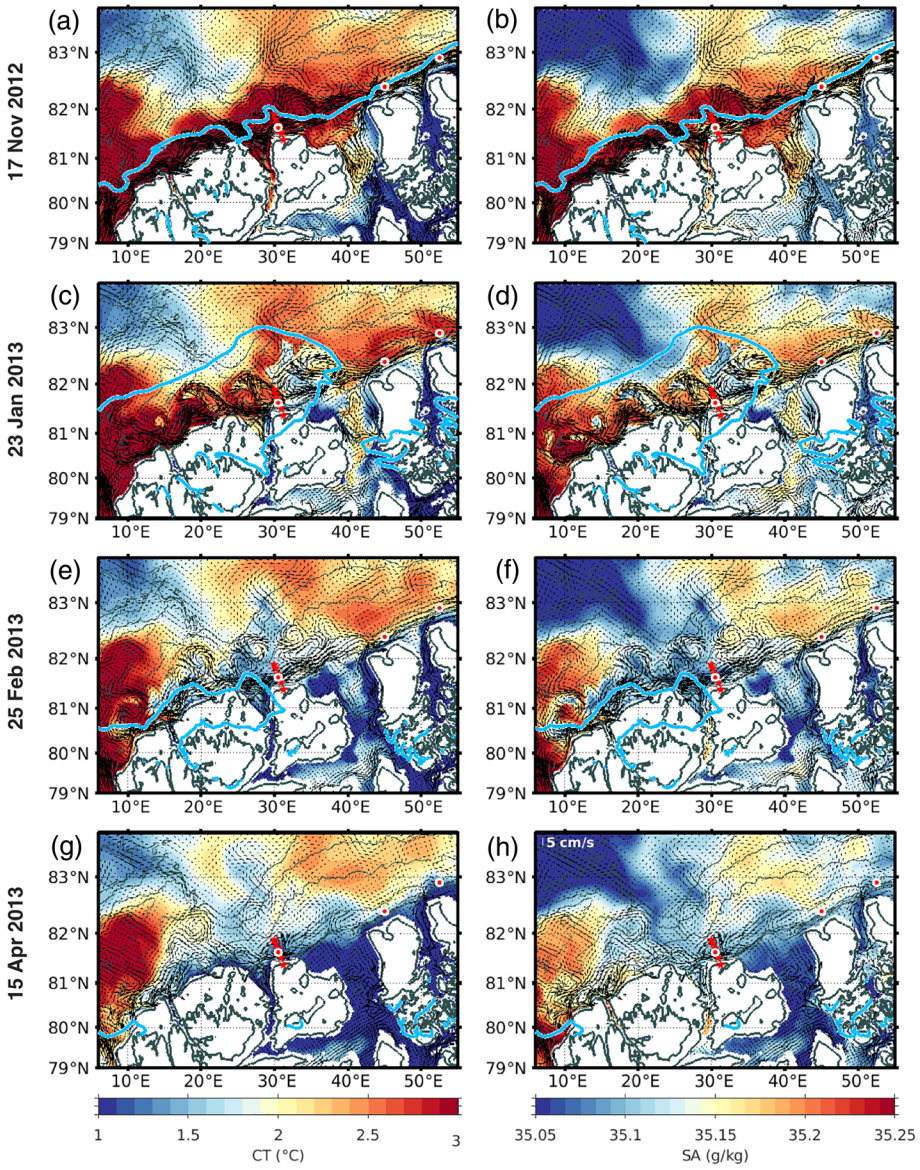

Figure 15. (a) Conservative temperature (CT, °C) and (b) absolute salinity (SA, g/kg) fields at 265 m on 17 November 2012. The thick blue contour is the sea-ice edge (40% ice cover) on that date. Arrows are current velocities at 265 m. red dots at 30°E are A-TWAIN moorings, red dots circled in white correspond to points KT, FVT and BCT in Figure 13. (c)-(d) same on the 23 January 2013, (e)-(f) on 25 February 2013 and (g)-(h) on 15 April 2013.

N^2 waters down to 28.0 σ-horizon (Figures 14b and c). The low-N^2 waters from the troughs likely resulted from convection in the Barents Sea (e.g. Pfirman et al., 1994; Steele et al., 1995). Therefore, both local and distant convection in the Barents Sea contributed to AW modification along the slope.

On April 15, an apparent disruption of the AW layer at 31°E (Figure 7d, and point KT in Figure 13f) was also observed on A-TWAIN moorings at the same date (Renner et al., 2018; see section 3.4. and Figure 7c). The corresponding CT-SA diagram (Figure 14d) featured an exceptionally dense ($\sigma > 28.02$ kg/m^3) low-N^2 pattern. This unique event in the period 2012/13 is examined below.

5. Aw Boundary Current Exchange With the Deep Nansen Basin and Barents Sea: Examples From Winter 2012/13

Along the continental slope, exchange with the deep Nansen Basin and the Barents Sea contributed to modify AW characteristics.

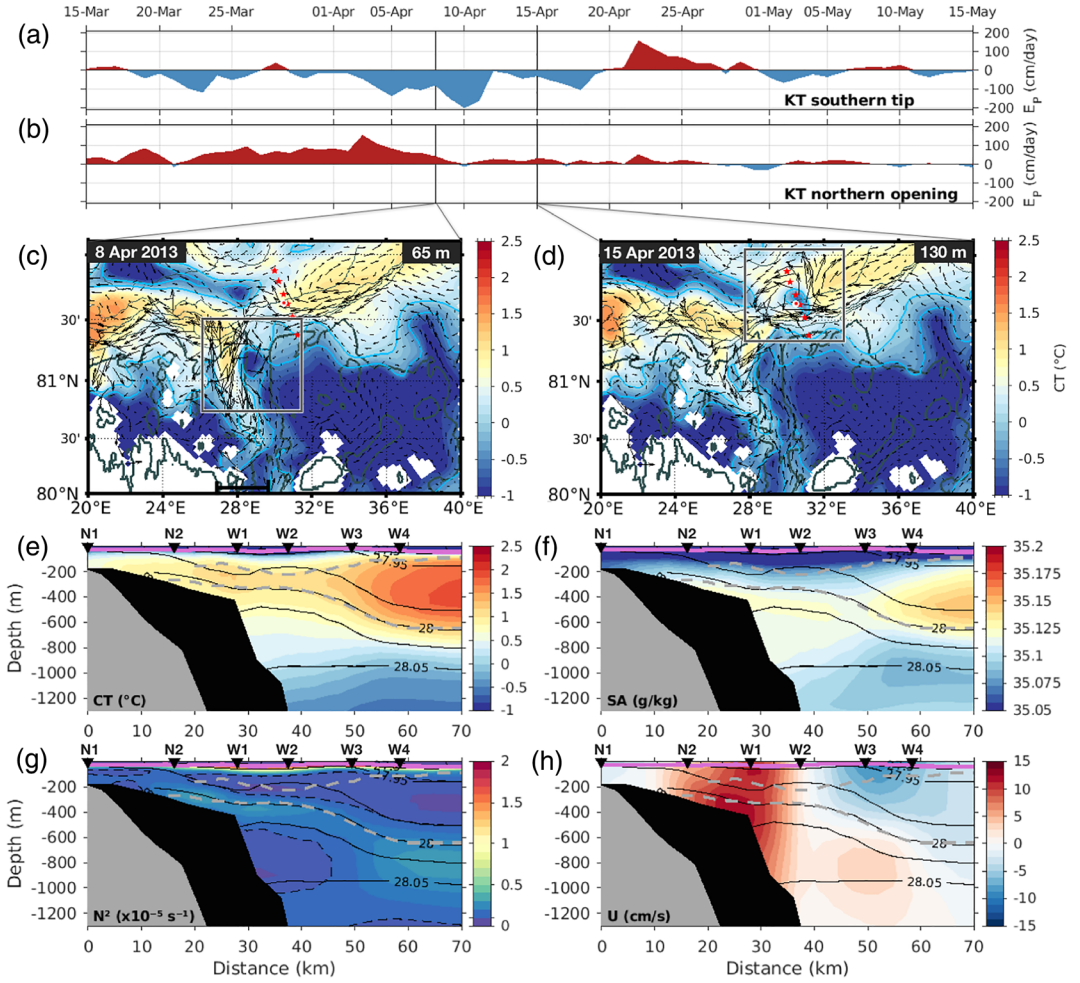

Figure 16. Time series of Ekman pumping (a) at the southern tip and (b) northern opening of Kvitøya trough (KT), between mid-march and mid-may 2013. Ekman pumping was computed from daily averaged wind stress components over 27–30°E,79.6–80°N, and 27–30°E,81.4–81.7°N south and north of KT respectively. Vertical lines are dates shown in (c), (d). Conservative temperature (CT, °C) field (c) at 65 m on 8 April 2013, when a cold-core cyclonic eddy formed within Kvitøya trough and (d) at 130 m on 15 April 2013 when the eddy was passing the A-TWAIN array. Arrows are the current velocity (cm/s) at that depth. Blue contours are isotherms −0.5 and 0 °C. red dots are A-TWAIN moorings, red dots correspond to point KT in Figure 13. Gray boxes indicate the location of the eddy. IBCAO bathymetry is in gray contours. (e) Conservative temperature (CT,°C), (f) absolute salinity (SA, g/kg), (g) brunt-Väisälä frequency (N^2, s^{-1}) and (h) cross-section velocity (U, cm/s) colocated along the A-TWAIN mooring array in the model fields on 15 April 2013 (to be compared with the mean conditions on Figures 6b-c). On (e)-(h), the MLD is the thick pink line. Isopycnals (black contours) are plotted from 27.9 to 28.05 kg/m^3 every 0.025 kg/m^3. Dashed black lines on (g) are contours such as $N^2 < 10^{-6}$ s^{-1}. Dashed gray lines are the AW layer boundaries. IBCAO bathymetry is in gray, model bathymetry in black.

5.1. Overview of the Circulation in the Core of the AW

To complement the along-slope sections shown in Figure 13, we produced mapped-snapshots of temperature, salinity, and horizontal velocity fields at 265 m (in the core of the AW layer) on the same dates (Figure 15). They illustrated the wealth of the mesoscale field along the slope, the flow in the troughs, and the cooling and freshening of AW.

The offshore area showed an interesting persistent large-scale pattern all winter round with colder and fresher modified AW from the interior intruding between warm and salty AW on the Yermak Plateau and an offshore less warm plume at 30°E (Figure 15). The energetic winter AW boundary current, with velocities often exceeding 15 cm/s, was unstable and developed an intense mesoscale field with meanders evolving into energetic eddy dipoles (Figures 15a, b). Eddies seemed to escape offshore along two preferred paths: a

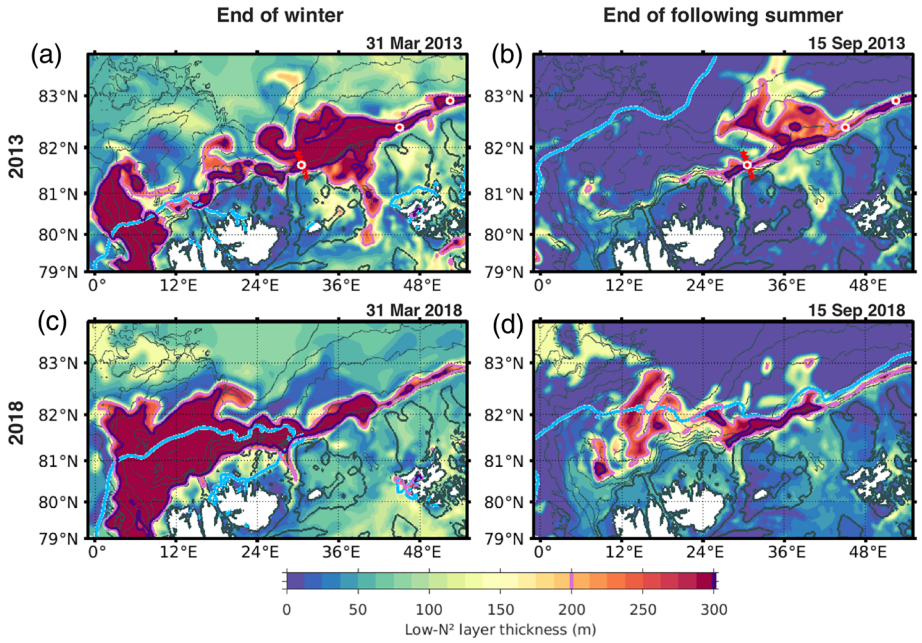

Figure 17. (a) Thickness of layers of low-N^2 ($< 10^{-6}$ s^{-1}) in the upper 800 m of the ocean, at the end of winter 2012–2013 on 31 march 2013. (b) Same at the end of the following summer, on 15 September 2013. Areas where low-N^2 layers exceeded 200 m (300 m) at that date are delineated in pink (purple) contours. The thick blue contour is the sea-ice edge (40% ice cover) at that date. Red stars at 30°E are A-TWAIN moorings, red dots correspond to points KT, FVT and BCT in Figure 13. (c)-(d) same for winter 2017–2018.

northward path at 30°E (Figures 15c to f) and a more northeastward path parallel to the continental slope east of 40°E (Figures 15c, d). In January and February some eddies trapped colder and fresher water from the slope and carried it offshore (Figures 15c-f). At the end of winter, the AW boundary current was significantly weaker (8 cm/s) with lower temperatures (CT < 2 °C) in agreement with the seasonal cycle (e.g., Beszczynska-Möller et al., 2012).

Trough outflows, which often showed velocities on the order of those of the boundary current, contributed to modifying AW on the slope. The model trough outflows, identified with low N^2 values, consisted of plumes of variable size: 100 to 400 m thick and 10 to 100 km wide (Figures 13c–13f, 16g). The water in the troughs continuously cooled and freshened throughout winter (at 265 m CT < 0.5 °C, SA < 35.05 g/kg at the end of winter in all troughs; Figure 15). Once sea-ice was back and local convection stopped, cooling and freshening of the boundary current continued because of trough outflows (Figures 15e, f). As a result, in April 2013 the AW boundary current was the coldest and freshest at the exit of the troughs (Figures 15g, h).

5.2. Disruption of the AW Layer on the 15 April 2013

We analyzed the conditions that led to the disruption of the AW layer observed on 15 April 2013 (Figures 7, 12f) that stood out in the A-TWAIN time series (Pérez-Hernández et al., 2019; Renner et al., 2018). Two simultaneous features from Kvitøya trough were concurrently involved: a cyclone in the upper 300 m and below, a low-N^2 plume with density in the range of intermediate water.

In early-April, wind stress curl conditions (very negative over Kvitøya trough and positive over the slope; Figures 16a, b) favored the outflow of a cyclonic fresh, cold-core, eddy (CT ~ -0.5 °C, SA ~ 35 g/kg, low-N^2, core radius of about 20 km) from the trough where it developed (i.e. April 7 snapshot in Figure 16c). The cold-core eddy crossed the mooring array location on April 15 (Figure 16d, core at an offshore distance of ~40 km in Figures 16e-h) and was observed in the upper 300 m at the same date in the mooring line (Renner et al., 2018). The modeled eddy tangential velocities reached 10 cm/s in the upper 70 m on April 15 at the mooring site (Figures 16d, h). The eddy was then advected offshore north-eastward while losing its temperature signature and its spinning motion and could be followed until May 15 when it reached

34°E, 82°N. Several such cold-core upper layer eddies can be identified in the A-TWAIN records (for example over 10 such eddies at NPI-2, Figure 7c).

In the model, the large uprising of isopycnals observed around mid-April (28.00 kg/m^3 σ-horizon rose from 600 to 300 m-depth between 29 and 31°E, Figure 13f) was associated with a homogeneous dense plume of water (CT ~ 0 °C, SA ~ 35.125 g/kg, σ > 28 kg/m^3, Figures 16e-h) cascading from Kvitøya trough. The low-N^2 plume settled within the upper-density range of Arctic Intermediate Water (AIW) in the depth range 500 to 1,000 m (Figures 16e-h) and was advected northeastward. The plume uplifted the upper part of intermediate waters (larger N^2 values between 300 and 500 m in Figure 16g). Comparisons to the mean conditions (Figures 6b, c) highlighted the extreme disruption of the AW layer over the slope.

These April 15 conditions are reminiscent of observations by Schauer et al. (1997) along the slope in the Western Nansen Basin. They described the two different types of northern Barents Sea water found on the slope in summer 1993: an upper patch intruding in the core of AW and a lower patch at about 500 m depth, resulting from a dense bottom water plume from troughs encroaching the intermediate waters. Schauer et al. (1997) suggested intermittent draining of cold dense water from the shelf through the troughs. Our hypothesis is that this extremely dense water (σ > 28.05 kg/m^3) was conditioned in the Barents Sea during winter and is seen outflowing from Kvitøya Trough into Nansen Basin following the appropriate wind conditions mentioned at the beginning of the section. Such an uplift of isopycnals was an exceptional event along the slope in winter 2012/13 and certainly influenced the mesoscale dynamics on the slope (Figure 16b). The remarkable concordance in the timing of this uplift in the observations and in the model suggested that the event was deterministically wind-driven (Figures 16a, b). However, an investigation of the dynamical processes at stake is beyond the scope of the present work.

6. Summary and Discussion

The evaluation of the Mercator Ocean operational physical system (PSY4), using nearly 1,500 independent temperature-salinity profiles and five years of mooring data (T, S, and currents) in the West-Spitsbergen Current, highlighted its performance in representing realistic Atlantic Water (AW) inflow and hydrographic properties, in spite of its inherent limitations.

Indeed, the model resolution is not fully eddy-resolving in the Western Nansen Basin (i.e. grid size of 4 km, and Rossby deformation radius of ~10 km; Crews et al., 2018), it lacks tides which are important on the Yermak Plateau (Koenig, Provost, Sennéchael, et al., 2017; Padman et al., 1992) and on the shelf (Renner et al., 2018), and its bathymetry could be improved (Figure A1).

Winter mixed layers observations are rather scarce in the Western Nansen Basin. The PSY4 system agreed with the few observations available in the area, such as the 2012/13 A-TWAIN mooring data over the continental slope (Pérez-Hernández et al., 2019) and IAOOS buoys during N-ICE 2015 (Koenig, Provost, Villacieros-Robineau, et al., 2017; Meyer et al., 2017). In particular, favorable comparisons with A-TWAIN mooring time series of deep winter mixed layers and changes in AW over winter led us to examine winter conditions in the WNB over the 2007–2020 period. The model helped to describe the interannual variations of winter mixed layers and documented several processes at stake in modifying AW beyond winter convection: shelf-slope exchange via troughs, lateral exchange through vigorous eddies, and occasional uplift of deep waters.

We identified winters during which extreme deep mixed layers developed in areas that used to be ice-covered, that one could call “Marginal Convection Zones”: 2017/18 over the northern part of Yermak Plateau and 2012/13 on the continental slope northeast of Svalbard. In contrast with the neighboring Whalers' Bay where deep winter mixed layers are recurrent, “Marginal Convection Zones” only occasionally undergo deep winter convection.

Winter surface convection dramatically altered AW properties over Yermak Plateau and Sofia Deep in winter 2017/18. Over the continental slope, trough outflows were an additional important process in further AW modification, as documented for winter 2012/13. Recently modified AW was identified through low-N^2 values (i.e. homogeneous layers). At the end of winter, the layers of low-N^2 were around 100 m-thick (vertical extent E ~ 100 m) in the Western Nansen Basin (which corresponded to the winter mixed layer) except in areas where deep convection occurred (Figures 17a, 17c). The thick (E > 300 m) low-N^2 layers were

laterally bordered with thin low-N^2 layers (E < 20 m) where active ice melt likely prevented the development of convection. The spatial distribution of thick low-N^2 AW layers (E > 300 m) were different at the end of the two extreme winters (Figures 17a, 17c). In March 2013, thick low-N^2 layers between 24 and 44°E extended from the slope offshore to the north of 82.5°N (Figure 17a). In contrast, in March 2018 they widely covered Yermak Plateau and Sofia Deep (as far as 82°N and from 4 to 18°E) and were reduced over the slope (Figure 17c). We followed the evolution of the thick homogeneous layers in time (Supporting Information S1 and S2). At the end of the following summer, they were eroded. The remaining thick low-N^2 layers were mostly found east of 30°E in September 2013 (Figure 17b) and in the Sofia Deep in September 2018 (Figure 17d). The volume of the low-N^2 waters significantly reduced over summer, suggesting that mixing was important. Whether the pathways followed by part of the modified AW, embedded in mesoscale features, in 2013 (towards the basin interior over the slope) and 2018 (in Sofia Deep towards the tip of Yermak Plateau) constitute persistent advection routes is being evaluated in another work.

The recurrent outflows from the troughs, continuing throughout summer, led to horizontally narrow strips of thick low-N^2 layers, observed along the slope at the end of summer in both years (Figures 17b and 17d). Observations have suggested outflows from troughs in the northwest Barents Sea (e.g. Matishov et al., 2009; Pfirman et al., 1994; Schauer et al., 1997). These remain poorly documented yet. As noted in Schauer et al. (1997) the dense winter-conditioned waters that drain from the shelf into the Nansen Basin as discrete local buoyancy-driven plumes from the troughs have regionally different temperature-salinity properties. These characteristics most likely vary seasonally and inter-annually (Lind & Ingvaldsen, 2012). Further work is needed to examine model performance in the Barents Sea and distinguish and quantify contributions from the different troughs.

Winter 2012/13 was exceptional with respect to winter mixed layer depths in the Western Nansen Basin and the northern Barents Sea and was only outclassed by winter 2017/18 over the northern Yermak Plateau and Sofia Deep (Figure 8e).

The 14 years of model fields highlighted the considerable interannual variations over the Marginal Convection Zones of the Yermak Plateau and continental slope, with diverse ice-atmosphere conditions and winter MLDs varying from tens (e.g. 2010/11, 2014/15 and 2019/20) to hundreds of meters (e.g. 2012/13 and 2017/18; Figure 9). Model fields tended to indicate that the absence of ice cover was a necessary condition for the onset of deep winter convection. They also suggested that imported ice and meltwater, pushed by favorable winds, resulted in a stronger surface stratification causing deep convection to end (Figure 10). However, these hypotheses need further examination and quantification, in particular considering the large wind and sea-ice variability in the area (Supporting Information S1 and S2).

The time series showed that conditions previously encountered in 2007–2011 in both areas with no open-ocean, 50 m-ocean temperatures below 0 °C and MLDs shallower than 100 m changed significantly around mid-2011. From then on, the ocean was occasionally ice-free, 50-m-ocean temperatures always above 0 °C and MLD and ocean-to-atmosphere heat fluxes exhibited large interannual variations (including the extreme winters reported in this study; Figure 9). In the northern YP and continental slope areas, the increased occurrences of these conditions previously only observed in the "Whalers' Bay" (a quasi-permanent polynya northwest of Svalbard; Onarheim et al., 2014) confirmed the evolution inferred by Polyakov et al. (2017) in the eastern Eurasian Basin over 2003–2015, with sea-ice decline and shoaling of the AW layer allowing deeper winter ventilation. The causes for these changes remain unclear, as a wide variety of feedbacks and pre-conditioning processes come into play (Cullather et al., 2016; Ivanov et al., 2016; Skagseth et al., 2020) and drive the upper-ocean conditions both locally and upstream.

Winter convection is a key process in the formation of the lower halocline waters of the Arctic Ocean (e.g. Pfirman et al., 1994; Rudels et al., 2004; Steele et al., 1995). Recently, using the NO geochemical tracer, Bertosio et al. (2020) showed that the base of the lower halocline which used to be associated with SA ~ 34.46 g/kg (34.3 psu) was now found on a saltier level of 34.9 g/kg in the Eurasian Basin. This denser level, corresponding to isopycnal 27.85 kg/m^3, is in agreement with the deeper winter mixed layers reproduced by PSY4 in Nansen Basin: during the extreme winters 2012/13 and 2018/17, deep convection reached the 27.95 kg/m^3 isopycnal. Exploratory 2-D Lagrangian trajectories using PSY4 velocities suggested advective pathways from the continental slope to the center of the Nansen Basin in the 30–150 m layer (i.e. halocline waters), with time scales larger than 3 years (Bertosio et al., 2020). Full 3-D Lagrangian

tracking would extend this precursory work and improve our understanding of the fate of the convected water and its impact on the halocline water properties.

In this region where observations require considerable efforts and resources, the PSY4 physical system proved to be a good tool to assess AW modification through winter convection. PSY4 showed the additionally important role of shelf-to-basin exchange across the Arctic troughs of the Western Nansen Basin. Mixed layer depths exhibited large interannual variations, explaining the diverse *in-situ* observations. As the transition towards a seasonally ice-free Arctic Ocean continues, more years of extreme deep mixed layers and enhanced convection can be expected.

Appendix A: Evaluation of PSY4 bathymetry in the Western Nansen Basin

The International Bathymetric Chart of the Arctic Ocean (IBCAO) is a regional, Arctic Ocean-dedicated bathymetry (Figure A1a). The latest version 3.0 used in this study has a 500 m grid spacing and gathers a significant number of new bathymetric data from diverse sources (Jakobsson et al., 2012).

In contrast, the bathymetry used in the PSY4 is a combination of the ETOPO1 bathymetry (Earth Topography and bathymetry; Amante & Eakins, 2009) for deeper oceans and the GEBCO8 bathymetry (General Bathymetric Chart of the Oceans; Becker et al., 2009) on the coast and continental shelf (as described in section 2.1). ETOPO1 is a 1 arc-minute global relief model integrating both land topography and ocean bathymetry. GEBCO8 is a global bathymetry product with 30 arc-second grid resolution. The resulting composite bathymetry is interpolated on the PSY4 native grid (Figure A1b).

We interpolated IBCAO to the PSY4 grid to allow the evaluation of the model bathymetry in the Western Nansen Basin. Comparisons between the PSY4 and IBCAO bathymetries highlighted significant discrepancies on the continental slope north-east of Svalbard. Indeed, the mouth of Kvitøya Trough (KT) was too wide in PSY4, with a western flank reaching as far as 25°E instead of 28°E in IBCAO. As a consequence, the shelf west of KT was up to 400 m too deep (blue signal in Figure A1c). Additionally, the abrupt northward bifurcation of isobaths 2000 to 3,000 m, found at 32–34°E in IBCAO, was smoother and began further west in the PSY4 bathymetry (from 30°E). The PSY4 slope (500 to 1,000 m isobaths) was also about 15–20 km more

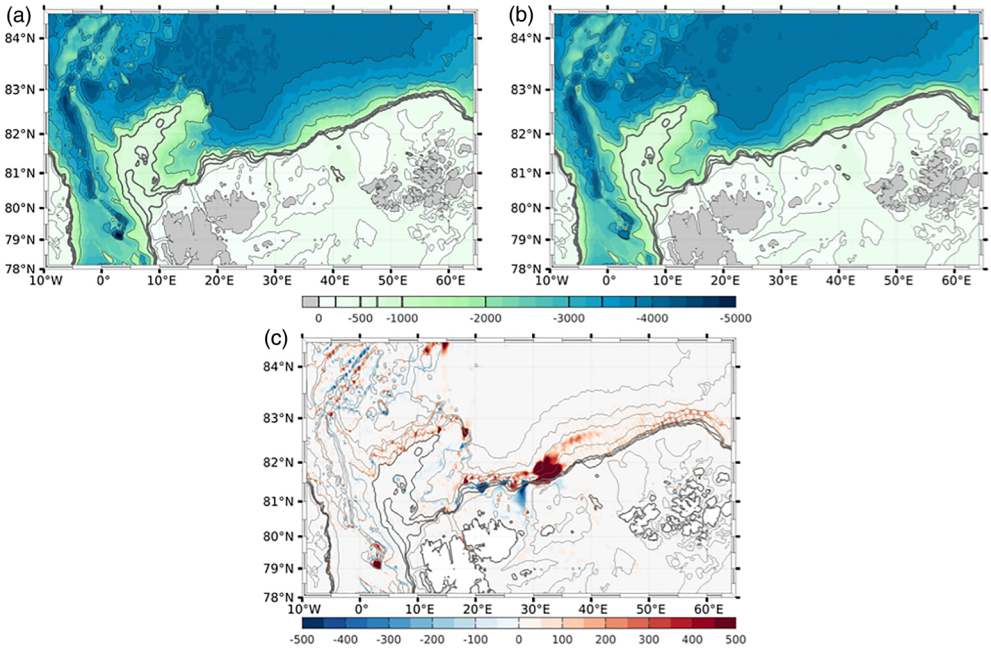

Figure A1. Comparison of (a) IBCAO bathymetry and (b) PSY4 bathymetry. Isobaths 0, 200, 500, 1,000, 2000, 3,000, 3,400, 3,800 m are plotted and indicated in the color bar. (c) Differences between the two bathymetries (ETOPO-IBCAO) blue implies that the model bathymetry (ETOPO) is too deep, red that it is too shallow. Isobaths plotted in background are from IBCAO for sake of reference.

north at 30–35°E. Hence, the model bathymetry stood out with shallower bathymetry in this area (red signal in Figure A1c). Elsewhere in the basin, the comparison was very satisfactory, with local differences larger than 50 m only in sharp slope areas, and never exceeding 50 m otherwise.

Acknowledgments

We are grateful to all the people that contributed to gather the observations used for model validation in this study. The data sources and corresponding web sites are compiled in Table 1. The model outputs are available at Copernicus Marine Environment Monitoring Service (CMEMS; http://marine.copernicus.eu/). Discussions with Léa Poli are greatly acknowledged. Marylou Athanase was supported through the Pan-Arctic Options Belmont Forum project (ANR-14-AORS-003-01). Cecilia Bertosio was supported through IAOOS grant A18JROI002 at Sorbonne University. M. Dolores Pérez-Hernández is supported through the "Programa Postdoctoral de la Universidad de Las Palmas de Gran Canaria". We are deeply grateful to editor Laurence Padman and three anonymous reviewers for their thorough comments which helped us improve the manuscript.

References

Aagaard, K., Foldvik, A., & Hillman, S. R. (1987). The West Spitsbergen current: Disposition and water mass transformation. *Journal of Geophysical Research*, *92*(C4), 3778–3784. https://doi.org/10.1029/JC092iC04p03778

Alkire, M. B., Polyakov, I., Rember, R., Ashik, I. M., Ivanov, V., & Pnyushkov, A. V. (2017). Lower halocline water formation and modification, a comparison of physical and geochemical methods. *Ocean Science*, *13*(6), 983–995. https://doi.org/10.5194/os-13-983-2017

Amante, C. & Eakins, B. W. (2009): ETOPO1 1 arc-minute global relief model: Procedures, data sources and analysis, NOAA Technical Memorandum NESDIS NGDC-24, 25 pp.

Appen, W. J. V., Schauer, U., Hattermann, T., & Beszczynska-Möller, A. (2016). Seasonal cycle of mesoscale instability of the West Spitsbergen current. *Journal of Physical Oceanography*, *46*(4), 1231–1254. https://doi.org/10.1175/JPO-D-15-0184.1

Athanase, M., Sennéchael, N., Garric, G., Koenig, Z., Boles, E., & Provost, C. (2019). New hydrographic measurements of the upper Arctic Western Eurasian Basin in 2017 reveal fresher mixed layer and shallower warm layer than 2005–2012 climatology. *Journal of Geophysical Research: Oceans*, *124*, 1091–1114. https://doi.org/10.1029/2018JC014701

Becker, J. J., Sandwell, D. T., Smith, W. H. F., Braud, J., Binder, B., & Depner, J. (2009). Global bathymetry and elevation data at 30 arc seconds resolution: SRTM30PLUS. *Marine Geodesy*, *32*(4), 355–371. https://doi.org/10.1080/01490410903297766

Behrendt, A., Sumata, H., Rabe, B., & Schauer, U. (2018). UDASH - unified data base for arctic and subarctic hydrography. *Earth System Science Data*, *10*(2), 1119–1138. https://doi.org/10.5194/essd-10-1119-2018

Bertosio, C., Provost, C., Sennéchael, N., Artana, C., Athanase, M., Boles, E., et al. (2020). The Western Eurasian Basin Halocline in 2017: Insights From Autonomous NO Measurements and the Mercator Physical System. *Journal of Geophysical Research: Oceans*, *125*. https://doi.org/10.1029/2020jc016204

Beszczynska-Möller, A., Fahrbach, E., Schauer, U., & Hansen, E. (2012). Variability in Atlantic water temperature and transport at the entrance to the Arctic Ocean, 1997–2010. *ICES Journal of Marine Science*, *69*(5), 852–863. https://doi.org/10.1093/icesjms/fss056

Boyd, T. J., & D'Asaro, E. A. (1994). Cooling of the West Spitsbergen current: Wintertime observations west of Svalbard. *Journal of Geophysical Research*, *99*(C11), 22,597–22,618. https://doi.org/10.1029/94JC01824

Boyer Montégut, C., Madec, G., Fischer, A., Lazar, A., & Iudicone, D. (2004). Mixed layer depth over the global ocean: An examination of profile data and a profile-based climatology. *Journal of Geophysical Research*, *109*, C12003. https://doi.org/10.1029/2004JC002378

Cokelet, E. D., Tervalon, N., & Bellingham, J. G. (2008). Hydrography of the West Spitsbergen current, Svalbard branch: Autumn 2001. *Journal of Geophysical Research*, *113*, C01006. https://doi.org/10.1029/2007JC004150

Crews, L., Sundfjord, A., Albretsen, J., & Hattermann, T. (2018). Mesoscale eddy activity and transport in the Atlantic water inflow region north of Svalbard. *Journal of Geophysical Research: Oceans*, *123*, 201–215. https://doi.org/10.1002/2017JC013198

Crews, L., Sundfjord, A., & Hattermann, T. (2019). How the Yermak pass branch regulates Atlantic water inflow to the Arctic Ocean. *Journal of Geophysical Research: Oceans*, *124*, 267–280. https://doi.org/10.1029/2018JC014476

Cullather, R. I., Lim, Y. K., Boisvert, L. N., Brucker, L., Lee, J. N., & Nowicki, S. M. (2016). Analysis of the warmest Arctic winter, 2015–2016. *Geophysical Research Letters*, *43*, 10,808–10,816. https://doi.org/10.1002/2016GL071228

Good, S. A., Martin, M. J., & Rayner, N. A. (2013). EN4: Quality controlled ocean temperature and salinity profiles and monthly objective analyses with uncertainty estimates. *Journal of Geophysical Research: Oceans*, *118*, 6704–6716. https://doi.org/10.1002/2013JC009067

Goszczko, I., Ingvaldsen, R. B., & Onarheim, I. H. (2018). Wind-driven cross-shelf exchange—West Spitsbergen current as a source of heat and salt for the adjacent shelf in Arctic winters. *Journal of Geophysical Research: Oceans*, *123*, 2668–2696. https://doi.org/10.1002/2017JC013553

Hattermann, T., Isachsen, P. E., von Appen, W. J., Albretsen, J., & Sundfjord, A. (2016). Eddy-driven recirculation of Atlantic water in Fram Strait. *Geophysical Research Letters*, *43*, 3406–3414. https://doi.org/10.1002/2016GL068323

Hu, X., Myers, P. G., & Lu, Y. (2019). Pacific water pathway in the Arctic Ocean and Beaufort gyre in two simulations with different horizontal resolutions. *Journal of Geophysical Research: Oceans*, *124*, 6414–6432. https://doi.org/10.1029/2019JC015111

Ivanov, V., Alexeev, V., Koldunov, N. V., Repina, I., Sandø, A. B., Smedsrud, L. H., & Smirnov, A. (2016). Arctic Ocean heat impact on regional ice decay: A suggested positive feedback. *Journal of Physical Oceanography*, *46*(5), 1437–1456. https://doi.org/10.1175/JPO-D-15-0144.1

Ivanov, V., Smirnov, A., Alexeev, V., Koldunov, N. V., Repina, I., & Semenov, V. (2018). Contribution of convection-induced heat flux to winter ice decay in the Western Nansen Basin. *Journal of Geophysical Research: Oceans*, *123*, 6581–6597. https://doi.org/10.1029/2018JC013995

Jakobsson, M., Mayer, L., Coakley, B., Dowdeswell, J. A., Forbes, S., Fridman, B., et al. (2012). The international bathymetric chart of the Arctic Ocean (IBCAO) version 3.0. *Geophysical Research Letters*, *39*, L12609. https://doi.org/10.1029/2012GL052219

Koenig, Z., Meyer, A., Provost, C., Sennéchael, N., Sundfjord, A., Beguery, L., et al. (2018). Cooling and freshening of the West Spitsbergen current by shelf-origin cold Core lenses. *Journal of Geophysical Research: Oceans*, *123*, 8299–8312. https://doi.org/10.1029/2018JC014463

Koenig, Z., Provost, C., Sennéchael, N., Garric, G., & Gascard, J.-C. (2017). The Yermak pass branch: A major pathway for the Atlantic water north of Svalbard? *Journal of Geophysical Research: Oceans*, *122*, 9332–9349. https://doi.org/10.1002/2017JC013271

Koenig, Z., Provost, C., Villacieros-Robineau, N., Sennéchael, N., Meyer, A., Lellouche, J.-M., & Garric, G. (2017). Atlantic waters inflow north of Svalbard: Insights from IAOOS observations and Mercator Ocean global operational system during N-ICE2015. *Journal of Geophysical Research: Oceans*, *122*, 1254–1273. https://doi.org/10.1002/2016JC012424

Lellouche, J. M., Greiner, E., le Galloudec, O., Garric, G., Regnier, C., Drevillon, M., et al. (2018). Recent updates to the Copernicus marine service global ocean monitoring and forecasting real-time 1/ 12° high-resolution system. *Ocean Science*, *14*(5), 1093–1126. https://doi.org/10.5194/os-14-1093-2018

Lind, S., & Ingvaldsen, R. B. (2012). Variability and impacts of Atlantic water entering the Barents Sea from the north. *Deep Sea Research Part I: Oceanographic Research Papers*, *62*, 70–88. https://doi.org/10.1016/j.dsr.2011.12.007

Matishov, G. G., Matishov, D. G., & Moiseev, D. V. (2009). Inflow of Atlantic-origin waters to the Barents Sea along glacial troughs. *Oceanologica*, *51*(3), 321–340. https://doi.org/10.5697/oc.51-3.321

Meyer, A., Sundfjord, A., Fer, I., Provost, C., Villacieros Robineau, N., Koenig, Z., et al. (2017). Winter to summer oceanographic observations in the Arctic Ocean north of Svalbard. *Journal of Geophysical Research: Oceans*, *122*, 6218–6237. https://doi.org/10.1002/2016JC012391

Nilsen, F., Skogseth, R., Vaardal-Lunde, J., & Inall, M. (2016). A simple shelf circulation model: Intrusion of Atlantic water on the West Spitsbergen shelf. *Journal of Physical Oceanography*, *46*(4), 1209–1230. https://doi.org/10.1175/JPO-D-15-0058.1

Onarheim, I. H., Smedsrud, L. H., Ingvaldsen, R. B., & Nilsen, F. (2014). Loss of sea ice during winter north of Svalbard. *Tellus A: Dynamic Meteorology and Oceanography*, *66*(1), 23933. https://doi.org/10.3402/tellusa.v66.23933

Padman, L., Plueddemann, A., Muench, R., & Pinkel, R. (1992). Diurnal Tides Near the Yermak Plateau. *Journal of Geophysical Research*, *97*, 12,639–12,652. https://doi.org/10.1029/92JC01097

Peralta-Ferriz, C., & Woodgate, R. A. (2015). Seasonal and interannual variability of pan-Arctic surface mixed layer properties from 1979 to 2012 from hydrographic data, and the dominance of stratification for multiyear mixed layer depth shoaling. *Progress in Oceanography*, *134*, 19–53. https://doi.org/10.1016/j.pocean.2014.12.005

Pérez-Hernández, M. D., Pickart, R. S., Pavlov, V., Våge, K., Ingvaldsen, R., Sundfjord, A., et al. (2017). The Atlantic water boundary current north of Svalbard in late summer. *Journal of Geophysical Research: Oceans*, *124*, 1699–1716. https://doi.org/10.1029/2018JC014299

Pérez-Hernández, M. D., Pickart, R. S., Torres, D. J., Bahr, F., Sundfjord, A., Ingvaldsen, R., et al. (2019). Structure, transport, and seasonality of the Atlantic water boundary current north of Svalbard: Results from a yearlong mooring Array. *Journal of Geophysical Research: Oceans*, *124*, 1679–1698. https://doi.org/10.1029/2018JC014759

Pfirman, S. L., Bauch, D., & Gammelsrød, T. (1994). The Northern Barents Sea: Water Mass Distribution and Modification. In O. M. Johannesen, et al. (Eds.), *The Polar Oceans and Their Role in Shaping the Global Environment*, *Geophysical Monograph Series* (Vol. 85, pp. 77–94). Washington, DC: AGU. https://doi.org/10.1029/GM085p0077

Polyakov, I. V., Pnyushkov, A. V., Alkire, M. B., Ashik, I. M., Baumann, T. M., Carmack, E. C., et al. (2017). Greater role for Atlantic inflows on sea-ice loss in the Eurasian Basin of the Arctic Ocean. *Science*, *356*(6335), 285–291. https://doi.org/10.1126/science.aai8204

Renner, A. H. H., Sundfjord, A., Janout, M. A., Ingvaldsen, R., Beszczynska-Möller, A., Pickart, R., & Pérez-Hernández, M. (2018). Variability and redistribution of heat in the Atlantic water boundary current north of Svalbard. *Journal of Geophysical Research: Oceans*, *123*, 6373–6391. https://doi.org/10.1029/2018JC013814

Rudels, B., Jones, E. P., Schauer, U., & Eriksson, P. (2004). Arctic sources of the Arctic Ocean surface and halocline waters. *Polar Research*, *23*(2), 181–208. https://doi.org/10.1111/j.1751-8369.2004.tb00007.x

Rudels, B., Korhonen, M., Schauer, U., Pisarev, S., Rabe, B., & Wisotzki, A. (2015). Circulation and transformation of Atlantic water in the Eurasian Basin and the contribution of the Fram Strait inflow branch to the Arctic Ocean heat budget. *Progress in Oceanography*, *132*, 128–152. https://doi.org/10.1016/j.pocean.2014.04.003

Schauer, U., Fahrbach, E., Osterhus, S., & Rohardt, G. (2004). Arctic warming through the Fram Strait: Oceanic heat transport from 3 years of measurements. *Journal of Geophysical Research*, *109*, C06026. https://doi.org/10.1029/2003JC001823

Schauer, U., Muench, R. D., Rudels, B., & Timokhov, L. (1997). Impact of eastern Arctic shelf waters on the Nansen Basin intermediate layers. *Journal of Geophysical Research*, *102*(C2), 3371–3382. https://doi.org/10.1029/96JC03366

Skagseth, O., Eldevik, T., Arthun, M., Asbjornsen, H., Lien, V. S., & Smedsrud, L. H. (2020). Reduced efficiency of the Barents Sea cooling machine. *Nature Climate Change*, *10*(7), 661–666. https://doi.org/10.1038/s41558-020-0772-6

Steele, M., Morison, J., & Curtin, T. B. (1995). Halocline water formation in the Barents Sea. *Journal of Geophysical Research*, *100*(C1), 881–894. https://doi.org/10.1029/94JC02310

Våge, K., Pickart, R. S., Pavlov, V., Lin, P., Torres, D. J., Ingvaldsen, R., et al. (2016). The Atlantic water boundary current in the Nansen Basin: Transport and mechanisms of lateral exchange. *Journal of Geophysical Research: Oceans*, *121*, 6946–6960. https://doi.org/10.1002/2016JC011715

Wekerle, C., Wang, Q., von Appen, W. J., Danilov, S., Schourup-Kristensen, V., & Jung, T. (2017). Eddy-resolving simulation of the Atlantic water circulation in the Fram Strait with focus on the seasonal cycle. *Journal of Geophysical Research: Oceans*, *122*, 8385–8405. https://doi.org/10.1002/2017JC012974

CHAPTER 4

Circulation and pathways of Atlantic Water in the Western Nansen Basin

Contents

4.1. Introduction

Some studies using in-situ measurements (from moorings, cruise campaigns and autonomous platforms) have documented the branching of the Atlantic Water inflow between the Svalbard Branch, Yermak Branch and Yermak Pass Branch over the southern Yermak Plateau (Koenig et al., 2017b, Menze et al., 2019). However, Atlantic Water pathways remain unclear over the northern Yermak Plateau and downstream of the Plateau. In particular, large uncertainties persist on how the branches eventually merge again and contribute to the AW boundary current on the continental slope.

We take advantage of 12 years (2008-2020) of available Mercator system fields to investigate AW volume transport and circulation in the Western Nansen Basin (WNB). In particular, we examine and interannual variations in AW volume transport and the evolution of the circulation in the WNB: indeed, Polyakov et al. (2020) documented the intensification of near-surface currents in the eastern Eurasian Basin over 2004-2018, as a result of the increased winds-ocean coupling associated with the declining sea-ice cover. The WNB could have undergone similar changes in the recent years.

The following section is constituted of a paper that has just been accepted for publication in Journal of Geophysical Research: Oceans, and was reformatted for sake of readability.

4.2. Changes in Atlantic Water circulation patterns and volume transports North of Svalbard over the last 12 years (2008-2020)

Changes in Atlantic Water circulation patterns and volume transports North of Svalbard over the last 12 years (2008-2020)

Marylou Athanase[1], Christine Provost[1], Camila Artana[2], M. Dolores Pérez-Hernández[3], Nathalie Sennéchael[1], Cécilia Bertosio[1], Gilles Garric[2], Jean-Michel Lellouche[2] and Pierre Prandi[4]

[1] : Laboratoire LOCEAN-IPSL, Sorbonne Université (UPMC, Univ. Paris 6), CNRS, IRD, MNHN, Paris, France.

[2] : MERCATOR-OCEAN, Parc Technologique du Canal, 8-10 rue Hermès, Ramonville Saint Agne, France.

[3] : Unidad de Océano y Clima, Instituto de Oceanografía y Cambio Global, IOCAG, Universidad de Las Palmas de Gran Canaria, ULPGC-CSIC, Spain.

[4] : CLS, 11, rue Hermès, Parc Technologique du Canal, 31520 Ramonville Saint-Agne, France

Abstract

Atlantic Water (AW) enters the Arctic through Fram Strait as the West Spitsbergen Current (WSC). When reaching the south of Yermak Plateau, the WSC splits into the Svalbard, Yermak Pass and Yermak Branches. Downstream of Yermak Plateau, AW pathways remain unclear and uncertainties persist on how AW branches eventually merge and contribute to the boundary current along the continental slope. We took advantage of the good performance of the 1/12° Mercator Ocean model in the Western Nansen Basin (WNB) to examine the AW circulation and volume transports in the area. The model showed that the circulation changed in 2008-2020. The Yermak Branch strengthened over the northern Yermak Plateau, feeding the Return Yermak Branch along the eastern flank of the Plateau. Coincidently, AW recirculations towards Fram Strait shifted further north. Downstream of the Yermak Plateau, an offshore current developed above the 3800 m isobath, fed by waters from the Yermak Plateau tip. East of 18°E, enhanced mesoscale activity from the boundary current injected additional AW basin-ward, further contributing to the offshore circulation. A recurrent anticyclonic circulation in Sofia Deep developed, which also occasionally fed the western part of the offshore flow. West of Yermak Plateau, the Transpolar Drift likely shifted westward while AW recirculations progressed further north. The intensification of the circulation coincided with an overall warming in the upper WNB (0-1000 m), consistent with the progression of AW. This regional description of the changing circulation provides a background for the interpretation of upcoming observations.

1. Introduction

The Atlantic Water (AW), which flows along the west slope of Svalbard with the West Spitsbergen Current (WSC, red arrows on Figure 1) in Fram Strait, constitutes the largest source of heat and salt to the Arctic Ocean. The AW inflow varies seasonally, being stronger and warmer in winter than in summer (Ivanov et al., 2009; Beszczynska-Moller et al., 2012). A fraction of the AW carried by the WSC recirculates towards Fram Strait south of 81°N, maily through eddies, and does not enter the Arctic Ocean (e.g. Hatterman et al., 2016). North of Svalbard, the WSC reaches the Yermak Plateau, and splits into three branches: the shallow Svalbard Branch (SB) circulating eastward, along the 400–500 m isobaths of the Svalbard continental slope (Muench et al., 1992; Cokelet et al., 2008; Sirevaag et al., 2011); the deeper Yermak Branch (YB), following the 1500 m isobath along the western slope of Yermak Plateau (Manley et al., 1992; Manley, 1995); and the Yermak Pass Branch (YPB), flowing across the Yermak Plateau along the 700–800 m isobaths and constituting the major route for AW in winter (Figure 1; Koenig et al., 2017b; Menze et al., 2019; Crews et al., 2019). Water pathways, their variations, and how they eventually join to form the AW boundary current (AWBC) remain unclear in the area because of the lack of in-situ measurements (Koenig et al., 2017a; Meyer et al. 2017; Menze et al., 2019).

Along its paths, the AW is cooled and freshened through ice-melt, heat loss to the atmosphere and mixing with shelf waters (Boyd and D'Asaro, 1994; Onarheim et al., 2014; Rudels et al., 2015; Renner et al., 2018; Fer et al., 2020). In the Western Nansen Basin (WNB) in particular, deep winter mixed layers reaching 500 m (Ivanov et al., 2018; Pérez-Hernández et al., 2019), exchanges with fjords West of Svalbard (Koenig et al., 2018) and troughs outflows from the Barents Sea (Schauer et al., 1997; Athanase et al., 2020) contribute to alter AW properties. The rather unstable AWBC has been observed to shed Atlantic Water eddies, further contributing to the erosion of AW properties over the slope (Våge et al., 2016; Pérez-Hernández et al., 2017; Athanase et al., 2019).

Several studies pointed out to the development of a more energetic ocean state under a declining sea-ice cover (Polyakov et al., 2017, 2020b; Timmermans and Marshall, 2020). Polyakov et al. (2020b) documented an intensification of current velocities in the upper 50 m of the eastern Eurasian Basin between 2004 and 2018 (by about 20%),

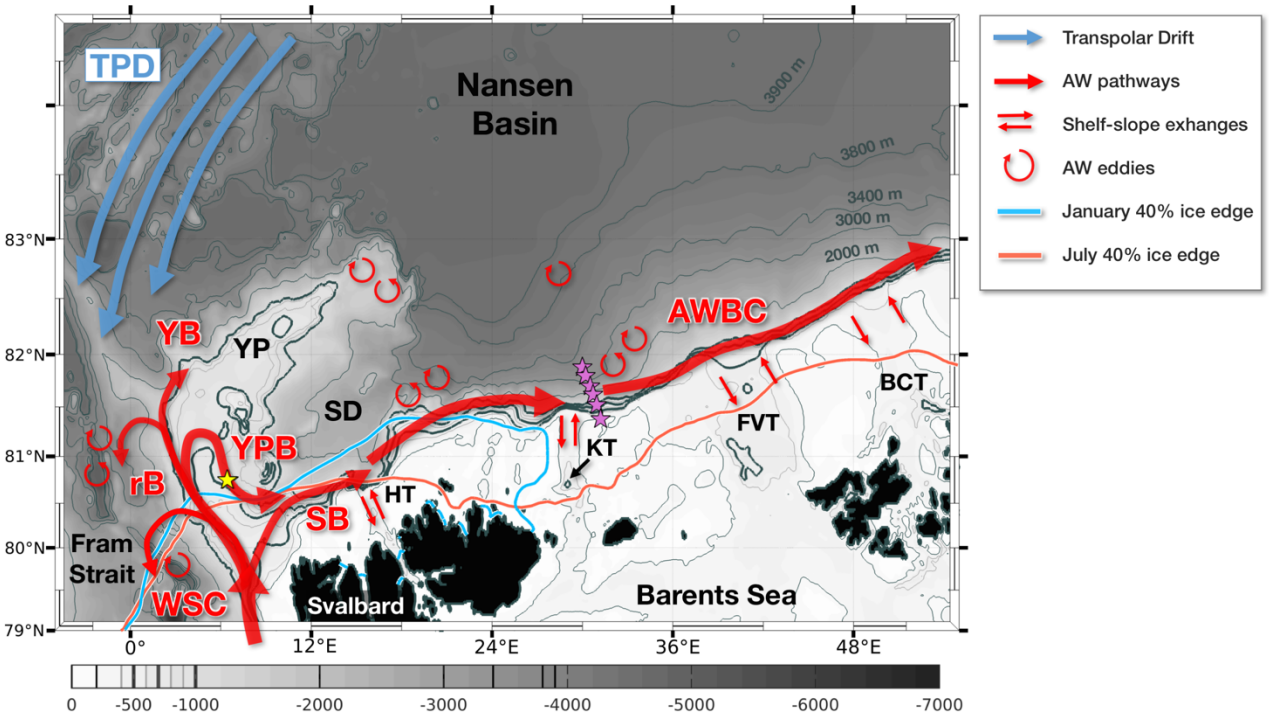

Figure 1: Schematic of the upper circulation in the Western Nansen Basin. IBCAO bathymetry is in greyscale. Red arrows correspond to the mean AW circulation in PSY4 over 2008-2010. Blue arrows represent the near-surface Transpolar Drift (TPD). Orange and blue contours are respectively the mean July and January ice edge (40% ice concentration) from PSY4 over 2008-2020. WSC: West Spitsbergen Current; SB: Svalbard Branch; YPB: Yermak Pass Branch; YB: Yermak Branch; AWBC: AW Boundary Current; rB: recirculation Branches; SD: Sofia Deep; YP: Yermak Plateau; HT, KT, FVT and BCT: Hinlopen, Kvitøya, Franz-Victoria and British Chanel Troughs. Pink stars indicate the A-TWAIN moorings, the yellow star a recent mooring in the YPB.

associated with an enhanced coupling between winds and the increasingly ice-free ocean. Recent observations north of Svalbard suggested previously unnoticed circulation patterns (Kolås et al., 2020). As observations require substantial resources and efforts and remain scarce in the Arctic, models can be useful to investigate possible changes in circulation and currents.

The 1/12° Mercator Ocean operational physical system, called PSY4 hereafter, has shown some skills in reproducing the hydrography, mesoscale structures and seasonal signals in the upper Western Eurasian Basin (Koenig et al., 2017a, 2017b; Athanase et al., 2019 and 2020; Bertosio et al., 2020). PSY4 model fields covering 14 years (2007-2020) documented interannual variations of deep winter mixed layers in the WNB, and several processes at stake in modifying AW properties (Athanase et al., 2020). A major change was observed in 2011, with the emergence of new "Marginal Convection Zones"

(northern Yermak Plateau, Sofia Deep and continental slope) exhibiting from then on, occasional ice-free conditions and intense winter convection events.

The objective here is to use the PSY4 system to examine the circulation of Atlantic Water in the Western Nansen Basin over 2007-2020 in this context of rapid Arctic changes. We examine and quantify the evolution of AW characteristics and pathways across the Yermak Plateau, on the continental slope and its vicinity, on seasonal and interannual time scales. This study is structured as follows. Section 2 introduces the Mercator Ocean operational system and reminds the model strengths and limitations. Further model evaluation includes comparisons with new unpublished data. Section 3 revisits the mean and seasonal Atlantic Water circulation and volume transports in the WNB, while section 4 focuses on interannual variations over 2008-2020. Section 5 examines the 12-year trends in water properties and circulation in the upper 1000 m of the WNB. Results are summarized and discussed in section 6.

2. The PSY4 system: performance and limitations

2.1. The Mercator Ocean operational system (PSY4)

In the frame of Copernicus Marine Environment Monitoring Service (CMEMS; http://marine.copernicus.eu/) Mercator Ocean delivers the high resolution 1/12° global operational PSY4 system since October 2006 (Lellouche et al., 2018). Forcings and data assimilation in the Arctic region are summarized in Athanase et al. (2020). The model component is based on the NEMO ocean model, with a 1/12° ORCA grid type (i.e. daily outputs with horizontal resolution of 4 km in the WNB; Hu et al., 2019). The water column is composed of 50 vertical levels, with typically 1 m resolution at the surface decreasing to 450 m at the bottom and 22 levels within the upper 100 m. When oceans are ice-covered, only sea ice concentration is assimilated. This is in stark contrast with the open ocean regions, where PSY4 assimilates along-track satellite altimetry sea level anomalies, sea surface temperature and *in-situ* vertical profiles of temperature and salinity. The PSY4 system starts in October 2006 from a “cold” start (initial currents are null) using initial climatological conditions from EN4.2.1 hydrographic temperature and salinity data (Good et al., 2013).

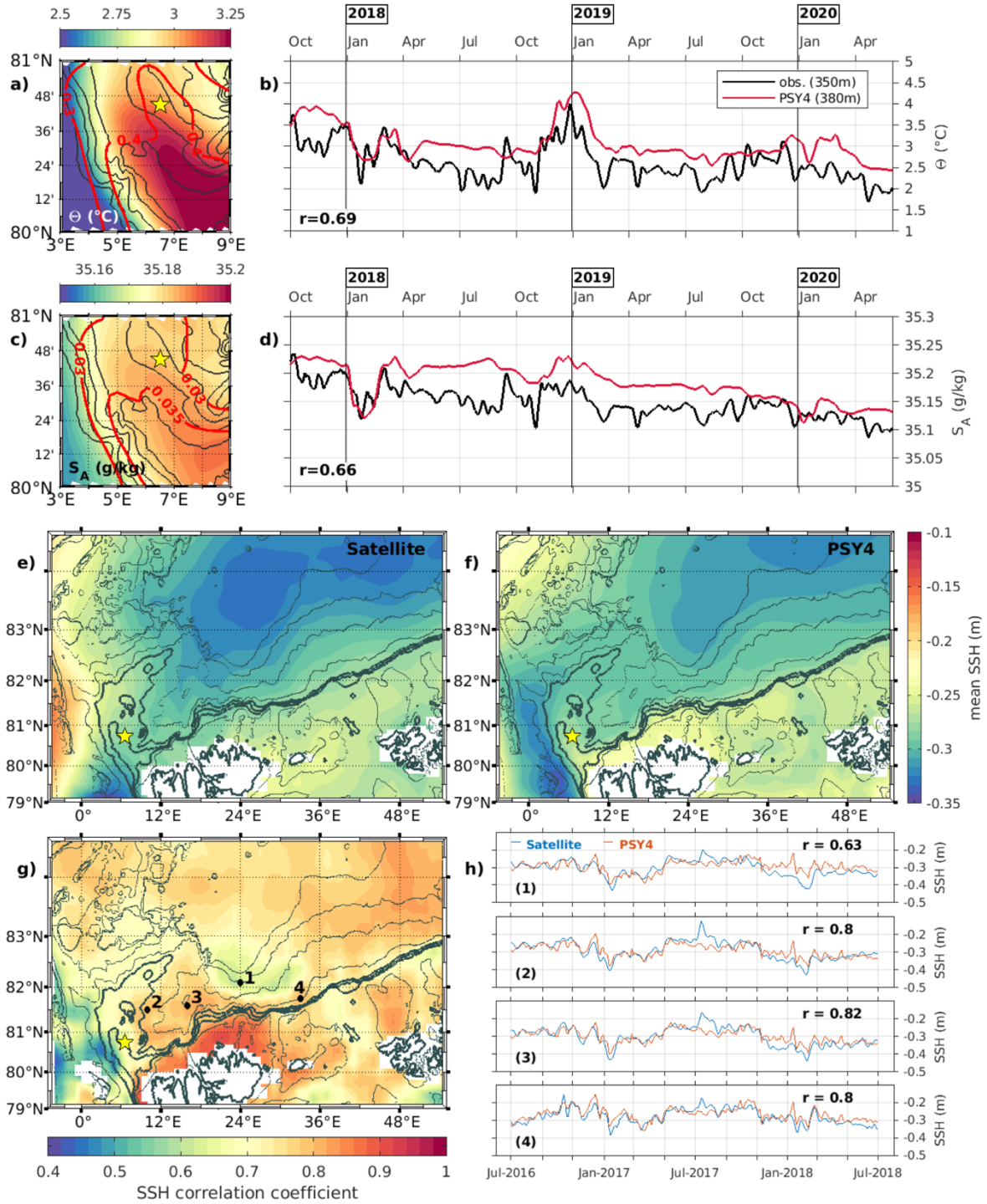

Figure 2: (a) Map of PSY4 Conservative Temperature (Θ, °C) at 380 m averaged over October 2016-May 2020. Isobaths are plotted every 100m from 500 to 1000 m. Red lines delineate contours of STDs over the same period. The yellow star is the location of the mooring as in Figure 1. (b) 10-day smoothed time series of Θ (°C) from the mooring SBE at 350m (black curve) and from PSY4 at 380 m, i.e. the closest vertical level available. (c) and (d) same for Absolute Salinity (S_A, g/kg). (e) Mean sea surface height (SSH, m) from the CNES/CLS satellite altimetry prototype product over July 2016 - June 2018. (f) Mean SSH (m) from PSY4 over the same period and degraded to the same temporal resolution (3 days). Both the PSY4 and satellite-derived SSH were interpolated on a regular grid (horizontal grid spacing 0.1° in latitude, 1° in longitude). (g) Correlation coefficients between the SSH time series at each point. Examples of SSH time series at the points 1 to 4 in (g) are presented in (h).

Here, the first 15 months were considered as a spin-up period in the WNB (see appendix). Hence, daily outputs from April 2008 to May 2020 are used in this paper, carefully avoiding the estimated spin-up period.

An extensive evaluation of PSY4 in the Western Nansen Basin was performed in Athanase et al. (2020), using nearly 1500 independent *in-situ* temperature-salinity profiles and mooring data in the AWBC (1-year long, at 30°E) and in the WSC (5-year long). PSY4 represented a realistic Atlantic Water (AW) inflow and well reproduced hydrographic properties, in spite of some inherent limitations that one should bear in mind. Indeed, the model resolution is not fully eddy-resolving in the Western Nansen Basin (i.e. grid size of 4 km, and Rossby deformation radius of ~10 km; Crews et al., 2018). Moreover, the model lacks tides which are important on the Yermak Plateau (Padman et al., 1992; Koenig et al., 2017b) and on the shelf (Renner et al., 2018). Finally, the PSY4 bathymetry matched the IBCAO bathymetry (Jakobsson et al., 2014) in the WNB, except for a small region at the Kvitøya Trough opening (see appendix in Athanase et al., 2020).

2.2. Further PSY4 evaluation: comparisons with recent observations

We took advantage of a newly retrieved 32 month-long time series of temperature and salinity at 350 m (in the AW layer) from a mooring deployed in the Yermak Pass (from September 2017 to May 2020; yellow stars in Figure 1; Labaste et al., 2020) to evaluate PSY4 in the recent years. The mooring was located in a region of rather large mean gradients and large standard deviations (STDs) (Figures 2a and 2c). The colocalized PSY4 temperature and salinity well reproduced the mean and variations of the 10-day smoothed *in-situ* time-series (Figures 2b and 2d). PSY4 was on average 0.3°C warmer (respectively 2.9 and 2.6°C) and 0.03 g/kg saltier (respectively 35.18 and 35.15 g/kg) than observations at this location. Model STDs were on the same order than those of the 10-day smoothed observations (0.4°C and 0.03g/kg). Variations were correlated at the 99% significance level (r=0.68).

We also compared PSY4 sea surface height (SSH) to satellite SSH from a multi-mission altimetry product prototype for the Arctic Ocean (non-assimilated in PSY4), available from July 2016 to June 2018. The satellite product is based on the combination of measurements from three altimeters (SARAL/AltiKa, CryoSat-2 and Sentinel-3A)

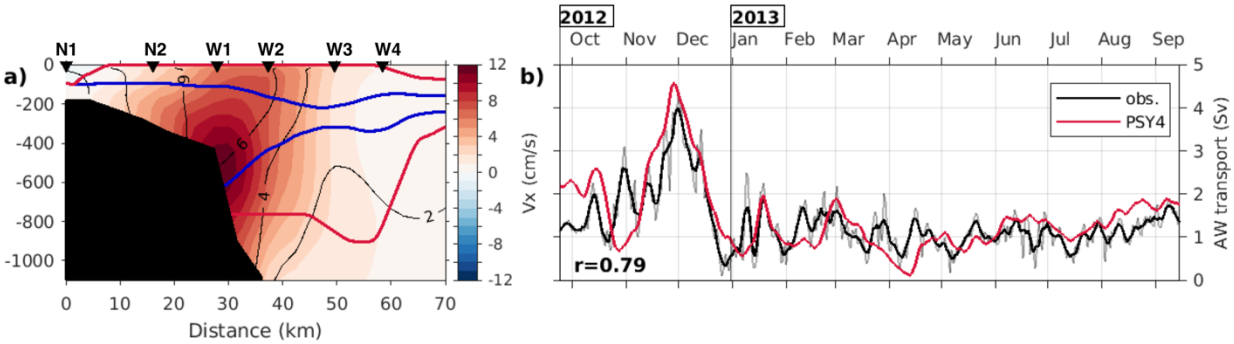

Figure 3: (a) Average cross-section velocity (Vx, cm/s) at the A-TWAIN mooring array (pink stars in Figure 1), between September 2012 and September 2013 (A-TWAIN acquisition period). Black contours are the associated Vx STDs (2, 4 and 6 cm/s). Blue and red lines delineate respectively the minimal and maximal AW layer vertical extent during the period. Black markers N (W) are moorings deployed by the Norwegian Polar Institute (Woods Hole Oceanographic Institution). (b) 10-day smoothed Atlantic Water (defined as Θ>1°C, S_A>35.05 g/kg) volume transport at the A-TWAIN mooring array in the 100-1200 m layer, from mooring data (thick black) and PSY4 (red). The thin black line is the daily in-situ AW transport.

through an optimal interpolation scheme (Bretherton et al., 1976; Ducet et al., 2000). A dedicated low level processing (Poisson et al., 2018) of altimeter waveforms ensures consistency between open ocean and ice covered areas of the Arctic Ocean. This satellite product provides sea level anomaly (SLA) and absolute dynamic topography (ADT) fields on a 25 km grid every three days for latitudes greater than 50°N. The product is freely available from AVISO (https://www.aviso.altimetry.fr/en/data/) along with a detailed description of the processing (https://www.aviso.altimetry.fr/fileadmin/documents/data/tools/gridded_sla_arctic_multimission.pdf).

The SSH mean fields exhibited similar patterns in both the PSY4 and the satellite-derived data, with larger values in the Transpolar Drift, on the shelf and slope than in WNB interior (Figures 2e, 2f). In particular, they both exhibited low SSH values north of the 3800 m isobath (Figure 1) east of 15°E (Figures 2e, 2f). The PSY4 and satellite-derived SSH were well correlated, with correlation coefficients always above 0.5 in the WNB area (significant to the 95% confidence level; Figure 2g). Significant correlations were above 0.7 north of Svalbard, along the continental slope and in the basin interior, and were the lowest yet still around 0.45-0.6 west of Yermak Plateau and near 24°E-82°N (Figures 2g, 2h).

2.3. AW volume transport at 30°E: PSY4 performance

Following the TEOS-10 (Thermodynamic Equations of Seawater) international standard (e.g. Valladares et al., 2011), Absolute Salinity S_A (g/kg) and Conservative Temperature Θ (°C) are used in this paper.

The PSY4 performance in reproducing the mean and variations of AW properties was previously assessed at the A-TWAIN mooring array (30°E, purple stars in Figure 1) in Athanase et al. (2020). Here, we compared modelled and observed AW volume transports across the A-TWAIN section from September 2012 to September 2013. At this location, the boundary current intensity was variable (Figure 3a), and the Atlantic Water layer had vertical extents ranging from the upper 800 m of the water column (red contours in Figure 3a) to about 200 m in the 200-400 m layer (blue contours in Figure 3a). The Atlantic Water layer was defined here as Θ >1°C, S_A>35.05 g/kg (corresponding to a potential density always larger than 27.6 kg/m^3 in PSY4), as in Pérez-Hernández et al. (2019). Pérez-Hernández et al. (2019) computed geostrophic AW volume transports taking into account only positive (eastward) across-section velocities in the 100-1200 m layer (black line in Figure 3b). AW volume transport from PSY4 (same water mass criteria) were computed over the 100-1200 m layer (red line in Figure 3b). The model AW volume transport in the upper 100 m was close to zero (mean of 0.07 Sv, STD of 0.1 Sv). The PSY4 AW transports closely followed the 10-day smoothed observed one. Observations and PSY4 had respective means of 1.3 and 1.5 Sv, STDs of 0.7 and 0.8 Sv, with a correlation coefficient of r=0.79 significant at the 99% confidence level. The model only seldomly missed peaks in volume transport (as in November 2012 and January 2013). We now use the model to further examine AW transport in the WNB.

3. Atlantic Water circulation and volume transport: means and seasonal variations over 12 years

North of Svalbard, the AW heat maintains the Whalers' Bay ice free year-round (Figure 4a; Onarheim et al., 2014), despite the northerly winds which tend to push sea-ice into the area (Figures 4a and b). The WSC, reaching the Yermak Plateau, splits into the Yermak Branch, Yermak Pass Branch and Svalbard Branch (Figures 1, 4c, 4d). The upper part of the AW layer, cooling and freshening through sea-ice melt and heat loss

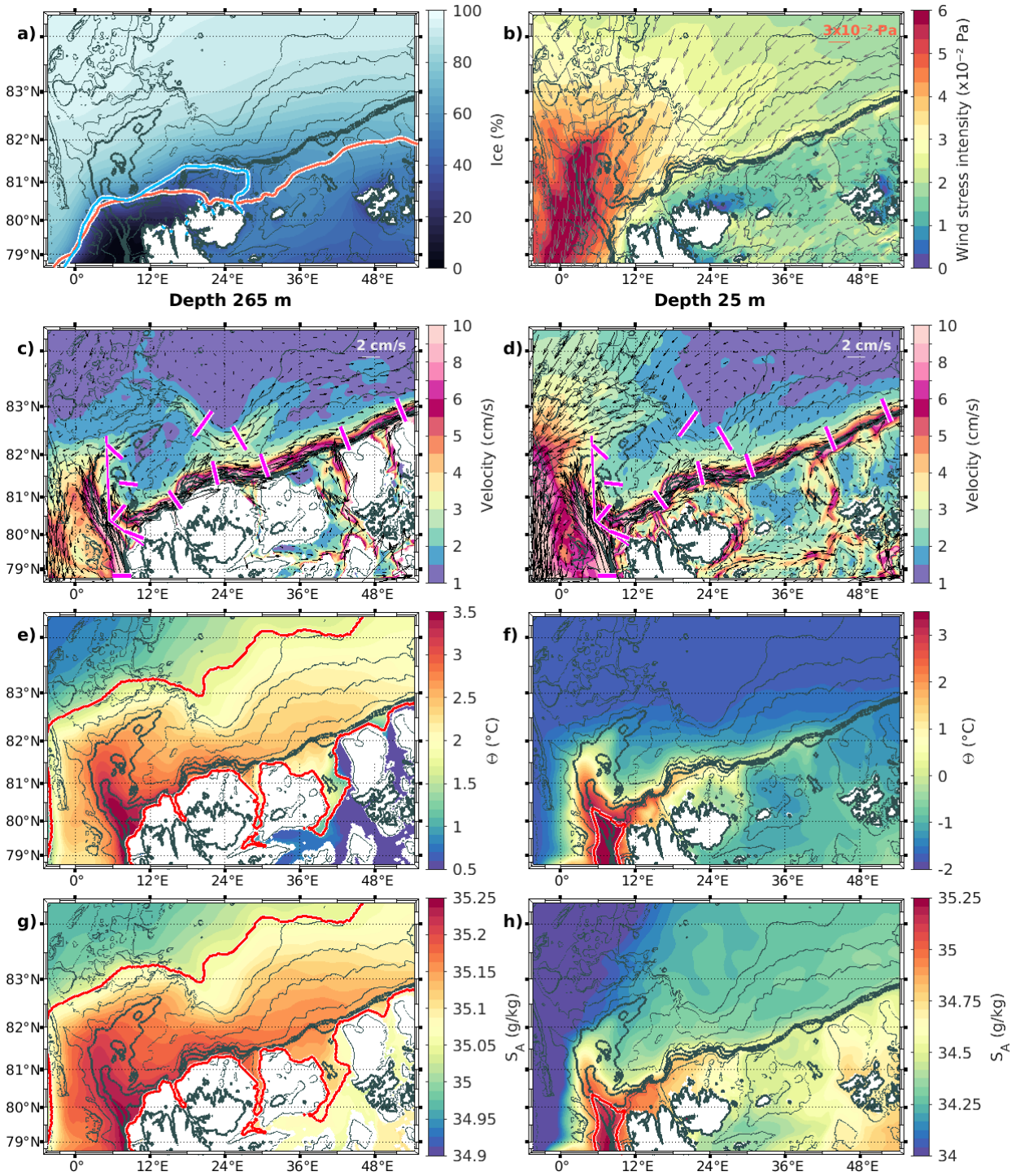

Figure 4: Mean PSY4 fields over 2008-2020 in the Western Nansen Basin. (a) Mean ice concentration (%). Orange and blue solid contours are respectively the mean July and January ice edge (40% ice concentration). (b) Mean wind stress (Pa, grey arrows), with intensity in background color. (c) Mean velocity vectors (black arrows) and intensity (color, cm/s) at 265 m and (d) 25m. Magenta sections are used for AW volume transport computations. (e) Mean Conservative Temperature (Θ, °C) at 265 m and (f) 25 m. (g)-(h) Same for Absolute Salinity (S_A, g/kg). Red contours delineate the horizontal limit of Atlantic Water (such as Θ>1°C and S_A>35.05 g/kg) at 265 and 25 m. Isobaths 500, 700, 1000 m are in thick lines, 200, 2000, 3400, 3800 and 3900 m in thin lines.

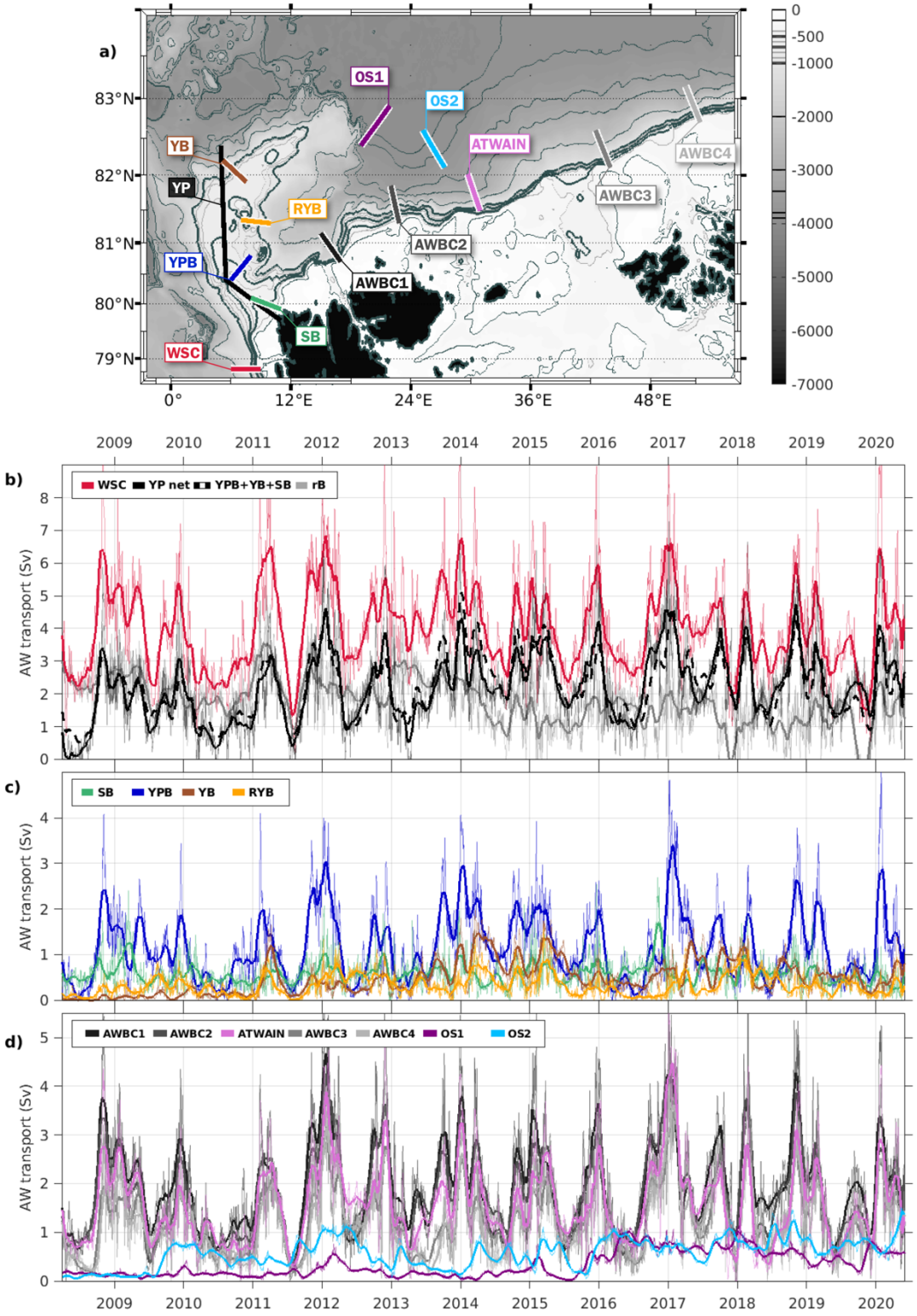

Figure 5: (a) Location of the 13 sections across which Atlantic Water (such as Θ>1°C, S_A>35.05 g/kg) volume transports were computed and presented in Table 1. WSC: West Spitsbergen Current; YP: Yermak Plateau; SB: Svalbard Branch; YPB: Yermak Pass Branch; YB: Yermak Branch; RYB: Return Yermak Branch; AWBC: Atlantic Water Boundary Current; A-TWAIN: mooring array at 30°E; OS1 and OS2: Offshore Sections 1 and 2. (b) Time series of AW volume transports (Sv) between April 2008 and May 2020 for the WSC, AW crossing the Plateau (YP net; sum of YPB, YB and SB) and recirculation branches (rB, computed as WSC – YP net). (c) Same for sections located over the Yermak Plateau. (d) Same for sections located downstream of Yermak Plateau.

to the atmosphere, is transformed into a less dense surface layer (Rudels et al., 2015;

Figures 4e to 4h). On average, the AW signature at 265 m could be found as far offshore as the 3900 isobath (red contours in Figures 4e, 4g). Near the surface the AW mean horizontal extent was reduced to the southern Yermak Plateau and the slope west of 11°E (red contours in Figures 4f, 4h).

As in Koenig et al. (2017b), we used the PSY4 system to investigate the partition of the AW flow downstream of the WSC. We examined the AW volume transport across 13 sections near the Yermak Plateau and in the WNB (Table 1; Figure 5): West Spitsbergen Current (WSC); Svalbard Branch (SB); Yermak Pass Branch (YPB); Yermak Branch (YB); Return Yermak Branch (RYB); at the A-TWAIN mooring location in the boundary current; Atlantic Water Boundary Current sections 1 to 4 (AWBC 1 to 4); Offshore Section 1 (OS1) and Offshore Section 2 (OS2). Note that sections in the WSC, SB and YPB are identical to Koenig et al. (2017b), extending the time series until 2020. The remaining sections complement the analysis further east. To ensure we capture all recirculations over the Plateau, an additional longer section (noted YP) was taken along the axis of the Yermak Plateau.

AW volume transports were computed following two methods: net transport as in Koenig et al. (2017b), and taking into account only positive cross-section velocities as in Pérez-Hernández et al. (2019). The net transport was on average 25% lower over the Yermak Plateau and 5% lower near the continental slope (Table 1), yet time-series were highly correlated (with $r>0.9$ for all 13 sections, significant to the 99.9% level). Transports shown hereafter were estimated using only positive cross-section velocities. Two AW definitions were used ($\Theta>1°C$, $S_A>35.05$ g/kg as in Pérez-Hernández et al. 2019 –shown hereafter–, and $\Theta>1.5°C$ as in Koenig et al., 2017b). The two definitions provided similar results (see Supplementary Material S1).

3.1. AW volume transport across and around Yermak Plateau

The AW carried by the modelled WSC ranged from 1.5 to 7 Sv, with a mean of 4 Sv and STD of 1.5 Sv, and exhibiting large seasonal variations (red curve in Figures 5b and 6a). Maximum values of AW volume transport in the WSC were reached on average in January (5.2 Sv, Table 1) and were minimal in July (2.9 Sv, Table 1).

Table 1: Statistics of the AW volume transport (Sv) in 2008-2020 across 13 sections near the Yermak Plateau and in the Western Nansen Basin, marked (and colored) in Figure 5. AW is defined as Θ>1°C, S_A>35.05 g/kg. Only positive cross-section velocities are considered (as indicated by the mean flow in Figure 4c). Values in italics and parentheses are for net AW volume transports. Section names are as in Figure 5.

Section	Mean	STD	January		July	
			mean	min/max	mean	min/max
WSC	4.0 *(3.8)*	1.5 *(1.6)*	5.2 *(4.9)*	1.7/9.7	2.9 *(2.5)*	1.0/4.5
YP	2.95 *(2.2)*	1.2 *(1.2)*	3.8 *(3.1)*	1.0/7.85	2.0 *(1.3)*	0.5/3.6
SB	0.6 *(0.45)*	0.3 *(0.4)*	0.7 *(0.6)*	0.0/2.1	0.5 *(0.5)*	0.1/1.1
YPB	1.2 *(1.0)*	0.8 *(0.9)*	1.75 *(1.6)*	0.0/5.1	0.5 *(0.3)*	0.0/1.3
YB	0.5 *(0.4)*	0.4 *(0.4)*	0.45 *(0.4)*	0.0/1.8	0.4 *(0.3)*	0.0/1.5
RYB	0.3 *(0.2)*	0.25 *(0.3)*	0.3 *(0.2)*	0.0/1.3	0.3 *(0.2)*	0.0/0.8
AWBC1	1.9 *(1.8)*	1.1 *(1.1)*	2.9 *(2.7)*	0.6/6.1	1.0 *(0.9)*	0.0/2.6
AWBC2	1.8 *(1.7)*	1.0 *(1.1)*	2.6 *(2.4)*	0.6/5.6	1.0 *(0.9)*	0.1/2.0
A-TWAIN	1.6 *(1.4)*	0.9 *(1.0)*	2.3 *(2.2)*	0.3/5.7	1.0 *(0.75)*	0.2/2.05
AWBC3	1.3 *(1.2)*	0.8 *(0.85)*	1.9 *(1.8)*	0.3/4.6	0.65 *(0.5)*	0.0/1.55
AWBC4	1.25 *(1.2)*	0.8 *(0.8)*	1.9 *(1.8)*	0.0/4.7	0.65 *(0.6)*	0.1/1.6
OS1	0.3 *(0.3)*	0.3 *(0.3)*	0.4 *(0.3)*	0.0/1.3	0.3 *(0.3)*	0.0/0.9
OS2	0.6 *(0.5)*	0.3 *(0.3)*	0.5 *(0.5)*	0.0/1.2	0.5 *(0.4)*	0.1/1.4

The modelled Yermak Pass Branch (YPB) constituted the main path for AW over Yermak Plateau with an AW volume transport of 1.2 ± 0.8 Sv (mean ± STD), which was largely correlated with the WSC AW transport over the 2008-2020 period (r=0.78) and exhibited the same seasonal variations (Table 1, blue curve in Figures 5b, 6a, 6c and 6d). In summer, AW transport in the YPB was on the same order as in the Svalbard Branch (SB; in agreement with Menze et al., 2019). The SB carried a smaller volume of AW on average (0.6 ± 0.3 Sv), showed marginal seasonality (maximum in January of about 0.7 Sv, minimum in July of about 0.5 Sv) and a smaller correlation to the WSC AW transport (r=0.48; green curve in Figure 5b, 6a).

The mean modelled Yermak Branch (YB) carried some AW along the western flank of Yermak Plateau, losing AW to westward recirculations (Figure 4c). As a result, the AW volume transport was 0.5 ± 0.4 in the YB at 82°N on average (Table 1). Past 82°N, the YB flow either continued along the western edge of the Yermak Plateau or crossed over the Plateau (Figure 4c). Along the eastern flank of the Plateau, a southward flow at 81.5°N was called the Return Yermak Branch (RYB), being essentially fed by the YB (r=0.63 between YB and RYB). The RYB carried about 0.3 ± 0.25 Sv, representing 70% of the YB AW volume transport (Table 1, Figures 5a, 5b). These branches (YB and RYB) exhibited no seasonal variations (brown and yellow curves in Figures 6a; 6c and 6d) and little correlation with the WSC AW transport (r=0.31, yet significant at the 90% confidence level).

The sum of AW volume transports across the YPB, SB, and YB at 82°N (mean of 2.2 Sv, STD of 1.1 Sv) corresponded to the net AW volume transport across YP (mean of 2.2 Sv, STD of 1.2 Sv) and to about 55% of the AW volume transport from the WSC section (Table 1). This implies that about 45% (1.7 Sv on average) of the modelled WSC AW inflow recirculated towards Fram Strait south of 82°N (AW transport from recirculation branches noted rB, grey curve in Figure 5b).

3.2. AW progression downstream of Yermak Plateau

3.2.1. Atlantic Water boundary current

The AW transport at the AWBC1 section (16°E; 1.9 Sv) was on average 5% larger than -and very correlated (r=0.88) with- the sum of the AW transports of YPB and SB. This suggested that to the first order, the AW boundary current was mainly fed by these two branches. The complex and rather weak recirculations in the Sofia Deep (Figures 4c and 4d) were therefore minor contributors to the boundary current. Along the continental slope, the AW volume transport diminished eastward, with 1.9 ± 1.1 Sv at 16°E (mean ± STD), 1.8 ± 1.0 Sv at 23°E, 1.6 ± 0.9 Sv at the A-TWAIN location (30°E), to reach a value of about 1.3 ± 0.8 Sv at 43°E and 52°E (Table 1, grey and pink curves in Figures 5c and 6b). On average, the largest AW volume transport reductions occurred between 23°E and 43°E (Table 1). In this area, processes have potential to reduce the AW volume transport, with the meandering and shedding of eddies, and deep convection in winter transforming AW into halocline water (Ivanov et al., 2018; Athanase et al., 2020). As in the WSC, YPB and SB, seasonal variations in AW volume

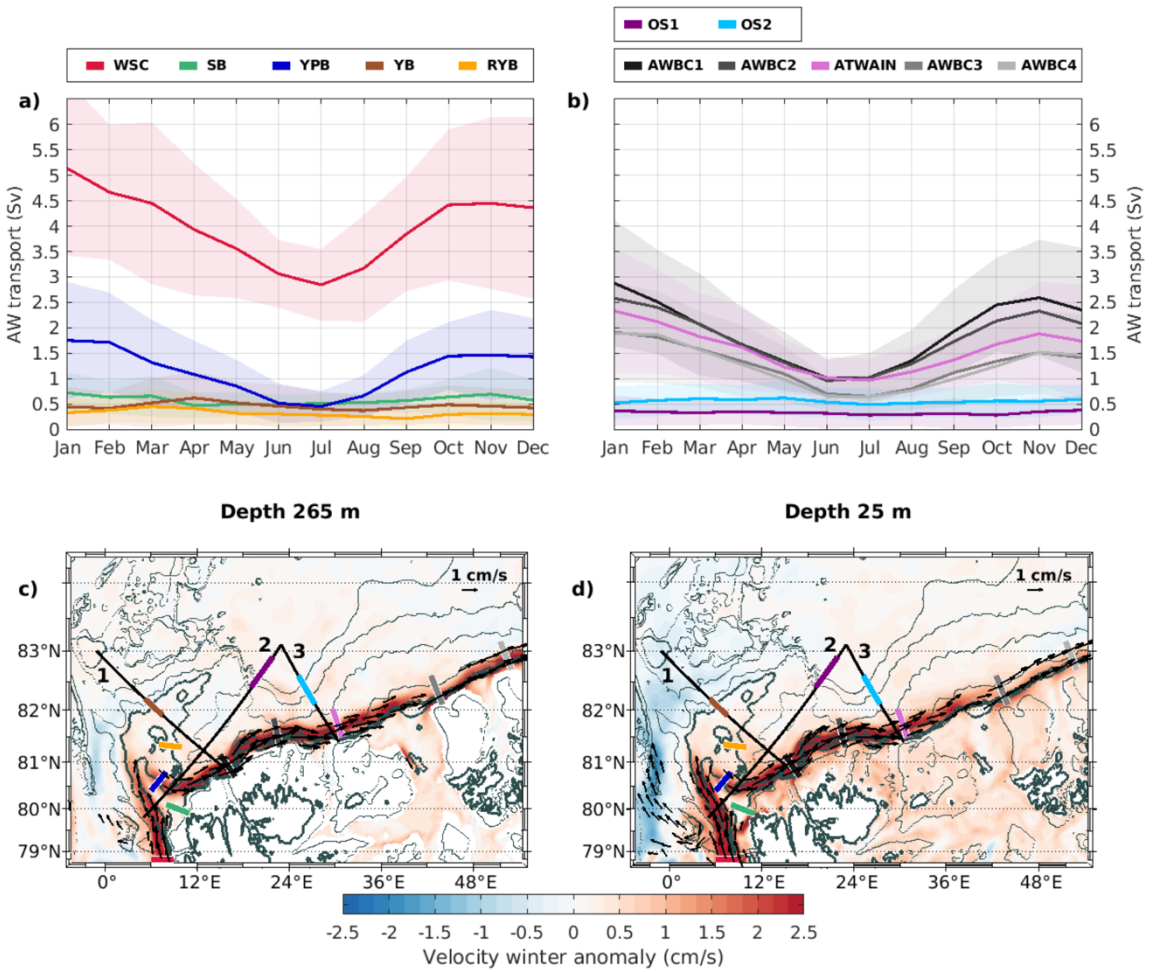

Figure 6: (a) Monthly means of AW volume transport (Sv) across the 5 sections over Yermak Plateau, in 2008-2020. (b) Monthly means of AW volume transport (Sv) across the 7 sections downstream of Yermak Plateau, in 2008–2020. Shaded envelopes in (a) and (b) are interannual STDs for each month. (c) Winter velocity anomaly (cm/s) (with respect to the 12-year mean) at 265 m and (d) 25 m. Winter is defined at the October-to-March period. Seasonal velocity anomaly vectors are plotted in black arrows for velocity anomalies larger than 1 cm/s. Sections names and color codes are as in Figure 5. Transects 1, 2 and 3 are shown in Figures 7, 9 and 10.

transport were large in the AWBC (amplitude ~2 Sv), with maximum values reached on average in January and minimum values in July (Table 1, Figures 6a compared to 6b; 6c and 6d). The daily AW volume transports across the five sections in the boundary current were highly correlated, with correlation coefficients to AWBC1 (16°E) decreasing from r=0.9 at AWBC2 (23°E) to r=0.8 at AWBC4 (52°E; Figure 5c).

3.2.2. Offshore circulation

At 265 m, the mean velocity fields highlighted an offshore "V-shaped" circulation pattern straddling the 3800-3900 m isobaths (Figure 1 and Figure 4c), with its

southernmost extremity located near 82°N, 24°E (mean velocities larger than 3 cm/s in Figures 4c, 4d). The offshore circulation followed the large lateral gradients of temperature and salinity (and thus density; Figures 4c, 4e, 4g).

The western part of the V-shaped circulation consisted in a southeastward current carrying some AW (mean of 0.3 ± 0.3 Sv; Table 1 and purple lines in Figure 5c). On the mean, this current straddled the 35.1 g/kg and 2°C isolines (Figures 4f, 4h). The northeastward flow following 3800-3900 m isobaths, i.e. eastern part of the V-shaped offshore circulation, carried on average 0.6 ± 0.3 Sv of AW (Figures 4c, 4d and blue lines in Figure 5c). Concurrently, relatively warm and salty AW (Θ>2°C, S_A>35.1 g/kg) spread offshore east of 24°E, following the bulk of the isobaths, suggesting that part of the boundary current AW may be advected by this northeastward flow (Figures 4e, 4g). In contrast with the continental slope, this offshore circulation exhibited no seasonal variations in AW volume transport (Table 1, purple and blue lines in Figure 6b) and in velocity (Figures 6c and 6d). Interestingly, time-series of AW volume transport suggested a development of the V-shaped circulation in winter 2009 for the eastern part (blue line in Figure 5c) and in 2016 for the western part after a peak in 2012 (purple line in Figure 5c).

4. Interannual variations of AW volume transport

Time-series of AW volume transport across the 13 sections in the WNB exhibited large variations on interannual time scales (Figure 5). To investigate further interannual variations we examined the evolution of properties and velocities along three transects (Figures 6c-d): one encompassing the YB and AWBC1 sections and crossing the northern part of Yermak Plateau (transect 1, Figure 7), and two from the slope offshore. Transect 2 comprised OS1 and YPB sections while transect 3 extended from the A-TWAIN section out to 83°N across OS2 (Figures 9 and 10). Linear trends were estimated over the time span of available model fields (12 years, 2008-2020) and compared to STD values (of detrended time-series) (panels d to h in Figures 7, 9 and 10; Figures 12 and 13). An animation of PSY4 mapped velocity fields at 265m over 2008-2020 with a 3-day temporal resolution is provided in Supplementary Material (S2).

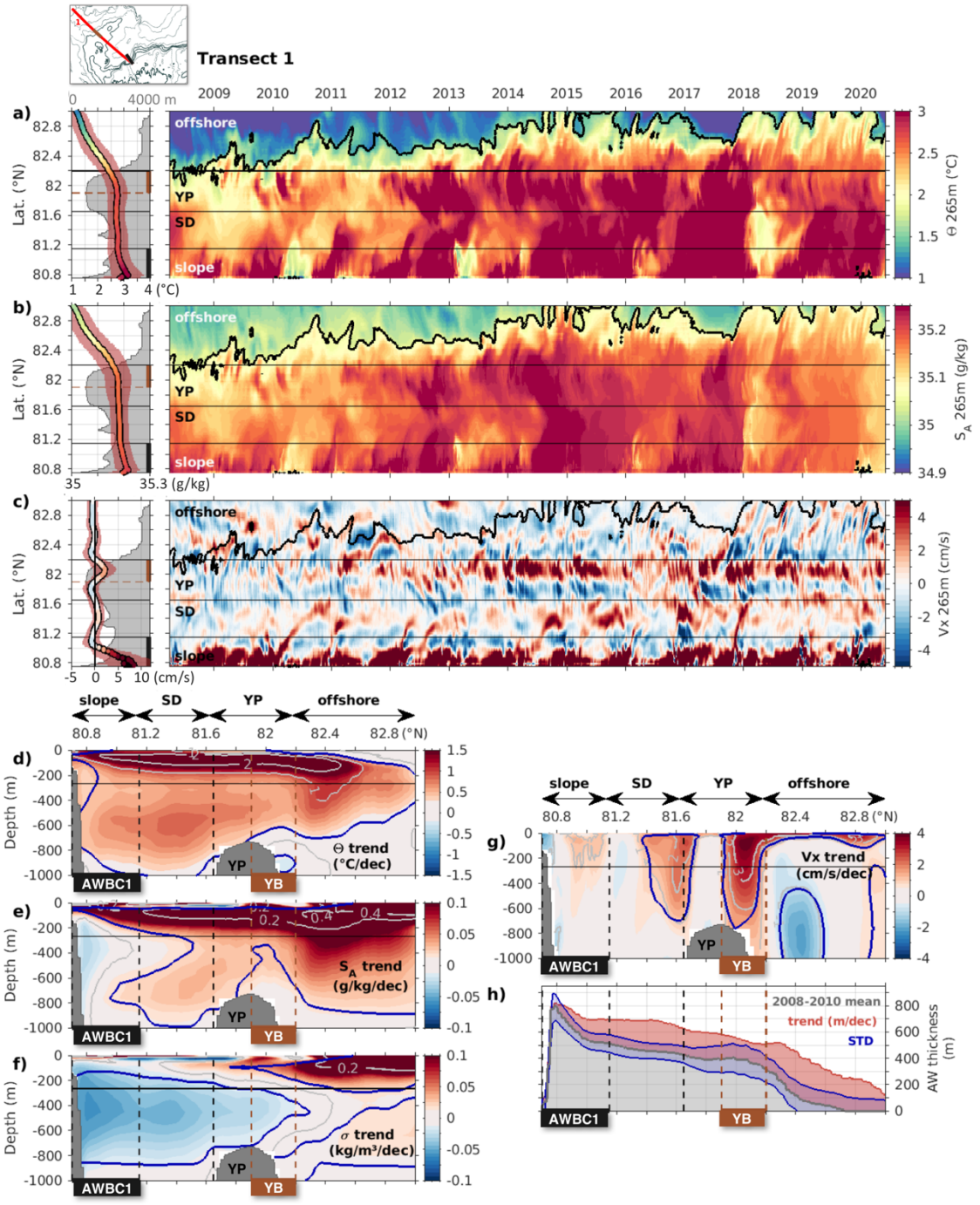

Figure 7: (a) Conservative Temperature (Θ, °C) at 265 m along transect 1 (shown in the insert), (left) mean and STD (shaded envelope) in 2008-2020, with bathymetry in shaded grey, and (right) daily resolution. Same for (b) Absolute Salinity (S_A, g/kg) and (c) cross-section velocity (Vx positive when directed northeastward, cm/s). Main geographical features are delineated with horizontal lines. Thick black contours delineate AW (Θ>1°C and S_A>35.05 g/kg). (d) Linear trend in Conservative Temperature (Θ, °C/decade) along transect 1 (0-1000 m), computed over 2008-2020. (e) Same in Absolute Salinity (S_A, g/kg/decade), (f) in potential density (σ, kg/m^3/decade) and (g) cross-section velocity (Vx, cm/s/decade). Grey contours are decadal trend isolines. Blue contours on (d) to (g) delineate areas where the 12-year trend is larger than the STD. (h) AW layer thickness along transect 1, 2008-2010 mean (grey area, m), 12-year STD (blue envelope centered on the 2008-2010 mean, m) and linear trend (red area, m/decade) added to the 2008-2010 mean. The horizontal line indicates the 265 m level shown in (a)-(c), vertical lines delineate geographic regions as reported below. SD: Sofia Deep; YP: Yermak Plateau. AWBC1 and YB (Yermak Branch) as in Figure 5.

4.1. Interannual variations in AW volume transport across and around Yermak Plateau

4.1.1 Strengthening of the Yermak Branch

A striking feature in transect 1 was the strengthening of the Yermak Branch at 82°N on the western flank of Yermak Plateau, with larger northeastward velocities at 265 m from 2011 onwards (Figure 7c) and warmer and saltier waters (Figures 7a, 7b). Vertical sections along transect 1 illustrated these YB changes throughout the upper 1000 m of the water column, with a large increase in AW layer thickness (up to +150 m/decade, Figure 7h) and in cross-section velocities down to the seafloor (Figure 7g). Velocity trends reached 3.5 cm/s/decade near the surface. The temperature and salinity trends in the YB were large in the upper 200 m with values of +2°C/decade and +0.2 g/kg/decade (Figures 7d, 7e).

Positive trends in velocity and AW thickness led to an increased AW volume transport across the YB section (mean of 0.2 Sv in 2008-2012 and 0.7 Sv in 2013-2020, brown bars in Figure 8b). AW transport through the YB at 82°N was the largest in 2014/15 (annual mean of 0.9 Sv), making up for 23% of the WSC AW transport (compared to 12% on average over 2008-2020) (Figure 8b). That year, the net AW volume transport across the Yermak Plateau accounted for 70% of the WSC transport (YP, black bars in Figure 8a). In other words, in 2014/15 only 30% of the AW volume carried by the WSC recirculated towards Fram Strait south of 82°N instead of 45% on average (rB, grey bars in Figure 8a). The year 2014/15 also corresponded to a clear decline of the AW volume recirculating towards Fram Strait south of 82°N, from a mean of ~2.2 Sv in 2008-2013 (i.e. 55% of the WSC), to ~1.3 Sv from 2014 onwards (i.e. 32% of the WSC) (grey bars in Figure 8a).

4.1.2. Contrasting variations of the YPB and SB

Waters in the YPB became progressively warmer and saltier (Figures 9a, 9b), with a substantial increase near the surface (+2°C/decade, +0.2 g/kg/decade), while below 100 m they became lighter by about -0.05 kg/m^3/decade as a result of warming (+0.5°C/decade) and freshening (-0.05g/kg/decade) (Figures 9d to 9f). Positive trends in velocity (+2cm/s/decade) and AW thickness (+150m/decade) were centered over the lower slope (900 m isobath, Figures 9g, 9h), suggesting a slight displacement of the core of the YPB to deeper isobaths. However, the velocity trends were small compared

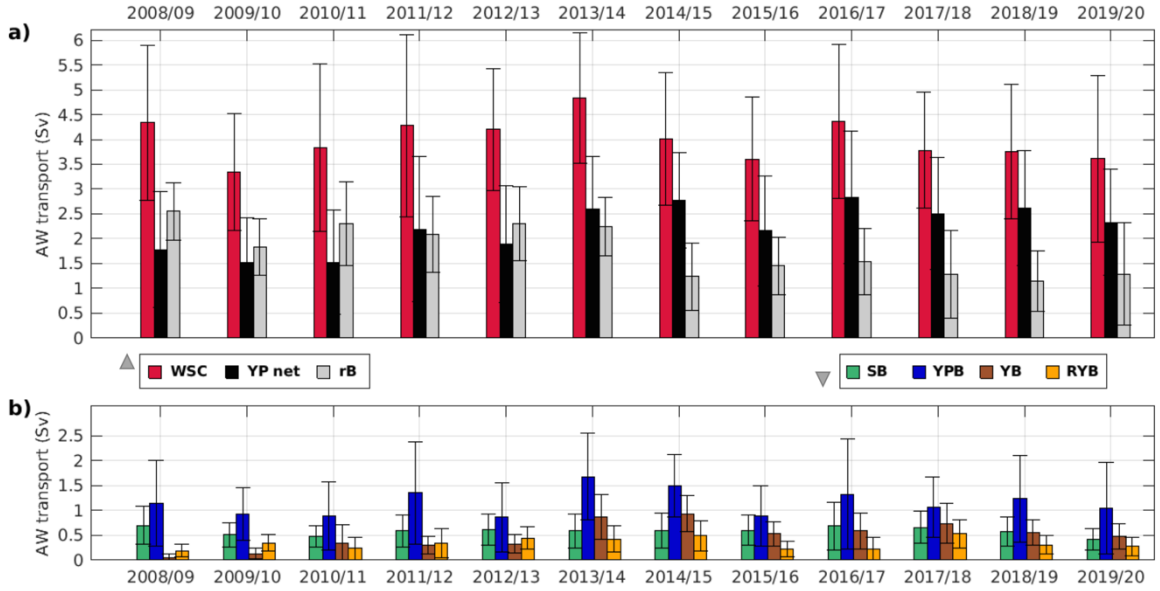

Figure 8: (a) Annual means of AW volume transport in the WSC, AW crossing the Plateau (YP net; sum of YPB, YB and SB) and recirculation branches (rB, computed as WSC – YP net) in 2008-2020. Year-long intervals are taken from June to May of the following year in order to include complete winters. Black bars are STDs for individual years. (b) Same for the 4 sections located over Yermak Plateau. Sections names and color codes are as in Figure 5.

to the large STDs in the YPB (STD of 5 cm/s at 265 m, for a mean of 5 cm/s, Figure 9c). This variable YPB flow, with seldom occurrences of northwestward velocities (Vx<0 in summer 2016 for example; cf. Koenig et al., 2017b) (Figure 9c) was consistent with previous studies (Koenig et al., 2017b; Menze et al., 2019).

The resulting interannual variations in AW volume transport through YPB were large, ranging from 0.8 Sv in 2012-2013 (20% of the WSC AW transport) to 1.7 Sv in 2013-2014 (34% of the WSC AW transport; blue bars in Figure 8b). In contrast with the YPB, the SB exhibited little variations in AW volume transport (0.4 to 0.65 Sv, representing 11 to 17% of the WSC transport, green bars in Figure 8b).

4.1.3. Intensification of the circulation in Sofia Deep

Transects 1 and 2 also provided information on the relatively small and variable velocities in Sofia Deep (mean Vx~2 cm/s, STDs of about 2-3 cm/s, Figures 7c and 9c). At 265 m, these velocities resulted in a mean flow predominantly southward along the eastern flank of the Yermak Plateau (centered around 81.8°N) and in a mean anticyclonic circulation in the Sofia Deep (velocities of 1-2 cm/s; Figures 7c and 9c).

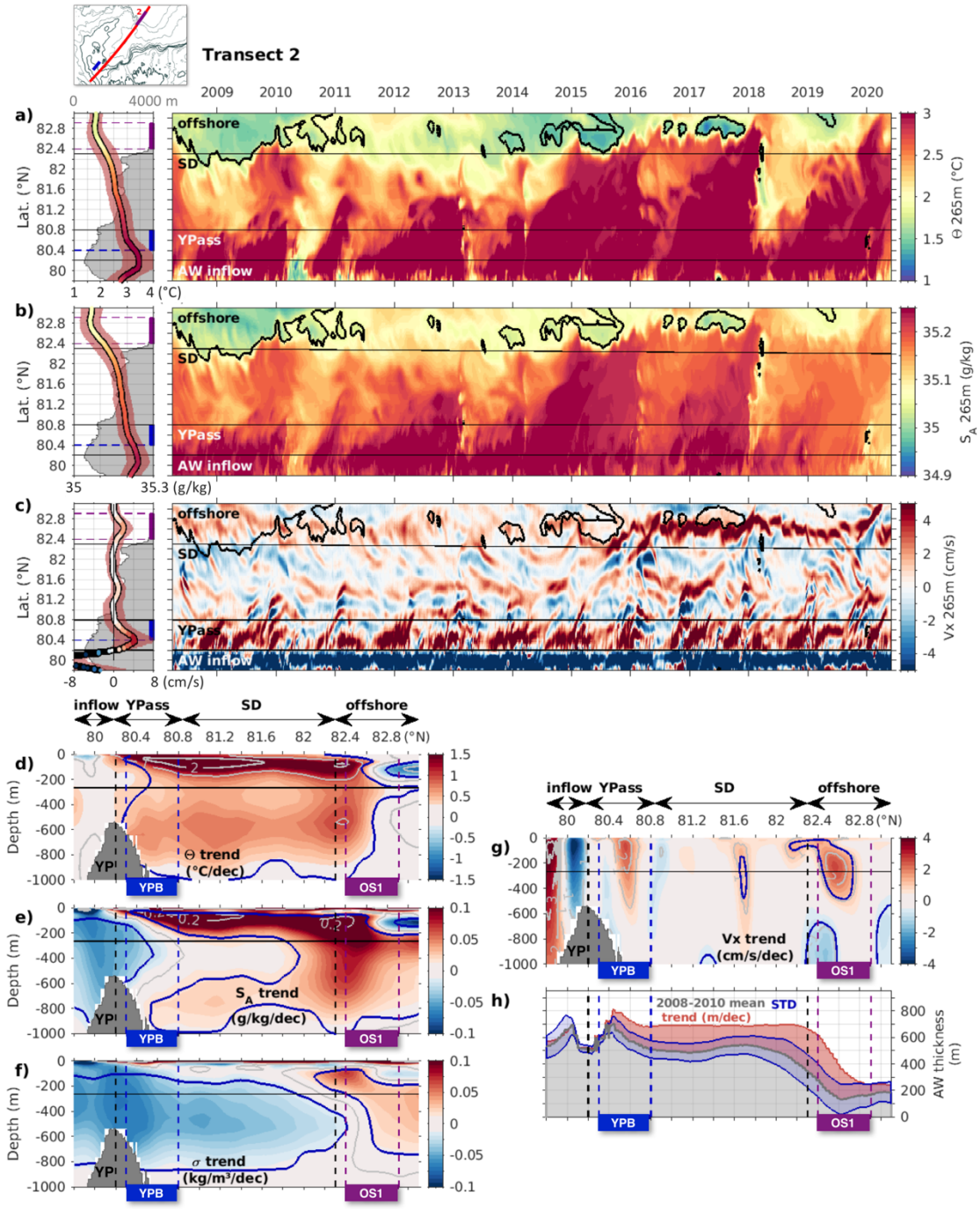

Figure 9: Same as Figure 7, along transect 2. YP: Yermak Plateau; YPass: Yermak Pass; SD: Sofia Deep. YPB (Yermak Pass Branch) and OS1 (Offshore Section 1) as in Figure 5.

Mirroring the northeastward YB interannual variations (see section 4.1.1), the largest velocities and AW volume transport in the RYB were reached in 2013-2020 (Figures 7c, 8b). These flows (YB pathways and RYB) are schematized with yellow and orange arrows in Figure 14.

The mean anticyclonic circulation in Sofia Deep consisted of a northeastward flow in the center of the Sofia Deep (near 81.4°N) and a southwestward flow (near 81.1°N) to the north of the eastward boundary current along transect 1 (Figure 7c). This mean anticyclonic circulation showed up in transect 2 as a southeastward flow near 81.4°N, and a northwestward flow near 81.1°N (Figure 9c). Animations of velocity fields at 265 m (Supplementary Material S2) indicated meanders recurrently detaching from the AWBC near 18°E, where the steep slope abruptly changes direction, contributed to the anticyclonic circulation in Sofia Deep (Figures 1 and 7c). Meanders either became elongated, following a U-turn anticyclonically (schematized with plain green arrows in Figure 14), or evolved in long-lived slowly-moving AW anticyclonic eddies with rather large radii R∼45 km (schematized with dashed green arrows in Figure 14). A particularly vigorous and persistent anticyclonic eddy was observed in December 2016, with azimuthal velocities Vx>5 cm/s lasting for over a month (Figures 7, 9).

The flow in Sofia Deep evolved from weak and highly variable velocities in 2008-2010 to a recurrent anticyclonic circulation, bringing progressively warmer and saltier waters towards the north from 2010 onwards (Figures 7a-c and 9a-c). In the center of Sofia Deep, trends in northeastward velocities reached +2 cm/s/decade in the upper 600 m (81.4 to 81.7°N in Figure 7g). The Sofia Deep exhibited large positive trends in temperature and salinity, strongest near the surface (+1 to +2°C and +0.1 to +0.2 g/kg in the upper 200 m, Figures 9d, 9e) as for the YB, and associated with a mild temperature-driven density decrease below 200 m (-0.03 kg/m^3, Figures 9f). This is in agreement with the vertical and lateral progression of Atlantic Water (thickening about +200 m/decade in the Sofia Deep, Figures 7h and 9h). Notable exceptions to this overall temperature and salinity increase were the seldom occurrences of local and upstream intense winter convection events leading to anomalously cold water at 265 m extending from the slope into Sofia Deep (February 2013 and 2018, Figures 7a-b, 9a-b; Athanase et al., 2020).

4.2. Interannual variations in the boundary current along the slope

AW volume transport across the boundary current sections was largely correlated with the YPB (section 3.2.1., Figures 5b and 5c). Shelf-slope and slope-basin exchanges also contributed to modulate AW volume transport across the boundary current sections (AWBC1 to 4 and A-TWAIN, Figures 5c, 11a). For example, exchanges with the Franz-

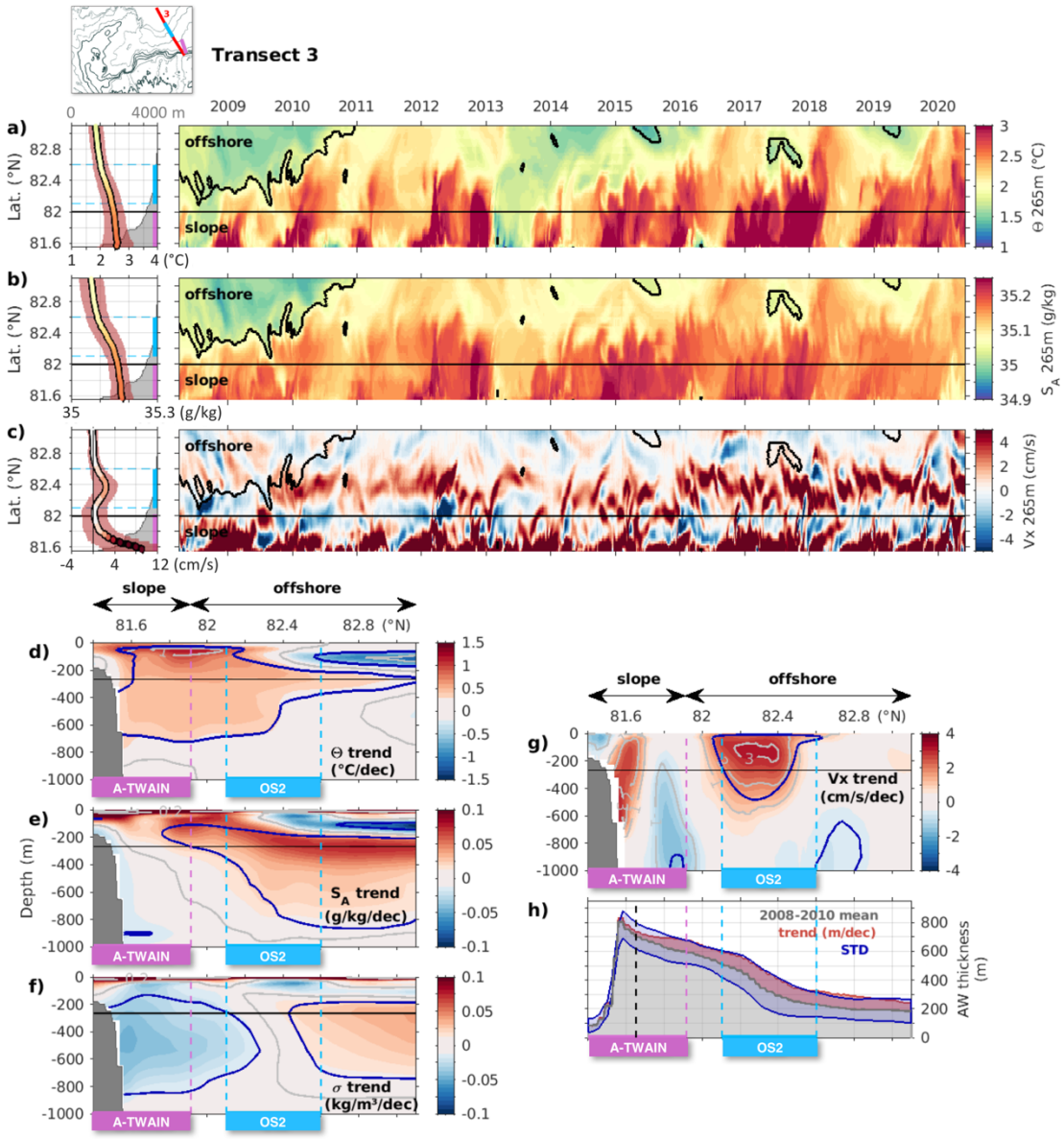

Figure 10: Same as Figure 7, along transect 3. A-TWAIN and OS2 (Offshore Section 2) as in Figure 5.

Victoria or Kvitøya troughs contributed to large decreases in annual AW volume transport (e.g. 2018/19 between AWBC2 and A-TWAIN, 2013/14 between A-TWAIN and AWBC3, Figure 11a; Athanase et al., 2020). On several occasions, the boundary current was observed meandering along the slope (Supplementary Material S2). In particular, the development of persistent meanders "avoiding" AWBC1, leaving the shore near 14°E and rejoining the boundary current at the shelf break near 18°E, led to an annual AW volume transport larger at AWBC2 than at AWBC1 (e.g. 2014/15 and 2016/17 in Figure 11a; August-October 2014 and February-May 2017 in Supplementary Material S2). In April-May 2012, large eddies detached from the slope

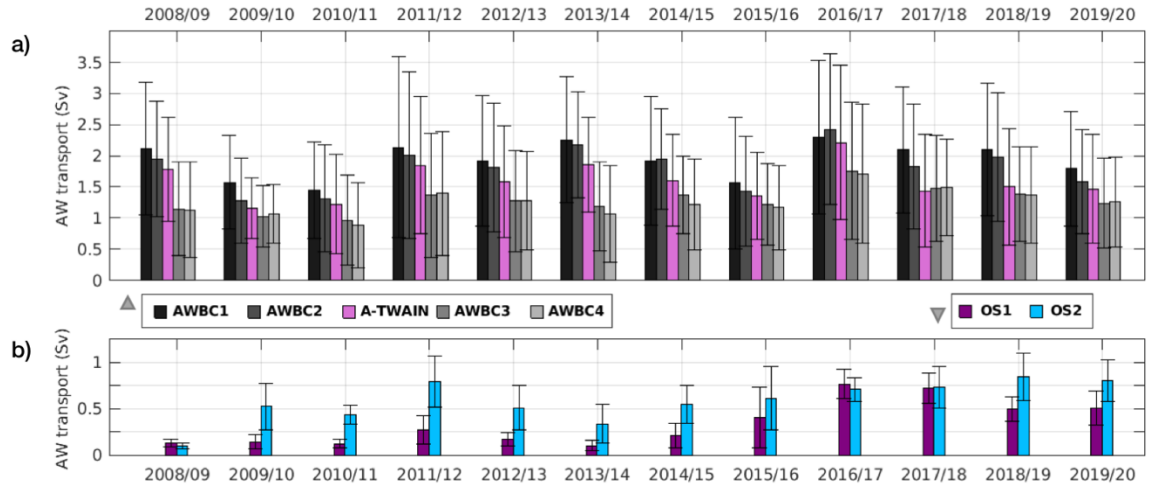

Figure 11: Annual means of AW volume transport (Sv) in 2008-2020, (a) across the 5 sections along the continental slope and (b) at the 2 offshore sections downstream of Yermak Plateau. Year-long intervals are taken from June to May of the following year in order to include complete winters. Black bars are STDs for individual years. Sections names and color codes are as in Figure 5.

between A-TWAIN and AWBC3 to join the offshore circulation at OS2 inducing a drastic decrease in AW volume transport at this location in the boundary current and an increased AW transport at OS2 (Figure 11). Such mesoscale activity between the boundary current and the offshore circulation was common.

Velocities in the boundary current were highly variable and linear positive trends in velocity were comparatively small (STD>5-6 cm/s, Figures 7c, 10c; trends of +1-2 cm/s/decade, Figures 7g, 10g). The boundary current exhibited an overall warming and salinification in the upper 100 m, reaching +1 to 2°C/decade and +0.2 g/kg/decade. Below 100m, temperature increased by about +0.5°C/decade and density decreased by -0.05 kg/ m^3/decade, likely due to a mild salinity decrease (Figures 7d-e, 10d-e). The AW layer thickened over the lower slope in the boundary current, by +200 m/decade at the upstream AWBC1 (Figure 7h) and about +50 m/decade at A-TWAIN (Figure 10h).

4.3. Offshore AW circulation

The western and eastern parts (OS1 and OS2, Figure 5) of the offshore circulation (purple arrows in Figure 14) carried relatively cold and fresh waters in 2008-2010 (Θ<1.8°C, S_A<35.05g/kg at 265 m; Figures 9a-b, 10a-b). From 2011-onwards, the flow across OS1 and OS2 at 265 m mostly comprised AW (with Θ>1.5°C, S_A>35.05 g/kg), in spite of occurrences of colder, fresher waters (e.g. winter 2013/14, years 2015, 2017)

(Figures 9a-b, 10a-b). The offshore circulation showed up as large positive (eastward) cross-section velocity trends in transects 2 and 3 (+2 to +3 cm/s/decade, Figures 9g, 10g).

The circulation across OS1 at 265m evolved from a weak (Vx<2 cm/s) flow in 2008-2015, adjusting into a stronger and more organized flow from 2015-onwards (Figure 9c). The eastern part of the offshore circulation (OS2) at 265 m strengthened earlier in winter 2009/10 (Vx>2 cm/s, Figure 10c). As a result, AW volume transport across OS1 remained small until 2014 (<0.25 Sv) and increased abruptly in 2015 to reach 0.5 to 0.75 Sv in 2016-2020, while the AW transport at OS2 was moderate (0.25-0.75 Sv) in 2009-2014 and exceeded 0.5 Sv from 2015-onwards (Figure 11b).

The western part of the offshore circulation (OS1) was regularly fed by the YB reaching the Yermak Plateau tip, either flowing along the western edge of Yermak Plateau (plain yellow arrow in Figure 14), or through shortcuts across Plateau (dashed yellow arrows in Figure 14), and joining the northeastward flow in the Sofia Deep (green arrows in Figure 14; Supplementary Material S2). Furthermore, the cyclonic recirculation centered around 24°E, 83.8°N (grey arrow in Figure 14) recurrently advected colder and fresher waters from the deep WNB interior (>3900 m isobaths) towards OS1 (Figures 4c-h). Interestingly, waters carried across OS2 were on average warmer and saltier than at OS1 ($\Theta\sim$ +0.4°C, $S_A\sim$ +0.02g/kg), indicating an additional contribution from the boundary current through enhanced basin-ward mesoscale activity injecting AW offshore.

5. Changes in AW properties and pathways in the WNB over 2008-2020

Velocity trends at 265 m highlighted the major circulation changes that is, the intensification of the YB at 82°N (with a local significant maximum of +3 cm/s/decade) and the development of the "V-shaped" offshore circulation (with a salient trend of +4 cm/s/decade) (Figure 12a). Other interesting features were the velocity decrease in the recirculation branches around the Molloy Deep (79°N) (-2 cm/s/decade) and intensification of recirculations north of 82°N (up to +2 cm/s/decade) (Figure 12a). The boundary current exhibited large positive velocity trends in the vicinity of

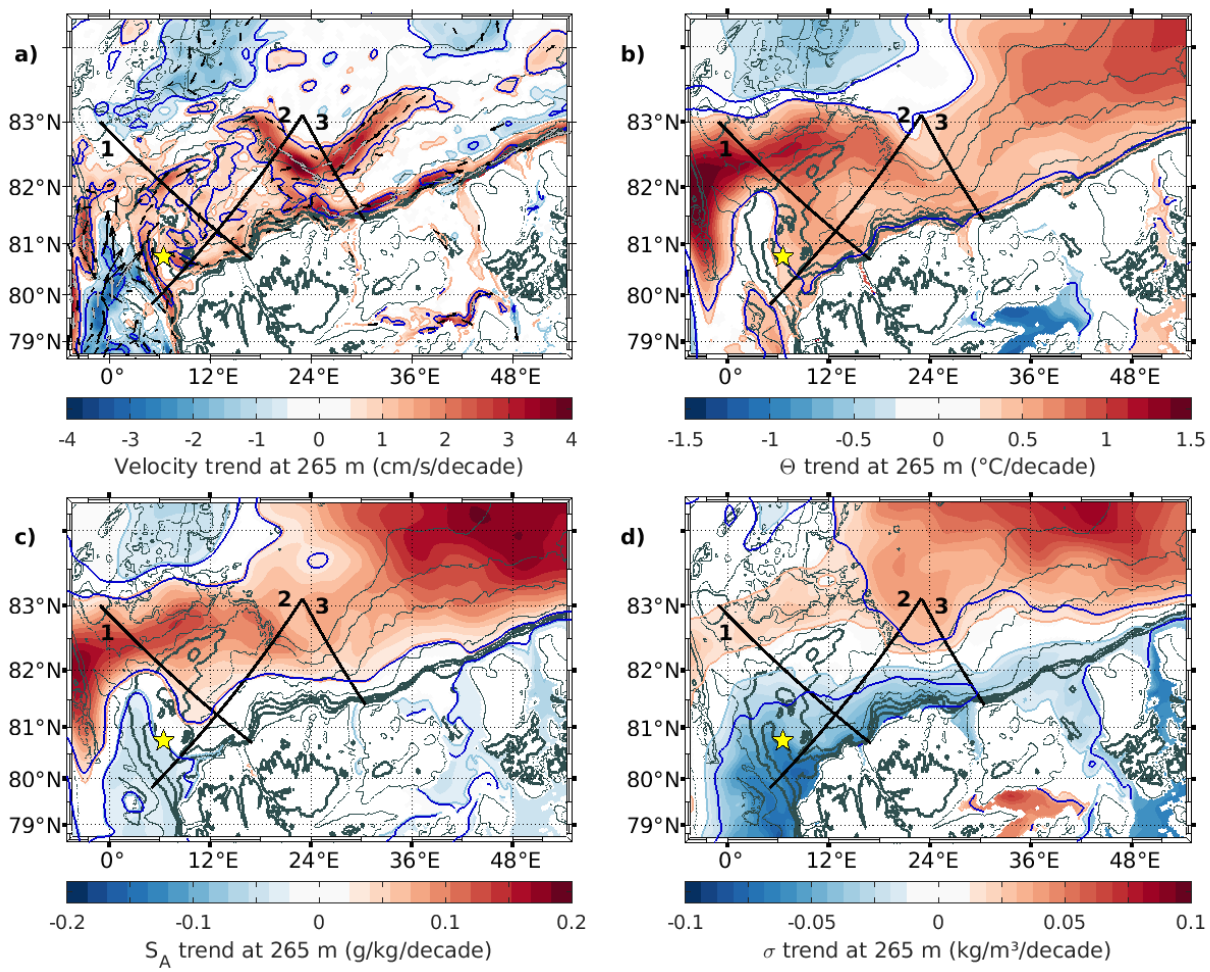

Figure 12: (a) Linear velocity trends (cm/s/decade) at 265 m, computed over a 12-year period (2008-2020). Velocity trend vectors are plotted in black arrows (grey arrows) for intensity trends larger than ±1 cm/s/decade (±2.5 cm/s/decade). (b) Linear trends of Conservative Temperature (Θ, °C/decade) at 265 m. (c) Same for Absolute Salinity trends (S_A, g/kg/decade) and (d) potential density trends (σ, kg/m³/decade). For (a) to (d), values under the 99.9% significance level are whitened. Blue contours delineate points where the 12-year trend is larger than the STD. The yellow star is the location of the mooring as in Figure 1. Isobaths contours are as in Figure 4. Thick black lines numbered 1 to 3 are the transects presented in Figures 7, 9 and 10.

trough openings: this could indicate enhanced instabilities and mesoscale activity, such as the frequent meandering described in section 4.2.

Positive trends in temperature and salinity at 265 m (core of the AW layer, Figures 12b and 12c) were consistent with these strengthening AW pathways (Figure 12a). Large positive trends to the north and northwest of Yermak Plateau (up to +1.5°C/decade, +0.15 g/kg/decade, +0.03 kg/m³/decade; Figures 12b, 12c, 12d) corresponded to the intensification of the YB and northward shift of AW recirculation branches (Figure 12a). Another large increase in temperature, salinity and density at 265 m was located

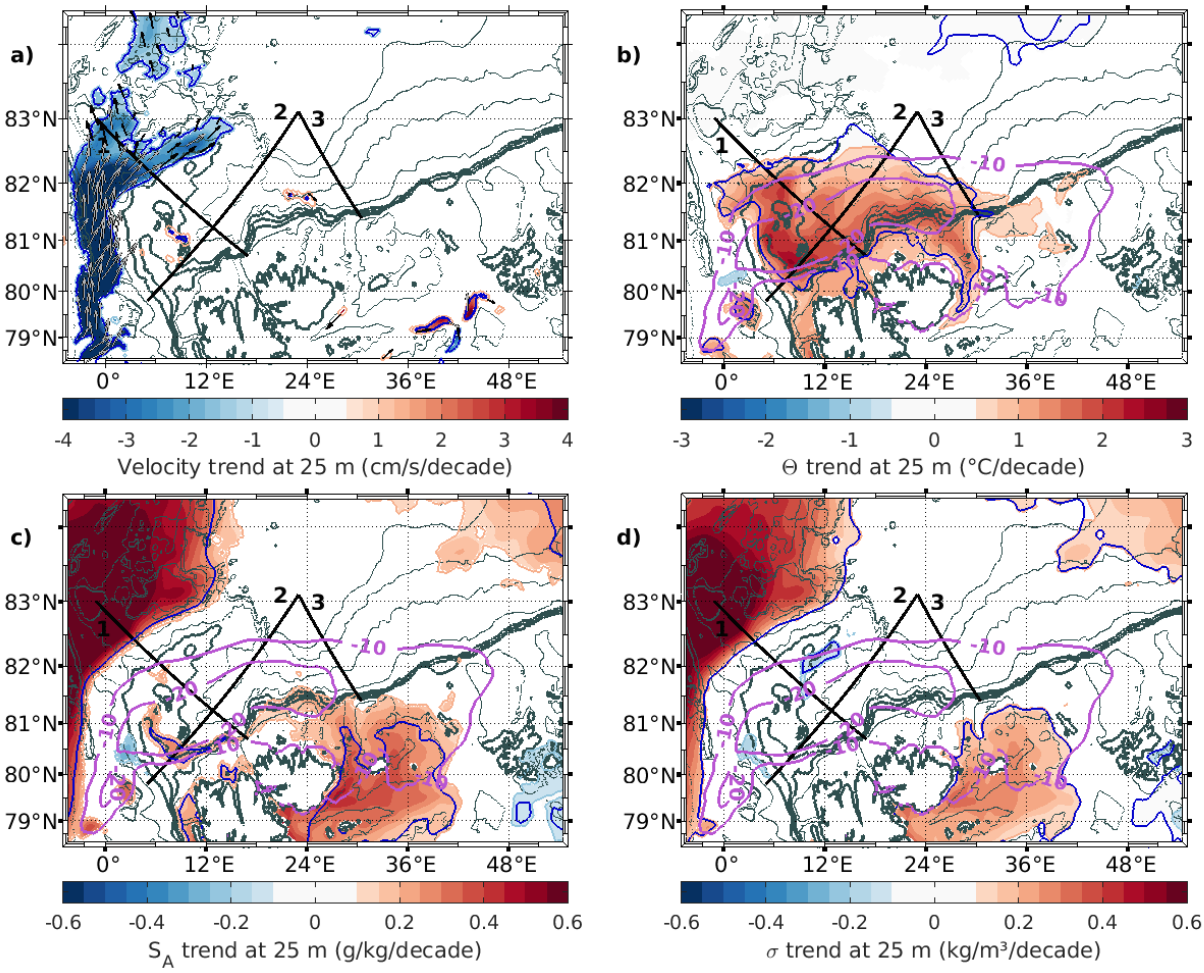

Figure 13: (a) Linear velocity trends (cm/s/decade) at 25 m, computed over a 12-year period (2008-2020). Velocity trend vectors are plotted in black arrows (grey arrows) for intensity trends larger than ±1 cm/s/decade (±2.5 cm/s/decade). (b) Linear trends of Conservative Temperature (Θ, °C/decade) at 25 m. (c) Same for Absolute Salinity trends (S_A, g/kg/decade) and (d) potential density trends (σ, kg/m³/decade). For (a) to (d), values under the 99.9% significance level are whitened. The pink contours on (b) to (d) are the -10 and -20% trends in sea-ice cover (%/decade). Blue contours delineate points where the 12-year trend is larger than the STD. Isobaths contours are as in Figure 4. Thick black lines numbered 1 to 3 are the transects presented in Figures 7, 9 and 10.

northeast of 83°N, 30°E (Figure 12b, 12c, 12d) downstream of the intensifying "V-shaped" offshore circulation, bringing more warm and salty AW from the boundary current towards the basin interior (Figure 12a).

The warming AW inflow (+0.5°C/decade, Figure 12b) exhibited notable freshening in 2018-2020 (Figures 9a-b, 12c). This recent salinity decrease was consistent with the 2017-2020 mooring data in the YPB (Figures 2b, 2d) and likely caused by the propagation of extreme fresh anomalies observed in 2012-2018 in the upstream North Atlantic and Norwegian Sea (Mork et al., 2019; Holliday et al., 2020). As a result, the

density decreased along the slope south of 82°N at 265 m (-0.05 kg/m^3/decade, Figure 12d) in the 100-900 m layer (Figures 7f, 9f, 10f). As discussed in section 4, the significant warming spread over the upper 1000 m of the WNB and was maximum in the upper 200 m (+2°C/decade) (Figures 7d, 9d, 10d). This near-surface warming was associated with a maximum salinity increase (exceeding +0.2 g/kg/decade at 100 m) (Figures 7e, 9e, 10e) and the shoaling of the AW layer.

Near the surface, negative velocity trends west of 0°E (-1 to -4 cm/s/decade) possibly indicated a reduction or shift of the Transpolar Drift (TPD) and the increasing influence of the YB near the surface on the northwestern flank of Yermak Plateau (Figure 13a).

The warming trend at 25 m, reaching 2.5°C/decade over the YPB, did not extend further than 83°N and coincided with a sea-ice cover decline larger than -10%/decade (reaching up to -30%/decade over YPB; Figure 13b). A striking signal in salinity and density at 25 m was the dramatic positive trends within the Transpolar Drift pathway (blue in Figure 13a), centered around 83°N, 0°E (> +0.6 g/kg/decade, +0.5 kg/m^3/decade; Figures 7e-f, 13c, 13d). Along transect 1, salinity at 25 m showed the northwestward AW progression, and the reducing ice cover allowed the atmosphere to maintain close-to-freezing temperatures (not shown).

There were no significant trends in salinity and density at 25 m in the WNB interior; however, the continental shelf exhibited positive trends exceeding local STD values (+0.2 g/kg/decade, +0.15 kg/m^3/decade; Figures 13c, 13d). This could be due to a change in the upstream Barents Sea conditions, out of the scope of this study.

6. Summary and discussion

We used 12 years of PSY4 fields to examine the evolution of the circulation, volume transport and properties of AW in their major entry region, the Western Nansen Basin (WNB). Previous examination of the model performance in the WNB underlined the good skill of PSY4 in representing realistic AW inflow and properties (Athanase et al., 2020), despite some inherent limitations. Indeed, the model is not fully eddy-resolving in the area (i.e. grid size of 4 km, and Rossby deformation radius of ~10 km; Crews et al., 2017) and does not simulate tides which are important above and on the slopes of the Yermak Plateau (e.g. Padman et al., 1992; Koenig et al., 2017b; Fer et al., 2020). Further comparisons with a 32 month-long (2017-2020) time series of temperature

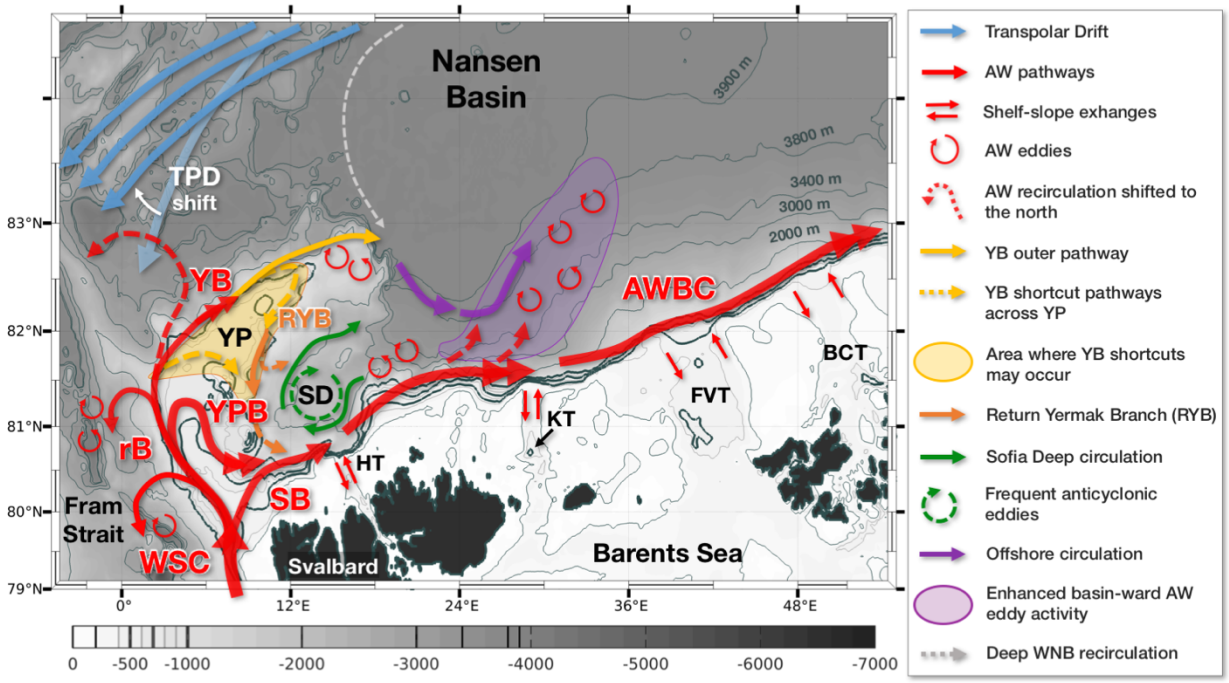

Figure 14: Schematic circulation and water pathways over the Yermak Plateau and in the WNB in the recent 2011-2020 period, as suggested by PSY4. Blue arrows represent the near-surface Transpolar Drift (TPD). Red arrows are the Atlantic Water (AW) circulation documented in the literature; orange, green and purple arrows are the newly suggested AW pathways. WSC: West Spitsbergen Current; SB: Svalbard Branch; YPB: Yermak Pass Branch; YB: Yermak Branch; RYB: Return Yermak Branch; AWBC: AW Boundary Current; rB: recirculation Branches; SD: Sofia Deep; YP: Yermak Plateau; HT, KT, FVT and BCT: Hinlopen, Kvitøya, Franz-Victoria and British Chanel Troughs.

and salinity at 350 m in the Yermak Pass (Labaste et al., 2020) and with a CNES/CLS multi-mission altimetry product prototype for the Arctic Ocean (2016-2018) confirmed the good performance of PSY4 in recent years. The skill of the model in reproducing the properties and velocity in the AW boundary current was further demonstrated by comparing modelled and observed AW volume transport at 30°E in 2012-2013 (correlation of r=0.79 with 10-day smoothed A-TWAIN observations, significant at the 99% confidence level). PSY4 was thus trusted to examine AW circulation and volume transport in the WNB.

Circulation patterns at 265 m have changed in the WNB over 2008-2020 (compare Figures 14 and 1; trends in Figures 12 and 13). Major changes include the strengthening of the Yermak Branch (YB) (yellow arrows in Figure 14) feeding the Return Yermak Branch (RYB) along the eastern flank of the Plateau (orange arrows). Downstream of Yermak Plateau, a circulation developed offshore following a V-shape

above isobaths 3800-3900 m (purple arrows). The western part of the offshore flow was fed with waters from the Yermak Plateau tip starting in 2015. As early as 2009, enhanced basin-ward mesoscale activity contributed to the northeastward part of the offshore current, bringing warm and salty AW (purple area in Figure 14). Indeed, the AWBC strengthened east of 18°E, with more frequent meandering (schematized with double red arrows in Figure 14). A recurrent anticyclonic circulation in Sofia Deep developed, either via long-lived eddies or anticyclonic meanders (green arrows), which also occasionally fed the western part of the offshore flow. West of Yermak Plateau, the Transpolar Drift likely shifted westward (blue arrows) while AW recirculations progressed further north (dashed red arrow).

These circulation changes have yet to be considered with caution. Indeed, it is possible that the offshore intensification from 2011-onwards could result from a spin-up period larger than the 15 months estimated here (see Appendix), due to particularly small velocities in the WNB interior (about 2-3 cm/s). Nonetheless, the changes were consistent with the few available observational studies. The development of the offshore circulation was concordant with the existence of a local minimum in SSH fields north of the 3800 m isobath (see section 2.2.), inducing horizontal SSH gradients along the 3800-3900m isobaths and thus surface geostrophic velocities. Furthermore, several studies documented AW mesoscale structures along the track of the eastern, basin-ward part of the offshore flow (Våge et al., 2016; Pérez-Hernández et al., 2017; Athanase et al., 2019). Observations over the continental slope also supported the evolution of the boundary current: indeed, Ivanov et al. (2009) reported a highly persistent direction of the flow in the AWBC near 30°E in 2004, while at the same location the boundary current was observed to be baroclinically unstable, meandering across the slope and shedding eddies in 2012-2013 (Våge et al., 2016; Pérez-Hernández et al., 2017, 2019). Recent in-situ data from Kolås et al. (2020) in summer and fall 2018 in the Sofia Deep documented a westward countercurrent just to the north of the boundary current in the Sofia Deep and detaching from the slope at 18°E, in agreement with the modelled anticyclonic circulation in Sofia Deep. Finally, a meander of AW turning back towards Fram Strait was observed at 82.8°N, 3°W in December 2017 (Athanase et al., 2019), supporting the northward shift of recirculation branches.

The intensification of the circulation coincided with an overall warming and salinification in the upper 1000 m of the WNB interior, consistent with the progression of AW in the region (Figures 7, 9, 10, 12b). Interestingly, the warming AW inflow exhibited negative salinity trends (Figure 12c), resulting from a notable freshening in 2018-2020 (Figures 7a-b, 9a-b, 10a-b). The recent 2017-2020 mooring data in the YPB further documented this salinity decrease (Figures 2b, 2d). The freshening of the AW inflow was in agreement with the extreme fresh anomalies observed in the upstream North Atlantic in 2012-2016 and in the Norwegian Sea in 2017-2018, caused by wind-driven changes in the ocean circulation which advected fresher waters of Arctic origin into the subpolar North Atlantic (Mork et al., 2019; Holliday et al., 2020). This underlines the crucial role of upstream atmospheric and oceanic conditions in determining the properties of AW entering the Arctic.

PSY4 yielded insights on AW pathways and volume transports in the rapidly transitioning Western Nansen Basin. This regional description of the changing circulation provides a background for the interpretation of upcoming mooring and synoptic cruise data, which might revise the present conclusions.

Appendix: Initial conditions in the PSY4 system

The PSY4 system was initialized with temperature and salinity from EN4.2.1 fields in October 2006 (Good et al., 2013). The October 2006 salinity field exhibited an unexpected pattern with a local minimum (S_A(265m)<34.9 g/kg) radiating from the Franz-Josef shelf towards the pole along the 50°E longitude (Figure A1), likely created by undesirable interpolations or extrapolations of remote observations in this data-sparse area.

Time-series of vertical profiles in the spurious initial salinity minimum at 55°E (Figure A1d, A1e) illustrate the evolution of temperature and salinity from these initial conditions. In the AW layer (265 m), AW salinity near 50°E decreased sharply from its anomalously fresh values until stabilizing around 35 g/kg in early 2008. Hence, the spin-up time in the Western Nansen Basin was considered to be 15 months and time series were only considered from April 2008 onwards.

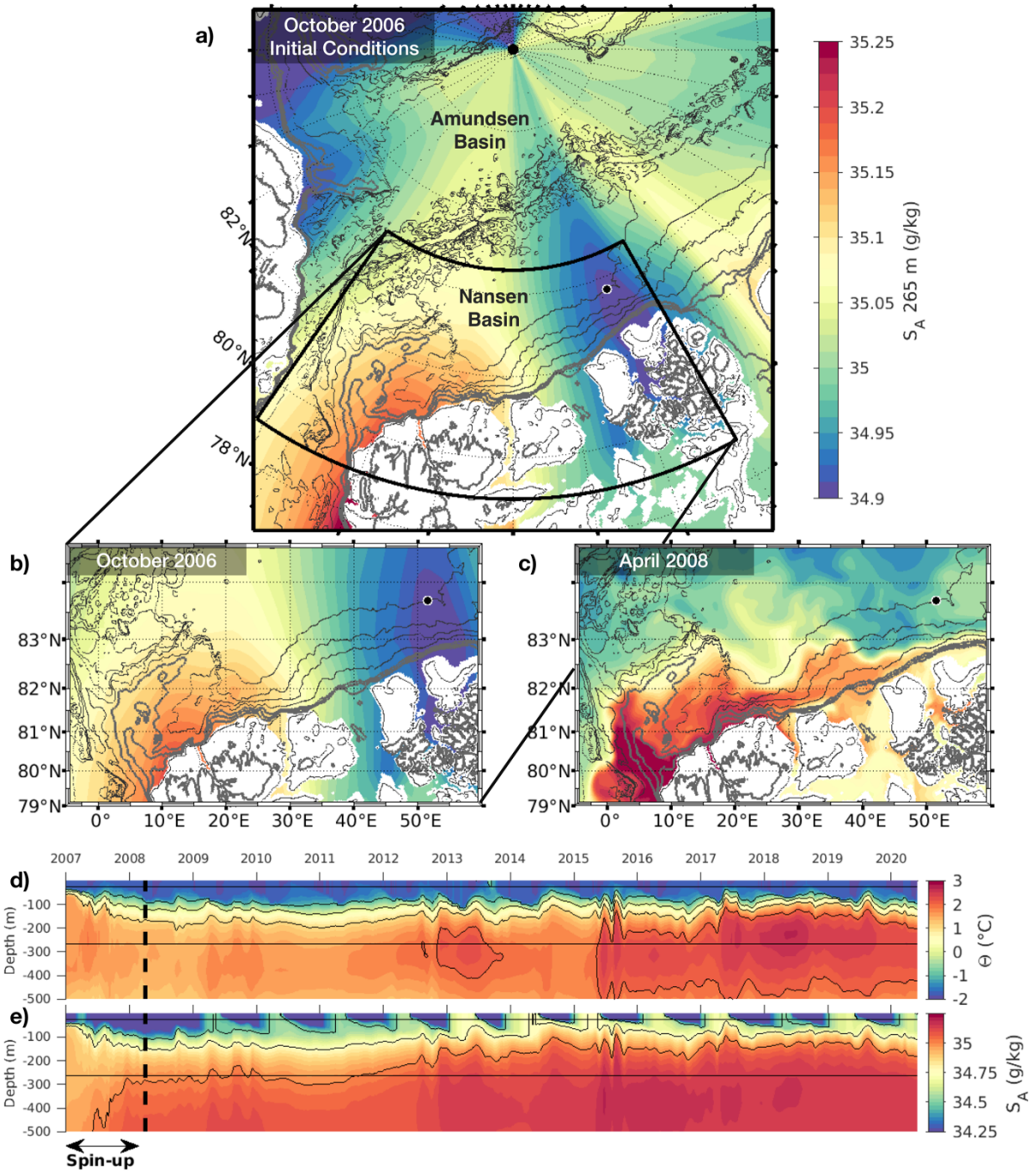

Figure A1: (a) Initial conditions of the PSY4 system in October 2006 over the Western Eurasian Basin, in Absolute Salinity (S_A, g/kg) at 265 m. Grey contours is the IBCAO bathymetry. (b) Same as (a), focused on the Western Nansen Basin (WNB) area (black box on (a)). (c) Absolute Salinity (g/kg) at 265 m, in April 2008. (d) Time series (upper 500 m) of Conservative Temperature (Θ, °C) and (e) Absolute Salinity (g/kg) at the location of the initial local salinity minimum (black point on (a) to (c)). Depths 25 and 265 m are reported as horizontal lines. The spin-up period (January 2007-April 2008) for the WNB area is delineated by the thick dashed line.

Indeed, the WNB region considered here constitutes in a trapeze-shaped area of 600 km width (north-south), and minimum (northern edge) and maximum (southern edge) length of 600 and 1200 km. In this region, the assimilation of parameters other than sea-ice are primarily confined to the ice-free Fram Strait. Times of advection from Fram Strait to the ice-covered basin interior were estimated to be roughly on the order of 10 to 15 months.

The computations shown in the manuscript were also performed on a shorter time-series (April 2009 to May 2019) and the results were not significantly different.

Acknowledgments:

We gratefully acknowledge all the people that contributed to gather the observations used for model validation in this study. The model outputs are available at Copernicus Marine Environment Monitoring Service (CMEMS; http://marine.copernicus.eu/). Marylou Athanase was supported through the Pan-Arctic Options Belmont Forum project (ANR-14-AORS-003-01), Cecilia Bertosio through IAOOS grant A18JROI002 at Sorbonne University, and M. Dolores Pérez-Hernández through the "Programa Postdoctoral de la Universidad de Las Palmas de Gran Canaria". We are deeply grateful to editor Laurie Padman and two anonymous reviewers, whose detailed comments and suggestions helped improve the manuscript.

References:

Athanase, M., Sennéchael, N., Garric, G., Koenig, Z., Boles, E., & Provost, C. (2019). New Hydrographic Measurements of the Upper Arctic Western Eurasian Basin in 2017 Reveal Fresher Mixed Layer and Shallower Warm Layer Than 2005–2012 Climatology. Journal of Geophysical Research: Oceans, 124(2), 1091-1114. DOI: 10.1029/2018JC014701

Athanase, M., Provost, C., Pérez-Hernández, M. D., Sennéchael, N., Bertosio, C., Artana, C., et al. (2020). Atlantic Water modification North of Svalbard in the Mercator Physical System from 2007 to 2020. Journal of Geophysical Research: Oceans, e2020JC016463. DOI: 10.1029/2020JC016463

Bertosio, C., Provost, C., Sennéchael, N., Artana, C., Athanase, M., Boles, E., et al. (2020). The Western Eurasian Basin halocline in 2017: insights from autonomous NO measurements and the Mercator physical system. Journal of Geophysical Research: Oceans, 125(7), e2020JC016204. DOI:10.1029/2020JC016204

Beszczynska-Möller, A., Fahrbach, E., Schauer, U., & Hansen, E. (2012). Variability in Atlantic water temperature and transport at the entrance to the Arctic Ocean, 1997–2010. ICES Journal of Marine Science, 69(5), 852-863. DOI: 10.1093/icesjms/fss056

Boyd, T. J., & D'Asaro, E. A. (1994). Cooling of the West Spitsbergen Current: wintertime observations west of Svalbard. Journal of Geophysical Research: Oceans, 99(C11), 22597-22618. DOI: 10.1029/94JC01824

Bretherton, F. P., Davis, R. E. & C.B. Fandry (1976). A technique for objective analysis and design of oceanographic experiments applied to MODE-73, Deep Sea Research and Oceanographic Abstracts, Volume 23, Issue 7, Pages 559-582, ISSN 0011-7471. DOI: 10.1016/0011-7471(76)90001-2.

Cokelet, E. D., N. Tervalon, & J. G. Bellingham (2008), Hydrography of the West Spitsbergen Current, Svalbard Branch: Autumn 2001, Journal Geophysical Research, 113, C01006, DOI:10.1029/2007JC004150

Crews, L., Sundfjord, A., Albretsen, J., & Hattermann, T. (2018). Mesoscale eddy activity and transport in the Atlantic Water inflow region north of Svalbard. Journal of Geophysical Research: Oceans, 123, 201–215. DOI: 10.1002/2017JC013198

Crews, L., Sundfjord, A., & Hattermann, T. (2019). How the Yermak Pass Branch Regulates Atlantic Water Inflow to the Arctic Ocean. Journal of Geophysical Research: Oceans, 124(1), 267-280. DOI: 10.1029/2018JC014476

Ducet, N., Le Traon, P. Y., & Reverdin, G. (2000). Global high-resolution mapping of ocean circulation from TOPEX/Poseidon and ERS-1 and -2, Journal of Geophysical Research: Oceans, 105(C8), 19477– 19498, DOI: 10.1029/2000JC900063.

Fer, I., Koenig, Z., Kozlov, I. E., Ostrowski, M., Rippeth, T. P., & Padman, L., et al. (2020). Tidally forced lee waves drive turbulent mixing along the Arctic Ocean margins. Geophysical Research Letters, 47, e2020GL088083. DOI: 10.1029/2020GL088083

Good, S. A., Martin, M. J., & Rayner, N. A. (2013), EN4: Quality controlled ocean temperature and salinity profiles and monthly objective analyses with uncertainty estimates. Journal of Geophysical Research: Oceans, 118, 6704–6716. DOI:10.1002/2013JC009067

Hattermann, T., Isachsen, P. E., von Appen, W. J., Albretsen, J., & Sundfjord, A. (2016). Eddy-driven recirculation of Atlantic water in Fram Strait. Geophysical Research Letters, 43(7), 3406-3414. DOI: 10.1002/2016GL068323

Holliday, N. P., Bersch, M., Berx, B., Chafik, L., Cunningham, S., Florindo-López, C., et al. (2020). Ocean circulation causes the largest freshening event for 120 years in eastern subpolar North Atlantic. Nature communications, 11(1), 1-15. DOI: 10.1038/s41467-020-14474-y

Hu, X., Myers, P. G., & Lu, Y. (2019). Pacific Water Pathway in the Arctic Ocean and Beaufort Gyre in Two Simulations With Different Horizontal Resolutions. Journal of Geophysical Research: Oceans, 124(8), 6414-6432. DOI: 10.1029/2019JC015111

Ivanov, V. V., Polyakov, I. V., Dmitrenko, I. A., Hansen, E., Repina, I. A., Kirillov, S. A., et al. (2009). Seasonal variability in Atlantic water off Spitsbergen. Deep Sea Research Part I: Oceanographic Research Papers, 56(1), 1-14. DOI: 10.1016/j.dsr.2008.07.013

Ivanov, V., Smirnov, A., Alexeev, V., Koldunov, N. V., Repina, I., & Semenov, V. (2018). Contribution of Convection-Induced Heat Flux to Winter Ice Decay in the Western Nansen Basin. Journal of Geophysical Research: Oceans, 123(9), 6581-6597. DOI: 10.1029/2018JC013995

Jakobsson, M., Mayer, L., Coakley, B., Dowdeswell, J. A., Forbes, S., Fridman, B., et al. (2012). The international bathymetric chart of the Arctic Ocean (IBCAO) version 3.0. Geophysical Research Letters, 39(12). DOI:10.1029/2012GL052219

Koenig, Z., C. Provost, N. Villacieros- Robineau, N. Sennéchael, A. Meyer, J.-M. Lellouche, and G. Garric (2017a), Atlantic waters inflow north of Svalbard: Insights from IAOOS observations and Mercator Ocean global operational system during N-ICE2015, J. Geophys. Res. Oceans, 122, 1254–1273. DOI:10.1002/ 2016JC012424.

Koenig, Z., Provost, C., Sennéchael, N., Garric, G., & Gascard, J.-C. (2017b). The Yermak Pass Branch: A major pathway for the Atlantic Water north of Svalbard? Journal of Geophysical Research: Oceans, 122. DOI: 10.1002/2017JC013271

Koenig, Z., Meyer, A., Provost, C., Sennéchael, N., Sundfjord, A., Beguery, L., et al. (2018). Cooling and Freshening of the West Spitsbergen Current by Shelf-Origin Cold Core Lenses. Journal of Geophysical Research: Oceans, 123(11), 8299-8312. DOI: 10.1029/2018JC014463

Kolås, E. H., Koenig, Z., Fer, I., Nilsen, F., & Marnela, M. Structure and transport of Atlantic Water north of Svalbard from observations in summer and fall 2018. Journal of Geophysical Research: Oceans, e2020JC016174. DOI: 10.1029/2020JC016174

Labaste M., Gascard J-C., Provost C., Sennéchael N., & Athanase M. (2020). Yermak Plateau mooring: SBE37 CTD at 350 m, in 2017-2020. SEANOE. DOI: 10.17882/76330

Lellouche, J. M., Greiner, E., Le Galloudec, O., Garric, G., Regnier, C., Drevillon, M. et al. (2018). Recent updates to the Copernicus Marine Service global ocean monitoring and forecasting real-time 1⁄12° high-resolution system. Ocean Science, 14(5), 1093-1126. DOI: 10.5194/os-14-1093-2018

Manley, T. O., Bourke, R. H., & Hunkins, K. L. (1992). Near-surface circulation over the Yermak Plateau in northern Fram Strait. Journal of Marine Systems, 3(1-2), 107-125. DOI: 10.1016/0924-7963(92)90033-5

Manley, T. O. (1995). Branching of Atlantic water within the Greenland-Spitsbergen passage: an estimate of recirculation. Journal of Geophysical Research: Oceans, 100(C10), 20627-20634. DOI: 10.1029/95JC01251

Menze, S., Ingvaldsen, R. B., Haugan, P., Fer, I., Sundfjord, A., Beszczynska-Moeller, A., & Falk-Petersen, S. (2019). Atlantic water pathways along the north-western Svalbard shelf

mapped using vessel-mounted current profilers. Journal of Geophysical Research: Oceans, 124(3), 1699-1716. DOI: 10.1029/2018JC014299

Meyer, A., Sundfjord, A., Fer, I., Provost, C., Villacieros Robineau, N., Koenig, Z., et al. (2017). Winter to summer oceanographic observations in the Arctic Ocean north of Svalbard. Journal of Geophysical Research: Oceans, 122(8), 6218-6237. DOI:10.1002/2016JC012391.

Mork, K. A., Skagseth, Ø., & Søiland, H. (2019). Recent warming and freshening of the Norwegian Sea observed by Argo data. Journal of Climate, 32(12), 3695-3705. DOI: 10.1175/JCLI-D-18-0591.1

Muench, R. D., McPhee, M. G., Paulson, C. A., & Morison, J. H. (1992). Winter oceanographic conditions in the Fram Strait-Yermak Plateau region. Journal of Geophysical Research: Oceans, 97(C3), 3469-3483. DOI: 10.1029/91JC03107

Onarheim, I. H., Smedsrud, L. H., Ingvaldsen, R. B., & Nilsen, F. (2014). Loss of sea ice during winter north of Svalbard. Tellus A: Dynamic Meteorology and Oceanography, 66(1), 23933. DOI: /10.3402/tellusa.v66.23933

Padman, L., Plueddemann, A., Muench, R. & Pinkel, R. (1992). Diurnal Tides Near the Yermak Plateau. Journal of Geophysical Research. 97. 12639-12652. DOI: 10.1029/92JC01097.

Pérez-Hernández, M. D., Pickart, R. S., Pavlov, V., Våge, K., Ingvaldsen, R., Sundfjord, A., et al. (2017). The Atlantic Water boundary current north of Svalbard in late summer. Journal of Geophysical Research: Oceans, 122(3), 2269-2290. DOI: 10.1029/2018JC014299

Pérez-Hernández, M. D., Pickart, R. S., Torres, D. J., Bahr, F., Sundfjord, A., Ingvaldsen, R., et al. (2019). Structure, Transport, and Seasonality of the Atlantic Water Boundary Current North of Svalbard: Results From a Yearlong Mooring Array. Journal of Geophysical Research: Oceans, 124(3), 1679-1698. DOI: 10.1029/2018JC014759

Poisson, J., Quartly, G. D. , Kurekin, A. A., Thibaut, P., Hoang, D. & Nencioli, F. (2018). Development of an ENVISAT Altimetry Processor Providing Sea Level Continuity Between Open Ocean and Arctic Leads," in IEEE Transactions on Geoscience and Remote Sensing, vol. 56, no. 9, pp. 5299-5319. DOI: 10.1109/TGRS.2018.2813061.

Polyakov, I. V., Pnyushkov, A. V., Alkire, M. B., Ashik, I. M., Baumann, T. M., Carmack, E. C., et al. (2017). Greater role for Atlantic inflows on sea-ice loss in the Eurasian Basin of the Arctic Ocean. Science, 356(6335), 285-291. DOI: 10.1126/science.aai8204

Polyakov, I. V., Rippeth, T. P., Fer, I., Baumann, T. M., Carmack, E. C., Ivanov, V. V., et al. (2020b). Intensification of Near-Surface Currents and Shear in the Eastern Arctic Ocean. Geophysical Research Letters, e2020GL089469. DOI: 10.1029/2020GL089469

Renner, A. H. H., Sundfjord, A., Janout, M. A., Ingvaldsen, R., Beszczynska-Möller, A., Pickart, R., & Pérez-Hernández, M., (2018). Variability and redistribution of heat in the Atlantic Water boundary current north of Svalbard. Journal of Geophysical Research: Oceans, 123, 6373–6391. DOI: 10.1029/2018JC013814

Rudels, B., Korhonen, M., Schauer, U., Pisarev, S., Rabe, B., & Wisotzki, A. (2015). Circulation and transformation of Atlantic water in the Eurasian Basin and the contribution of the Fram Strait inflow branch to the Arctic Ocean heat budget. Progress in Oceanography, 132, 128-152. DOI: 10.1016/j.pocean.2014.04.003

Schauer, U., Muench, R. D., Rudels, B., & Timokhov, L. (1997). Impact of eastern Arctic shelf waters on the Nansen Basin intermediate layers. Journal of Geophysical Research: Oceans, 102(C2), 3371-3382. DOI: 10.1029/96JC03366

Sirevaag, A., de La Rosa, S., Fer, I., Nicolaus, M., Tjernström, M., & McPhee, M. G. (2011). Mixing, heat fluxes and heat content evolution of the Arctic Ocean mixed layer. Ocean Science, 7(3), 335-349. DOI: 10.5194/os-7-335-2011

Timmermans, M.-L., & Marshall, J. (2020). Understanding Arctic Ocean circulation: a review of ocean dynamics in a changing climate. Journal of Geophysical Research: Oceans, 125, e2018JC014378. DOI: 10.1029/2018JC014378

Våge, K., R. S. Pickart, V. Pavlov, P. Lin, D. J. Torres, R. Ingvaldsen, et al. (2016). The Atlantic Water boundary current in the Nansen Basin: Transport and mechanisms of lateral exchange, Journal of Geophysical Research: Oceans, 121, 6946–6960. DOI:10.1002/2016JC011715.

Valladares, J., Fennel, W., & Morozov, E. (2011). Replacement of EOS-80 with the International Thermodynamic Equation of Seawater–2010 (TEOS-10). Deep-Sea Res. Pt. I, 58, 978. DOI: 10.1016/j.dsr.2011.07.005

CHAPTER 5

Conclusions and perspectives

Contents

5.1. Summary and conclusions

We examined the oceanic conditions in the Western Eurasian Basin, using in-situ observations and the 1/12° Mercator Ocean global system (called PSY4 hereafter).

In 2017, two IAOOS (Ice Atmosphere Ocean Observing System) platforms gathered a unique 8-month long hydrographic dataset in the upper Western Eurasian Basin (WEB, 0-350m). The IAOOS 2017 physical data documented four hydrographic regions (Amundsen Basin, Gakkel Ridge, Nansen Basin and Fram Strait) and featured two halocline eddies in the Amundsen Basin and two AW mesoscale structures in the Nansen Basin (named AW1 and AW2; Figure 5.1) (Athanase et al., 2019). The surface layer was fresher (-0.2 to -1.5 g/kg) in 2017 than in the 2005-2012 World Ocean Atlas (WOA13) monthly climatology. In the Amundsen Basin, this was mainly due to the southeastward shift of the frontal region between fresher Makarov waters and saltier Eurasian waters. Compared to WOA13, the frontal region was located about 40°E further southeast in 2017 due to the southward displacement of the Transpolar Drift, carrying waters from the Siberian shelves (Bertosio et al., 2020). In the Nansen Basin, the cause of the surface freshening remains unclear, as surface salinities exhibit large seasonal and interannual variations (Peralta-Ferriz and Woodgate, 2015) and several factors could be responsible for this change: concurrent enhanced sea-ice melt in summer and/or delayed freeze-up, increased river-discharges or a reduced export of low salinity water through Fram Strait (Rabe et al., 2014). Below, the warm layer was also 22 m shallower in 2017 than in 2005-2012, in agreement with the continuation of the Atlantification in the Eurasian Basin.

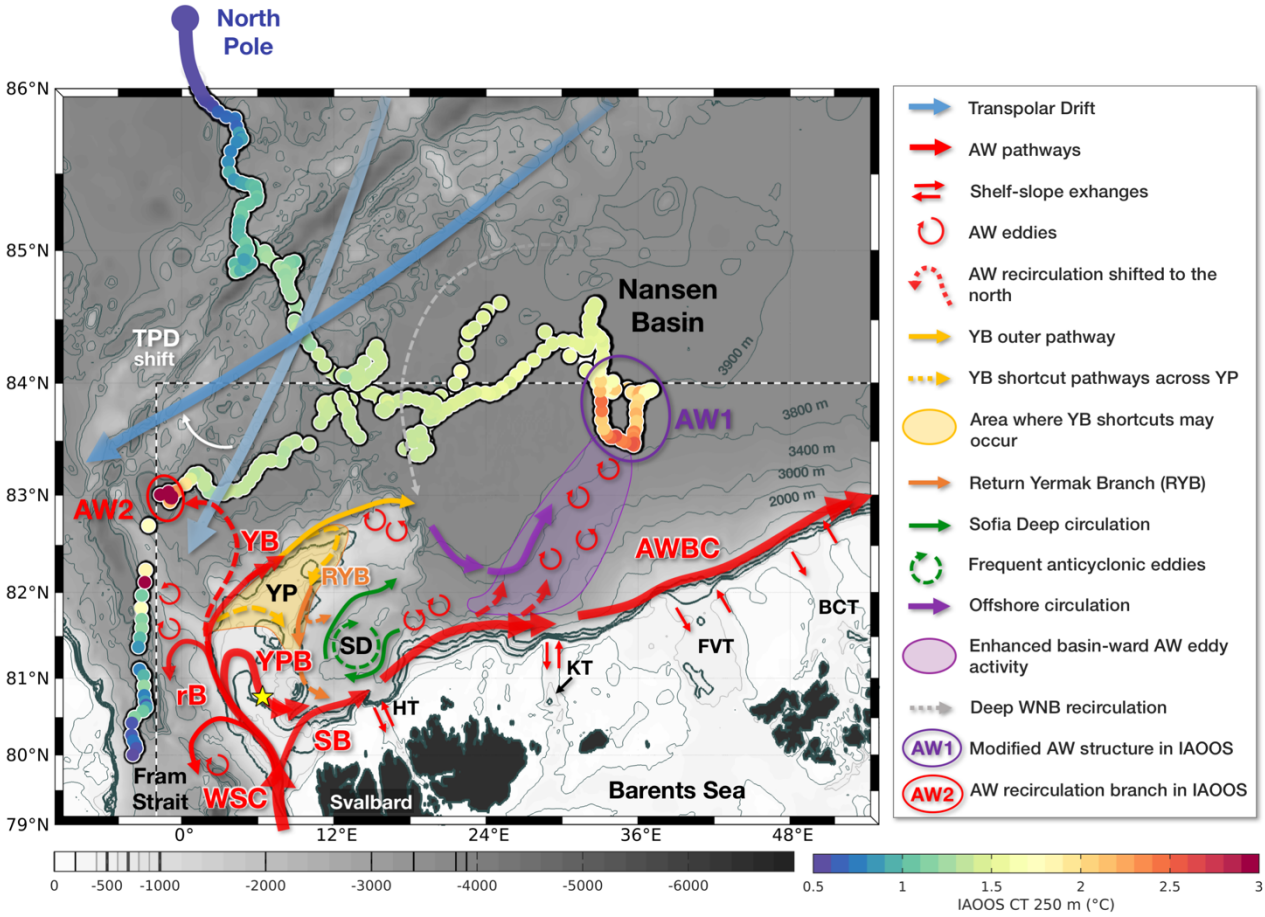

Figure 5.1: Schematic circulation and water pathways in the WNB in the recent 2011-2020 period, as suggested by the PSY4 fields. Bathymetry is in background grey scale. The colored dots are the conservative temperature (CT,°C) documented at 250 m by the IAOOS 2017 drift. The IAOOS drift track north of 86°N, starting near the North at 89°N, is schematized in dark blue. The dashed frame indicate the geographic limits of Figures 5.2 and 5.3 (84°N, 2°W). The yellow star marks the location of the Yermak Pass mooring. WSC: West Spitsbergen Current; SB: Svalbard Branch; YPB: Yermak Pass Branch; YB: Yermak Branch; AWBC: AW Boundary Current; rB: recirculation Branches; SD: Sofia Deep; YP: Yermak Plateau; HT, KT, FVT and BCT: Hinlopen, Kvitoya, Franz-Victoria and British Chanel Troughs. Adapted from Athanase et al. (submitted).

Vertical sections of model-observation differences underlined the good performance of PSY4, in particular in reproducing the observed mesoscale structures. PSY4 fields suggested that the halocline eddies resulted from instabilities in the Makarov-Eurasian waters frontal zone. The large AW1 structure in the Nansen Basin (140 km, purple ellipse in Figure 5.1) was identified as AW from the boundary current, turning into an anticyclonic eddy about one month after the platforms passage. Crossed in December 2017 at at 82.8°N, 3°W, AW2 corresponded to a particularly north AW recirculating branch detaching from the Yermak Plateau back toward Fram Strait (red ellipse in Figure 5.1).

The PSY4 performance was further evaluated in the Western Nansen Basin (WNB) over 2007-2020, period of available model fields (Athanase et al., 2020). At Fram Strait, PSY4 reproduced well the AW inflow properties, spatial structure and temporal variability documented by 5 years of mooring data (temperature, salinity and velocities). PSY4 T-S time-series in the variable Yermak Pass Branch were consistent with mooring data in 2017-2020, with correlation coefficients r~0.7. Comparisons with 12 years (2007-2018) of non-assimilated observations in the WNB showed that the model represented a realistic AW layer in the WNB. PSY4 well reproduced the 1-year long A-TWAIN mooring dataset (temperature, salinity and velocities), with deep winter mixed depths, changes in AW properties and AW volume transport matching the observations. Finally, the modelled SSH compared well to SSH from a multi-mission altimetry product prototype for the Arctic Ocean (available in 2016-2018).

We took advantage of the good performance of the PSY4 system in the WNB to examine the AW circulation in the WNB over 2008-2020 (Athanase et al., submitted). PSY4 showed the strengthening of Yermak Branch (YB) from 2011-onwards, feeding the southward Return Yermak Branch along the eastern flank of Yermak Plateau (orange arrows in Figure 5.1). The YB either flowed along the outer edge of the Yermak Plateau or crossed over the Plateau.

A 'V-shaped' offshore circulation developed downstream of Yermak Plateau, following the 3800-3900 m (purple arrows in Figure 5.1). The western part of the offshore flow was fed with waters from the Yermak Plateau tip. From 2009-onwards, enhanced basin-ward mesoscale activity contributed to the northeastward part of the offshore current, bringing warm and salty AW (purple area in Figure 5.1). Indeed, the AWBC strengthened east of 18°E, with more frequent meandering (schematized with double red arrows in Figure 5.1). This was in striking agreement with the AW1 structure documented by IAOOS platforms in 2017 (Athanase et al., 2019; purple ellipse in Figure 5.1). AW structures such as AW1 are likely increasingly common along the path of the strengthening offshore circulation.

A recurrent anticyclonic circulation in Sofia Deep developed, either via long-lived eddies or anticyclonic meanders (green arrows), which also occasionally fed the western part of the offshore flow. West of Yermak Plateau, the Transpolar Drift likely shifted westward (blue arrows in Figure 5.1). PSY4 showed that AW detached further

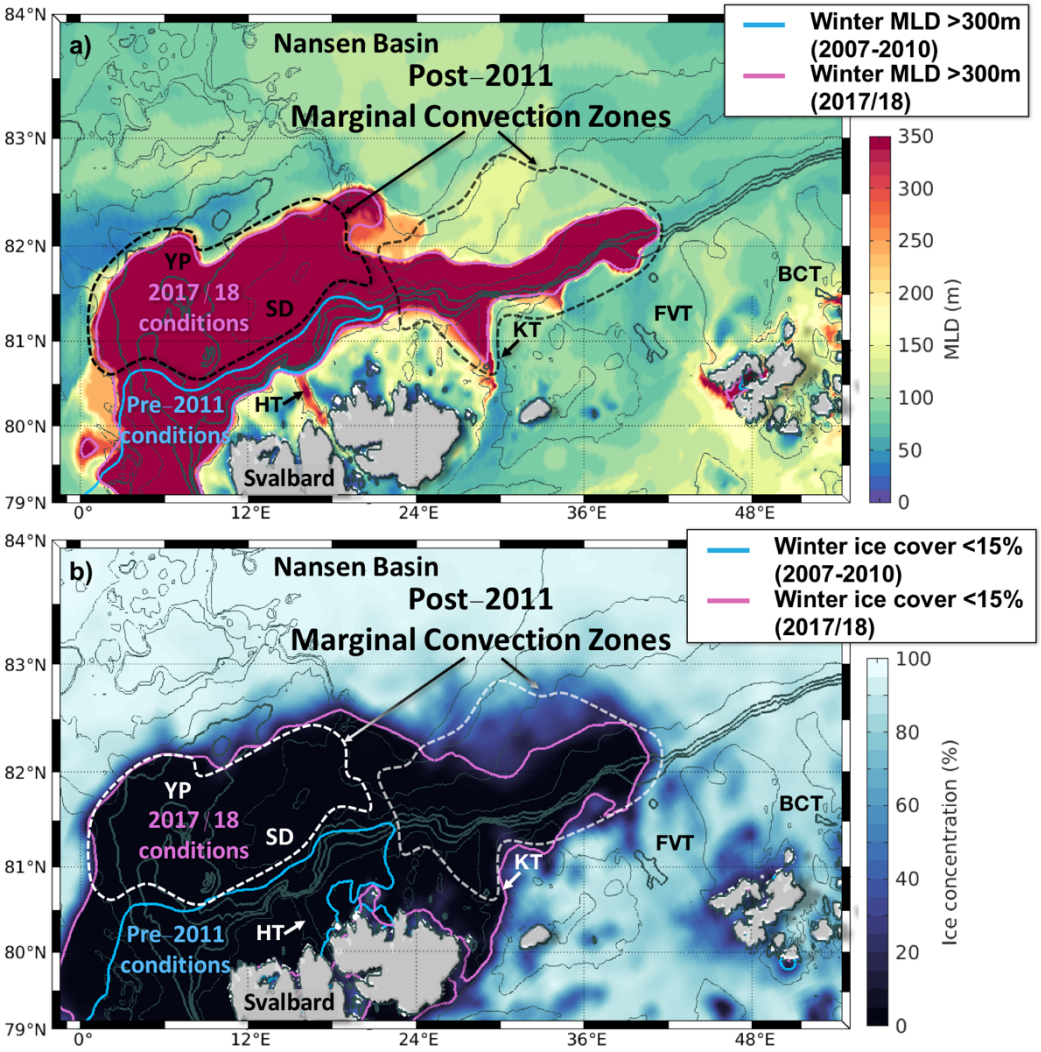

Figure 5.2 : (a) Maximum mixed layer depth (MLD, m) reached at each point in winter 2017/18, pink contours delineating areas where MLD>300m. (b) Associated sea-ice coverage (%), pink contours delineating the ice edge (15% ice cover). Blue contours are the 2007-2010 average (pre-2011) conditions of deep MLD (>300 m) on (a) and ice edge location (ice cover <15%) on (b). Areas circled in dashed lines used to be ice-covered in 2007-2010, and have been identified as « Marginal Convection Zones » from 2011-onwards, with occasionally ice-free conditions in winter and occurrences of convection-induced deep winter mixed layers. Geographic acronyms are as in Figure 5.1.

north from the Yermak Plateau slope to recirculate towards Fram Strait (dashed red arrow): this is particularly consistent with the warm AW2 recirculating meander crossed by the 2017 IAOOS platforms (Athanase et al., 2019) (Figure 5.1).

The intensification of the circulation coincided with an overall warming and salinification in the upper 1000 m of the WNB interior, and with a thickening of the AW layer (Athanase et al., 2019; Athanase et al., submitted) consistent with the progression

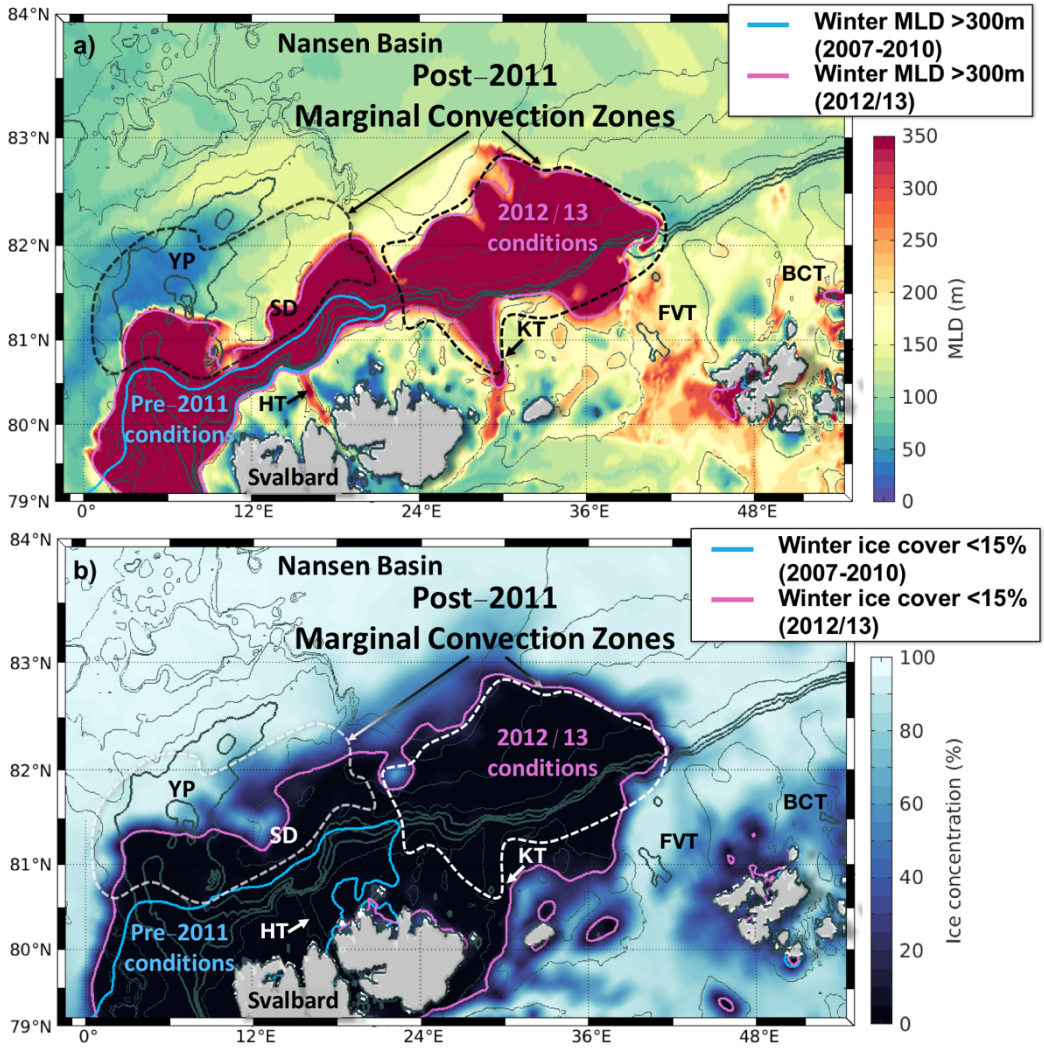

Figure 5.3 : Same as Figure 5.2, for winter 2012/13 over the continental slope northeast of Svalbard.

of AW in the region. As the winter sea-ice retreats and AW shoals North of Svalbard, enhanced deep winter convection could be expected.

Indeed, the 13 years of PSY4 fields showed that the previously ice-covered northern Yermak Plateau and continental slope areas became “Marginal Convection Zones" in 2011 with, from then on, occasionally ice-free conditions in winter, 50-m-ocean temperatures always above 0°C, and highly variable mixed layer depths and ocean-to-atmosphere heat fluxes (Athanase et al., 2020). Two winters stood out of the 2008-2020 period, with extreme deep mixed layers and exceptionally large sea-ice retreat: winter 2017/18 over the northern Yermak Plateau-Sofia Deep (Figure 5.2), and winter 2012/13 on the continental slope northeast of Svalbard (Figure 5.3). During these extreme winters, deep convection reached down to the 27.95 kg/m^3 isopycnal, considerably cooling and freshening the AW layer. As a result, the base of the halocline

corresponded to the dense 27.85 kg/m^3 isopycnal in the Nansen Basin in 2017 (Bertosio et al., 2020).

Over the continental slope, recurrent trough outflows of cooler, denser water (σ>27.95 kg/m^3) additionally contributed to modify AW properties year-round (Athanase et al., 2020). In order to quantify the contribution of these shelf-waters outflows to the budget of heat and salt of the boundary current, further investigations on the upstream Barents Sea conditions must be carried out. As the Barents Sea undergoes numerous changes, with a drastic sea-ice retreat altering the modification of the Atlantic Water inflow, what will be the evolution of the Barents Sea outflows properties? The Barents Sea Branch Water (BSBW) being a major contributor to the warm layer downstream of the Laptev slope, changes in BSBW properties could have impacts on the hydrography of the Makarov and Canada Basins.

5.2. Drivers of changes in the WNB : ongoing work

PSY4 documented changes around 2011 in AW properties (Chapter 3) and circulation (Chapter 4) in the WNB. We present some ongoing investigations on the mechanisms driving such abrupt changes in 2011.

Several studies addressed the influence of large-scale atmospheric circulation (e.g. North Atlantic and Arctic Oscillations) on ocean circulation patterns (e.g. Transpolar Drift; Morison et al., 2012; Armitage et al., 2018) and on interannual variations of the AW inflow (e.g. Dickson et al., 2001; Armitage et al., 2018). However, more regional atmospheric patterns have been shown to play a determinant role in the AW inflow variability.

South of the Fram Strait, the main conveyor of the Atlantic inflow towards the Arctic is the topographically steered Norwegian Atlantic Current (NwAC) (Figure 5.4). The NwAC is constituted of two branches: the eastern branch follows the Norwegian shelf (with a portion flowing into the Barents Sea and the other continuing north towards Fram Strait) while the western branch is a topographically guided jet in the Polar Front (Orvik and Niiler, 2002).

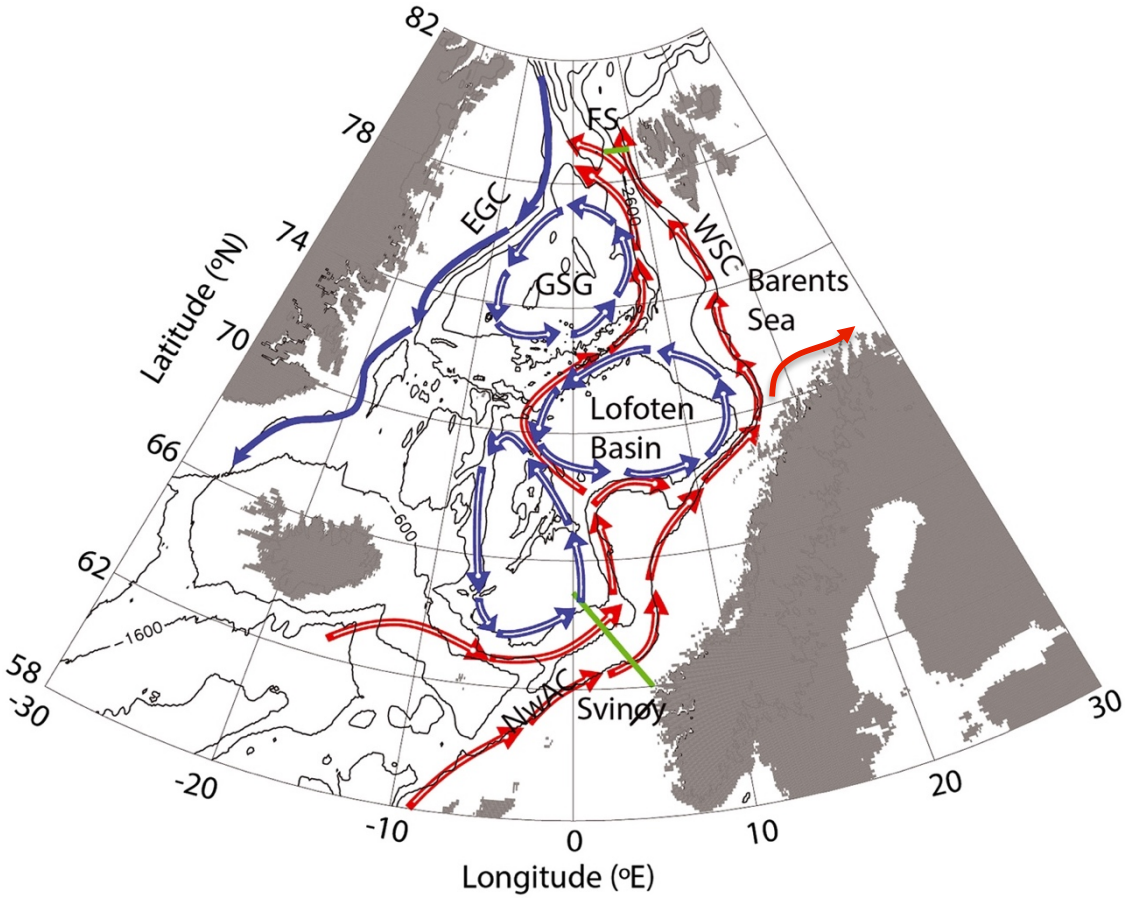

Figure 5.4: Schematic of major currents in the Nordic Seas, with AW pathways (red arrows), gyre circulations (hollow blue arrows), and polar water flow in the East Greeland Current (solid blue arrows). Green lines indicate the Fram Strait and Svinøy vertical sections. Bathymetry is in contours. From Chatterjee et al. (2018).

Chafik et al. (2015) showed that on interannual time scales, a strong NwAC was well correlated to anomalously low SSH and sea-level pressure (SLP) over the Nordic Seas, while the volume transport through Fram Strait was influenced by regional atmospheric conditions over Svalbard and the northern Barents Sea.

On the other hand, Chatterjee et al. (2018) suggested a link between the strength of the Greenland Sea Gyre (GSG) and interannual variations of AW temperatures at Fram Strait. Indeed, a positive (negative) wind stress curl anomaly over the Nordic Seas would induce negative (positive) SSH anomalies at the GSG center due to Ekman transport and result in anomalously intensified (reduced) cyclonic circulation around the gyre, along the SSH anomaly slope. As a consequence, the velocity of the northward AW inflow would increase (decrease), resulting in warmer (colder) AW reaching Yermak Plateau due to less (more) heat loss to the atmosphere and less (more) mixing with colder shelf waters.

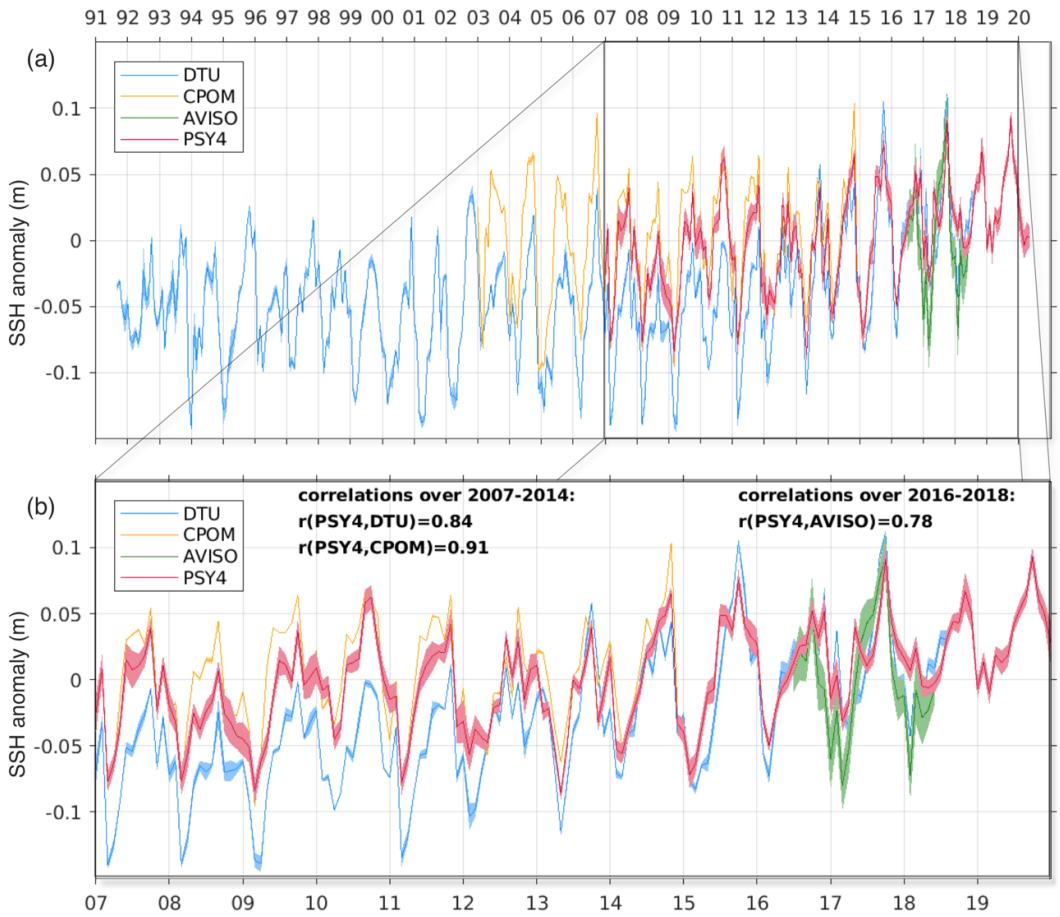

Figure 5.5: (a) Time-series of SSH anomaly in Fram Strait (5-10°E, 76-80°N), from PSY4 (red), DTU (blue), CPOM (yellow) and CLS-AVISO (green). Shaded envelops are spatial STDs. (b) Same zoom over the 2007-2020 period.

To test this mechanism over the 2007-2020 period, SSH variations at the center of the GSG (74-75°N, 5°W-0°) were used as a proxy of the GSG strength. Comparisons between PSY4 and three satellite altimetry products demonstrated the good performance of PSY4 SSH in Fram Strait (Figure 5.5). Additionally, the 12-month running mean of AW temperature (AW being defined as water with CT>2°C) at Fram Strait from PSY4 was in very good agreement with observations over 2007-2011 (blue and dashed red lines in Figure 5.6b).

Time-series of 12-month running means of SSH at the GSG center and AW temperature at Fram Strait showed a clear anti-correlation (Figure 5.6b). The detrended time-series had a maximum correlation coefficient r=-0.73 (significant at the 99.9% level) for an 80-day lag (SSH variations leading). This tends to confirm the link between stronger GSG (with lower SSH in its center) and warmer AW temperature at Fram Strait on interannual time scales (Chatterjee et al., 2018).

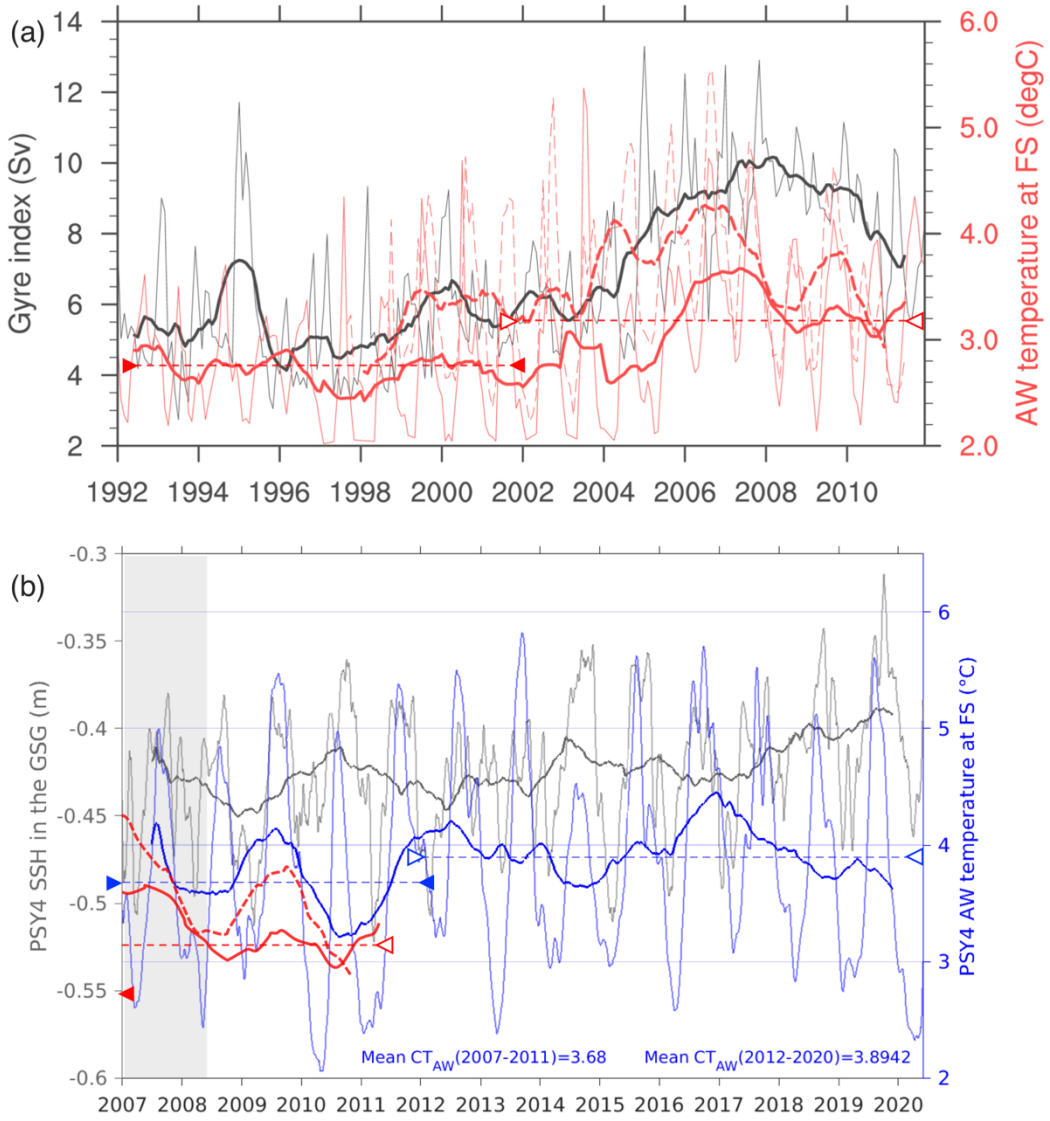

Figure 5.6: (a) AW temperature (°C, red) at Fram Strait (green line in Figure 5.5) from TOPAZ4 reanalysis (solid line) and observations (dashed line), and gyre index (large index corresponding to an intensified GSG). Annotated from Chatterjee et al. (2018). (b) PSY4 AW temperature (°C, blue) at Fram Strait and SSH at the GSG center (m, grey). AW temperatures from (a) are reported in red. The thin/bold lines are the monthly/12-month running averages. Horizontal dashed lines are mean AW temperature from TOPAZ4 (red) over 1992-2001 (solid triangles) and 2002-2011 (hollow triangles), and from PSY4 (blue) over 2007-2011 (solid triangles) and 2012-2020 (hollow triangles). Grey area corresponds to the spin-up time estimated in Chapter 4, removed in Figure 5.8.

On interannual time scales, variations of AW volume transport in the WSC, YPB and AWBC (Chapter 4) followed those of the Greenland Sea Gyre strength (Figure 5.7). The largest peaks both in AW temperature and volume transport were found in winters 2011/12 and 2016/17 (Figures 5.7b and 5.8). These two winters preceded the extreme winters identified in Chapter 3, with intense convection and anomalously large sea-ice retreat north of Svalbard. Such "low frequency pulses" of warmer AW inflow (i.e. larger

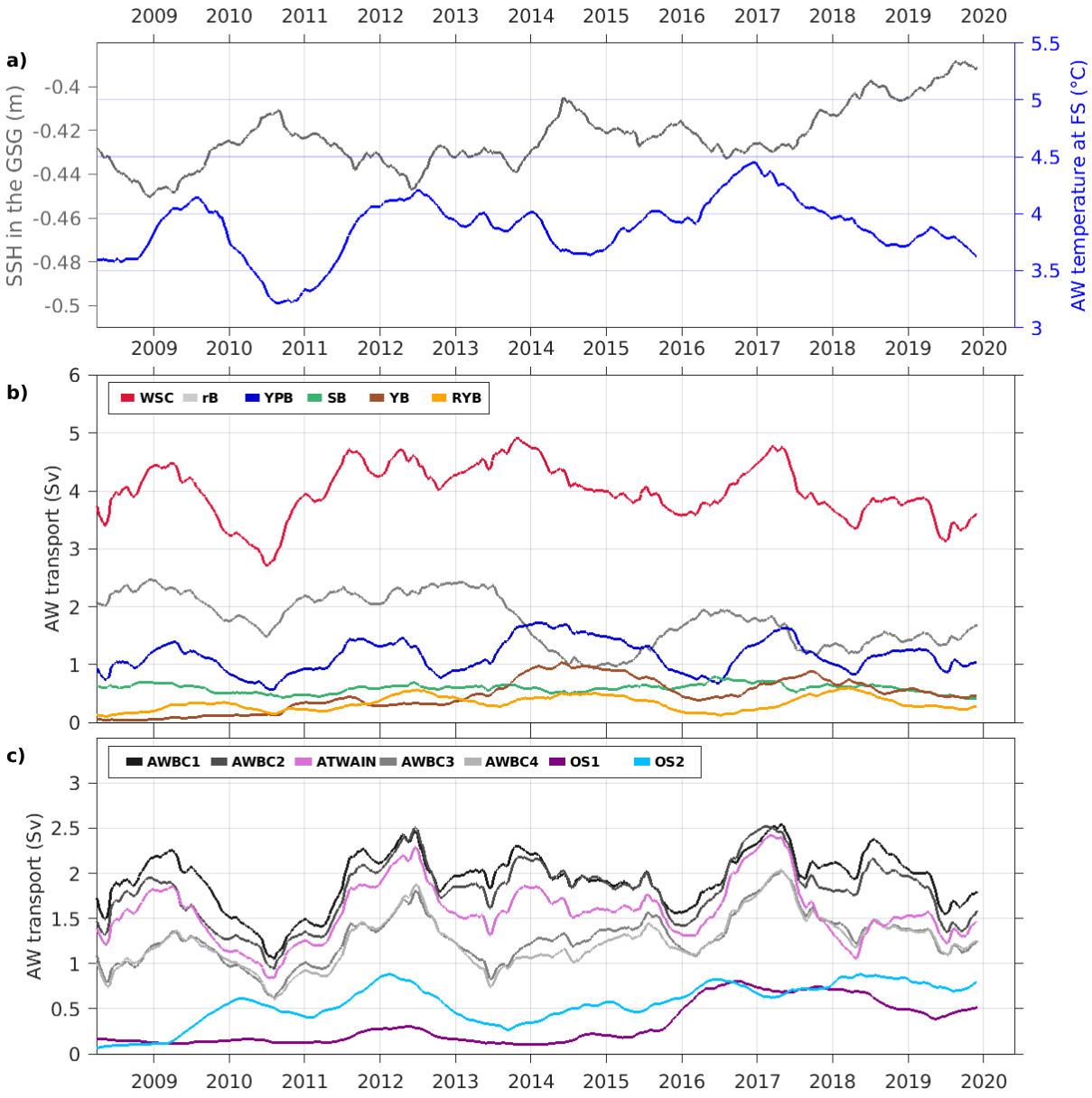

Figure 5.7: (a) 12-month running mean of PSY4 AW temperature at Fram Strait (°C, blue) and of SSH at the GSG center (m, grey). (b) 12-month running mean of AW volume transport (Sv) carried by the WSC, by recirculations (rB) and across the four sections of the Yermak Plateau, see Chapter 4. rB was computed as: WSC-(YPB+SB+YB). (c) Same for the sections downstream of Yermak Plateau, see Chapter 4.

AW volume carried by the WSC) may have been instrumental in pre-conditioning the WNB for extreme winter convection events in the warmer, more variable post-2011 period.

AW temperatures at Fram Strait from the TOPAZ4 reanalysis (12 km resolution) exhibited a clear increase from 2002, with a mean of 2.72°C in 1992-2001 raising to 3.14°C in 2002-2011 (Chatterjee et al., 2018) (Figure 5.6a). PSY4 showed here the

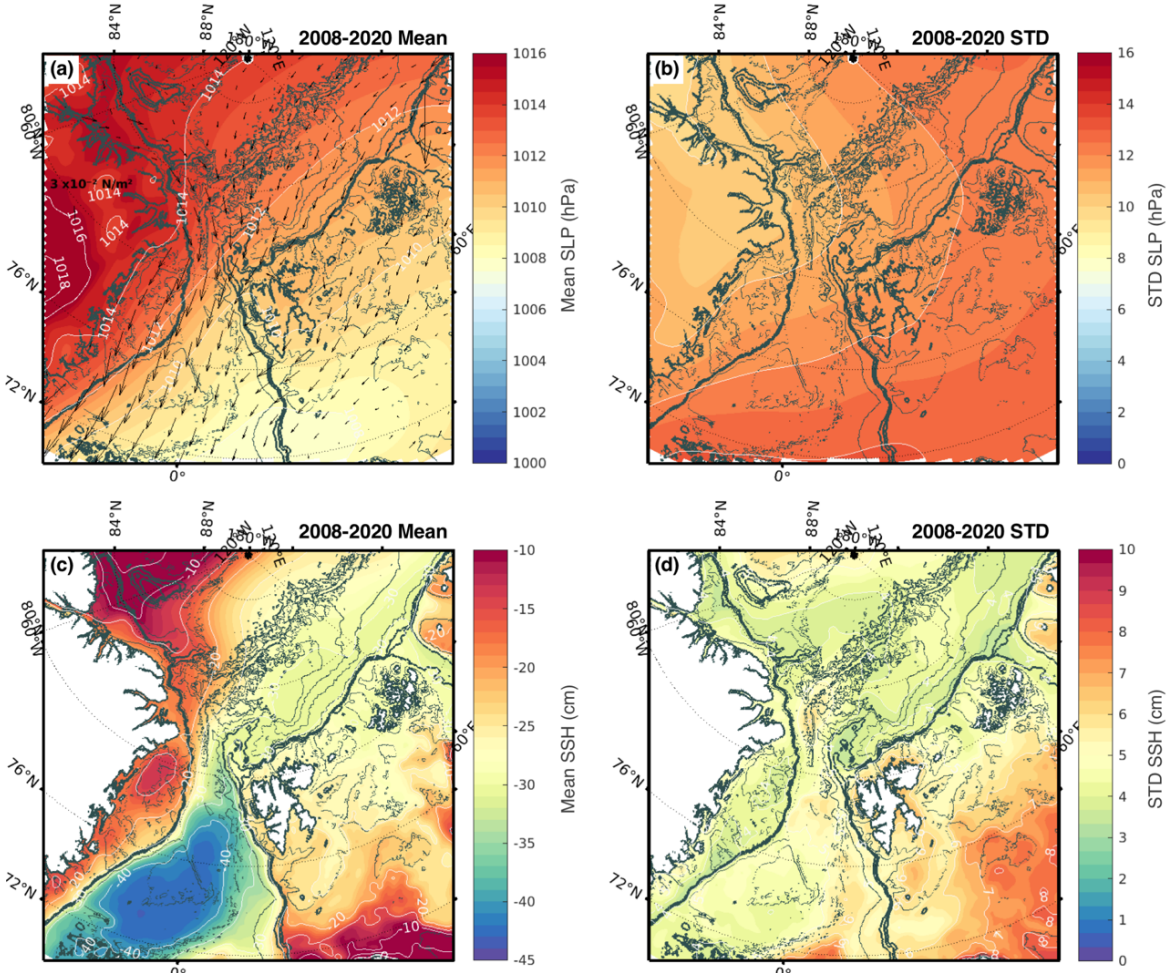

Figure 5.8: (a) Mean SLP (hPa, background color) and wind stress (N/m², arrows) over 2008-2020. (b) Associated SLP STD (hPa). (c)-(d) Same in SSH. Fields of SSH and wind stress are from PSY4, SLP is from ERA-5.

continuation of this warming, with a mean AW temperature increasing from 3.68°C in 2007-2011 to 3.89°C in 2012-2020 (Figure 5.6b). The AW inflow temperature increase in 2011 coincided with the changes in the Marginal Convection Zones (Chapter 3) and AW circulation (Chapter 4).

Processes driving the strengthening of the YB in 2014 and the associated decline in AW recirculations are currently under investigation.

Ongoing research includes the examination of SSH, SLP and wind stress fields in the Nordic Seas and Western Nansen Basin regions to understand changes in ocean circulation patterns (e.g. Greenland Sea Gyre) and WSC partitioning west and north of Svalbard (Chafik et al., 2015; Chatterjee et al., 2018; Crews et al., 2019) (Figure 5.8).

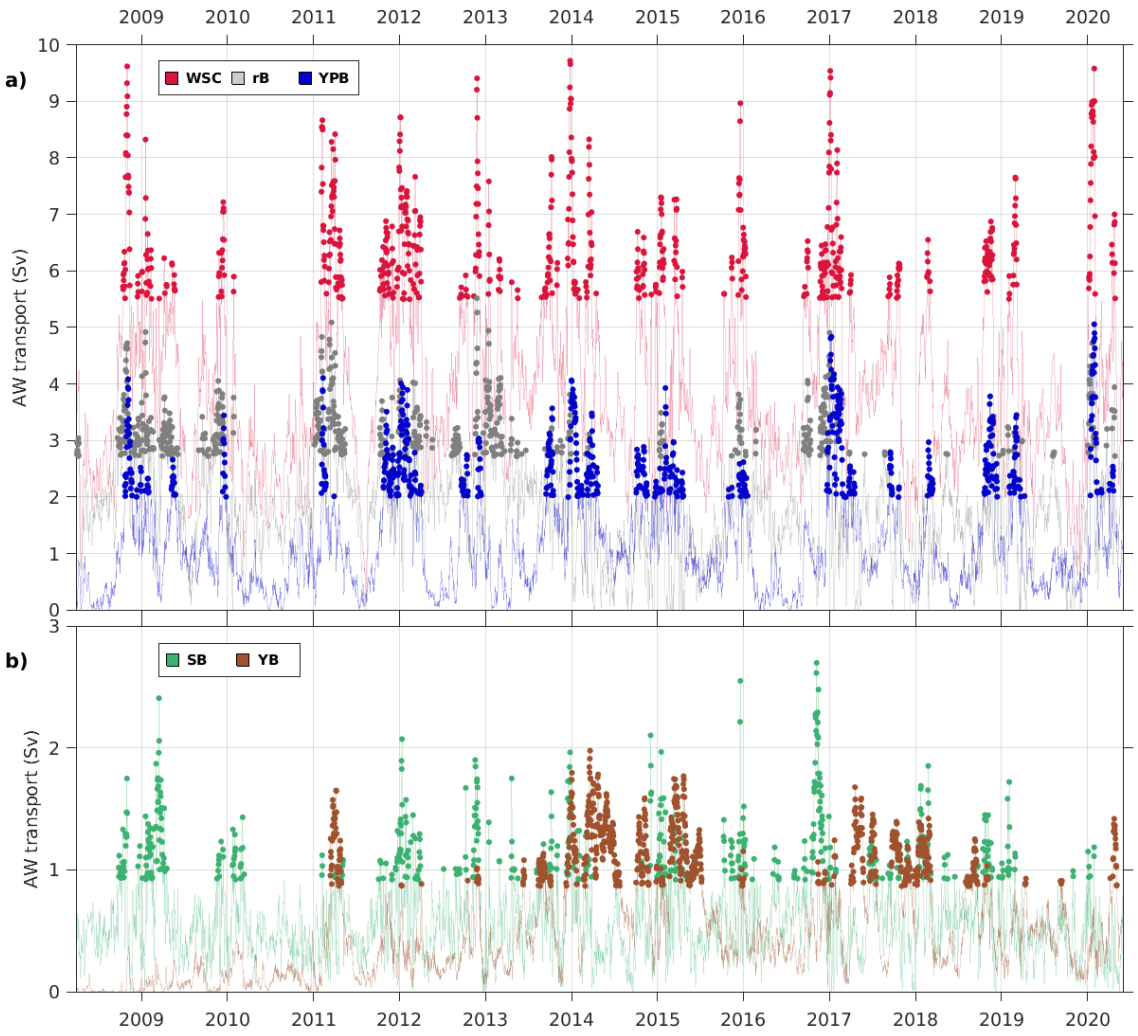

Figure 5.9: AW volume transport (Sv) (a) in the WSC, rB and YPB, and (b) in the SB and YB. Solid dots are days of "pulses". WSC, SB, YPB and YB sections are as in Chapter 5, and AW transport in rB was computed as WSC–(SB+YPB+YB). WSC: West Spitsbergen Current; YPB: Yermak Pass Branch; YB: Yermak Branch; SB: Svalbard Branch; rB: recirculation Branches.

Following Crews et al. (2019), composite fields of SSH and atmospheric conditions are being compiled during days of "high-frequency pulses" of AW volume transport in the WSC and in the four branches downstream: either entering the Arctic Ocean through the Svalbard Branch (SB), Yermak Pass Branch (YPB) or Yermak Branch (YB); or flowing back towards Fram Strait as Recirculation Branches (rB) (Figure 5.9). "Pulses" were identified as days when the AW volume transport in a given branch was at least one STD above average (as in Crews et al., 2019) (Figure 5.8). Composite maps can thus be obtained by averaging the SSH and atmospheric fields during these "pulse days".

Atmospheric conditions during pulses in the WSC were very consistent with Chafik et al. (2015) and Chatterjee et al. (2018), with anomalous low pressure, cyclonic winds

over the Nordic Seas inducing positive SSH anomalies over the shelves and negative SSH anomalies in the Fram Strait (not shown). The larger SSH gradient along the continental slope thus results in anomalously large velocities in the WSC (Armitage et al., 2018).

First examination of regional patterns in sea level pressure during recirculations (rB), YPB and SB pulses were in good agreement with those documented by Crews et al. (2019) over the 2005-2009 period. Pulses in all these three branches (rB, YPB, SB) corresponded to SSH anomalies favouring a stronger NwAC and WSC (not shown).

In contrast with the other branches, pulses in the YB were associated with atmospheric patterns similar to the mean conditions (Figure 5.8). Indeed, note that while the WSC, YPB, rB, and SB all exhibited peaks mostly in early-winter (November-January), pulses in the strengthening YB were found at various times of the year, with the largest peaks often in late-winter or early-spring (February-April) (Figure 5.9).

This different seasonality, impacting the obtained composite fields, will be the focus of future investigations. For example, the large seasonal signal in SSH and atmospheric conditions should likely be removed before comparisons between composites for the different branches' pulses. Additionally, a finer selection of pulse days may be required. For example, pulse days for the YB may be overestimated as the YB strengthened significantly from 2011 onwards: STDs of AW volume transport in the YB could thus be computed only over the more variable 2011-2020 period to provide a more realistic pulse day selection. Examining atmospheric conditions during the days preceding pulses maxima could provide a better understanding of the processes driving these sudden flow increases in each branch.

As the Arctic sea-ice becomes thinner and more mobile, coupling between winds, ice, and ocean will become increasingly important. Coupled observing systems such as the IAOOS buoys are thus of major interest to help understand their interactions. The data acquired in the framework of the European project INTAROS (Integrated Arctic Observation System) will likely contribute to fill observational gaps and build a pan-Arctic view of the changing Arctic system. Finally, the MOSAiC (Multidisciplinary drifting Observatory for the Study of the Arctic Climate) expedition aimed to study the coupled Arctic Climate during a 1-year long drift across the Eurasian Basin, from September 2019 to September 2020. The ice camp deployed near the R/V

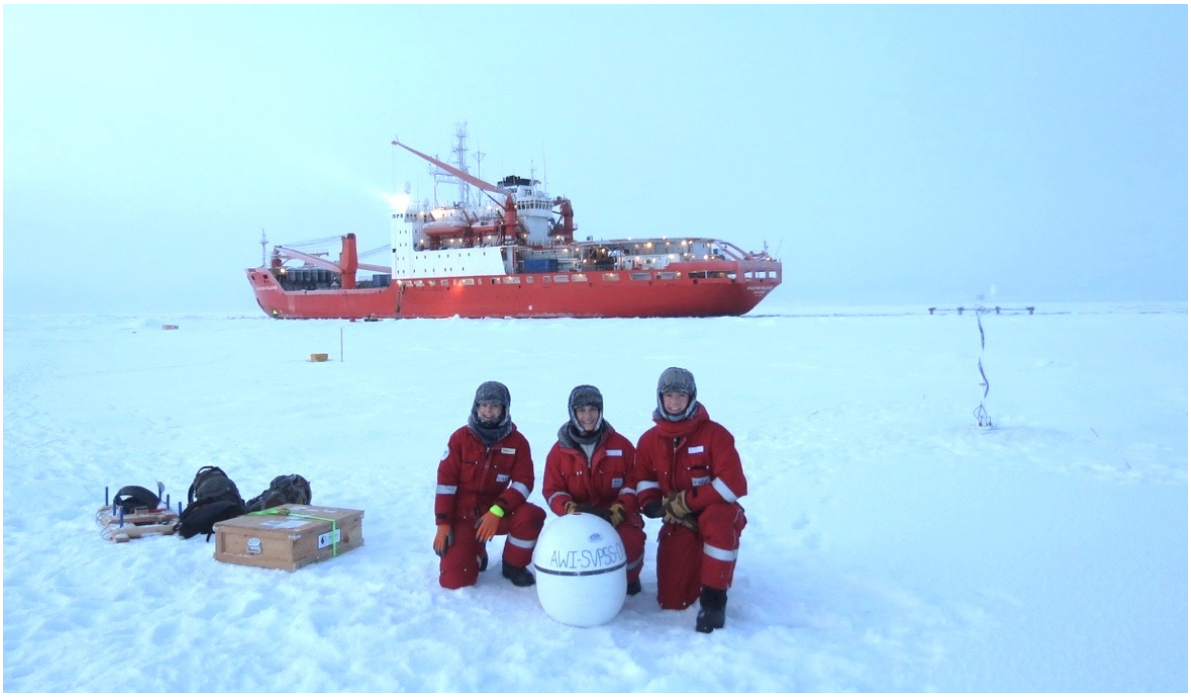

Figure 5.10: Picture taken during the deployment of a Sea-Ice Tethered buoy for the MOSAiC Distributed Network, October 2019. From left to right: Marylou Athanase, Natalie Ribeiro, Sam Cornish. © Natalia Ribeiro.

Polarstern was the central observatory of MOSAiC, and was complemented by a "Distributed Network" (DN) of instruments set up within a 40 km radius. I had the opportunity to participate to the deployment of the DN in September-October 2019 (Figure 5.10). The Polarstern and Distributed Network, drifting together with the sea-ice, gathered valuable observations of the atmosphere, ocean, ice, snow, biogeochemistry, and ecosystems, which will most likely contribute to shed light on the complex coupling at play in the Arctic Ocean.

References

Aagaard, K. (1984). The Beaufort Undercurrent, in The Alaskan Beaufort Sea: Ecosystems and Environments, edited by P.W. Barnes, D.M. Schell and E. Reimnitz, pp. 47-71, Academic Press, Inc., Orlando

Aagaard, K., Foldvik, A., & Hillman, S. R. (1987). The West Spitsbergen Current: disposition and water mass transformation. Journal of Geophysical Research: Oceans, 92(C4), 3778-3784. DOI: 10.1029/JC092iC04p03778

Aagaard, K. (1989) A synthesis of the arctic ocean circulation. Rapp. P.-V Reun. Cons. Int. Explor. Mer.

Aagaard, K., & E. C. Carmack (1989), The role of sea ice and other fresh water in the Arctic circulation, J. Geophys. Res., 94(C10), 14485-14498

Alkire, M. B., Falkner, K. K., Rigor, I., Steele, M., & Morison, J. (2007). The return of Pacific waters to the upper layers of the central Arctic Ocean. Deep Sea Research, I, 54(9), 1509–1529. DOI: 10.1016/j.dsr.2007.06.004

Alkire, M. B., Polyakov, I., Rember, R., Ashik, I. M., Ivanov, V., & Pnyushkov, A. V. (2017). Lower halocline water formation and modification, a comparison of physical and geochemical methods. Ocean Science, 13(6), 983–995. DOI: 10.5194/os-13-983-2017

Alkire, M. B., Rember, R., & Polyakov, I. (2019). Discrepancy in the identification of the Atlantic/Pacific front in the central Arctic Ocean: NO versus nutrient relationships. Geophysical Research Letters, 46, 3843–3852. DOI: 10.1029/2018GL081837.

Anderson, L. G., Andersson, P. S., Björk, G., Peter Jones, E., Jutterström, S., & Wåhlström, I. (2013). Source and formation of the upper halocline of the Arctic Ocean. Journal of Geophysical Research: Oceans, 118(1), 410-421.

Armitage, T. W. K., Bacon, S., & Kwok, R. (2018). Arctic sea level and surface circulation response to the Arctic Oscillation. Geophysical Research Letters, 45, 6576–6584. DOI: 10.1029/2018GL078386

Bertosio C., C. Provost, N. Sennéchael, C. Artana, M. Athanase, E. Boles, J.-M. Lellouche & G. Garric (2020). The Western Eurasian Basin halocline in 2017: insights from autonomous NO measurements and the Mercator physical system. Journal of Geophysical Research: Oceans DOI:10.1029/2020JC016204

Beszczynska-Möller, A., Fahrbach, E., Schauer, U., & Hansen, E. (2012). Variability in Atlantic water temperature and transport at the entrance to the Arctic Ocean, 1997–2010. ICES Journal of Marine Science, 69(5), 852–863. DOI: 10.1093/icesjms/fss056

Boles, E., Provost, C., Garçon, V., Bertosio, C., Athanase, M., Koenig, Z., & Sennéchael, N. (2020). Under-ice phytoplankton blooms in the Central Arctic Ocean: Insights from the first biogeochemical IAOOS platform drift in 2017. Journal of Geophysical Research: Oceans, 125, e2019JC015608. DOI: 10.1029/2019JC015608

Bourgain, P., & Gascard, J.C. (2011). The Arctic Ocean halocline and its interannual variability from 1997 to 2008. Deep Sea Research, I, 58, 745-756. DOI: 10.1016/j.dsr.2011.05.001.

REFERENCES

Boyd, T. J. & D'Asaro, E. A. (1994). Cooling of the West Spitsbergen Current: wintertime observations west of Svalbard. Journal of Geophysical Research: Oceans, 99(C11), 22597-22618. DOI: 10.1029/94JC01824

Cetinić, I., Perry, M. J., D'Asaro, E., Briggs, N., Poulton, N., Sieracki, M. E., & Lee, C. M. (2015). A simple optical index shows spatial and temporal heterogeneity in phytoplankton community composition during the 2008 North Atlantic bloom experiment. Biogeosciences, 12, 2179–2194. DOI: 10.5194/bg-12-2179-2015

Chafik, L., J. Nilsson, Ø. Skagseth, & P. Lundberg (2015), On the flow of Atlantic water and temperature anomalies in the Nordic Seas toward the Arctic Ocean, J. Geophys. Res. Oceans, 120, 7897–7918, doi:10.1002/ 2015JC011012.

Chatterjee, S., Raj, R. P., Bertino, L., Skagseth, Ø., Ravichandran, M., & Johannessen, O. M. (2018). Role of Greenland Sea gyre circulation on Atlantic water temperature variability in the Fram Strait. Geophysical Research Letters, 45(16), 8399-8406. DOI: 10.1029/2018GL079174

Cokelet, E. D., Tervalon, N., & Bellingham, J. G. (2008). Hydrography of the West spitsbergen current, svalbard branch: autumn 2001. Journal of Geophysical Research: Oceans, 113(C1).

Comiso, J. C., Parkinson, C. L., Gersten, R., & Stock, L. (2008). Accelerated decline in the Arctic sea ice cover. Geophysical Research Letters, 35, L01703. DOI: 10.1029/2007GL031972

Crews, L., Sundfjord, A., Albretsen, J., & Hattermann, T. (2017). Mesoscale eddy activity and transport in the Atlantic Water inflow region north of Svalbard. Journal of Geophysical Research: Oceans, 123, 201–215. DOI: 10.1002/2017JC013198

Crews, L., Sundfjord, A., & Hattermann, T. (2019). How the Yermak Pass Branch Regulates Atlantic Water Inflow to the Arctic Ocean. Journal of Geophysical Research: Oceans, 124(1), 267-280. DOI: 10.1029/2018JC014476

Dickson, R. R., Osborn, T. J., Hurrell, J. W., Meincke, J., Blindheim, J., Adlandsvik, B. et al. (2000). The Arctic ocean response to the North Atlantic oscillation. Journal of Climate, 13(15), 2671-2696. DOI: 10.1175/1520-0442(2000)013<2671:TAORTT>2.0.CO;2

Dmitrenko, I. A., Kirillov, S. A., Ivanov, V. V., & Woodgate, R. A. (2008). Mesoscale Atlantic water eddy off the Laptev Sea continental slope carries the signature of upstream interaction. Journal of Geophysical Research, 113, C07005. DOI: 10.1029/2007JC004491

Dmitrenko, I. A., Rudels, B., Kirillov, S. A., Aksenov, Y. O., Lien, V. S., Ivanov, V. V., Schauer, U., Polyakov, I. V., Coward, A., and Barber, D. G. (2015). Atlantic water flow into the arctic ocean through the st. anna trough in the northern kara sea. Journal of Geophysical Research: Oceans, 120(7): 5158–5178.

Gascard, J. C., Richez, C., & Rouault, C. (1995). New Insights on Large-Scale Oceanography in Fram Strait: The West Spitsbergen. Arctic Oceanography: Marginal Ice Zones and Continental Shelves, 49, 131-182.

Goszczko, I., Ingvaldsen, R. B., & Onarheim, I. H. (2018). Wind-driven cross-shelf exchange-West Spitsbergen Current as a source of heat and salt for the adjacent shelf in Arctic winters. Journal of Geophysical Research: Oceans, 123, 2668–2696. DOI: 10.1002/ 2017JC013553

REFERENCES

Graham, R. M., Itkin, P., Meyer, A., Sundfjord, A., Spreen, G., Smedsrud, L. H., ... & Fer, I. (2019). Winter storms accelerate the demise of sea ice in the Atlantic sector of the Arctic Ocean. Scientific reports, 9(1), 1-16.

Grassi, B., Redaelli, G., and Visconti, G. (2013). Arctic sea ice reduction and extreme climate events over the mediterranean region. Journal of Climate, 26(24):10101– 10110.

Hattermann, T., Isachsen, P. E., von Appen, W.-J., Albretsen, J., & Sundfjord, A. (2016). Eddy-driven recirculation of Atlantic Water in Fram Strait. Geophysical Research Letters, 43, 3406–3414. DOI: 10.1002/2016GL068323

Honda, M., Inoue, J., and Yamane, S. (2009). Influence of low arctic sea-ice minima on anomalously cold eurasian winters. Geophysical Research Letters, 36(8).

Hunkins, K. (1974). Subsurface eddies in the arctic ocean. In Deep Sea Research and Oceanographic Abstracts, volume 21, pages 1017–1033. Elsevier.

Ivanov, V. V., Polyakov, I. V., Dmitrenko, I. A., Hansen, E., Repina, I. A., Kirillov, S. A., ... & Timokhov, L. A. (2009). Seasonal variability in Atlantic water off Spitsbergen. Deep Sea Research Part I: Oceanographic Research Papers, 56(1), 1-14.

Ivanov, V. V., Alexeev, V. A., Repina, I., Koldunov, N. V., & Smirnov, A. (2012). Tracing Atlantic Water signature in the Arctic sea ice cover east of Svalbard. Advances in Meteorology, 2012.

Ivanov, V., Alexeev, V., Koldunov, N. V., Repina, I., Sandø, A. B., Smedsrud, L. H., & Smirnov, A. (2016). Arctic Ocean heat impact on regional ice decay: A suggested positive feedback. Journal of Physical Oceanography, 46(5), 1437-1456. DOI: 10.1175/JPO-D-15-0144.1

Ivanov, V., Smirnov, A., Alexeev, V., Koldunov, N.V., Repina, I., & Semenov, V. (2018). Contribution of Convection-Induced Heat Flux to Winter Ice Decay in the Western Nansen Basin. Journal of Geophysical Research: Oceans, 123, 6581–6597. DOI: 10.1029/2018JC013995

Jones, E. (2001). Circulation in the arctic ocean. Polar Research, 20:139–146.

Jones, E. P., Anderson, L. G., & Swift, J. H. (1998). Distribution of Atlantic and Pacific waters in the upper Arctic Ocean: Implications for circulation. Geophysical Research Letters, 25(6), 765-768. DOI : 10.1029/98GL00464

Jones, E.P., & Anderson, L.G. (1986). On the origin of the chemical properties of the Arctic Ocean halocline. Journal of Geophysical Research: Oceans, 91, 10759-10767. DOI: 10.1029/JC091iC09p10759.

Koenig, Z., Provost, C., Villacieros- Robineau, N., Sennechael, N., Meyer, A., Lellouche, J.-M., & Garric, G. (2017). Atlantic waters inflow north of Svalbard: Insights from IAOOS observations and Mercator Ocean global operational system during N-ICE2015. Journal of Geophysical Research: Oceans, 122, 1254–1273. DOI: 10.1002/2016JC012424

Koenig, Z., Provost, C., Sennéchael, N., Garric, G., & Gascard, J.C. (2017b). The Yermak Pass Branch: a major pathway for the Atlantic water north of Svalbard? Journal of Geophysical Research: Oceans, 122, 9332-9349. DOI: 10.1002/2017JC013271.

REFERENCES

Koenig, Z., Meyer, A., Provost, C., Sennéchael, N., Sundfjord, A., Beguery, L., ... & Gascard, J. C. (2018). Cooling and Freshening of the West Spitsbergen Current by Shelf-Origin Cold Core Lenses. Journal of Geophysical Research: Oceans, 123(11), 8299-8312. DOI: 10.1029/2018JC014463

Kuzmina, N., Rudels, B., Zhurbas, V., & Stipa, T. (2011). On the structure and dynamical features of intrusive layering in the Eurasian Basin in the Arctic Ocean. Journal of Geophysical Research: Oceans, 116(C8).

Lellouche, J. M., Greiner, E., le Galloudec, O., Garric, G., Regnier, C., Drevillon, M., et al. (2018). Recent updates to the Copernicus Marine Service global ocean monitoring and forecasting real-time 1/ 12° high-resolution system. Ocean Science, 14(5), 1093–1126. DOI: 10.5194/os-14-1093-2018

Lind, S., & Ingvaldsen, R. B. (2012). Variability and impacts of Atlantic Water entering the Barents Sea from the north. Deep Sea Research Part I: Oceanographic Research Papers, 62, 70-88. DOI: 10.1016/j.dsr.2011.12.007

Lique, C., Johnson, H.L. & Plancherel, Y. (2018) Emergence of deep convection in the Arctic Ocean under a warming climate. Climate Dynamics 50, 3833–3847. DOI: 10.1007/s00382-017-3849-9

Liu, J., Curry, J. A., Wang, H., Song, M., and Horton, R. M. (2012). Impact of declining arctic sea ice on winter snowfall. Proceedings of the National Academy of Sciences, 109(11): 4074–4079.

Manley, T. and Hunkins, K. (1985). Mesoscale eddies of the arctic ocean. Journal of Geophysical Research: Oceans, 90(C3):4911–4930.

Matishov, G.G., Matishov, D.G., Moiseev, D.V., 2009. Inflow of Atlantic-origin waters to the Barents Sea along glacial troughs. Oceanologica 51, 321–340.

McDougall, T. J. (2012). The International Thermodynamic Equation of Seawater–2010; Introductory Lecture Slides. Available at: www. TEOS-10. org.

Menze, S., Ingvaldsen, R. B., Haugan, P., Fer, I., Sundfjord, A., Beszczynska-Moeller, A., & Falk-Petersen, S. (2019). Atlantic water pathways along the north-western Svalbard shelf mapped using vessel-mounted current profilers. Journal of Geophysical Research: Oceans, 124(3), 1699-1716.

Meyer, A., Sundfjord, A., Fer, I., Provost, C., Villacieros Robineau, N., Koenig, Z., et al. (2017), Winter to summer oceanographic observations in the Arctic Ocean north of Svalbard, J. Geophys. Res. Oceans, 122, 6218–6237, DOI:10.1002/2016JC012391.

Morison, J., Kwok, R., Peralta-Ferriz, C., Alkire, M., Rigor, I., Andersen, R., & Steele, M. (2012). Changing Arctic ocean freshwater pathways. Nature, 481(7379), 66–70. DOI: 10.1038/nature10705

Muench, R. D., McPhee, M. G., Paulson, C. A., & Morison, J. H. (1992). Winter oceanographic conditions in the Fram Strait-Yermak Plateau region. Journal of Geophysical Research: Oceans, 97(C3), 3469-3483.

Nencioli, F., Chang, G., Twardowski, M., & Dickey, T. D. (2010). Optical characterization of an eddy-induced diatom bloom west of the island of Hawaii. Biogeosciences, 7, 151–162. DOI: 10.5194/bg-7-151-2010

Nilsen, F., Skogseth, R., Vaardal-Lunde, J., & Inall, M. (2016). A simple shelf circulation model: Intrusion of Atlantic water on the West Spitsbergen shelf. Journal of Physical Oceanography, 46(4), 1209–1230. DOI: 10.1175/JPO-D-15-0058.1

REFERENCES

Onarheim, I. H., Smedsrud, L. H., Ingvaldsen, R. B., & Nilsen, F. (2014). Loss of sea ice during winter north of Svalbard. Tellus A: Dynamic Meteorology and Oceanography, 66(1), 23933. DOI: 10.3402/tellusa.v66.23933

Onarheim, I. H., Eldevik, T., Smedsrud, L. H., & Stroeve, J. C. (2018). Seasonal and regional manifestation of Arctic sea ice loss. Journal of Climate, 31(12), 4917-4932. DOI: 10.1175/JCLI-D-17-0427.1

Orvik, K. A., & Niiler, P. (2002). Major pathways of Atlantic water in the northern North Atlantic and Nordic Seas toward Arctic. Geophysical Research Letters, 29(19), 2-1. DOI: 10.1029/2002GL015002

Padman, L., & Dillon, T. M. (1987). Vertical heat fluxes through the Beaufort Sea thermohaline staircase, Journal of Geophysical Research, 92(C10), 10,799–10,806, DOI: 10.1029/JC092iC10p10799.

Padman, L., & Dillon, T. M. (1988). On the horizontal extent of the Canada Basin thermohaline steps, Journal of Physical Oceanography, 18(10), 1458–1462, DOI: 10.1175/1520-0485(1988)018<1458:OTHEOT>2.0.CO;2.

Pérez-Hernández, M. D., Pickart, R. S., Pavlov, V., Våge, K., Ingvaldsen, R., Sundfjord, A., et al. (2017). The Atlantic Water boundary current north of Svalbard in late summer. Journal of Geophysical Research: Oceans, 122(3), 2269-2290. DOI: 10.1029/2018JC014299

Pérez-Hernández, M. D., Pickart, R. S., Torres, D. J., Bahr, F., Sundfjord, A., Ingvaldsen, R., et al. (2019). Structure, transport, and seasonality of the Atlantic Water boundary current north of Svalbard: Results from a yearlong mooring array. Journal of Geophysical Research: Oceans, 124(3), 1679-1698. DOI: 10.1029/2018JC014759

Plueddemann, A., Krishfield, J., R., Takizawa, T., Hatakeyama, K. & Honjo, S. (1998). Upper ocean velocities in the Beaufort Gyre, Geophys. Res. Lett., 25(2), 183-186. DOI: 10.1029/97GL53638

Polyakov, I. V., Pnyushkov, A. V., Alkire, M. B., Ashik, I. M., Baumann, T. M., Carmack, E. C., et al. (2017). Greater role for Atlantic inflows on sea-ice loss in the Eurasian Basin of the Arctic Ocean. Science, 356(6335), 285–291. DOI: 10.1126/science.aai8204

Polyakov, I. V., Padman, L., Lenn, Y. D., Pnyushkov, A., Rember, R., & Ivanov, V. V. (2018). Eastern Arctic Ocean diapycnal heat fluxes through large double-diffusive steps. Journal of Physical Oceanography, 2018.

Polyakov, I. V., Rippeth, T. P., Fer, I., Baumann, T. M., Carmack, E. C., Ivanov, V. V., ... & Rember, R. (2020). Intensification of Near-Surface Currents and Shear in the Eastern Arctic Ocean. Geophysical Research Letters, e2020GL089469.

Provost, C., Pelon, J., Sennéchael, N., Calzas, M., Blouzon, F., Desautez, A., et al. (2015). IAOOS (ice-atmosphere-arctic ocean observing system, 2011-2019). Mercator Ocean Quarterly Newsletter, 51, 13–15.

Renner, A. H. H., Sundfjord, A., Janout, M. A., Ingvaldsen, R., Beszczynska-Möller, A., Pickart, R., & Pérez-Hernández, M., (2018). Variability and redistribution of heat in the Atlantic Water boundary current north of Svalbard. Journal of Geophysical Research: Oceans, 123, 6373–6391. DOI: 10.1029/2018JC013814

Rudels, B. (1989). The formation of polar surface water, the ice export and the exchanges through the fram strait. Progress in Oceanography, 22(3):205–248.

Rudels, B., Anderson, L. G., & Jones, E.P. (1996). Formation and evolution of the surface mixed layer and

halocline of the Arctic Ocean. Journal of Geophysical Research: Oceans, 101, 8807-8821. DOI: 10.1029/96JC00143

Rudels, B., Björk, G., Muench, R. D. & Schauer, U. (1999a). Double-diffusive layering in the Eurasian Basin of the Arctic Ocean, J. Mar. Syst., 21(1), 3–27, DOI: 10.1016/S0924-7963(99)00003-2.

Rudels, B., Friedrich, H. J., & Quadfasel, D. (1999b). The Arctic circumpolar boundary current. Deep Sea Research Part II: Topical Studies in Oceanography, 46(6-7), 1023-1062. DOI: 10.1016/S0967-0645(99)00015-6

Rudels, B., Meyer, R., Fahrbach, E., Ivanov, V. V., Østerhus, S., Quadfasel, D., et al. (2000). Water mass distribution in Fram Strait and over the Yermak Plateau in summer 1997. Annales Geophysicae, 18(6), 687–705. DOI: 10.1007/s00585-000-0687-5

Rudels, B., Jones, E. P., Schauer, U., & Eriksson, P. (2004). Arctic sources of the Arctic Ocean surface and halocline waters, Polar Research, 32 (2), 181-208. DOI: 10.1111/j.1751-8369.2004.tb00007.x

Rudels, B., Kuzmina, N., Schauer, U., Stipa, T. & Zhurbas, V. (2009). Double-diffusive convection in the Arctic Ocean – distribution and importance. Geophysica 45, 199–213.

Rudels, B., Schauer, U., Björk, G., Korhonen, M., Pisarev, S., Rabe, B., and Wisotzki, A. (2013). Observations of water masses and circulation in the eurasian basin of the arctic ocean from the 1990s to the late 2000s. OS Special Issue: Ice-Atmosphere-Ocean interactions in the Arctic Ocean during IPY: the Damocles project, 9(1):147–169.

Rudels, B., Korhonen, M., Schauer, U., Pisarev, S., Rabe, B., & Wisotzki, A. (2015). Circulation and transformation of Atlantic water in the Eurasian Basin and the contribution of the Fram Strait inflow branch to the Arctic Ocean heat budget. Progress in Oceanography, 132, 128-152. DOI: 10.106/j.pocean.2014.04.003

Schauer, U., Muench, R. D., Rudels, B., & Timokhov, L. (1997): Impact of eastern Arctic shelf waters on the Nansen Basin intermediate layers, J. Geophys. Res., 102, 3371–3382.

Schauer, U., Fahrbach, E., Osterhus, S., & Rohardt, G. (2004). Arctic warming through the Fram Strait: oceanic heat transport from 3 years of measurements. Journal of Geophysical Research, 109(C06026). DOI: 10.1029/2003JC001823.

Shu, Q., Wang, Q., Su, J., Li, X., & Qiao, F. (2019). Assessment of the Atlantic water layer in the Arctic Ocean in CMIP5 climate models. Climate Dynamics, *53*(9-10), 5279-5291.

Saloranta, T. M., & Haugan, P. M. (2004). Northward cooling and freshening of the warm core of the West Spitsbergen Current. Polar Research, 23(1), 79–88. DOI: 10.3402/polar.v23i1.6268

Shibley, N. C., Timmermans, M.-L., Carpenter, J. R. & Toole, J. M. (2017). Spatial variability of the Arctic Ocean's double-diffusive staircase, J. Geophys. Res. Oceans, 122, 980–994, DOI: 10.1002/ 2016JC012419.

Shimada, K., McLaughlin, F., Carmack, E., Proshutinsky, A., Nishino, S., & Itoh, M. (2004). Penetration of the 1990s warm temperature anomaly of Atlantic Water in the Canada Basin, Geophys. Res. Lett., 31(20), DOI: 10.1029/2004GL020860

Sirevaag, A., de La Rosa, S., Fer, I., Nicolaus, M., Tjernström, M., & McPhee, M. G. (2011). Mixing, heat fluxes and heat content evolution of the Arctic Ocean mixed layer. Ocean Science, *7*(3), 335-349.

Sirevaag, A., & Fer, I. (2012). Vertical heat transfer in the Arctic Ocean: The role of double-diffusive mixing. Journal of Geophysical Research: Oceans, 117(C7).

Smithson, P. A. (2002). Ipcc, 2001: climate change 2001: the scientific basis. Contribution of working group 1 to the third assessment report of the intergovernmental panel on climate change, International Journal of Climatology, 22(9):1144–1144.

Solomon, S., Qin, D., Manning, M., Chen, Z., Marquis, M., Averyt, K., Tignor, M., and Miller, H. (2007). IPCC, 2007: summary for policymakers, climate change 2007: the physical science basis. Contribution of working group I to the fourth assessment report of the intergovernmental panel on climate change.

Spreen, G., R. Kwok, and D. Menemenlis (2011), Trends in Arctic sea ice drift and role of wind forcing: 1992–20 09, Geophys. Res. Lett., 38, L19501. DOI:10.1029/2011GL048970

Steele, M., & Boyd, T. (1998). Retreat of the cold halocline layer in the Arctic Ocean. Journal of Geophysical Research: Oceans, 103, 10419-10435. DOI: 10.1029/98JC00580.

Stocker, T., Qin, D., Plattner, G., Tignor, M., Allen, S., Boschung, J., Nauels, A., Xia, Y., Bex, B., and Midgley, B. (2013). IPCC, 2013: climate change 2013: the physical science basis. Contribution of working group I to the fifth assessment report of the intergovernmental panel on climate change.

Stroeve, J. C., Serreze, M. C., Holland, M. M., Kay, J. E., Malanik, J., & Barrett, A. P. (2012). The Arctic's rapidly shrinking sea ice cover: A research synthesis. Climatic Change, 110(3–4), 1005–1027. DOI: 10.1007/s10584-011-0101-1

Timmermans, M., Toole, J., Krishfield, R., and Winsor, P. (2008). Ice-tethered profiler observations of the double-diffusive staircase in the canada basin thermocline. Journal of Geophysical Research: Oceans, 113(C1).

Timmermans, M., Proshutinsky, A., Golubeva, A., Jackson, J., Krishfield, R., McCall, M., et al. (2014). Mechanisms of pacific summer water variability in the arctic's central canada basin. Journal of Geophysical Research: Oceans, 119(11):7523–7548.

Turner, J. S., (1965). The coupled turbulent transports of salt and heat across a sharp density interface, Int. J. Heat Mass Transfer, 8(5), 759–767, DOI: 10.1016/0017-9310(65)90022-0.

Turner, J. S., & Stommel, H. (1964). A new case of convection in the presence of combined vertical salinity and temperature gradients. Proceedings of the National Academy of Sciences of the United States of America, 52(1), 49. DOI: 10.1073/pnas.52.1.49

Turner, J. S., & Chen, C. F. (1974). Two-dimensional effects in double-diffusive convection. Journal of Fluid Mechanics, 63(3), 577-592. DOI: 10.1017/S0022112074001790

Våge, K., Pickart, R. S., Pavlov, V., Lin, P., Torres, D. J., Ingvaldsen, R., Sundfjord, A., et al. (2016). The Atlantic Water boundary current in the Nansen Basin: Transport and mechanisms of lateral exchange. Journal of Geophysical Research: Oceans, 121, 6946–6960. DOI: 10.1002/2016JC011715

Von Appen, W.-J., Schauer, U., Hattermann, T., & Beszczynska-Möller, A. (2016). Seasonal cycle of mesoscale instability of the West Spitsbergen Current. Journal of Physical Oceanography, 46(4), 1231–1254. DOI: 10.1175/JPO-D-15-0184.1

Walsh, J. J., McRoy, C. P., Coachman, L. K., Goering, J. J., Nihoul, J. J., Whitledge, T. E., Blackburn, T. H., et al (1989). Carbon and nitrogen cycling within the Bering/Chukchi Seas: Source regions for organic

matter effecting AOU demands of the Arctic Ocean. Progress in Oceanography, 22(4), 277-359. DOI: 10.1016/0079-6611(89)90006-2

Wendisch, M., Brückner, M., Burrows, J., Crewell, S., Dethloff, K., Ebell, K., Lüpkes, C., Macke, A., Notholt, J., Quaas, J., et al. (2017). Understanding causes and effects of rapid warming in the arctic. EOS, 98.

Wekerle, C., Wang, Q., von Appen, W. J., Danilov, S., Schourup-Kristensen, V., & Jung, T. (2017). Eddy-resolving simulation of the Atlantic water circulation in the Fram Strait with focus on the seasonal cycle. Journal of Geophysical Research: Oceans, *122*(11), 8385-8405. DOI: 10.1002/2017JC012974

Woodgate, R., Aagaard, K., Muench, R., Gunn, J., Björk, G., Rudels, B., Roach, A., and Schauer, U. (2001). The arctic ocean boundary current along the eurasian slope and the adjacent lomonosov ridge: Water mass properties, transports and transforma- tions from moored instruments. Deep Sea Research, 48(8):1757–1792.

Woodgate, R., Weingartner, T. & Lindsay, R. (2010), The 2007 Bering Strait Oceanic Heat Flux and anomalous Arctic Sea-ice Retreat, Geophysical Research Letters, 37, L01602. DOI: 10.1029/2009GL041621

Woodgate, R. (2013). Arctic ocean circulation: going around at the top of the world. Nature Education Knowledge, 4:8.

Woods, C. and Caballero, R. (2016). The role of moist intrusions in winter arctic warming and sea ice decline. Journal of Climate, 29(12):4473–4485.

Zhang, J., Steele, M., Runciman, K., Dewey, S., Morison, J., Lee, C., Rainville, L., Cole, S., Krishfield, R., Timmermans, M., et al. (2016). The beaufort gyre intensification and stabilization: A model-observation synthesis. Journal of Geophysical Research: Oceans, 121(11):7933–7952.

Zhao, M., Timmermans, M. L., Cole, S., Krishfield, R., Proshutinsky, A., & Toole, J. (2014). Characterizing the eddy field in the Arctic Ocean halocline. Journal of Geophysical Research: Oceans, 119, 8800–8817. DOI: 10.1002/2014JC010488